ISSN 1949-8470 (online)

World Journal of *Radiology*

World J Radiol 2019 January 28; 11(1): 1-18

Published by Baishideng Publishing Group Inc

World Journal of Radiology

Contents

Monthly Volume 11 Number 1 January 28, 2019

ORIGINAL ARTICLE

Basic Study

Retrospective Study

World Journal of Radiology
Volume 11 Number 1 January 28, 2019

Contents

NAME OF JOURNAL
World Journal of Radiology

ISSN
ISSN 1949-8470 (online)

LAUNCH DATE
January 31, 2009

FREQUENCY
Monthly

EDITORS-IN-CHIEF
Venkatesh Mani

EDITORIAL BOARD MEMBERS
https://www.wjgnet.com/1949-8470/editorialboard.htm

EDITORIAL OFFICE
Jin-Lei Wang, Director

PUBLICATION DATE
January 28, 2019

INSTRUCTIONS TO AUTHORS
https://www.wjgnet.com/bpg/gerinfo/204

GUIDELINES FOR ETHICS DOCUMENTS
https://www.wjgnet.com/bpg/GerInfo/287

GUIDELINES FOR NON-NATIVE SPEAKERS OF ENGLISH
https://www.wjgnet.com/bpg/gerinfo/240

PUBLICATION MISCONDUCT
https://www.wjgnet.com/bpg/gerinfo/208

ARTICLE PROCESSING CHARGE
https://www.wjgnet.com/bpg/gerinfo/242

STEPS FOR SUBMITTING MANUSCRIPTS
https://www.wjgnet.com/bpg/GerInfo/239

ONLINE SUBMISSION
https://www.f6publishing.com

World Journal of Radiology

Submit a Manuscript: https://www.f6publishing.com

World J Radiol 2019 January 28; 11(1): 1-9

DOI: 10.4329/wjr.v11.i1.1

ISSN 1949-8470 (online)

ORIGINAL ARTICLE

Basic Study

Effects of muscle fiber orientation to main magnetic field on muscle metabolite profiles for magnetic resonance spectroscopy acquisition

Duanghathai Pasanta, Tipparat Kongseha, Suchart Kothan

ORCID number: Duanghathai Pasanta (0000-0001-6921-2915); Tipparat Kongseha (0000-0002-2416-4902); Suchart Kothan (0000-0001-7390-8878).

Author contributions: Pasanta D, Kongseha T and Kothan S contributed to the conception and design of this study; as well as the acquisition, analysis, and interpretation of all data. These authors wrote drafts of the article and made critical revisions related to the intellectual content of the manuscript and approved the final version of the article for publication.

Supported by Department of Radiologic Technology, Faculty of Associated Medical Sciences, Chiang Mai University, Thailand.

Conflict-of-interest statement: All authors have no conflicts of interest to report.

Manuscript source: Unsolicited manuscript

Duanghathai Pasanta, Tipparat Kongseha, Suchart Kothan, Department of Radiologic Technology, Faculty of Associated Medical Sciences, Chiang Mai University, Chiang Mai 50200, Thailand

Corresponding author: Suchart Kothan, PhD, Associate Professor, Department of Radiologic Technology, Faculty of Associated Medical Sciences, Chiang Mai University, 110 Intawaroros Rd., Sripoom, Chiang Mai 50200, Thailand. suchart.kothan@cmu.ac.th
Telephone: +66-53-939213
Fax: +66-53-939207

Abstract

BACKGROUND

Proton magnetic resonance spectroscopy (^{1}H MRS) is a technique widely used for investigating metabolites in humans. Lipids are stored outside the muscle cell are called extramyocellular lipids (EMCL), and lipids stored on the inside of muscle cells are called intramyocellular lipids (IMCL). The relationship between metabolic syndrome and IMCL has been extensively studied.

AIM

To determine the effects of muscle fiber orientations on muscle metabolites using ^{1}H MRS.

METHODS

Chicken muscles were used as the subject in this study. MRS spectra were performed on a 1.5T Magnetic resonance imaging machine (1.5 Tesla Philips Achieva). A single voxel (8 mm × 8 mm × 20 mm) was placed on the chicken extensor iliotibialis lateralis muscle with the muscle fiber oriented at 0°, 30°, 60°, and 90° to the main magnetic field. ^{1}H MRS spectra were acquired using a point-resolved spectroscopy, TR = 2000 ms, TE = 30 ms, and NSA = 256. Metabolites of interest from each orientation to the main magnetic field were compared using Wilcoxon signed-rank test. Differences less than 0.05 were considered to be statistically significant with 95%CI.

RESULTS

The metabolite profiles were different for each orientation of muscle fibers to the main magnetic field. The orientation at 90° was the most different compared to other orientations. The quantity of IMCL and EMCL exhibited statistically significantly changes with impacts at 30°, 60°, and 90° when compared with muscles aligned at 0° to the main magnetic field. Statistical analysis showed statistically significant IMCL (CH_3), EMCL (CH_3), and IMCL (CH_2) at 30°, 60°, and

Received: August 6, 2018
Peer-review started: August 7, 2018
First decision: October 16, 2018
Revised: November 14, 2018
Accepted: January 9, 2019
Article in press: January 10, 2019
Published online: January 28, 2019

90° (P = 0.017, 0.018, and 0.018, respectively) and EMCL (CH_2) at 30° and 60° (P = 0.017 and 0.042, respectively). EMCL (CH_2) at 90° was unable to be measured in this study. The muscle lipids quantified at 30°, 60°, and 90° tended to be lower when compared to 0°.

CONCLUSION
Careful positioning is one of the most important factors to consider when studying ^{1}H MRS metabolites in muscles to ensure reproducibility and uniformity of muscle metabolite spectra.

Key words: Proton magnetic resonance spectroscopy; Metabolite; Muscle fiber orientation; Intramyocellular lipids; Extramyocellular lipids; Magnetic susceptibility

Core tip: Proton magnetic resonance spectroscopy (^{1}H MRS) is a technique that is widely used for intramyocellular lipids and extramyocellular lipids quantification in muscles, as evidenced in various studies. However, different muscle positions can potentially lead to inconsistency in metabolite quantification and can also impede interpretation of data, which can lead to misinformation. This study reveals that the muscle orientation at 0°, 30°, 60°, and 90° to the main magnetic field significantly affects the metabolite profile and quantification. The metabolite profile changes due to the muscle fiber orientation demonstrate that the positioning potentially causes inaccuracy in ^{1}H-MRS spectrum analysis.

Citation: Pasanta D, Kongseha T, Kothan S. Effects of muscle fiber orientation to main magnetic field on muscle metabolite profiles for magnetic resonance spectroscopy acquisition. *World J Radiol* 2019; 11(1): 1-9
URL: https://www.wjgnet.com/1949-8470/full/v11/i1/1.htm
DOI: https://dx.doi.org/10.4329/wjr.v11.i1.1

INTRODUCTION

Proton magnetic resonance spectroscopy (^{1}H MRS) is a technique widely used for investigating metabolites in humans. With insulin resistance, the body stores more lipids in various compartments of organs that normally do not contain fat, such as the liver and muscles. The lipids stored outside muscle cells are called extramyocellular lipids (EMCL), and lipids stored inside muscle cells are called intramyocellular lipids (IMCL). Various studies have shown that IMCL levels are inversely associated with type II diabetes. It is also thought that this relationship is the cause of skeleton muscle insulin resistance and may be an early sign of defective glucose uptake[1,2]. The relationship between metabolic syndrome and IMCL has been studied extensively. Unlike muscle biopsy, ^{1}H MRS is a noninvasive technique suitable for studies that require constant follow-ups and has been popular for use in metabolomics research. Ectopic fat accumulation among various organs, specifically IMCL, is being investigated to gain a better understanding of the pathological mechanisms[3]. The ^{1}H MRS in muscle is usually performed in lower extremity muscles, such as the tibialis anterior, soleus, and gastrocnemius, due to their accessibility for MRI positioning. Nevertheless, much research demonstrates that muscle ^{1}H MRS is influenced by the positioning of the organ of interest[4-6]. It has also been discovered that the orientation of muscle with respect to the direction of the main magnetic field (B_0) affects residual dipolar coupling and bulk magnetic susceptibility on spectra profiles, leading to inconsistencies of metabolite quantification. Hence, it can impede the interpretation and therefore lead to misinformation[7]. Muscle fiber orientation can be determined from dipolar coupling; however, this is an indirect method for measuring muscle fiber orientation[8].

Currently, there are no studies that directly measure muscle alignment to B_0 or how the muscle fibers are aligned to B_0 as it is impossible to measure the exact angle of muscle to B_0 in humans.

The purpose of this study is to determine the effects the muscle fiber angle to B_0 has on the spectrum profile and to obtain muscle lipid quantification without the effect of

muscle contraction. This study used extensor iliotibialis lateralis muscles from chicken thighs as the muscle of interest. Because it is an upper muscle, it is able to give a clear visualization of the muscle fiber alignment to B_0.

MATERIALS AND METHODS

Study subjects

Chicken extensor iliotibialis lateralis muscle was used in this study. A chicken thigh was purchased at local store and was properly skinned, carefully avoiding any muscle tissue. Next, the chicken thigh was placed into a sterile package and stored at 4°C until the time of study.

Data acquisition and analysis

Magnetic resonance imaging with a 1.5 Tesla Philips Achieva (Philips Medical Systems, Best, the Netherlands) equipped with a knee coil was used for the ^{1}H MRS spectrum acquisition. The chicken extensor iliotibialis lateralis muscle fiber alignment was used as the reference point and placed in the middle of the coil, positioned at 0˚, 30˚, 60˚, and 90˚ to B_0. T2-weighted turbo spin echo images in coronal plane and axial plane of muscle were first acquired for voxel localization. Single-voxel point resolved spectroscopy pulse sequence was used for spectrum acquisition with TR = 2000 ms, TE = 30 ms, and NSA = 256 when equipped with automatic shimming. A voxel of size 8 × 8 × 20 mm^3 was carefully placed on the iliotibialis lateralis muscle, carefully avoiding any other muscle fasciae, bulk fat, and air, with verification being obtained from MRI images. Spectra acquisition was repeated 7 times at each angle. All of the spectra in this study were acquired within two hours.

JMRUI version 6.0 β was used for metabolite peak assignment and analysis[9-11]. Spectrum fitting was done by the AMARES algorithm[12] with prior knowledge for line width, and chemical shifts of each peak were obtained from previous studies[13]. Residual water tail was used as the chemical shift reference at 4.72 ppm and then was suppressed with an HLSVD filtering algorithm[14]. The spectrum line shape was estimated with Lorentzian. The zero order phases were estimated by AMARES, and first order phase was fixed at zero with data being truncated by two points for baseline correction. The fitted spectrum showed various peaks of metabolites of interest in the following manner: IMCL (CH_3) at 0.9 ppm, EMCL (CH_3) at 1.1 ppm, IMCL (CH_2) at 1.3 ppm, EMCL (CH_2) at 1.5 ppm, and creatine (Cr) at 3.02 ppm. IMCL and EMCL amplitudes fitted by AMARES were calculated into the ratio per signal intensity of Cr as the internal reference.

Statistical analysis

The data analysis was performed using Origin 8.0 software (OriginLab, Northampton, MA, United States). The calculated results of spectrum fitting at 0°, 30°, 60°, and 90° of muscle fiber orientation to B_0 were compared using Wilcoxon signed-rank test. Statistically significant differences were those less than 0.05, and there was a 95% level of confidence based on this testing. Any metabolite that was undetectable or any measurement that yielded unreliable results by JMRUI was excluded from the statistical analysis.

RESULTS

Chicken muscle spectra were acquired with a carefully placed voxel on the iliotibialis lateralis muscle, avoiding other muscle fasciae, bulk fat, and air, at different angles to B_0 (Figure 1). In previous nuclear magnetic resonance studies, the chicken pectoral muscle tissue showed similar spectra and lipid chemical shifts to that of human muscles[15]. In this study, metabolites of interest were assigned with IMCL (CH_3) at 0.9 ppm, EMCL (CH_3) at 1.1 ppm, IMCL (CH_2) at 1.3 ppm, EMCL (CH_2) at 1.5 ppm, and Cr at 3.02 ppm. This was then quantified with an AMARES algorithm provided by a JMRUI.

The representative spectra profile shown in Figure 2 clearly reveals that muscle spectra were affected by relative muscle fiber orientation to B_0. The spectrum profile at 0° show more well-defined EMCL and IMCL spectra in both the CH_3 and CH_2 groups. The line widths of IMCL and EMCL in both CH_3 and CH_2 groups appear to be broadening, with an increasing angle of muscle alignment to B_0, resulting in overlapping peaks. Additionally, the spectra at 30°, 60°, and 90° appeared to have smaller signal intensity and higher noise when compared to the spectra from 0°, as they were multiplied by a factor of 2. However, Cr at 3.02 ppm remained unaffected

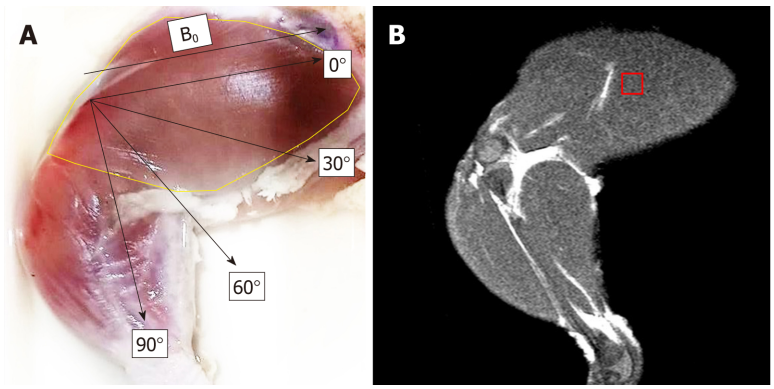

Figure 1 Chicken's extensor iliotibialis was used to perform muscle quantification for muscle metabolites by proton magnetic resonance spectroscopy. A: Skinned chicken thigh showing the extensor iliotibialis lateralis muscle fiber orientation (in the yellow marked area) at various angles (0°, 30°, 60°, and 90°) with regard to the main magnetic field (B_0); B: T2-weighted turbo spin echo MRI images show areas of proton magnetic resonance spectroscopy voxel placement. B_0: Main magnetic field direction.

at every angle. The spectrum profile of orientation at 90° was the most different compared to other orientations. Figure 3 shows the muscle spectrum at 30°, 60°, and 90° subtracted by the baseline at 0°, which revealed drastically different spectrum profiles with alterations in each angle of muscle fiber from the residual form spectra subtraction.

The AMARES algorithm with prior knowledge was performed by spectrum fitting into individual metabolites. Figure 4 shows that the quantification results obtained for EMCL (CH_2) at 1.5 ppm were undetectable for any spectra obtained from 90° orientation and that EMCL (CH_2) was undetectable from 2 spectra at 60°. It appears likely that the spectrum peak broadening made it difficult to differentiate metabolite peaks. The IMCL (CH_3), EMCL (CH_3), IMCL (CH_2), and EMCL (CH_2) were then calculated into a ratio to Cr as the internal reference in each spectrum acquired. The Wilcoxon signed-rank test was used for statistical analysis of lipid ratios to Cr at 0° and to other angles with *P*-values < 0.05. Lipid ratios to Cr were significantly different when comparing spectra at different orientations to 0° (Table 1). However, at 90°, the EMCL (CH_2) peak could not be determined and was excluded from statistical analysis. EMCL and IMCL ratios to Cr were normalized by the mean lipid ratio at 0° to access the differences in ratios when compared to the relative muscle fiber orientation at 0°. The bar graph in Figure 5 demonstrates that the lipid ratios at different angles tended to be lower when compared to lipid ratios obtained at 0°. The comparisons between 0° and at 30°, 60°, and 90° were performed with Wilcoxon signed-rank test and were found to be significantly different from EMCL and IMCL ratios that were obtained from orientations at 0° in every muscle orientation (*P*-value < 0.05).

DISCUSSION

Muscle ^{1}H MRS spectra are known for their unique characteristics, such as dipolar coupling and bulk magnetic susceptibility. Bulk susceptibility was observed to be involved with separation of the EMCL and IMCL peaks, while residual dipolar coupling influenced the resonance of Cr and phosphocreatine. Both dipolar couplings and bulk magnetic susceptibility are orientation dependent. The dipolar coupling effect the aqueous metabolite, while the bulk magnetic susceptibility effects are seen on orientation-dependent structures such as EMCL.

Bulk magnetic susceptibility is an effect that depends on orientation and tissue type, causing nuclei to differently experience the magnetic fields from the external B_0[16]. Our study has shown that the effects of bulk magnetic susceptibility are caused by orientation with B_0. The IMCL and EMCL qualification was affected by the muscle orientation to B_0. Bulk magnetic susceptibility plays an important role in differentiating IMCL and EMCL resonance peaks, and causes wider spectrum bands, leading to shifts of resonance peaks that can affect the EMCL resonance. The results of the EMCL/Cr ratios in this study appear to be consistent with wider standard deviation (SD) values that are obtained when compared to IMCL/Cr taken from the same angle to B_0.

In this study, the spectra obtained at the other angles appear to have smaller

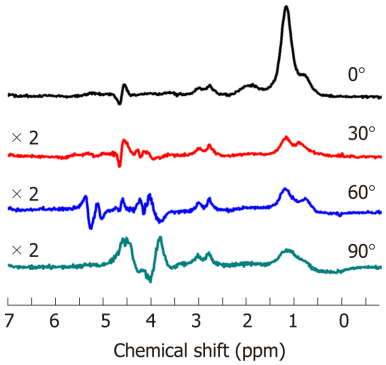

Figure 2 Original proton magnetic resonance spectroscopy spectra at different angles. Muscle spectra at 0° are shown with spectra oriented at 30°, 60°, and 90° multiplied by a factor of 2. The spectrum at 0° showed the most-well defined lipid peaks IMCL (CH_3), EMCL (CH_3), IMCL (CH_2), and EMCL (CH_2). EMCL: Extramyocellular lipids; IMCL: Intramyocellular lipids.

amplitudes when compared to those taken at 0°. Cr is able to pass through cell membranes and therefore is not affected by muscle alignment with the main magnetic field. EMCL is more affected by positioning because of the EMCL environment, which is attached to muscle fiber, and because it is orientation dependent. IMCL can rotate in muscle cytosol in an aqueous state and can therefore average bulk magnetic susceptibility effects[16,17]. In this study, spectrum profiles were different for each orientation of muscle fibers to the main magnetic field. The results suggest that the ^{1}H MRS spectrum was affected not only by pennation angle, as observed in earlier studies[5] but also by the relative muscle alignment to B_0.

Any prior knowledge concerning AMARES algorithms is known to improve metabolite quantification, but it also potentially causes error if the spectrum that was fitted is not a typical spectrum profile. A possible explanation for these results may be because the prior knowledge in the algorithm was obtained from typical human muscle spectrum, while spectrum profiles taken from various positions and orientations of muscle will tend to have peaks that are overlapped, and therefore are almost indistinguishable. This is particularly true for IMCL and EMCL resonance frequencies that were affected by bulk magnetic susceptibility.

These changes in spectrum profiles lead to inaccuracies in metabolite quantification. Different positions with the same qualification algorithms can lead to inaccuracies in metabolite quantification as well. This phenomenon occurs because prior knowledge and the metabolite qualification of metabolites was taken from typical orientations or from a muscle that almost parallels the main magnetic field, such as the tibialis anterior. It is impossible and unlikely to obtain a typical spectrum or prior knowledge from each and every angle. Additionally, the metabolites need to be studied in various muscles for various reasons, especially in deep muscles that are difficult to biopsy. It is important to set a universal standard for muscle orientation in ^{1}H MRS or to obtain a typical spectrum for each muscle of interest to reduce any potential errors and to increase reproducibility.

However, this study observed only small changes from Cr at 3.02 ppm, which was possibly caused by the group rotation of a Cr methyl group that averages these effects out. While phosphocreatine peaks occurred at 4.1 ppm, there were no splitting peaks from any residual dipolar coupling effects. In agreement with previous studies, the residual dipolar coupling vanished after 1-2 h postmortem. This was approximately the same time at which phosphocreatine depletion occurred from energy failure[18]. Our results demonstrated that bulk magnetic susceptibility may play a vital role in the separation and qualification of IMCL and EMCL, without the effects being caused from muscle contraction and residual dipolar coupling.

This present study also indicates the effects of muscle orientation on ^{1}H MRS spectrum data acquired from clinical field evidence and from other species. These results agree with the findings of other studies[18] in that bulk magnetic susceptibility is not exclusively seen in human muscles but is also found in both other mammals and poultry. This tendency occurs even when considering any observed bulk magnetic susceptibility that persists even for postmortem ^{1}H MRS muscle spectra. A limitation of this pilot study that needs to be acknowledged is that the sample size is relatively small, and data were acquired from chickens with no diet control prior to the study. Additionally, there have been no previous studies done on any of the factors that affect IMCL and EMCL levels in chickens. Furthermore, prior knowledge for AMARES algorithms was obtained from human muscles, which can potentially

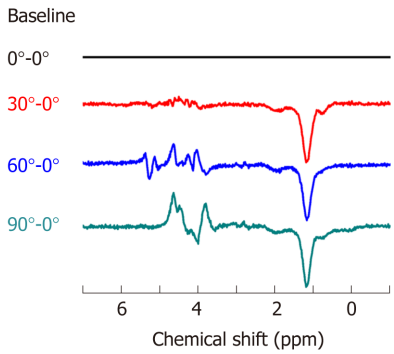

Figure 3 Muscle metabolite spectra at 30°, 60°, and 90° subtracted from baseline set at 0°. Muscle spectra at 30°, 60°, and 90° without multiplied factors are subtracted from spectrum baseline at 0°.

cause quantification errors.

After taking these variables into account, these findings confirm previous findings and provide additional evidence suggesting that muscle spectra can be affected by the relative muscle orientation to the main magnetic field. Taken together, these findings indicate that these variables of muscle orientation must be taken into consideration. There are limitations in this study, such as the small number of samples and the small size of chicken muscles compared to human muscle. In conclusion, the metabolite profile changes are due to the muscle fiber orientation, which demonstrates that positioning potentially causes inaccuracies in ^{1}H-MRS spectrum analysis.

Table 1 The median (25th-75th percentile) values of IMCL (CH_3), EMCL (CH_3), IMCL (CH_2), and EMCL (CH_2) ratios to creatine with the muscle positioned at 0°, 30°, 60°, and 90° to the main magnetic field

Angle	Metabolite							
	IMCL (CH_3), 0.9 ppm	*P* value	EMCL (CH_3), 1.1 ppm	*P* value	IMCL (CH_2), 1.3 ppm	*P* value	EMCL (CH_2), 1.5 ppm	*P* value
0°	1.44 (1.36-1.47)	-	4.25 (4.22-5.35)	-	2.96 (2.53-2.99)	-	3.08 (2.09-3.46)	-
30°	0.80 (0.77-0.81)	0.017[a]	1.23 (1.16-1.33)	0.017[a]	0.55 (0.46-0.60)	0.017[a]	0.28 (0.04-0.44)	0.017[a]
60°	1.15 (0.86-1.19)	0.018[a]	2.03 (1.69-2.08)	0.018[a]	0.77 (0.68-0.91)	0.018[a]	0.04 (0.04-0.11)	0.042[a]
90°	0.64 (0.62-0.64)	0.018[a]	1.29 (1.27-1.32)	0.018[a]	0.30 (0.72-0.31)	0.018[a]	-	-

The *P*-value shows the comparison between the metabolite ratios to creatine at 0° *vs* the different angles, as determined by Wilcoxon signed-rank test (n = 7). Data are expressed as medians (25th-75th percentiles).
[a]*P*-value < 0.05, significantly different.
EMCL: Extramyocellular lipids; IMCL: Intramyocellular lipids.

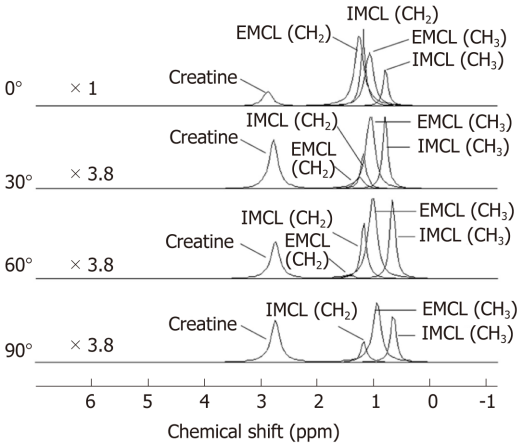

Figure 4 Metabolites identified by AMARES algorithm. Metabolites are shown in the following quantities: IMCL (CH_3) at 0.9 ppm, EMCL (CH_3) at 1.1 ppm, IMCL (CH_2) at 1.3 ppm, EMCL (CH_2) at 1.5 ppm, and creatine at 3.02 ppm. At 30°, 60°, and 90°, spectra were shown by a factor of 3.8. Spectrum of muscle positioned at 90° to the main magnetic field was unable to be identified for EMCL (CH_2) at 1.5 ppm. EMCL: Extramyocellular lipids; IMCL: Intramyocellular lipids.

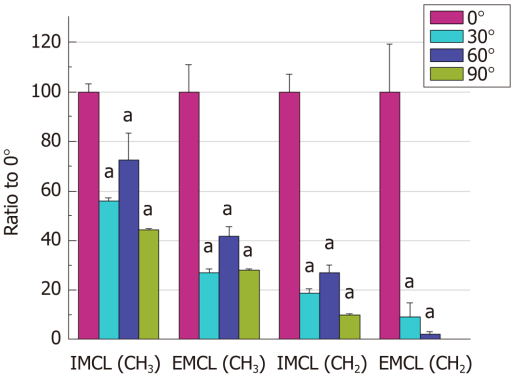

Figure 5 Metabolites at different angle ratios to muscle metabolite at 0°. Each lipid (IMCL (CH_3), EMCL (CH_3), IMCL (CH_2), and EMCL (CH_2)) was calculated as a ratio to creatine and then was normalized with the average of lipid/Cr ratio set at 0°. At 30°, 60°, and 90°, there was a tendency for the ratio to decrease when compared to 0°. The comparisons between 0° and the different angles were performed using Wilcoxon signed-rank test with [a]*P*-value < 0.05 being significantly different. Cr: Creatine; EMCL: Extramyocellular lipids; IMCL: Intramyocellular lipids.

ARTICLE HIGHLIGHTS

Research background

Proton magnetic resonance spectroscopy (^{1}H MRS) is a technique widely used for investigating metabolites in humans. Lipids that are stored outside the muscle cell are called extramyocellular lipids (EMCL), and lipids stored on the inside of muscle cells are called intramyocellular lipids

(IMCL). The relationship between metabolic syndrome and IMCL has been extensively studied. However, muscle position in relation to the main magnetic field can affect spectra profiles, leading to inconsistency of metabolite quantification, which can then lead to misinterpretation.

Research motivation

There is no current study that has directly measured muscle alignment to the main magnetic field or how the muscle fibers are aligned between studies, as it is impossible exactly measure the angle of muscle relative to the main magnetic field in humans.

Research objectives

To determine the effects of the muscle fiber angle to the main magnetic field for obtaining spectrum profiles and muscle lipid quantification without the effects of muscle contraction. This study used extensor iliotibialis lateralis muscles taken from the thigh of a chicken as the muscle of interest. Since it is the uppermost muscle, it provides a clear visualization of the muscle fiber alignment related to the main magnetic field.

Research methods

Chicken extensor iliotibialis lateralis muscles were used as the muscle of interest in this study. Magnetic resonance imaging (1.5 Tesla Philips Achieva) was used for the ^{1}H MRS spectrum acquisition. The chicken extensor iliotibialis lateralis muscle fiber alignment was used as the reference and was place in the middle of the coil, positioned at 0˚, 30˚, 60˚, and 90˚ to the main magnetic field. Single voxel Point Resolved Spectroscopy pulse sequence was used for spectrum acquisition, having a voxel size of 8 mm × 8 mm × 20 mm. It was carefully placed on the iliotibialis lateralis muscle. Spectra acquisition was repeated 7 times for each angle. JMRUI version 6.0 β was used for metabolite peak assignment and analysis. Spectrum fitting was done by an AMARES algorithm with prior knowledge. The fitted spectrum showed various peaks of metabolites of interest in the following manner: IMCL (CH_3) at 0.9 ppm, EMCL (CH_3) at 1.1 ppm, IMCL (CH_2) at 1.3 ppm, EMCL (CH_2) at 1.5 ppm, and Cr at 3.02 ppm. IMCL and EMCL amplitudes fitted by AMARES were calculated into the ratio per signal intensity of Cr in each spectrum as the internal reference. The results of spectrum fitting at 0°, 30°, 60°, and 90° of muscle fiber orientation to the main magnetic field were compared using Wilcoxon signed-rank test.

Research results

The results showed that the metabolite profiles in each orientation of muscle fiber to the main magnetic field were different. The orientation at 90° was the most different compared to the other orientations. The quantity of muscle metabolites was statistically significantly changed at 30°, 60°, and 90° of muscle fiber relative to the main magnetic field when compared to 0° relative to the main magnetic field. Statistical analysis showed statistically significant differences for IMCL (CH_3), EMCL (CH_3), IMCL (CH_2) at 30°, 60°, and 90° (P = 0.017, 0.018, and 0.018, respectively) and EMCL (CH_2) at 30° and 60° (P = 0.017 and 0.042, respectively). EMCL (CH_2) at 90° was unable to be measured in this study. Furthermore, the muscle lipids quantified at 30°, 60°, and 90° tended to be lower when compared to 0°. The metabolite profile changed due to the muscle fiber orientation, indicating that positioning potentially causes inaccuracies in ^{1}H-MRS spectrum analysis.

Research conclusions

This study has determined that the basic muscle orientations to the main magnetic field can and do affect ^{1}HMRS spectrum profiles and quantification. Muscle orientation is often treated with less care in studies on ^{1}H MRS. These metabolite profile changes are due to the muscle fiber orientation, which demonstrates that the positioning potentially causes inaccuracy in ^{1}H-MRS spectrum analysis.

Research perspectives

^{1}H MRS practitioners and users need to be especially careful when positioning any muscles or any organs of interest in order to reduce error, to be able to compare spectrum results across various institutions and to ensure reproducibility and uniformity.

REFERENCES

1 **Machann J**, Stefan N, Schick F. (1)H MR spectroscopy of skeletal muscle, liver and bone marrow. *Eur J Radiol* 2008; **67**: 275-284 [PMID: 18406092 DOI: 10.1016/j.ejrad.2008.02.032]

2 **Jacob S**, Machann J, Rett K, Brechtel K, Volk A, Renn W, Maerker E, Matthaei S, Schick F, Claussen CD, Häring HU. Association of increased intramyocellular lipid content with insulin resistance in lean nondiabetic offspring of type 2 diabetic subjects. *Diabetes* 1999; **48**: 1113-1119 [PMID: 10331418 DOI: 10.2337/diabetes.48.5.1113]

3 **Baum T**, Cordes C, Dieckmeyer M, Ruschke S, Franz D, Hauner H, Kirschke JS, Karampinos DC. MR-based assessment of body fat distribution and characteristics. *Eur J Radiol* 2016; **85**: 1512-1518 [PMID: 26905521 DOI: 10.1016/j.ejrad.2016.02.013]

4 **Velan S**, Said N, Narasimhan K, Spencer R, Raylman R, Rajendran V, Alway S. Ankle orientation alters bulk susceptibility and residual dipolar couplings during plantar flexion and dorsiflexion of skeletal muscle. Proceedings 16th Scientific Meeting, International Society for Magnetic Resonance in Medicine; 2008 May 3-9; Canada.

5 **Takashima H**, Shishido H, Imamura R, Akatsuka Y, Taniguchi K, Nakanishi M, Suzuki J, Nagahama H,

Sakurai Y, Sakata M. Effect of ankle flexion on the quantification of MRS for intramyocellular lipids of the tibialis anterior and the medial gastrocnemius. *Radiol Phys Technol* 2015; **8**: 209-214 [PMID: 25676697 DOI: 10.1007/s12194-015-0309-2]

6 **Marjańska M**, Eberly LE, Adriany G, Verdoliva SN, Garwood M, Chow L. Influence of foot orientation on the appearance and quantification of 1H magnetic resonance muscle spectra obtained from the soleus and the vastus lateralis. *Magn Reson Med* 2012; **68**: 1731-1737 [PMID: 22298295 DOI: 10.1002/mrm.24198]

7 **Khuu A**, Ren J, Dimitrov I, Woessner D, Murdoch J, Sherry AD, Malloy CR. Orientation of lipid strands in the extracellular compartment of muscle: effect on quantitation of intramyocellular lipids. *Magn Reson Med* 2009; **61**: 16-21 [PMID: 19097207 DOI: 10.1002/mrm.21831]

8 **Vermathen P**, Boesch C, Kreis R. Mapping fiber orientation in human muscle by proton MR spectroscopic imaging. *Magn Reson Med* 2003; **49**: 424-432 [PMID: 12594744 DOI: 10.1002/mrm.10396]

9 **Naressi A**, Couturier C, Devos JM, Janssen M, Mangeat C, de Beer R, Graveron-Demilly D. Java-based graphical user interface for the MRUI quantitation package. *MAGMA* 2001; **12**: 141-152 [PMID: 11390270 DOI: 10.1007/bf02668096]

10 **Stefan D**, Cesare FD, Andrasescu A, Popa E, Lazariev A, Vescovo E, Strbak O, Williams S, Starcuk Z, Cabanas M, Ormondt DV, Graveron-Demilly D. Quantitation of magnetic resonance spectroscopy signals: the jMRUI software package. *Meas Sci Technol* 2009; **20**: 104035 [DOI: 10.1088/0957-0233/20/10/104035]

11 Physical status: the use of and interpretation of anthropometry, report of a WHO expert committee. Geneva: World Health Organization, 1995. Available from: URL: http://www.who.int/iris/handle/10665/37003

12 **Vanhamme L**, van den Boogaart A, Van Huffel S. Improved method for accurate and efficient quantification of MRS data with use of prior knowledge. *J Magn Reson* 1997; **129**: 35-43 [PMID: 9405214 DOI: 10.1006/jmre.1997.1244]

13 **Weis J**, Johansson L, Ortiz-Nieto F, Ahlström H. Assessment of lipids in skeletal muscle by LCModel and AMARES. *J Magn Reson Imaging* 2009; **30**: 1124-1129 [PMID: 19780186 DOI: 10.1002/jmri.21900]

14 **Pijnappel WWF**, van den Boogaart A, de Beer R, van Ormondt D. SVD-based quantification of magnetic resonance signals. *J Magn Reson* 1969; **97**: 122-134 [DOI: 10.1016/0022-2364(92)90241-X]

15 **Le Roy CI**, Mappley LJ, La Ragione RM, Woodward MJ, Claus SP. NMR-based metabolic characterization of chicken tissues and biofluids: a model for avian research. *Metabolomics* 2016; **12**: 157 [PMID: 27729831 DOI: 10.1007/s11306-016-1105-7]

16 **Boesch C**, Machann J, Vermathen P, Schick F. Role of proton MR for the study of muscle lipid metabolism. *NMR Biomed* 2006; **19**: 968-988 [PMID: 17075965 DOI: 10.1002/nbm.1096]

17 **Szczepaniak LS**, Dobbins RL, Stein DT, McGarry JD. Bulk magnetic susceptibility effects on the assessment of intra- and extramyocellular lipids in vivo. *Magn Reson Med* 2002; **47**: 607-610 [PMID: 11870849 DOI: 10.1002/mrm.10086]

18 **Ntziachristos V**, Kreis R, Boesch C, Quistorff B. Dipolar resonance frequency shifts in 1H MR spectra of skeletal muscle: confirmation in rats at 4.7 T in vivo and observation of changes postmortem. *Magn Reson Med* 1997; **38**: 33-39 [PMID: 9211377 DOI: 10.1002/mrm.1910380107]

P- Reviewer: Cheng TH, Gao BL, Labusca L

S- Editor: Ma YJ **L- Editor:** A **E- Editor:** Bian YN

World Journal of Radiology

Submit a Manuscript: https://www.f6publishing.com

World J Radiol 2019 January 28; 11(1): 10-18

DOI: 10.4329/wjr.v11.i1.10

ISSN 1949-8470 (online)

ORIGINAL ARTICLE

Retrospective Study

Extravascular findings during upper limb computed tomographic angiography focusing on undiagnosed malignancy

Romman Nourzaie, Jeeban Das, Hiba Abbas, Narayanan Thulasidasan, Panos Gkoutzios, Shahzad Ilyas, Leo Monzon, Tarun Sabharwal, Steven Moser, Athanasios Diamantopoulos

ORCID number: Romman Nourzaie (0000-0003-4306-738x); Jeeban Das (0000-0001-7619-4241); Hiba Abbas (0000-0002-8383-2747); Narayanan Thulasidasan (0000-0001-6396-3881); Panos Gkoutzios (0000-0002-7426-790X); Shahzad Ilyas (0000-0002-9043-9425); Leo Monzon (0000-0002-2284-6424); Tarun Sabharwal (0000-0002-9659-256X); Steven Moser (0000-0003-1764-1720); Athanasios Diamantopoulos (0000-0001-9970-0522).

Author contributions: Nourzaie R performed the data collection and data analysis; Nourzaie R and Das J wrote the paper; Das J, Diamantopoulos A, Moser S and Abbas H revised and corrected the paper; Diamantopoulos A and Abbas H revised the data analysis; Thulasidasan N, Gkoutzios P, Ilyas S and Sabharwal T critically revised the manuscript for important intellectual content; Moser S and Diamantopoulos A designed the research and revised the final paper.

Institutional review board statement: Exempted due to retrospective nature of study.

Informed consent statement: Patients were not required to give informed consent to the study because the analysis used anonymous data that were obtained after each patient agreed to treatment by written consent.

Conflict-of-interest statement: No conflict of interest.

Romman Nourzaie, Jeeban Das, Hiba Abbas, Narayanan Thulasidasan, Panos Gkoutzios, Shahzad Ilyas, Leo Monzon, Tarun Sabharwal, Steven Moser, Athanasios Diamantopoulos, Department of Interventional Radiology, Guys' and St. Thomas' NHS Foundation Trust, London SE17EH, United Kingdom

Corresponding author: Athanasios Diamantopoulos, MD, PhD, EBIR, Department of Interventional Radiology, Guys' and St. Thomas' NHS Foundation Trust, Westminster Bridge Road, London SE1 7EH, United Kingdom. athanasios.diamantopoulos@gstt.nhs.uk
Telephone: +44-271-887188-89482
Fax: +44-271-887188-89483

Abstract

BACKGROUND

Computer tomography angiography (CTA) has been an established method for diagnostic vascular disease of lower limbs. Recently, the method is widely used for diagnosis of vascular pathologies in the upper limbs too. It also has increased the possibilities of this scans being reviewed by no specially trained radiologists. This increases the risk of incidental non vascular findings to be missed or misinterpreted. The study is focusing in the frequency of extravascular incidental finding (EVIF) and highlights the importance for both the reporting radiologist and the referring physician recognizing the frequency of EVIFs.

AIM

To analyse the frequency of EVIF identified on computed angiography (CT) of the upper limb.

METHODS

A total of 1383 CT angiographic studies of the peripheral arterial system were performed between August 2015 and August 2017. All upper limb CTAs (n = 79) were retrospectively reviewed for the presence of non-vascular incidental findings within the chest, abdomen/pelvis, musculoskeletal system or head and neck. These EVIFs were subsequently grouped into 3 categories based on clinical significance. EVIFs of immediate clinical relevance were included in category A, findings considered indeterminate but most likely benign were placed in category B, while incidental findings of no clinical significance were included in category C.

RESULTS

Complete imaging datasets were available in 74/79 (93.7%). Patient

Manuscript source: Invited manuscript

Received: October 24, 2018
Peer-review started: October 24, 2018
First decision: December 10, 2018
Revised: January 1, 2019
Accepted: January 10, 2019
Article in press: January 10, 2019
Published online: January 28, 2019

demographics included 39 (52.7%) females and 35 (47.2%) males with a mean age of 59 ± 19.5 years (range 19-93 years). A total of 153 EVIFs were reported in 52 patients (70.3%). Of these, 44 EVIFs (28.7%) were found in the chest, 83 (54.2%) in the abdomen, 14 (9.2%) in the musculoskeletal system and 9 (5.8%) in the head and neck. Thirteen EVIFs (8.4%) identified in 11 patients were noted to be of immediate clinical significance (Category A), 50 EVIFs (32.3%) were identified in 20 patients and were considered indeterminate but most likely benign, while the remaining 91 EVIFs (59.5%) identified in 21 patients were determined to be of no clinical significance (Category C). One index case of malignancy (1.3%) and four cases of new disseminated metastatic disease (5.4%) were identified.

CONCLUSION
Our study of upper limb CTA examinations demonstrated a frequency of 8.4% for extravascular incidental findings of immediate clinical significance. We highlight the importance for both the reporting radiologist and the referring physician of the need to recognize the frequency with which EVIFs are identified in the upper limb peripheral arterial system and of the necessity for further clinical and imaging work-up.

Key words: Extravascular incidental findings; Computed angiography; Upper limbs; Arterial; Extravascular findings

Core tip: We retrospectively analysed 79 upper limb computer tomography angiographys for extravascular incidental findings (EVIFs). These were grouped into 3 categories based on clinical significance, category A (immediate), category B (indeterminate) and category C (no clinical significance). A total of 153 EVIFs were reported in 52 patients. Of these 13 EVIFs (8.4%) were Category A, 50 EVIFs (32.3%) were Category B, while 91 EVIFs (59.5%) were Category C. One index case of malignancy (1.3%) and four cases of new disseminated metastatic disease (5.4%) were identified. This highlights the importance for both the reporting radiologist and the referring physician to recognize the frequency of EVIFs.

Citation: Nourzaie R, Das J, Abbas H, Thulasidasan N, Gkoutzios P, Ilyas S, Monzon L, Sabharwal T, Moser S, Diamantopoulos A. Extravascular findings during upper limb computed tomographic angiography focusing on undiagnosed malignancy. *World J Radiol* 2019; 11(1): 10-18
URL: https://www.wjgnet.com/1949-8470/full/v11/i1/10.htm
DOI: https://dx.doi.org/10.4329/wjr.v11.i1.10

INTRODUCTION

Invasive and cross-sectional arterial phase imaging of the upper extremities are performed less frequently in comparison with lower limb or "run-off" computer tomography angiography (CTA)[1]. Indications for CTA of the upper limb include trauma, suspected upper limb ischaemia, preoperative planning prior to reconstructive surgery or haemodialysis access, or as follow-up post open surgical or endovascular arterial procedure[2].

Digital subtraction angiography (DSA) has conventionally been used as the preferred imaging modality for the upper limb arterial vasculature. However, recent developments and improvements in image acquisition and spatial resolution with multi-detector computed tomography (MDCT), combined with its inherently less-invasive nature, has resulted in CTA becoming the first-line investigation for upper limb arterial pathology[2-4].

For investigation of arterial steno-occlusive disease, CTA has been demonstrated similar diagnostic capabilities compared to DSA, as well as reduced cost, better patient tolerance and the ability to image the extravascular anatomy[2].

The discovery of extravascular incidental findings (EVIFs) can be considered an added advantage of cross-sectional arterial phase imaging. Incidental findings

discovered on CT are defined as an unforeseen pathology encountered in a patient being scanned for another indication. In the case of CT angiography, EVIFs are becoming ever more frequently encountered in daily clinical practice, especially with the exponential proliferation of CT imaging and the gradual phasing out of DSA as a first-line modality for peripheral arterial disease and acute emergent arterial imaging.

CTA offers the possibility of identifying potentially life-threatening or life-shortening pathologies and providing improved health outcomes for patients[5]. EVIFs and their clinical relevance have been well described in CT imaging of the aorta and lower-limb arterial system[5-7], CTA for EVAR planning[8], aortic dissection[9] and CTA of the head and neck[10]. The frequency and significance of EVIF on CTA of the upper limb, however, has yet to be described.

The purpose of this study was to report the frequency and more importantly the clinical relevance of extravascular lesions in patients undergoing upper limb CTA, including the frequency of index cases and progression of known cancer cases.

MATERIALS AND METHODS

Patient selection and demographics

Institutional review board review was obtained for this retrospective study (approval number: 7669, 21/09/2017). Radiology reports, digital medical records and 1383 CTA datasets of the peripheral arterial system performed between August 2015 and August 2017 at Guys and St Thomas hospitals were identified.

Peripheral CTAs imaging the upper limbs were included in the study. Patients with incomplete imaging datasets were excluded. Data on patient demographics, study indication and EVIF were reviewed. Those with significant EVIFs were reviewed to determine their clinical outcome

CT image acquisition and technique

Patients were placed supine with the extremity of interest placed above the head, palm ventral and fingers extended and straightened. CT imaging was performed with a 128 slice MDCT scanner (Siemens Somatom Definition), using bolus tracking software used to trigger intravenous contrast injection (Omnipaque 350, GE Healthcare) at a rate of 4-5 mL per second, followed by saline flush. Images were obtained using a kV between 100-120 with a delay of 20-40 s.

Standard of reference

Radiology reports, digital records, radiological information systems (RIS) records, laboratory and procedure reports were reviewed where available to confirm the presence of pre-existing malignancy and all prior imaging studies were used as the standard of reference (SOR).

Data analysis

One consultant interventional radiologists (15 years of clinical experience) and one radiology IR fellow (6 years of clinical experience) examined all upper limb CTAs and reviewed digital reports for EVIFs. All incidental findings were compared to the SOR and subsequently grouped into three categories, based on clinical significance, category A (Immediate clinical relevance), category B (findings considered indeterminate but most likely benign) and category C (incidental findings of no clinical significance).

Statistical analysis

Statistical analysis was done using the SPSS statistical software (SPSS, version 18.0 for Windows; SPSS Inc., Chicago, IL, United States). Discrete and continuous variables are presented as counts and percentages, and as mean ± SD respectively. Non-normal variables were expressed as medians and interquartile ranges (25^{th} and 75^{th} percentiles).

RESULTS

A total of seventy nine cases (79/1343, 5.8%) of peripheral CTAs imaged the upper limbs and were subsequently analyzed. From these studies, four patients were excluded as a result of incomplete imaging datasets. Of the 74 patients (52.7% females, 47.3% males) with complete upper limb CTA imaging, the mean age was 59 59 ± 19.5 years (range 19-93 years).

One hundred fifty-three EVIFs were identified in 52 patients (70.3%). 44 EVIFs

(28.7%) were noted in the chest, 83 (54.2%) were found in the abdomen, 14 (9.2%) in the musculoskeletal system and 9 (5.8%) in the head and neck.

Thirteen (8.4%) EVIFs were identified in 11 patients and were considered of immediate clinical significance (category A), demonstrated in Table 1. The majority of category A findings were noted in the chest (n = 8), with additional highly significant findings (all cases were of ascites) noted in the abdomen/pelvis (n = 3) with sclerotic bone lesions (n = 1) and osteomyelitis (n = 1) identified on examination of the musculoskeletal system.

Six category A EVIFs were concerning for a new malignancy diagnosis (n = 1) or disease progression (n = 4) or recurrence (n = 1). Details regarding further investigation and follow-up are outlined in Table 2. One male patient, symptomatic with acute upper limb ischaemia was found to have an irregular 16mm nodule in the right upper lobe with ipsilateral hilar lymphadenopathy on CT. Subsequent CT-guided biopsy confirmed histopathological diagnosis of lung adenocarcinoma.

Three patients demonstrated new progression of existing malignancy on upper limb CTA, one case of cholangiocarcinoma with new pulmonary and osseous metastases and two patients with prostate cancer and new pulmonary metastasis. Breast cancer recurrence, confirmed on CT-guided mediastinal lymph node biopsy in a patient with new chest lymphadenopathy, was also diagnosed on upper limb CTA.

A single patient with a history of prior breast cancer was found to have a new spiculated breast nodule identified on upper limb CTA but did not have follow-up imaging available at our institution.

Fifty EVIFs (32.3%) were identified in 20 patients and were considered indeterminate but most likely benign (category B) and are demonstrated in Table 3.

The majority of EVIFs were of no clinical significance (n = 21, 59.5%) and placed in category C (Table 4). The most common category C finding was simple renal cysts (n = 12).

DISCUSSION

CTA has become the principal investigation when assessing vascular patients and with the added capability of imaging extravascular structures, it offers the opportunity to discover incidental findings unrelated to the study indication. Such incidental findings can subsequently lead to the diagnosis of a life-threatening condition and can be of paramount importance in these groups of patients.

In 13 (8.4%) patients, the EVIF were identified as requiring immediate follow-up with further diagnostic tests. This is of particular importance in cases of new cancer diagnosis or progression of malignancy as survival rates may decrease significantly the earlier the cancer is identified and treated.

The results of our study compare similarly with prior studies looking at EVIF with regards to the frequency of detecting new (1.3%) or progression of pre-existing malignancy (5%). Naidu *et al*[6] described 40 highly significant EVIFs of which nine (3%) were confirmed malignancies. Iezzi *et al*[5] noted 15 index cancer cases (3.5%) in their series while Preuß *et al*[7] identified 4 malignancies (2.8%). The most common solid malignancies identified in all studies were pulmonary neoplasms. Belgrano *et al*. identified 36 solid masses of possible malignant nature (4.5%) but did not provide follow-up or correlation with histopathology [11]. Of note, and similarly to the studies by Naidu *et al*[6] and Preuß *et al*[7], we correlated the EVIFs identified in our patient cohort with the patient's clinical background, including any past history of malignancy.

Our sample size was smaller (n = 79) in comparison with prior reports regarding the frequency and clinical relevance of EVIFs on CTA studies, with patient cohorts ranging from 141[7] to 821[12], despite the fact that our retrospective study was performed over a similar time-period (24 mo) to previous articles pertaining to this topic. We can potentially account for this by recognizing that CTA of the upper limb is a relatively infrequently performed examination in comparison with arterial CT imaging of the lower limbs, the latter performed far more consistently and for a wider variety of indications.

Furthermore, the mean age of patients in our study was 59 years old, a much younger demographic in comparison to prior studies examining for EVIF on CTA exams[5-7,12]. For example, the mean age of patients in the study by Preuß *et al*[7] was 80 years old. The younger mean age in our report can be accounted for by the fact that our study demonstrated a much broader range of patient ages (18-90 years old), the median age was 67 years old, which was similar to the median age of previous studies.

To the best of our knowledge, this study is the first to evaluate for the presence of

Table 1 A total of 13 category A extravascular incidental findings (immediate clinical significance) were identified

Region	EVIF	Number of cases
Chest	Lung nodule > 1 cm	4
	Breast nodule	1
	Mediastinal lymphadenopathy	1
	Oesophageal wall thickening	1
	Pleural effusion	1
Abdomen/pelvis	Ascites	3

EVIF: Extravascular incidental finding.

head and neck extravascular incidental findings on CTA of the upper limb. Nine EVIF were present in the head and neck, however, no Category A EVIFs were identified.

Our work shows the importance of detecting EVIFs. The early detection of cancer can be significant for patient outcomes and can ultimately reduce health costs by offering a curative surgical option. This may therefore, justify reporting and following up on incidental findings. However, a cost-effective analysis of pursuing incidental findings in addition to long term studies comparing CTAs in vascular patients who did not have their extravascular findings reported needs to be conducted to adequately understand the true value of EVIFs. Attempts to provide guidance on the management of incidental findings have been made[13] however data on cost-effectiveness is sparse.

Limitations

As a retrospective study, the correlation of clinical symptoms with radiological findings was not performed for all EVIFs. In our study, follow-up data was available in 5/13 (38.5%) of Category A EVIFs, all of which pertained to suspected primary malignancy or progression of disease. This was a limitation noted in past studies[5-9] of a similar nature where there was a lack of follow up imaging. For example, in the study by Naidu *et al*[6], 42% of patients did not have follow-up imaging. Secondly, the use of arterial phase imaging in the examination of the abdominal and pelvic viscera can limit evaluation of hypovascular lesions and pathology more reliably detected on portal venous or delayed phase studies. Thirdly, unilateral imaging was performed in all 79 patients, of either the left or right arm, or hemithorax, therefore potentially reducing the number of EVIFs identified in each patient.

We propose a new emailing alert system in which the radiologist reporting the scan flags up any significant EVIF which would send an automated email to both the referrer and the consultant the patient is under. In addition, a clinical nurse specialist has been allocated the responsibility of ensuring these are correctly followed up. This minimises the risk of losing patients to follow-up and we recommend a similar system is put into place across all hospitals.

Conclusion

In conclusion, our work signifies the importance of reporting both vascular and extravascular findings in CTAs, especially in this patient group of higher risk. Incidental findings are very common, and although most are of a benign nature, they do lead to the detection of serious life-threatening pathology which would otherwise be missed or diagnosed late. Although arterial phase CT imaging of the upper limb is a less commonly requested and performed peripheral arterial examination, both referring physicians and interpreting radiologists must recognize the frequency and relevance of incidental findings in this patient cohort allowing timely and appropriate clinical and imaging follow up.

Table 2 Details of the follow-up for the six patients with suspicious incidental findings

Incidental finding	Follow-up imaging study	Diagnosis
Multiple pulmonary nodules and sclerotic bone lesions	Plain film radiography of hip, femur, knee, CT TAP (staging)	Metastatic cholangiocarcinoma (new lung and bone lesions)
Pulmonary nodule (> 1 cm) with hilar lymph node enlargement	CT TAP (staging)	Lung adenocarcinoma (index diagnosis)
Mediastinal lymphadenopathy (prior breast cancer)	CT TAP (staging), CT-guided lymph node biopsy	Metastatic breast cancer (recurrence of primary cancer)
Breast nodule (prior breast cancer)	Breast ultrasound (recommended)	Follow up imaging unavailable
Multiple lung nodules	CT TAP (staging)	Metastatic prostate cancer (new lung lesions)
Lung nodule	CT TAP (staging)	Metastatic prostate cancer (new lung lesions)

CT: Computer tomography.

Table 3 Category B lesions (indeterminate but most likely benign) accounted for 50 extravascular incidental findings

Region	EVIF	Number of cases
Chest	Lung nodule (> 4, < 10 mm)	2
	Lung lobar atelectasis	1
	Pleural thickening	1
Abdomen/pelvis	Prominent lymph nodes (≤ 1 cm)	13
	Hiatal hernia	5
	Enlarged prostate gland	3
	Adrenal hyperplasia	2
	Renal infarct	1
	Urinary bladder wall thickening	1
	CBD dilatation	1
	Gallbladder distension	1
	Intrahepatic biliary duct dilatation	1
	Prostatic calcification	1
	Inguinal hernia	1
Musculoskeletal	Sclerotic bone lesions	5
	Pectoralis major atrophy	1
	Spinal stenosis	1
	Spondylolisthesis	1
	Spinal scoliosis	1
Head/neck	Thyroid nodule	1
	Prominent lymph nodes (≤ 1 cm)	6

EVIF: Extravascular incidental findings.

Table 4 Category C abnormalities (lesions of no clinical significance) accounted for 91 extravascular incidental findings

Region	EVIF	Number of cases
Chest	Interstitial lung disease	11
	Emphysema	8
	Pulmonary consolidation	5
	Pleural calcification	3
	Pneumatocele	3
	Bronchiectasis	1
	Pulmonary nodule < 4 mm	1
Abdomen/pelvis	Renal cyst	12
	Diverticular disease	10
	Cholecystolithiasis	6

	Atrophic kidney	5
	Focal liver fat sparing	4
	Hepatic cyst	4
	Fatty infiltration of the liver	3
	Adrenal lipoma	2
	Atrophic pancreas	1
	Calcified uterine fibroid	1
	Omental fat stranding	1
	Renal scar	1
	Splenic cyst	1
	Scrotal hydrocele	1
	Groin sinus tract	1
Musculoskeletal	Clavicle fracture (old)	1
	Pelvic fracture (old)	1
	Humeral head fracture (old)	1
	Generalised osteopenia (humeral head)	1
Head/neck	Thyroid goitre	1
	Paranasal sinus mucocele	1

EVIF: Extravascular incidental finding.

ARTICLE HIGHLIGHTS

Research background

Recent developments and improvements in image acquisition and spatial resolution with multi-detector computed tomography has resulted in computed tomographic angiography (CTA) to become the first line-line investigation for upper limb pathology, replacing the more invasive digital subtraction angiography. It has the added capability of imaging the surrounding extravascular anatomy leading to the detection of incidental mass/lesions. The significance of these "incidental" findings has mixed opinions. Whilst evidence has shown them to identify potentially life-threatening pathologies, they can also lead to an unnecessary diagnostic cascade of investigations only for the end result to be benign. We set out to report the frequency and more importantly the clinical relevance of these incidental findings to better understand their significance.

Research motivation

We set out to establish the frequency of incidental findings and to follow-up to determine their end significance in upper limb CTA. This has yet to be been described in the literature. Incidental findings can lead to an unnecessary investigation cascade and therefore we wanted to determine the proportion of incidental findings which do lead to the diagnosis of a life-threatening pathology. This will raise awareness in the medical field of the importance for both the reporting radiologist and the referring physician of the need to recognise these findings and arrange appropriate follow-up. Evidence has shown cancer pathology is picked up through their detection and therefore highlights the importance of the reporting radiologist spending extra time to report structures outside of the scan indication.

Research objectives

Our objective was to report the frequency of incidental findings in CTA of the upper limb over a 2 year period. Those with findings of significance were followed up to determine their clinical outcome. We found incidental findings in over two thirds of patients, with 8.4% of them being of immediate clinical significance and detecting one index case of malignancy and four cases of new disseminated metastatic disease. Spending extra time reporting masses/lesions outside of the intended anatomy can significantly improve patient outcomes.

Research methods

Consecutive upper limb CTAs performed at Guys and St Thomas hospitals between August 2015 to August 2017 were retrospectively reviewed for inclusion. Patient demographics, incidental findings and their follow-up were entered into an excel spreadsheet and statistical analysis was done using SPSS statistical software (SPSS, version 18.0 for Windows; SPSS Inc., Chicago, IL, United States). Incidental findings were grouped into category A (immediate), category B (indeterminate) or category C (no clinical significance). Conversely to other work in the literature, we retrospectively reviewed CTA reports rather than re-reviewing CTA images for incidental findings. This was to better reflect the current clinical practice as re-evaluation of images for incidental findings would theoretically increase their detection. Prior imaging studies were used as the standard of reference. Those with suspicious findings were followed to determine their significance.

Research results

A total of 153 extravascular incidental findings (EVIFs) were reported in 52 patients. Of these 13 EVIFs (8.4%) were Category A, 50 EVIFs (32.3%) were Category B, while 91 EVIFs (59.5%) were Category C. One index case of malignancy (1.3%) and four cases of new disseminated metastatic disease (5.4%) were identified. This is the first study to describe incidental findings in CTAs of the upper limbs. Detecting incidental findings can be of paramount importance however a large proportion also end of being benign. More work is needed in the recommendation of their follow-up and on cost-effective.

Research conclusion

The purpose of this study was to report the frequency and more importantly the clinical relevance of extravascular lesions in patients undergoing upper limb CTA, including the frequency of index cases and progression of known cancer cases. We identified one index case of malignancy, and four cases of new disseminated metastatic disease. Our work shows the importance of detecting EVIFs. The early detection of cancer can be significant for patient outcomes and can ultimately reduce health costs by offering a curative surgical option. This may therefore, justify reporting and following up on incidental findings. To the best of our knowledge, this study is the first to evaluate for the presence of head and neck extravascular incidental findings on CTA of the upper limb. Nine EVIF were present in the head and neck, however, no category A EVIFs was identified. Although arterial phase CT imaging of the upper limb is a less commonly requested and performed peripheral arterial examination, both referring physicians and interpreting radiologists must recognize the frequency and relevance of incidental findings in this patient cohort allowing timely and appropriate clinical and imaging follow up. However, a cost-effective analysis of pursuing incidental findings in addition to long term studies comparing CTAs in vascular patients who did not have their extravascular findings reported needs to be conducted to adequately understand the true value of EVIFs. Attempts to provide guidance on the management of incidental findings have been made however data on cost-effectiveness is sparse.

Research perspectives

Incidental findings are very common, and although most are of a benign nature, they do lead to the detection of serious life-threatening pathology which would otherwise be missed or diagnosed late. It is important for the reporting radiologist to be aware of their frequency to lead to their detection. More work is needed on guidelines for their management to aid in appropriate follow-up and to avoid an unnecessary cascade of investigations. Future work on their cost-effectives is needed and clinical outcomes to quantitively measure their importance. This can be completed in a long-term CTA study to assess if earlier detection of malignancy improves patient survival rates.

REFERENCES

1 **Bozlar U**, Ogur T, Norton PT, Khaja MS, All J, Hagspiel KD. CT angiography of the upper extremity arterial system: Part 1-Anatomy, technique, and use in trauma patients. *AJR Am J Roentgenol* 2013; **201**: 745-752 [PMID: 24059363 DOI: 10.2214/AJR.13.11207]

2 **Met R**, Bipat S, Legemate DA, Reekers JA, Koelemay MJ. Diagnostic performance of computed tomography angiography in peripheral arterial disease: a systematic review and meta-analysis. *JAMA* 2009; **301**: 415-424 [PMID: 19176443 DOI: 10.1001/jama.301.4.415]

3 **Marcus F**, Hosey MM. Purification and properties of liver fructose 1,6-bisphosphatase from C57BL/KsJ normal and diabetic mice. *J Biol Chem* 1980; **255**: 2481-2486 [PMID: 6244280 DOI: 10.1148/radiol.2372040616]

4 **Schernthaner R**, Stadler A, Lomoschitz F, Weber M, Fleischmann D, Lammer J, Loewe Ch. Multidetector CT angiography in the assessment of peripheral arterial occlusive disease: accuracy in detecting the severity, number, and length of stenoses. *Eur Radiol* 2008; **18**: 665-671 [PMID: 18094974 DOI: 10.1007/s00330-007-0822-8]

5 **Iezzi R**, Cotroneo AR, Filippone A, Di Fabio F, Merlino B, Bonomo L. Extravascular incidental findings at multislice CT angiography of the abdominal aorta and lower extremity arteries: a retrospective review study. *Abdom Imaging* 2007; **32**: 489-494 [PMID: 16967229 DOI: 10.1007/s00261-006-9136-6]

6 **Naidu SG**, Hara AK, Brandis AR, Stone WM. Incidence of highly important extravascular findings detected on CT angiography of the abdominal aorta and the lower extremities. *AJR Am J Roentgenol* 2010; **194**: 1630-1634 [PMID: 20489106 DOI: 10.2214/AJR.09.3538]

7 **Preuß A**, Elgeti T, Hamm B, Werncke T. Extravascular incidental findings in run-off CT angiography in patients with acute limb ischaemia: incidence and clinical relevance. *Clin Radiol* 2015; **70**: 622-629 [PMID: 25819627 DOI: 10.1016/j.crad.2015.02.014]

8 **Mazzei MA**, Guerrini S, Gentili F, Galzerano G, Setacci F, Benevento D, Mazzei FG, Volterrani L, Setacci C. Incidental extravascular findings in computed tomographic angiography for planning or monitoring endovascular aortic aneurysm repair: Smoker patients, increased lung cancer prevalence? *World J Radiol* 2017; **9**: 304-311 [PMID: 28794826 DOI: 10.4329/wjr.v9.i7.304]

9 **Prabhakar AM**, Le TQ, Abujudeh HH, Raja AS. Incidental findings and recommendations are common on ED CT angiography to evaluate for aortic dissection. *Am J Emerg Med* 2015; **33**: 1639-1641 [PMID: 26324008 DOI: 10.1016/j.ajem.2015.07.078]

10 **Crockett MT**, Murphy B, Smith J, Kavanagh EC. Prevalence and clinical significance of extravascular incidental findings in patients undergoing CT cervico-cerebral angiography. *Eur J Radiol* 2015; **84**: 1569-1573 [PMID: 26047822 DOI: 10.1016/j.ejrad.2015.05.014]

11 **Kelly ME**, Heeney A, Redmond CE, Costelloe J, Nason GJ, Ryan J, Brophy D, Winter DC. Incidental findings detected on emergency abdominal CT scans: a 1-year review. *Abdom Imaging* 2015; **40**: 1853-1857 [PMID: 25576049 DOI: 10.1007/s00261-015-0349-4]

12 **Belgrano M**, Pozzi Mucelli F, Spadacci A, Pizzolato R, Zappetti R, Cova M. Prevalence of extravascular collateral findings during 64-slice CT angiography of the abdominal aorta and lower limbs. *Radiol Med* 2010; **115**: 983-996 [PMID: 20574706 DOI: 10.1007/s11547-010-0557-5]

13 **Berland LL**, Silverman SG, Gore RM, Mayo-Smith WW, Megibow AJ, Yee J, Brink JA, Baker ME, Federle MP, Foley WD, Francis IR, Herts BR, Israel GM, Krinsky G, Platt JF, Shuman WP, Taylor AJ. Managing incidental findings on abdominal CT: white paper of the ACR incidental findings committee. *J Am Coll Radiol* 2010; **7**: 754-773 [PMID: 20889105 DOI: 10.1016/j.jacr.2010.06.013]

P- Reviewer: Bazeed MF, Bolboaca SD, Valek V
S- Editor: Ma YJ **L- Editor:** A **E- Editor:** Bian YN

Published By Baishideng Publishing Group Inc
7901 Stoneridge Drive, Suite 501, Pleasanton, CA 94588, USA
Telephone: +1-925-2238242
Fax: +1-925-2238243
E-mail: bpgoffice@wjgnet.com
Help Desk: https://www.f6publishing.com/helpdesk
https://www.wjgnet.com

ISSN 1949-8470 (online)

World Journal of *Radiology*

World J Radiol 2019 October 28; 11(10): 126-133

Published by Baishideng Publishing Group Inc

World Journal of Radiology

Contents

Monthly Volume 11 Number 10 October 28, 2019

MINIREVIEWS

Contents

World Journal of Radiology

Volume 11 Number 10 October 28, 2019

ABOUT COVER

Editorial Board Member of *World Journal of Radiology*, Barbara Palumbo, MD, Associate Professor, Department of Surgical, Radiological and Odontostomatological Sciences, University of Perugia, Perugia I-06124, Italy

AIMS AND SCOPE

The primary aim of *World Journal of Radiology* (*WJR*, *World J Radiol*) is to provide scholars and readers from various fields of radiology with a platform to publish high-quality basic and clinical research articles and communicate their research findings online.

WJR mainly publishes articles reporting research results and findings obtained in the field of radiology and covering a wide range of topics including state of the art information on cardiopulmonary imaging, gastrointestinal imaging, genitourinary imaging, musculoskeletal imaging, neuroradiology/head and neck imaging, nuclear medicine and molecular imaging, pediatric imaging, vascular and interventional radiology, and women's imaging.

INDEXING/ABSTRACTING

The *WJR* is now abstracted and indexed in Emerging Sources Citation Index (Web of Science), PubMed, PubMed Central, China National Knowledge Infrastructure (CNKI), China Science and Technology Journal Database (CSTJ), and Superstar Journals Database.

RESPONSIBLE EDITORS FOR THIS ISSUE

NAME OF JOURNAL
World Journal of Radiology

ISSN
ISSN 1949-8470 (online)

LAUNCH DATE
January 31, 2009

FREQUENCY
Monthly

EDITORS-IN-CHIEF
Venkatesh Mani

EDITORIAL BOARD MEMBERS
https://www.wjgnet.com/1949-8470/editorialboard.htm

EDITORIAL OFFICE
Ruo-Yu Ma, Director

PUBLICATION DATE
October 28, 2019

INSTRUCTIONS TO AUTHORS
https://www.wjgnet.com/bpg/gerinfo/204

GUIDELINES FOR ETHICS DOCUMENTS
https://www.wjgnet.com/bpg/GerInfo/287

GUIDELINES FOR NON-NATIVE SPEAKERS OF ENGLISH
https://www.wjgnet.com/bpg/gerinfo/240

PUBLICATION MISCONDUCT
https://www.wjgnet.com/bpg/gerinfo/208

ARTICLE PROCESSING CHARGE
https://www.wjgnet.com/bpg/gerinfo/242

STEPS FOR SUBMITTING MANUSCRIPTS
https://www.wjgnet.com/bpg/GerInfo/239

ONLINE SUBMISSION
https://www.f6publishing.com

World Journal of Radiology

Submit a Manuscript: https://www.f6publishing.com

World J Radiol 2019 October 28; 11(10): 126-133

DOI: 10.4329/wjr.v11.i10.126

ISSN 1949-8470 (online)

MINIREVIEWS

Coronary artery calcium data and reporting system: Strengths and limitations

Subramaniyan Ramanathan

ORCID number: Subramaniyan Ramanathan (0000-0002-4317-2414).

Author contributions: Ramanathan S designed the outline and performed writing of the whole paper.

Conflict-of-interest statement: There is no conflict of interest associated with the author who contributed to this manuscript.

Manuscript source: Unsolicited manuscript

Received: May 18, 2019
Peer-review started: May 20, 2019
First decision: August 2, 2019
Revised: September 5, 2019
Accepted: September 13, 2019
Article in press: September 13, 2019
Published online: October 28, 2019

P-Reviewer: Bazeed MF, Gao BL, Mani V
S-Editor: Ma RY
L-Editor: Filipodia
E-Editor: Qi LL

Subramaniyan Ramanathan, Department of Clinical Imaging, Al-Wakra Hospital, Hamad Medical Corporation, Doha 82228, Qatar

Subramaniyan Ramanathan, Department of Radiology, Weil Cornell Medical College, Qatar Foundation - Education City, Doha 24144, Qatar

Corresponding author: Subramaniyan Ramanathan, MD, FRCR Department of Clinical Imaging, Al-Wakra Hospital, Hamad Medical Corporation, Doha 82228, Qatar.
sramanathan@hamad.qa
Telephone: +974-50117935
Fax: +974-40114509

Abstract

Coronary artery calcium data and reporting system (CAC-DRS) is a recently introduced standardized reporting system for calcium scoring on computed tomography. CAC-DRS provides four risk categories (0, 1, 2 and 3) along with treatment recommendations for each category. As with any other new reporting platform, CAC-DRS has both advantages and disadvantages. Improved communication, better clarity of details, organized management recommendations and utility in future research and education are the major strengths of CAC-DRS. It has many limitations such as questionable need for a new system, few missing components, use of a less accurate visual method and treatment suggestions based on expert opinion instead of clinical trials. In this contemporary review, we discuss the new reporting system CAC-DRS, its application, strengths and limitations and conclude with some remarks for the future.

Key words: Coronary artery calcium; Reporting system; Agatston score; Strengths; Limitations; Management

Core tip: Coronary artery calcium data and reporting system (CAC-DRS) is a new standardized reporting system for calcium scoring on computed tomography. Four CAC-DRS categories have been described ranging from CAC-DRS 0 to CAC-DRS 3 with progressively increasing cardiac disease risk. Better communication, clarity of details, clinical management recommendations, research and education are the major strengths. Few missing components, visual method, treatment recommendations and lack of clear necessity for a new reporting system are the major limitations.

Citation: Ramanathan S. Coronary artery calcium data and reporting system: Strengths and limitations. *World J Radiol* 2019; 11(10): 126-133
URL: https://www.wjgnet.com/1949-8470/full/v11/i10/126.htm
DOI: https://dx.doi.org/10.4329/wjr.v11.i10.126

INTRODUCTION

Coronary artery disease (CAD) is one of the leading causes of death and disability-adjusted life years lost[1]. Approximately 15.5 million persons ≥ 20 years of age in the United States have CAD as per 2016 Heart Disease and Stroke Statistics update of the American Heart Association (AHA)[2]. Every year, nearly the same number of people undergo diagnostic testing for suspected CAD. It is well established that CAD has a long asymptomatic latent period and mortality, and morbidity can be decreased by early detection and targeted preventive therapy[3].

Coronary artery calcium (CAC) represents calcific atherosclerosis in the coronary arteries and correlates well with the overall burden of coronary atherosclerosis. CAC quantified on electrocardiogram-gated non-contrast computed tomography (CT) examinations is the most robust predictor of CAD events in the asymptomatic population, especially in those with an intermediate-risk[4]. It has been shown that CAC increases the predictive value of the Framingham Risk Score and the 2013 American College of Cardiology (ACC)/AHA Pooled Cohort Equations[5]. It has now been integrated into various cardiovascular risk prediction scores and guidelines issued by the American College of Cardiology Foundation, the AHA, Society of Cardiovascular Computed Tomography (SCCT), American College of Radiology, and Society of Thoracic Radiology. This has created a need for more standardized performance and interpretation of CAC scoring CT. A new standardized reporting system CAC - data and reporting system (DRS) was introduced recently in 2018 for this purpose and was developed on the same lines of CAD - reporting and data system (RADS), breast imaging (BI)-RADS, prostate imaging (PI)-RADS, and liver imaging (LI)-RADS[6-8]. This review aims to explain the essential features of this new reporting system, followed by the discussion of its various strengths and limitations.

CURRENT STATUS OF CAC SCORE

CAC score has become more popular recently as there is more and more evidence accumulating in favor of its strong role in predicting atherosclerotic cardiovascular disease (ASCVD) risk. Various scores are available to identify high and low risk patients for CAD like Pooled Cohort Equations, Framingham General CVD Risk Profile, and Reynolds risk score[5,9]. Most of these are "Total risk scores", and they have been found useful as they take into account multiple risk factors. However, they are able to predict only 65%-80% of future cardiovascular events[10]. This led to a continuous search for a better predictor or predictor model. CAC is intimately related to atherosclerosis, and the extent of calcium deposition in the coronary arteries can be considered a good predictor of the total burden of coronary atherosclerosis. Many large prospective studies have already proven the prognostic value of CAC score in predicting serious cardiac events leading to mortality in a variety of populations.

It has been found that CAC performs better than other risk assessment tools to identify those asymptomatic populations that would benefit from pharmacological therapies. A new concept 'Power of zero', which denotes CAC score of 0, has been investigated, and it was concluded that patients with CAC = 0 have a low mortality risk over a period of 15 years in low to intermediate FRS risk group and over 5 years in high FRS risk group. CAC testing is recommended to assess the CAD risk in that group of individuals with the 10-year ASCVD risk between 5% and 20%, and it can be used selectively in patients with < 5% 10-year risk with a strong family history of ASCVD[11]. It also provides treatment recommendations that are adopted in the new scoring system CAC-DRS. In 2017, The Walter Reed Cohort Study assessed the long-term risk of death and ASCVD outcomes in 23637 subjects without ASCVD risk and found that CAC scoring is an accurate tool for predicting major adverse cardiovascular events and mortality in all age groups and with multiple risk factors[12]. These results encourage CAC screening for better ASCVD risk assessment and prevention in low-risk, young adults. Apart from risk stratification, CAC has been shown to play a prominent role in management decisions. This has been supported by

many large studies, and one of them is National Institutes of Health supported clinical trial of 13644 patients that showed that CAC identified patients who are more likely to benefit from statin therapy[13].

Apart from its proven predictive role, other reasons for wider acceptance of CAC scoring include: (1) Easily performed noninvasive test with very low radiation; (2) Highly reproducible test, as it is a system generated score with little human involvement; (3) Objective assessment based on the absolute score and risk percentiles; and (4) As calcium deposition in vessels is a slow process depending on multiple factors, CAC scoring provides a long term risk prediction as compared to other scoring tests, which depend on one time measures like blood pressure, blood glucose, and cholesterol values, which can vary widely over a period.

CAC-DRS

CAC-DRS was introduced recently in the first quarter of 2018 to standardize the reporting of CAC scoring in both dedicated CAC scans and non-gated non-contrast chest CT scans. It is based on the expert consensus document published by SCCT in 2017[6,14]. Both SCCT and Society of Thoracic Radiology jointly recommend the routine reporting of CAC score in routine non-contrast CT chest irrespective of indication for early detection of CAD and for future research potential[9]. Various methods have been used for evaluation of CAC and included Agatston score (AS), volume score, mass score, semi quantitative vessel score, and visual scores. Out of these, CAC-DRS recommends the usage of either Agatston or visual score. Four CAC-DRS categories have been described ranging from CAC-DRS 0 to CAC-DRS 3 with progressively increasing risk of ASCVD (Table 1)[6]. Although the method of CAC scoring is different between Agatston and visual method, final categories, risk prediction, and management are similar[6].

AS

AS is a well-established and widely used CAC scoring system. It was first introduced by Arthur Agatston and his colleagues in 1990 and has undergone modifications with advances in CT technology, with the current score based on multidetector CT scanners[15]. SCCT has laid down standards for the performance of CAC scans. Gated or non-gated non-contrast scans with 2.5 or 3 mm slice thickness, 120 kVp, and individualized mAs with filtered back projection is recommended[9]. In Agatston method, an individual calcified plaque is identified as an area of 1 mm^2 (two pixels) with 130 Hounsfield units (HU) or more along the coronary arteries. Each calcific plaque is given a value of 1, 2, 3, and 4 based on the highest densities 130-199 HU, 200-299 HU, 300-399 HU, and ≥ 400 HU, respectively. Score of each plaque is calculated by multiplying the area with the density score. Summing up the scores of all calcific plaques gives the total AS for that CAC scan[9,15,16]. Based on the total AS, five risk categories have been made: 0 = very low risk, 1-99 = mildly increased, 100-299 = moderately increased, 300-1000 = moderate to severely increased, and > 1000 = severely increased risk of cardiac disease[14,15].

Visual method

Although AS can be used in non-gated scans and was found to be accurate in few studies, still there is no strong evidence of its accuracy in non-gated scans. Also, it is not standardized yet for non-gated scans, and it needs special software. Other methods like ordinal scoring of individual coronary arteries and visual method were considered[9]. Visual method has been found to be a simple, quick, and reasonably accurate method of assessing the CAC in non-gated chest CT scans. In this visual method, CAC is categorized into none, mild, moderate, and severe based on the overall visual eyeball analysis of the entire coronary circulation and correspond to CAC-DRS categories 0, 1, 2, and 3 respectively[17]. No specific criterion has been described for this method unlike ordinal scoring. Visual method is applicable only for non-gated CT chest scans and not recommended in gated scans where AS is preferred.

Modifiers

Two modifiers have been added in the CAC-DRS. First denotes the method of CAC score and can be either Agatston (A) or visual estimation (V). The second modifier 'N' denotes the number of vessels involved and can vary from 1-4, with N4 indicating involvement of all coronary arteries, namely left main (LM), left anterior descending (LAD), left circumflex, and right coronary artery. Two modifiers need to be separated by symbol "/" slash. If there is no calcium, then N modifier is not used, and the final category will be CAC-DRS A0 or V0 depending on the method used[6].

Table 1 Coronary artery calcium data and reporting system categories based on the Agatston and visual scoring

CAC-DRS category	Agatston score	Visual score	Risk
0	0	0	Very low
1	1-99	1	Mild
2	100-299	2	Moderate
3	> 300	3	Moderate to severe

CAC-DRS: Coronary artery calcium data and reporting system.

Other features

CAC-DRS also recommends reporting of valvular, pericardial, and aortic calcification in the report with none, mild, moderate, and severe stratification. However, there are no further details on how it should be done, and these are not considered in assigning the CAC-DRS categories. It also mentions reporting of extra cardiac findings with follow-up recommendations. Standard reporting templates have been provided in the document with details on the indication, technique, and findings in individual coronary arteries along with CAC-DRS categories and management recommendations[6,9,14].

STRENGTHS

Communication

As with any other standard reporting systems, usage of CAC-DRS categories leads to better and more effective communication with the referring physicians. Instead of an absolute score used currently with variable reporting of AS grading, standardized CAC-DRS categories will lead to more uniform reporting both among cardiac and general radiologists[14]. Although the simple absolute CAC score is often enough for specialists (cardiologists), it is confusing for non-specialists regarding further management and referral decisions. CA-DRS definitely helps non-specialists make quicker and more appropriate referrals using the categories as compared to conventional reports. Even for specialists, the standard template report saves time in identifying the key information from the long report during their busy clinics. With routine use of CAC-DRS, it is expected that there will be a significant drop in phone calls from clinical colleagues complaining about inconclusive reports. Also, it will be easy for trainees and junior staff to learn and report in a standardized format within a short time.

Clarity and details

CAC-DRS does not stop just at providing risk categories. The final category includes the method used for CAC score, either Agatston or visual estimation, which is important to know to understand the reliability and reproducibility of the scores. Also, it mentions the number of vessels involved in the form of modifiers (N). This is important, as in addition to total calcium score, the number of vessels involved is linked with the prognosis in the Multi-Ethnic Study of Atherosclerosis involving more than 6000 men and women[18,19]. This in turn will reflect the management of, for example, patients with AS 98 involving all four vessels, who will be categorized as CAC-DRS A1/N4. Based on the category, the recommended treatment is only moderate intensity statins. However, one might consider adding low dose aspirin in an individual patient due to involvement of four vessels, which is an additive risk to total CAC score, although the CA-DRS category remains the same.

Clinical management

The most attractive component in the CAC-DRS is the addition of management recommendations based on CAC score. This can be considered both as a strength and limitation. Strengths are discussed here and limitations in the next section. Most of these recommendations are from expert opinion with some support from the 2013 ACC/AHA Prevention Guidelines[5]. CAC score has been proven to be one of the strongest predictors of ASCVD risk in the asymptomatic population. CAC-DRS 0 has a very high negative predictive value, called "Power of Zero", and helps in downgrading the risk of patients who might be considered high risk based on other parameters[20,21]. CAC score is being used to guide preventive pharmacotherapy using

statins and aspirin in asymptomatic patients. High intensity statins therapy is recommended in any patients with a CAC > 300, moderate to high intensity statins with CAC 100-299, and moderate intensity statins therapy with CAC 1-99. Aspirin (81 mg) is recommended with CAC > 100, while the risk of bleeding complications may outweigh its benefits with CAC < 100 in the absence of other risk factors[9,22].

Research and education

Using a structured reporting system will help in accumulating quality data that is essential for future research. There is significant data gap on the risk factor predictions in South Asian and Middle East population. Using a universal standard reporting platform can help in data collection across boundaries and can help bridge knowledge gaps. In addition, in the near future, it is possible to assess the clinical usefulness of this new reporting system, which can help in further modifications and fine tuning. Already CAC is a near automatic evaluation performed with minimal human interference. Now software can be modified to give the final risk categories thereby avoiding or minimizing human error and improving the daily workflow in busy departments. We are now in the era of artificial intelligence, and such automated risk prediction software will go a long way in giving quicker and more accurate risk prediction and treatment options, thereby improving patient care.

LIMITATIONS

Is there a need?

CAC scoring is a semi-automated system with absolute values and established grading methods. Reporting is usually uniform and highly reproducible, unlike other pathologies like breast cancer, prostatic cancers, and liver cancers. So, it becomes questionable if there is a necessity for a standard reporting system for CAC scoring. At least in CAD-RADS it is more justified, as there are multiple components, like percentage of stenosis, acute or chronic presentation, and the specific vessel and number of vessels, leading to reporting inaccuracies, and a reporting system can make things more consistent and reproducible[7,8]. Whereas in CAC, things are clear already, and the net benefit from a new reporting system is minimal, except that it is linked with few management recommendations. One would expect the new reporting system to be named CAC-RADS, like the other established breast imaging-RADS, prostate-RADS, and CAD-RADS. However, it was named as CAC-DRS, as RADS is a trademark of the American College of Radiology.

Visual method

CAC-DRS includes both Agatston and visual methods of CAC scoring in describing risk categories. Agatston method is the widely used technique of CAC scoring and has been used in most of the clinical trials[4]. Visual method is a very simple way of categorizing calcium deposition in coronary arteries as none, mild moderate, and severe. There is no specific method described or is there any reference to specific vessel or number of vessels involved[9,17]. Also, there is limited literature on the accuracy of this method. Only one study has compared the visual and Agatston methods to date, and it showed overall good agreement with assignment of same risk category as the AS in 73.0% and to within one category in 99.7% with good inter-observer agreement[17]. Disadvantages include an over simplistic approach and lack of strong supporting data. More head to head studies are needed before recommending this method as an alternative to Agatston as management decisions are based on these categories.

Missing component

CAC-DRS provides risk categories based on the overall CAC score and also highlight the method used for scoring and the number of vessels involved. However, the severity of calcium deposition in a particular vessel is not considered in risk prediction. Regional distribution of CAC can be very heterogenous from the total CAC score[23]. This can affect the clinical management, as one vessel, for example LM, can have severe calcium deposition while the remaining three (LAD, left circumflex, and right coronary artery) can have no or mild severity, with resultant overall category being mild in spite of severe disease in LAD. As LM is a major vessel with great impact on cardiac events compared to other vessels, vessel based risk category could be more useful in the future.

Although extra coronary calcification is reported in CAC-DRS, it is not considered in final risk categories. It has been shown that calcification in the valves and thoracic aorta is associated with increased risk of cardiac events. Currently, there is no agreed method of scoring these extra coronary calcifications[24,25].

Management

As mentioned previously, management recommendations in CAC-DRS can be considered both as a strength and limitation. It is considered the most attractive component in this new reporting system, but it must be used cautiously as these are consensus recommendations based on expert opinion and not on prospective randomized controlled trials. Most of these recommendations are based on those from The 2013 ACC/AHA Prevention Guidelines and 2017 SCCT recommendations[5,9]. One more thing that needs to be highlighted is that these recommendations are applicable primarily for a specific population - asymptomatic individuals between 40-75 years of age in the 5%-20% 10-year ASCVD risk group based on pooled cohort equation. It is also used in the < 5% ASCVD group with a family history of premature coronary artery disease[20-22,26]. Its utility outside these risk groups has not been widely investigated, and hence providing risk categories on CAC scans performed in other populations is not based on evidence. Also, there is lack of follow-up guidelines in CAC-DRS.

FUTURE IMPROVEMENTS

Like any other new reporting system, this CAC-DRS has many new positive features with some limitations as enumerated in the previous sections. With continuous usage in daily practice, more of these strengths and limitations will be identified and can be improved in the next version. As the authors of CAC-DRS stated, a simplistic approach was employed to enhance better clinical adoption. This makes sense, because if a new system is difficult to practice in a daily busy schedule, it gets ignored and will not be embraced by the radiology and clinical community. Some components that could be improved in the future are listed below: (1) Visual method is an over simplistic approach and until it is proven to be an accurate technique, it should not be recommended in CAC-DRS; (2) Severity in individual vessels needs to be taken into account while assigning risk category. This can either be done as separate risk category for specific vessels or averaging risk category of all vessels; (3) Management recommendations should be highlighted to communicate to the physicians that this is applicable in a specific population group and not a universal recommendation; (4) Clinical cardiology groups or societies need to be involved to understand their expectations and concerns so that a more widely acceptable scoring system will be possible in the future.

CONCLUSION

It is beyond doubt that a standardized reporting system is the future for providing uniform and reproducible conclusions. It has the added advantage of efficient data collection, which is essential for future outcome studies. Following the recent introduction of CAD-RADS, CAC-DRS is a new addition in coronary artery imaging. CAC scoring is gaining more attention in recent times due to its strong predictive value in asymptomatic patients with low to intermediate ASCVD risk. CAC-DRS improvises on the Agatston scoring system with more relevant categories along with linked treatment guidelines. As discussed above, it has both advantages and some limitations. We hope it will be widely used in daily clinical practice due to its simplicity, and only in the long run shall we know its effect on improving patient care.

REFERENCES

1 **Roth GA**, Huffman MD, Moran AE, Feigin V, Mensah GA, Naghavi M, Murray CJ. Global and regional patterns in cardiovascular mortality from 1990 to 2013. *Circulation* 2015; **132**: 1667-1678 [PMID: 26503749 DOI: 10.1161/CIRCULATIONAHA.114.008720]

2 **Writing Group Members**. Mozaffarian D, Benjamin EJ, Go AS, Arnett DK, Blaha MJ, Cushman M, Das SR, de Ferranti S, Després JP, Fullerton HJ, Howard VJ, Huffman MD, Isasi CR, Jiménez MC, Judd SE, Kissela BM, Lichtman JH, Lisabeth LD, Liu S, Mackey RH, Magid DJ, McGuire DK, Mohler ER 3rd, Moy CS, Muntner P, Mussolino ME, Nasir K, Neumar RW, Nichol G, Palaniappan L, Pandey DK, Reeves MJ, Rodriguez CJ, Rosamond W, Sorlie PD, Stein J, Towfighi A, Turan TN, Virani SS, Woo D, Yeh RW, Turner MB; American Heart Association Statistics Committee; Stroke Statistics Subcommittee. Heart Disease and Stroke Statistics-2016 Update: A Report From the American Heart Association. *Circulation* 2016; **133**: e38-360 [PMID: 26673558 DOI: 10.1161/CIR.0000000000000350]

3 **Mark DB**, Anderson JL, Brinker JA, Brophy JA, Casey DE, Cross RR, Edmundowicz D, Hachamovitch R, Hlatky MA, Jacobs JE, Jaskie S, Kett KG, Malhotra V, Masoudi FA, McConnell MV, Rubin GD, Shaw LJ, Sherman ME, Stanko S, Ward RP. ACC/AHA/ASE/ASNC/HRS/IAC/Mended

Hearts/NASCI/RSNA/SAIP/SCAI/SCCT/SCMR/SNMMI 2014 health policy statement on use of noninvasive cardiovascular imaging: a report of the American College of Cardiology Clinical Quality Committee. *J Am Coll Cardiol* 2014; **63**: 698-721 [PMID: 24556329 DOI: 10.1016/j.jacc.2013.02.002]

4 **Hecht HS**. Coronary artery calcium scanning: past, present, and future. *JACC Cardiovasc Imaging* 2015; **8**: 579-596 [PMID: 25937196 DOI: 10.1016/j.jcmg.2015.02.006]

5 **Stone NJ**, Robinson JG, Lichtenstein AH, Bairey Merz CN, Blum CB, Eckel RH, Goldberg AC, Gordon D, Levy D, Lloyd-Jones DM, McBride P, Schwartz JS, Shero ST, Smith SC, Watson K, Wilson PW; American College of Cardiology/American Heart Association Task Force on Practice Guidelines. 2013 ACC/AHA guideline on the treatment of blood cholesterol to reduce atherosclerotic cardiovascular risk in adults: a report of the American College of Cardiology/American Heart Association Task Force on Practice Guidelines. *J Am Coll Cardiol* 2014; **63**: 2889-2934 [PMID: 24239923 DOI: 10.1016/j.jacc.2013.11.002]

6 **Hecht HS**, Blaha MJ, Kazerooni EA, Cury RC, Budoff M, Leipsic J, Shaw L. CAC-DRS: Coronary Artery Calcium Data and Reporting System. An expert consensus document of the Society of Cardiovascular Computed Tomography (SCCT). *J Cardiovasc Comput Tomogr* 2018; **12**: 185-191 [PMID: 29793848 DOI: 10.1016/j.jcct.2018.03.008]

7 **Cury RC**, Abbara S, Achenbach S, Agatston A, Berman DS, Budoff MJ, Dill KE, Jacobs JE, Maroules CD, Rubin GD, Rybicki FJ, Schoepf UJ, Shaw LJ, Stillman AE, White CS, Woodard PK, Leipsic JA. Coronary Artery Disease - Reporting and Data System (CAD-RADS): An Expert Consensus Document of SCCT, ACR and NASCI: Endorsed by the ACC. *JACC Cardiovasc Imaging* 2016; **9**: 1099-1113 [PMID: 27609151 DOI: 10.1016/j.jcmg.2016.05.005]

8 **Cury RC**, Abbara S, Achenbach S, Agatston A, Berman DS, Budoff MJ, Dill KE, Jacobs JE, Maroules CD, Rubin GD, Rybicki FJ, Schoepf UJ, Shaw LJ, Stillman AE, White CS, Woodard PK, Leipsic JA. CAD-RADS™: Coronary Artery Disease - Reporting and Data System: An Expert Consensus Document of the Society of Cardiovascular Computed Tomography (SCCT), the American College of Radiology (ACR) and the North American Society for Cardiovascular Imaging (NASCI). Endorsed by the American College of Cardiology. *J Am Coll Radiol* 2016; **13**: 1458-1466.e9 [PMID: 27318576 DOI: 10.1016/j.jacr.2016.04.024]

9 **Hecht HS**, Cronin P, Blaha MJ, Budoff MJ, Kazerooni EA, Narula J, Yankelevitz D, Abbara S. 2016 SCCT/STR guidelines for coronary artery calcium scoring of noncontrast noncardiac chest CT scans: A report of the Society of Cardiovascular Computed Tomography and Society of Thoracic Radiology. *J Cardiovasc Comput Tomogr* 2017; **11**: 74-84 [PMID: 27916431 DOI: 10.1016/j.jcct.2016.11.003]

10 **Nasir K**, Clouse M. Role of nonenhanced multidetector CT coronary artery calcium testing in asymptomatic and symptomatic individuals. *Radiology* 2012; **264**: 637-649 [PMID: 22919038 DOI: 10.1148/radiol.12110810]

11 **Nasir K**, Bittencourt MS, Blaha MJ, Blankstein R, Agatson AS, Rivera JJ, Miedema MD, Sibley CT, Shaw LJ, Blumenthal RS, Budoff MJ, Krumholz HM. Implications of Coronary Artery Calcium Testing Among Statin Candidates According to American College of Cardiology/American Heart Association Cholesterol Management Guidelines: MESA (Multi-Ethnic Study of Atherosclerosis). *J Am Coll Cardiol* 2015; **66**: 1657-1668 [PMID: 26449135 DOI: 10.1016/j.jacc.2015.07.066]

12 **Mitchell JD**, Paisley R, Moon P, Novak E, Villines TC. Coronary Artery Calcium and Long-Term Risk of Death, Myocardial Infarction, and Stroke: The Walter Reed Cohort Study. *JACC Cardiovasc Imaging* 2018; **11**: 1799-1806 [PMID: 29153576 DOI: 10.1016/j.jcmg.2017.09.003]

13 **Mitchell JD**, Fergestrom N, Gage BF, Paisley R, Moon P, Novak E, Cheezum M, Shaw LJ, Villines TC. Impact of Statins on Cardiovascular Outcomes Following Coronary Artery Calcium Scoring. *J Am Coll Cardiol* 2018; **72**: 3233-3242 [PMID: 30409567 DOI: 10.1016/j.jacc.2018.09.051]

14 **Hecht H**, Blaha MJ, Berman DS, Nasir K, Budoff M, Leipsic J, Blankstein R, Narula J, Rumberger J, Shaw LJ. Clinical indications for coronary artery calcium scoring in asymptomatic patients: Expert consensus statement from the Society of Cardiovascular Computed Tomography. *J Cardiovasc Comput Tomogr* 2017; **11**: 157-168 [PMID: 28283309 DOI: 10.1016/j.jcct.2017.02.010]

15 **Agatston AS**, Janowitz WR, Hildner FJ, Zusmer NR, Viamonte M, Detrano R. Quantification of coronary artery calcium using ultrafast computed tomography. *J Am Coll Cardiol* 1990; **15**: 827-832 [PMID: 2407762]

16 **Schmermund A**. The Agatston calcium score: a milestone in the history of cardiac CT. *J Cardiovasc Comput Tomogr* 2014; **8**: 414-417 [PMID: 25467829 DOI: 10.1016/j.jcct.2014.09.008]

17 **Chiles C**, Duan F, Gladish GW, Ravenel JG, Baginski SG, Snyder BS, DeMello S, Desjardins SS, Munden RF; NLST Study Team. Association of Coronary Artery Calcification and Mortality in the National Lung Screening Trial: A Comparison of Three Scoring Methods. *Radiology* 2015; **276**: 82-90 [PMID: 25759972 DOI: 10.1148/radiol.15142062]

18 **Joshi PH**, Patel B, Blaha MJ, Berry JD, Blankstein R, Budoff MJ, Wong N, Agatston A, Blumenthal RS, Nasir K. Coronary artery Calcium predicts Cardiovascular events in participants with a low lifetime risk of Cardiovascular disease: The Multi-Ethnic Study of Atherosclerosis (MESA). *Atherosclerosis* 2016; **246**: 367-373 [PMID: 26841074 DOI: 10.1016/j.atherosclerosis.2016.01.017]

19 **McClelland RL**, Jorgensen NW, Budoff M, Blaha MJ, Post WS, Kronmal RA, Bild DE, Shea S, Liu K, Watson KE, Folsom AR, Khera A, Ayers C, Mahabadi AA, Lehmann N, Jöckel KH, Moebus S, Carr JJ, Erbel R, Burke GL. 10-Year Coronary Heart Disease Risk Prediction Using Coronary Artery Calcium and Traditional Risk Factors: Derivation in the MESA (Multi-Ethnic Study of Atherosclerosis) With Validation in the HNR (Heinz Nixdorf Recall) Study and the DHS (Dallas Heart Study). *J Am Coll Cardiol* 2015; **66**: 1643-1653 [PMID: 26449133 DOI: 10.1016/j.jacc.2015.08.035]

20 **Blaha MJ**, Cainzos-Achirica M, Greenland P, McEvoy JW, Blankstein R, Budoff MJ, Dardari Z, Sibley CT, Burke GL, Kronmal RA, Szklo M, Blumenthal RS, Nasir K. Role of Coronary Artery Calcium Score of Zero and Other Negative Risk Markers for Cardiovascular Disease: The Multi-Ethnic Study of Atherosclerosis (MESA). *Circulation* 2016; **133**: 849-858 [PMID: 26801055 DOI: 10.1161/CIRCULATIONAHA.115.018524]

21 **Blaha MJ**, Dardari ZA, Blumenthal RS, Martin SS, Nasir K, Al-Mallah MH. The new "intermediate risk" group: a comparative analysis of the new 2013 ACC/AHA risk assessment guidelines versus prior guidelines in men. *Atherosclerosis* 2014; **237**: 1-4 [PMID: 25173946 DOI: 10.1016/j.atherosclerosis.2014.08.024]

22 **Galper BZ**, Wang YC, Einstein AJ. Strategies for Primary Prevention of Coronary Heart Disease Based on Risk Stratification by the ACC/AHA Lipid Guidelines, ATP III Guidelines, Coronary Calcium Scoring, and C-Reactive Protein, and a Global Treat-All Strategy: A Comparative--Effectiveness Modeling Study.

PLoS One 2015; **10**: e0138092 [PMID: 26422204 DOI: 10.1371/journal.pone.0138092]

23 **Blaha MJ**, Mortensen MB, Kianoush S, Tota-Maharaj R, Cainzos-Achirica M. Coronary Artery Calcium Scoring: Is It Time for a Change in Methodology? *JACC Cardiovasc Imaging* 2017; **10**: 923-937 [PMID: 28797416 DOI: 10.1016/j.jcmg.2017.05.007]

24 **Dirrichs T**, Penzkofer T, Reinartz SD, Kraus T, Mahnken AH, Kuhl CK. Extracoronary Thoracic and Coronary Artery Calcifications on Chest CT for Lung Cancer Screening: Association with Established Cardiovascular Risk Factors - The "CT-Risk" Trial. *Acad Radiol* 2015; **22**: 880-889 [PMID: 25957500 DOI: 10.1016/j.acra.2015.03.005]

25 **Yeboah J**, Young R, McClelland RL, Delaney JC, Polonsky TS, Dawood FZ, Blaha MJ, Miedema MD, Sibley CT, Carr JJ, Burke GL, Goff DC, Psaty BM, Greenland P, Herrington DM. Utility of Nontraditional Risk Markers in Atherosclerotic Cardiovascular Disease Risk Assessment. *J Am Coll Cardiol* 2016; **67**: 139-147 [PMID: 26791059 DOI: 10.1016/j.jacc.2015.10.058]

26 **Pletcher MJ**, Pignone M, Earnshaw S, McDade C, Phillips KA, Auer R, Zablotska L, Greenland P. Using the coronary artery calcium score to guide statin therapy: a cost-effectiveness analysis. *Circ Cardiovasc Qual Outcomes* 2014; **7**: 276-284 [PMID: 24619318 DOI: 10.1161/CIRCOUTCOMES.113.000799]

Published By Baishideng Publishing Group Inc
7041 Koll Center Parkway, Suite 160, Pleasanton, CA 94566, USA
Telephone: +1-925-2238242
E-mail: bpgoffice@wjgnet.com
Help Desk: https://www.f6publishing.com/helpdesk
https://www.wjgnet.com

ISSN 1949-8470 (online)

World Journal of *Radiology*

World J Radiol 2019 November 28; 11(11): 134-143

Published by Baishideng Publishing Group Inc

WJR

World Journal of Radiology

Contents

Monthly Volume 11 Number 11 November 28, 2019

ORIGINAL ARTICLE

Observational Study

Contents

World Journal of Radiology

Volume 11 Number 11 November 28, 2019

ABOUT COVER

Editorial Board Member of *World Journal of Radiology*, George Plataniotis, MD, MSc, PhD, Associate Professor, Doctor, Department of Oncology, Sussex Cancer Centre, Royal Sussex County Hospital, Brighton BN2 5 BE, United Kingdom

AIMS AND SCOPE

The primary aim of *World Journal of Radiology* (*WJR*, *World J Radiol*) is to provide scholars and readers from various fields of radiology with a platform to publish high-quality basic and clinical research articles and communicate their research findings online.

WJR mainly publishes articles reporting research results and findings obtained in the field of radiology and covering a wide range of topics including state of the art information on cardiopulmonary imaging, gastrointestinal imaging, genitourinary imaging, musculoskeletal imaging, neuroradiology/head and neck imaging, nuclear medicine and molecular imaging, pediatric imaging, vascular and interventional radiology, and women's imaging.

INDEXING/ABSTRACTING

The *WJR* is now abstracted and indexed in Emerging Sources Citation Index (Web of Science), PubMed, PubMed Central, China National Knowledge Infrastructure (CNKI), China Science and Technology Journal Database (CSTJ), and Superstar Journals Database.

RESPONSIBLE EDITORS FOR THIS ISSUE

NAME OF JOURNAL
World Journal of Radiology

ISSN
ISSN 1949-8470 (online)

LAUNCH DATE
January 31, 2009

FREQUENCY
Monthly

EDITORS-IN-CHIEF
Venkatesh Mani

EDITORIAL BOARD MEMBERS
https://www.wjgnet.com/1949-8470/editorialboard.htm

EDITORIAL OFFICE
Ruo-Yu Ma, Director

PUBLICATION DATE
November 28, 2019

INSTRUCTIONS TO AUTHORS
https://www.wjgnet.com/bpg/gerinfo/204

GUIDELINES FOR ETHICS DOCUMENTS
https://www.wjgnet.com/bpg/GerInfo/287

GUIDELINES FOR NON-NATIVE SPEAKERS OF ENGLISH
https://www.wjgnet.com/bpg/gerinfo/240

PUBLICATION MISCONDUCT
https://www.wjgnet.com/bpg/gerinfo/208

ARTICLE PROCESSING CHARGE
https://www.wjgnet.com/bpg/gerinfo/242

STEPS FOR SUBMITTING MANUSCRIPTS
https://www.wjgnet.com/bpg/GerInfo/239

ONLINE SUBMISSION
https://www.f6publishing.com

World Journal of Radiology

Submit a Manuscript: https://www.f6publishing.com

World J Radiol 2019 November 28; 11(11): 134-143

DOI: 10.4329/wjr.v11.i11.134

ISSN 1949-8470 (online)

ORIGINAL ARTICLE

Observational Study

Comparison of free breathing and respiratory triggered diffusion-weighted imaging sequences for liver imaging

Janio Szklaruk, Jong Bum Son, Wei Wei, Priya Bhosale, Sanaz Javadi, Jingfei Ma

ORCID number: Janio Szklaruk (0000-0002-6515-7776); Jong Bum Son (0000-0003-2548-5895); Wei Wei (0000-0002-0960-7269); Priya R Bhosale (0000-0003-4014-4941); Sanaz Javadi (0000-0003-2261-6757); Jingfei Ma (0000-0002-6274-174X).

Author contributions: All authors contributed to the manuscript preparation, study design and data analysis; Wei W performed all statistical analyses; Bhosale P, Javadi S, Son JB and Szklaruk J acquired the data; Ma J and Szklaruk J contributed to the overall study design and implementation, data analysis.

Institutional review board statement: This study was approved by the University of Texas MD Anderson Cancer Center Institutional Review Board.

Conflict-of-interest statement: All authors declare that they have nothing to disclose except for Ma J. Ma J has ongoing financial relationships with GE Healthcare, Siemens Healthineers, and C4 Imaging. There are no family members who present a potential conflict of interest.

Data sharing statement: Not applicable

STROBE statement: The authors have read the STROBE checklist, and the manuscript was prepared and revised according to the STROBE checklist.

Open-Access: This article is an open-access article which was selected by an in-house editor and fully peer-reviewed by external

Janio Szklaruk, Priya Bhosale, Sanaz Javadi, Department of Diagnostic Radiology, The University of Texas MD Anderson Cancer Center, Houston, TX 77030, United States

Jong Bum Son, Jingfei Ma, Department of Imaging Physics, The University of Texas MD Anderson Cancer Center, Houston, TX 77030, United States

Wei Wei, Department of Biostatistics, The University of Texas MD Anderson Cancer Center, Houston, TX 77030, United States

Corresponding author: Janio Szklaruk, MD, PhD, Doctor, Professor, Department of Diagnostic Radiology, The University of Texas MD Anderson Cancer Center, 1515 Holcombe Blvd, Unit 1473, Houston, TX 77030, United States. jszklaru@mdanderson.org
Telephone: +1-713-7453230

Abstract

BACKGROUND

Diffusion-weighted imaging (DWI) has become a useful tool in the detection, characterization, and evaluation of response to treatment of many cancers, including malignant liver lesions. DWI offers higher image contrast between lesions and normal liver tissue than other sequences. DWI images acquired at two or more b-values can be used to derive an apparent diffusion coefficient (ADC). DWI in the body has several technical challenges. This include ghosting artifacts, mis-registration and susceptibility artifacts. New DWI sequences have been developed to overcome some of these challenges. Our goal is to evaluate 3 new DWI sequences for liver imaging.

AIM

To qualitatively and quantitatively compare 3 DWI sequences for liver imaging: free-breathing (FB), simultaneous multislice (SMS), and prospective acquisition correction (PACE).

METHODS

Magnetic resonance imaging (MRI) was performed in 20 patients in this prospective study. The MR study included 3 separate DWI sequences: FB-DWI, SMS-DWI, and PACE-DWI. The image quality, mean ADC, standard deviations (SD) of ADC, and ADC histogram were compared. Wilcoxon signed-rank tests were used to compare qualitative image quality. A linear mixed model was used to compare the mean ADC and the SDs of the ADC values. All tests were 2-sided and P values of < 0.05 were considered statistically significant.

RESULTS

Manuscript source: Unsolicited manuscript

Received: June 25, 2019
Peer-review started: June 29, 2019
First decision: August 2, 2019
Revised: August 26, 2019
Accepted: September 25, 2019
Article in press: September 25, 2019
Published online: November 28, 2019

P-Reviewer: Bazeed MF, Gao BL, Kwok WE
S-Editor: Ma RY
L-Editor: A
E-Editor: Qi LL

There were 56 lesions (50 malignant) evaluated in this study. The mean qualitative image quality score of PACE-DWI was 4.48. This was significantly better than that of SMS-DWI (4.22) and FB-DWI (3.15) ($P < 0.05$). Quantitatively, the mean ADC values from the 3 different sequences did not significantly differ for each liver lesion. FB-DWI had a markedly higher variation in the SD of the ADC values than did SMS-DWI and PACE-DWI. We found statistically significant differences in the SDs of the ADC values for FB-DWI *vs* PACE-DWI ($P < 0.0001$) and for FB-DWI *vs* SMS-DWI ($P = 0.03$). The SD of the ADC values was not statistically significant for PACE-DWI and SMS-DWI ($P = 0.18$). The quality of the PACE-DWI ADC histograms were considered better than the SMS-DWI and FB-DWI.

CONCLUSION
Compared to FB-DWI, both PACE-DWI and SMS-DWI provide better image quality and decreased quantitative variability in the measurement of ADC values of liver lesions.

Key words: Diffusion; Magnetic resonance imaging; Liver; Apparent diffusion coefficient; Prospective acquisition correction; Multi-slice

Core tip: We compared 3 diffusion-weighted imaging (DWI) techniques for liver imaging: The free-breathing (FB), simultaneous multi-slice (SMS) and prospective acquisition correction (PACE) sequences. Three radiologists independently scored the images. We evaluated the image quality. We also compare the calculated apparent diffusion coefficient (ADC) for liver lesions and variability of ADC histogram for liver lesions for each sequence. The PACE and SMS provide better image quality and less variability in ADC values compared to FB-DWI.

Citation: Szklaruk J, Son JB, Wei W, Bhosale P, Javadi S, Ma J. Comparison of free breathing and respiratory triggered diffusion-weighted imaging sequences for liver imaging. *World J Radiol* 2019; 11(11): 134-143
URL: https://www.wjgnet.com/1949-8470/full/v11/i11/134.htm
DOI: https://dx.doi.org/10.4329/wjr.v11.i11.134

INTRODUCTION

Diffusion-weighted imaging (DWI) is sensitive to the Brownian motion of intracellular and extracellular water molecules. Because it can reveal changes in the tissue microenvironment, DWI has been found useful in imaging several different diseases. Although its first successful application was in the setting of acute stroke[1,2], DWI has become a useful tool in the detection, characterization, and evaluation of response to treatment of many cancers[3], including malignant liver lesions[4-9]. DWI offers higher image contrast between lesions and normal liver tissue than other sequences. This is achieved through bright signal suppression from free water fluid in the abdomen, bile ducts, and vessels. Additionally, DWI images acquired at two or more b-values can be used to derive an apparent diffusion coefficient (ADC). The quantitative ADC removes T2 "shine-through" artifacts, improves image interpretation, and strengthens liver lesion characterization[5,10]. ADC values are quantitative and changes in ADC have been used to evaluate lesions' response to treatment[7,9].

Although it is widely used, DWI in the body has several technical challenges. The large diffusion weighting gradients that make the technique sensitive to microscopic diffusion also make DWI sequences very susceptible to bulk macroscopic motion. Because of this motion sensitivity, the most successful and widely used DWI sequence is based on single-shot (ss) echo planar imaging (EPI), which acquires all the *k*-space data for an image after a single radiofrequency excitation and thus freezes the motion. ss-EPI sequences are prone to image ghosts and distortion in the presence of magnetic field inhomogeneity and uncompensated eddy currents. ss-EPI–based DWI images are also limited by their low signal-to-noise ratio (SNR) and often require averaging

multiple signals to improve image quality. The calculation of the quantitative ADC using DW images acquired with multiple b-values may pose additional challenges because mis-registration of DW images of different b-values from different motion sources (*e.g.*, respiratory or cardiac) can occur[11,12]. The resulting errors in the ADC values of a tumor region of interest (ROI) directly affect the usefulness of DWI for evaluating response to treatment in liver lesions[13,14]. High-quality DW images with an increased SNR and diminished motion artifacts yield increased confidence in assessing the mean ADC value and changes in the ADC caused by the underlying biological effects of treatment (such as tumor necrosis).

Respiratory-triggered acquisition, based either on external respiratory signals or internally placed navigators, is effective in reducing respiratory motion artifacts and mis-registration of DW images. Respiratory triggering, that are not breath hold techniques, increases the total scan time by as much as 3-fold, depending on the respiratory pattern of the patient. As a result, many institutions, including ours, use free breathing (FB) for abdominal DWI. One way to overcome these time limitations is the use of simultaneous multi-slice (SMS) acceleration, a novel technique that can speed DWI data acquisition by many times without incurring the typical SNR penalty found with other acceleration techniques such as parallel imaging[15,16]. The SMS technique is based on simultaneous multiband radiofrequency excitation and the acquisition of multiple slices in a shared readout time[15-17]. SMS is compatible with many different pulse sequences; it has recently been implemented with DWI, enabling respiratory-triggered DWI acquisition of the abdomen in a reasonable scan time. Prospective acquisition correction (PACE) is an internal navigator-based technique for respiratory signal monitoring and correction. The PACE navigator is typically placed at the diaphragm to detect its displacement as a monitoring signal of the respiratory cycles. The PACE navigator signal is used to acquire images only during a pre-defined triggering window. The PACE DWI allows the synchronization of the DWI acquisition with respiratory cycles without the need to place external monitoring devices on the patient[18].

The purpose of this study was to evaluate and compare qualitative assessments of image quality and quantitative measurements of ADC from 3 different DWI sequences for liver imaging: (1) Conventional ss-EPI–based DWI with free breathing (FB-DWI); (2) SMS DWI with FB (SMS-DWI); and (3) SMS DWI using PACE triggering (PACE-DWI).

MATERIALS AND METHODS

This prospective study was approved by the Institutional Review Board at The University of Texas MD Anderson Cancer Center. Patients with documented liver lesions on prior magnetic resonance imaging (MRI) studies who were scheduled for MRI scanning of the abdomen using DWI were eligible for participation in this study. Informed consent was obtained from all patients prior to their participation. The statistical methods of this study were reviewed by Wei W from The University of Texas MD Anderson Cancer Center, Department of Biostatistics.

DWI techniques

All patients included in this study underwent a standard abdominal MRI protocol, with and without contrast. In addition, the 3 DWI sequences (FB-DWI, SMS-DWI, and PACE-DWI) were acquired in random orders (Table 1). All the sequences were obtained with b-values of 50, 400 and 800 s/mm^2. ADC maps were generated for each of the 3 sequences. The average scan times for FB-DWI, SMS-DWI, and PACE-DWI were 4 min 56 s (4 min 44 s-6 min), 3 min 8 s (3 min 4 s-3 min 38 s), and 5 min 40 s (3 min 40 s-12 min). The readout bandwidth was kept the same at 2.44 kHz/pixel for all 3 DWI sequences. PACE DWI enabled a similar acquisition time for a respiratory triggered acquisition as that of FB DWI because of the scan time savings from SMS. Breath holds were not employed in any of the three DWI techniques.

Qualitative analysis

A qualitative analysis of the DWI images was performed independently by 3 radiologists with 4, 13 and 20 years of experience, respectively. The radiologists provided a qualitative score on a 5-point Likert scale (with 5 = excellent, 4 = good, 3 = moderate, 2 = poor, 1 = non-diagnostic) for each of the 3 DWI series for all 3 b-values (50, 400 and 800 s/mm^2). In addition, 1 radiologist (JS) selected an ROI for each liver lesion and placed it on all the DWI images. The average size of the ROIs was 4.09 cm^2.

For each ROI, ADC histograms were generated using the vendor-provided software (Syngo.via, Siemens Healthineers). Two readers independently and qualitatively compared the ADC histograms from all 3 DWI sequences side-by-side

Table 1 Imaging parameters used for the study on a 1.5-T magnetic resonance imaging scanner

Sequence	TE (ms)	TR (ms)	Slice Thickness/0-mm gap (mm)	Time	Matrix size
T1-gradient dual echo	2.1 and 4.2	170	5	2 s × 19 s BH	320 × 219
T2 fast-spin echo	93	5331	5	5 min	256 × 135
Dynamic pre-Gd and post-Gd VIBE	2.65	2.65	3	16 s BH	288 × 192
FB-DWI	67	7900	5	4 min 44 s	128 × 104
SMS-DWI	56	5000	5	3 min 4 s	128 × 104
PACE-DWI	56	2600	5	5 min 58 s	128 × 104

VIBE: Volumetric interpolated breath-hold examination; FB-DWI: Free-breathing diffusion-weighted imaging; SMS-DWI: Simultaneous multislice diffusion-weighted imaging; PACE-DWI: Prospective acquisition correction diffusion-weighted imaging; BH: Breath hold; TE: Echo time; TR: Repetition time.

on the basis of the ADC histogram distribution that reflected the tumor heterogeneity (*e.g.*, "bell shape" *vs* irregular distributions). The histogram with the most usable pixels was considered the superior one; the readers were blinded to the type of DWI sequence during the histogram comparison.

Quantitative analysis

For the quantitative analysis, the same radiologist (JS) placed an ROI for each liver lesion. For each ROI, the calculated mean ADC value was recorded and compared between sequences. The standard deviation (SD) of the ADC was also recorded and compared.

Statistical analysis

The image quality scores for each DWI sequence were summarized as frequencies and percentages. The image quality scores for each sequence were divided into 2 groups: Scores of 1 to 3 and scores of 4 or 5. The Wilcoxon signed-rank test was used to compare image quality scores between all pairs of 3 DWI sequences (*e.g.*, PACE *vs* FB; PACE *vs* SMS; SMS *vs* FB).

A linear mixed model was used to estimate and compare the means and SDs of ADC values among the sequences. The SDs of ADC values were transformed to a logarithmic scale before analysis. The image quality scores were compared using estimates from a linear mixed model with patient and reader as random effects. Pairwise comparisons between sequences were conducted and 95% confidence intervals were determined. Agreement between the 3 readers was assessed for image quality score and ADC histogram preference. All tests were 2-sided, and P values of 0.05 or less were considered statistically significant. The statistical analysis was conducted using SAS software version 9.4 (SAS Institute, Cary, NC, United States).

RESULTS

A total of 20 patients were included in the study. Their liver lesion diagnoses are listed in Table 2. Of the 56 total liver lesions, 50 were malignant. The mean qualitative image quality score of PACE-DWI (4.48) was significantly better than that of SMS-DWI (4.22) and FB-DWI (3.15) ($P < 0.05$, Table 3 and Figure 1). For PACE-DWI, all readers agreed on a score of 4 or 5 in 80% (16/20) of patients. For SMS-DWI, all readers agreed on a score of 4 or 5 in 55% (11/20) of patients. For FB-DWI, all readers agreed on a score of 1 to 3 in 55% (11/20) of patients. The quality of the ADC histograms was considered the best for PACE-DWI in 28 of 56 lesions by Reader 1 and 35 of 56 lesions by Reader 2 (Figure 2). In general, the histogram with more pixels per ADC value was considered superior quality. The FB-DWI ADC histogram was considered superior for 2 of 56 lesions by Reader 1 and no lesions by Reader 2. There was no difference between Reader 1 and Reader 2 regarding the quality of the PACE-DWI or SMS-DWI histograms.

Quantitatively, the mean ADC values from the 3 different sequences did not significantly differ (Table 4). FB-DWI had a markedly higher variation in the SD of the ADC values than did SMS-DWI and PACE-DWI. We found statistically significant differences in the SDs of the ADC values for FB-DWI *vs* PACE-DWI ($P < 0.0001$) and for FB-DWI *vs* SMS-DWI ($P = 0.03$). For PACE-DWI *vs* SMS-DWI, the SD of the ADC value pair was -0.119 ($P = 0.18$).

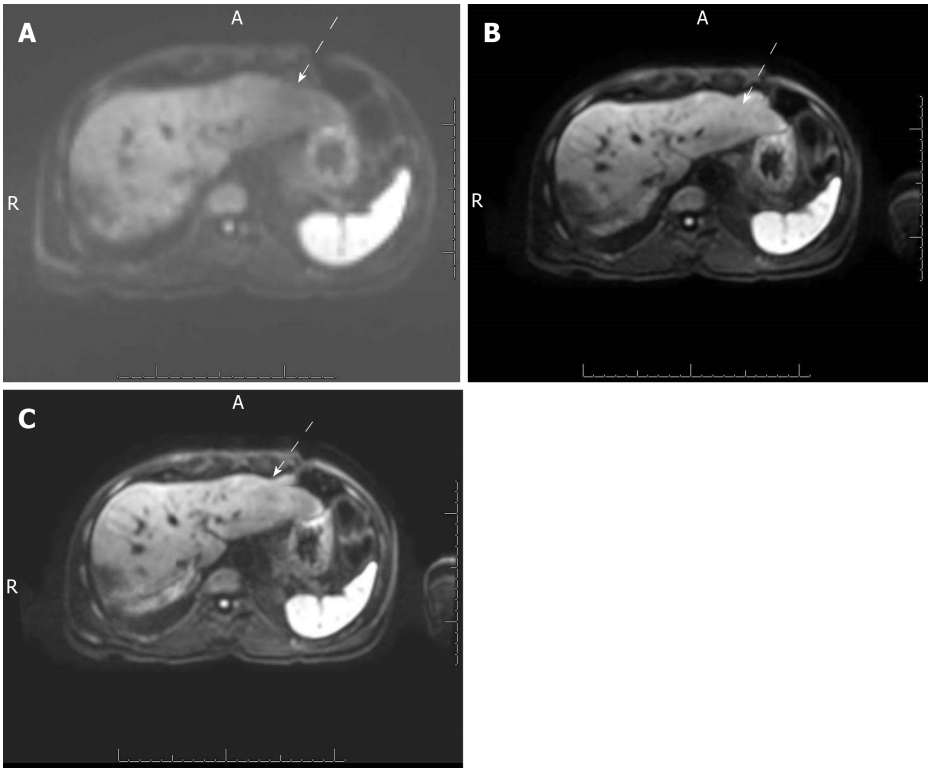

Figure 1 Axial diffusion-weighted images of the liver of a 61-year-old man with a history of hepatocellular carcinoma. The images were obtained with (A) free-breathing diffusion-weighted imaging (DWI), (B) simultaneous multislice DWI and (C) prospective acquisition correction DWI. The qualitative image quality scores of these series were 3, 5 and 5, respectively. Free-breathing DWI demonstrated artifacts on the left liver, seen as signal loss on the left liver compared to the right liver, (white arrows) that were absent on the other 2 sequences.

DISCUSSION

In this study, we found that the PACE-DWI and SMS-DWI techniques produced qualitatively better image quality than conventional FB-DWI. This was partially due to the presence of fewer artifacts, which in turn was likely a result of the shorter scan time for SMS-DWI[17,19] and the better respiration-triggering technique for PACE-DWI. We also note that TE for SMS-DWI and PACE-DWI is 11ms shorter than that of FB-DWI. The decrease in TE was enabled by the higher overall acceleration of SMS than parallel imaging alone and was likely helpful in improving the image SNR.

We noted that no patients in this study experienced a markedly irregular breathing pattern or motion during FB-DWI, which minimized the number of FB-DWI images that were substantially affected by artifacts. If the study population had included patients with irregular breathing patterns, we may have seen an even larger difference between the FB and SMS or PACE DWI sequences.

Qualitatively, all lesions were detected in all sequences. PACE-DWI had the best image quality according to all readers. PACE-DWI also had the highest level of agreement among the readers, with readers rating its image quality as 4 or 5 in 80% of cases. Kappa calculations of the level of inter-observer agreement were not performed because of the small sample size, so we believe that the percentage of agreement is an accurate representation of the results.

We also evaluated the mean ADC value for each lesion and evaluated ADC histograms instead of the SNR. The mean ADC values for each lesion did not significantly differ among the 3 sequences, suggesting that although the ADC maps were acquired using different techniques, they produced similar results and can be used interchangeably to characterize lesions and treatment response. We observed a trend towards similar mean ADC values for PACE-DWI, SMS-DWI and FB-DWI, which ranged from 1269 to 1313. Taouli *et al*[18] compared the ADC values of PACE-DWI and breath-hold-DWI for malignant lesions and found no statistically significant difference between the techniques[20].

We also compared the SDs of the ADC values. A larger SD may suggest that the technique produces more increased variability and decreased precision among ADC values. The SD of the ADC value was significantly smaller for PACE-DWI than for the other DWI techniques, suggesting that this technique has lower inherent variability. The variation in ADC values may also be due to the inherent heterogeneity of the liver

Table 2 Lesion type and distribution of the study patients

Lesion type	No. of patients	No. of lesions
Liver cyst	1	1
Treated metastasis	1	1
Desmoid tumor	2	2
Hemangioma	1	2
Metastatic thyroid cancer	1	3
Metastatic pancreatic cancer	1	4
Metastatic colon cancer	2	9
Hepatocellular carcinoma	5	11
Metastatic neuroendocrine tumor	6	23
Total	20	56

lesions.

Similarly, Taouli *et al*[18] also concluded that the PACE-DWI sequence provides a more precise ADC value. However, they did not compare ADC histograms and used different b-values from those used in our study (0, 50 and 500 s/mm^2). Boss *et al*[15] compared SMS-DWI and EPI-DWI for liver imaging[8], and Taron *et al*[17] evaluated SMS-DWI, both in healthy volunteers. Neither study compared the ADC histograms. Thus, an advantage of our study is that we were able to compare ADC values, and evaluate the precision of the ADC calculations.

It is well known that the source DWI images contain valuable information, especially for lesion detection. In our review, the ability of the sequences to detect lesions was similar. This may have been due to several factors. For instance, FB-DWI showed fewer artifacts, no lesions in our study population were located in the left liver (inferior to the heart), and the patients all breathed regularly. While ADC values are useful in characterizing liver lesions, in our patient population, most lesions were malignant; therefore, we could not determine the usefulness of ADC values for lesion characterization.

The ADC histogram provides additional data that can help in image interpretation. For example, a shift in the ADC histogram may be seen in treated liver lesions. In our study, the ADC histograms for each lesion were, by qualitative assessments, inferior for FB-DWI and superior for SMS-DWI and PACE-DWI. Recently, ADC histograms and calculated percentiles of the histograms have been used to differentiate types of metastases in the liver, tumor types[21], and tumor genomic profiles[22]. We found that the ADC histogram of PACE-DWI was superior to that of SMS-DWI, probably because of the improved SNR that results from longer scan time and better motion management through respiratory triggering. Because ADC histogram parameters ranging from the 10th through the 95th percentile of ADC have been used and are considered useful for assessment of tumors, it is imperative that the histogram have enough pixels to assess the tumor characteristics. Moreover, because a large SD indicates more variability than does a smaller SD, the smaller SD of the ADC values for PACE-DWI would be expected to provide a more robust tumor assessment, as it will produce similar and reliable values for different readers. To our knowledge, our study is the first to combine the SD value of ADC and ADC histogram for a comparison of these 3 different DWI sequences in malignant liver lesions.

There are some limitations to our study. We had a limited study population, with only 20 patients and 56 lesions. Most of the lesions were malignant. One lesion had been treated with local therapy, likely resulting in a heterogeneous ADC value for the ROI evaluated. Also, tumor necrosis, not the MRI technique alone, may have been responsible for some of the variability in ADC values. In addition, the studies were all performed on the 1.5-T scanners of a single vendor and using a single hardware and software platform. It is possible that the techniques may differ on different scanners and with different software. We were not able to use the kappa measure of inter-reader variability because of the small study population. However, we believe that the percentage of agreement provides a good representation of the results.

In conclusion, our study found that PACE-DWI provides a robust ADC histogram of liver lesions with less variability than the free breathing DWI techniques and a larger number of pixels for quantitative analysis. Therefore, this technique may provide a better characterization of the intrinsic diffusion characteristics of the tumor than that provided by FB-DWI and SMS-DWI. However, both PACE-DWI and SMS-DWI provided better image quality with fewer artifacts and less variability in the

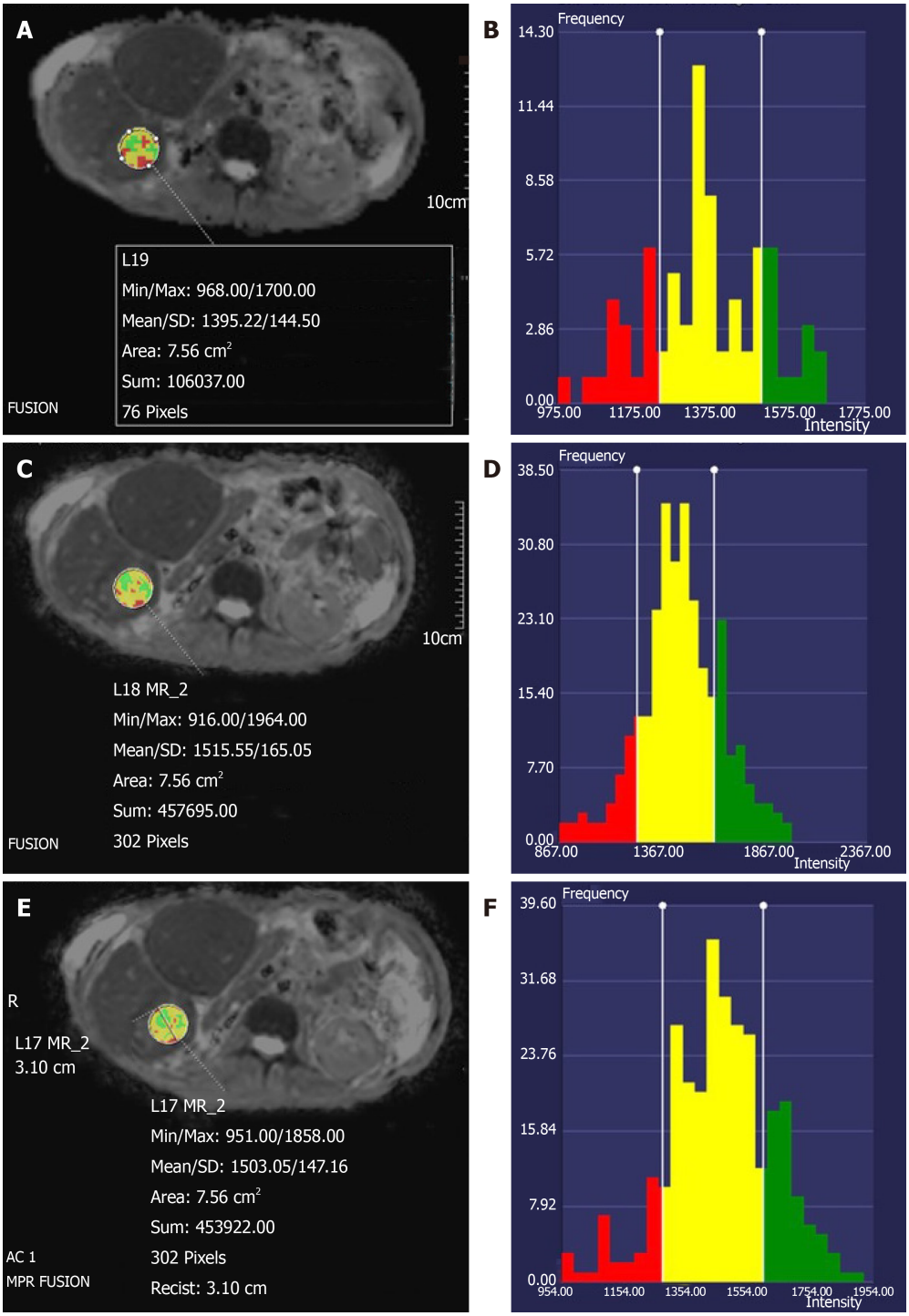

Figure 2 Axial apparent diffusion coefficients maps of the abdomen of a 61-year-old woman with colorectal cancer liver metastases, with corresponding apparent diffusion coefficients histograms. The top image corresponds to the apparent diffusion coefficients (ADC) map showing the region of interest (ROI), with color-coded ADC values. The diagram on the right is the corresponding ADC histogram. A: Axial ADC map obtained with free-breathing diffusion-weighted imaging (DWI); B: ADC histogram corresponding to the ROI in (A); C: Axial ADC map obtained with simultaneous multi-slice DWI; D: ADC histogram corresponding to the ROI in (C); E: Axial ADC map obtained with prospective acquisition correction (PACE)-DWI; F: ADC histogram corresponding to the ROI in (E). In this case, PACE-DWI and simultaneous multislice were selected as the qualitatively superior technique because of the higher number of pixels that were available for analysis, as shown by the frequency scale.

ADC values. These are valuable in assessing tumor treatment response and comparably better than the FB-DWI technique.

Table 3 Mean image quality scores by sequence for all readers

Sequence	Mean Score[1]	95% LCL	95% UCL
FB-DWI	3.15	2.79	3.51
PACE-DWI	4.48	4.12	4.85
SMS-DWI	4.22	3.85	4.58

[1]The Likert scale ratings for image quality were: 5 = superior, 4 = somewhat superior, 3 = same, 2 = somewhat inferior, and 1 = inferior. Higher scores reflect higher image quality. DWI: Diffusion-weighted imaging; FB: Free breathing; PACE: Prospective acquisition correction; SMS: Simultaneous multislice; LCL: Lower confidence level; UCL: Upper confidence level.

Table 4 Summary of the mean apparent diffusion coefficient and standard deviation by sequence

Sequence[1]	N	Mean (mm^2/s)	SD (mm^2/s)	Min (mm^2/s)	Median (mm^2/s)	Max (mm^2/s)
FB	56	1313.51	387.44	654.00	1290.38	2506.33
PACE	56	1273.28	403.30	453.71	1216.42	2401.55
SMS	56	1269.14	442.84	425.12	1155.53	2457.30
All	168	1285.31	409.87	425.12	1211.17	2506.33

[1]There were no significant differences among the mean apparent diffusion coefficient values of the 3 sequences (P = 0.51 by likelihood ratio test of the linear mixed model). N: Number of lesions; ADC: Apparent diffusion coefficient; SD: Standard deviation; FB: Free breathing; PACE: Prospective acquisition correction; SMS: Simultaneous multislice.

ARTICLE HIGHLIGHTS

Research background

Diffusion-weighted imaging (DWI) in the body has several technical challenges. This include ghosting artifacts, mis-registration and susceptibility artifacts.

Research motivation

New DWI sequences have been developed to overcome some of these challenges. Our goal is to evaluate 3 new DWI sequences for liver imaging.

Research objectives

To compare the image quality and quantitative apparent diffusion coefficients (ADC) of 3 DWI sequences for *in vivo* liver imaging: Free-breathing (FB)-DWI, simultaneous multislice (SMS)-DWI, and prospective acquisition correction (PACE)-DWI.

Research methods

Magnetic resonance imaging (MRI) of the abdomen was performed at 1.5 T on 20 patients with liver lesions in this Institutional Review Board-approved prospective study. The MR study included 3 separate DWI sequences: FB-DWI, SMS-DWI, and PACE-DWI. The image quality, mean ADC values, standard deviations (SD) of the ADC, and quality of the ADC histogram were compared. Wilcoxon signed-rank tests were used to compare qualitative image quality scores. A linear mixed model was used to compare the mean ADC values and the SDs of the ADC values. All tests were 2-sided and P values of 0.05 or less were considered statistically significant.

Research results

PACE-DWI had the highest mean image quality score (4.48), followed by SMS-DWI (4.22) and FB-DWI (3.15). The image quality of PACE-DWI was rated superior to that of SMS-DWI and FB-DWI ($P < 0.03$). The quality of the PACE-DWI ADC histograms were better than the SMS-DWI and FB-DWI. The SD of the ADC values was not statistically significant in terms of difference for PACE-DWI and SMS-DWI (P = 0.18), whereas FB-DWI had significantly more variation in the SD of its ADC.

Research conclusions

PACE-DWI and SMS-DWI are equivalent in their ability to measure ADC. Compared to FB-DWI, both PACE-DWI and SMS-DWI provide better image quality and decreased variability in the quantitative diffusion measurement of liver lesions.

Research perspectives

Therefore, this technique may provide a better characterization of the intrinsic diffusion characteristics of the tumor than that provided by FB-DWI and SMS-DWI. However, both PACE-DWI and SMS-DWI provided better image quality with fewer artifacts and less variability in the ADC values. These are valuable in assessing tumor treatment response and comparably better

than the FB-DWI technique.

ACKNOWLEDGEMENTS

We thank Ms. Amy Ninetto of the Department of Scientific Publications, The University of MD Anderson Cancer Center, Mr. Bryce P. Starr and Ms. Palencia Lewis for their help in the preparation of documents.

REFERENCES

1 **Schwamm LH**, Koroshetz WJ, Sorensen AG, Wang B, Copen WA, Budzik R, Rordorf G, Buonanno FS, Schaefer PW, Gonzalez RG. Time course of lesion development in patients with acute stroke: serial diffusion- and hemodynamic-weighted magnetic resonance imaging. *Stroke* 1998; **29**: 2268-2276 [PMID: 9804633]

2 **Johnston KC**, Wagner DP, Wang XQ, Newman GC, Thijs V, Sen S, Warach S; GAIN, Citicoline, and ASAP Investigators. Validation of an acute ischemic stroke model: does diffusion-weighted imaging lesion volume offer a clinically significant improvement in prediction of outcome? *Stroke* 2007; **38**: 1820-1825 [PMID: 17446421 DOI: 10.1161/STROKEAHA.106.479154]

3 **Padhani AR**, Liu G, Koh DM, Chenevert TL, Thoeny HC, Takahara T, Dzik-Jurasz A, Ross BD, Van Cauteren M, Collins D, Hammoud DA, Rustin GJ, Taouli B, Choyke PL. Diffusion-weighted magnetic resonance imaging as a cancer biomarker: consensus and recommendations. *Neoplasia* 2009; **11**: 102-125 [PMID: 19186405]

4 **Kim JH**, Joo I, Kim TY, Han SW, Kim YJ, Lee JM, Han JK. Diffusion-Related MRI Parameters for Assessing Early Treatment Response of Liver Metastases to Cytotoxic Therapy in Colorectal Cancer. *AJR Am J Roentgenol* 2016; **207**: W26-W32 [PMID: 27303858 DOI: 10.2214/AJR.15.15683]

5 **Calistri L**, Castellani A, Matteuzzi B, Mazzoni E, Pradella S, Colagrande S. Focal Liver Lesions Classification and Characterization: What Value Do DWI and ADC Have? *J Comput Assist Tomogr* 2016; **40**: 701-708 [PMID: 27454786 DOI: 10.1097/RCT.0000000000000458]

6 **Colagrande S**, Castellani A, Nardi C, Lorini C, Calistri L, Filippone A. The role of diffusion-weighted imaging in the detection of hepatic metastases from colorectal cancer: A comparison with unenhanced and Gd-EOB-DTPA enhanced MRI. *Eur J Radiol* 2016; **85**: 1027-1034 [PMID: 27130067 DOI: 10.1016/j.ejrad.2016.02.011]

7 **Willems SM**, Koekkoek PS, Kwee TC, van den Bosch MA. Diffusion-weighted MRI of the liver for early tumor response assessment: Promising technique but evidence is still lacking. *Acta Oncol* 2010; **49**: 252-255 [PMID: 20100159 DOI: 10.3109/02841860903464007]

8 **Nakamura Y**, Higaki T, Akiyama Y, Fukumoto W, Kajiwara K, Kaichi Y, Honda Y, Komoto D, Tatsugami F, Iida M, Ohmoto T, Date S, Awai K. Diffusion-weighted MR imaging of non-complicated hepatic cysts: Value of 3T computed diffusion-weighted imaging. *Eur J Radiol Open* 2016; **3**: 138-144 [PMID: 27489867 DOI: 10.1016/j.ejro.2016.07.001]

9 **Donati F**, Boraschi P, Pacciardi F, Cervelli R, Castagna M, Urbani L, Falaschi F, Caramella D. 3T diffusion-weighted MRI in the response assessment of colorectal liver metastases after chemotherapy: Correlation between ADC value and histological tumour regression grading. *Eur J Radiol* 2017; **91**: 57-65 [PMID: 28629572 DOI: 10.1016/j.ejrad.2017.03.020]

10 **Duran R**, Ronot M, Kerbaol A, Van Beers B, Vilgrain V. Hepatic hemangiomas: factors associated with T2 shine-through effect on diffusion-weighted MR sequences. *Eur J Radiol* 2014; **83**: 468-478 [PMID: 24364922 DOI: 10.1016/j.ejrad.2013.11.023]

11 **Kwee TC**, Takahara T, Niwa T, Ivancevic MK, Herigault G, Van Cauteren M, Luijten PR. Influence of cardiac motion on diffusion-weighted magnetic resonance imaging of the liver. *MAGMA* 2009; **22**: 319-325 [PMID: 19727877 DOI: 10.1007/s10334-009-0183-1]

12 **Mazaheri Y**, Do RK, Shukla-Dave A, Deasy JO, Lu Y, Akin O. Motion correction of multi-b-value diffusion-weighted imaging in the liver. *Acad Radiol* 2012; **19**: 1573-1580 [PMID: 22963726 DOI: 10.1016/j.acra.2012.07.005]

13 **Bonekamp D**, Bonekamp S, Halappa VG, Geschwind JF, Eng J, Corona-Villalobos CP, Pawlik TM, Kamel IR. Interobserver agreement of semi-automated and manual measurements of functional MRI metrics of treatment response in hepatocellular carcinoma. *Eur J Radiol* 2014; **83**: 487-496 [PMID: 24387824 DOI: 10.1016/j.ejrad.2013.11.016]

14 **Corona-Villalobos CP**, Halappa VG, Bonekamp S, Eng J, Reyes D, Cosgrove D, Rastegar N, Pan L, Pawlik TM, Kamel IR. Functional magnetic resonance imaging response of targeted tumor burden and its impact on survival in patients with hepatocellular carcinoma. *Invest Radiol* 2015; **50**: 283-289 [PMID: 25396692 DOI: 10.1097/RLI.0000000000000112]

15 **Boss A**, Barth B, Filli L, Kenkel D, Wurnig MC, Piccirelli M, Reiner CS. Simultaneous multi-slice echo planar diffusion weighted imaging of the liver and the pancreas: Optimization of signal-to-noise ratio and acquisition time and application to intravoxel incoherent motion analysis. *Eur J Radiol* 2016; **85**: 1948-1955 [PMID: 27776645 DOI: 10.1016/j.ejrad.2016.09.002]

16 **Filli L**, Ghafoor S, Kenkel D, Liu W, Weiland E, Andreisek G, Frauenfelder T, Runge VM, Boss A. Simultaneous multi-slice readout-segmented echo planar imaging for accelerated diffusion-weighted imaging of the breast. *Eur J Radiol* 2016; **85**: 274-278 [PMID: 26547123 DOI: 10.1016/j.ejrad.2015.10.009]

17 **Taron J**, Martirosian P, Erb M, Kuestner T, Schwenzer NF, Schmidt H, Honndorf VS, Weiβ J, Notohamiprodjo M, Nikolaou K, Schraml C. Simultaneous multislice diffusion-weighted MRI of the liver: Analysis of different breathing schemes in comparison to standard sequences. *J Magn Reson Imaging* 2016; **44**: 865-879 [PMID: 26919580 DOI: 10.1002/jmri.25204]

18 **Taouli B**, Sandberg A, Stemmer A, Parikh T, Wong S, Xu J, Lee VS. Diffusion-weighted imaging of the liver: comparison of navigator triggered and breathhold acquisitions. *J Magn Reson Imaging* 2009; **30**: 561-568 [PMID: 19711402 DOI: 10.1002/jmri.21876]

19 **Kenkel D**, Barth BK, Piccirelli M, Filli L, Finkenstädt T, Reiner CS, Boss A. Simultaneous Multislice

Diffusion-Weighted Imaging of the Kidney: A Systematic Analysis of Image Quality. *Invest Radiol* 2017; **52**: 163-169 [PMID: 27662577 DOI: 10.1097/RLI.0000000000000323]

20 **Li Q**, Wu X, Qiu L, Zhang P, Zhang M, Yan F. Diffusion-weighted MRI in the assessment of split renal function: comparison of navigator-triggered prospective acquisition correction and breath-hold acquisition. *AJR Am J Roentgenol* 2013; **200**: 113-119 [PMID: 23255749 DOI: 10.2214/AJR.11.8052]

21 **Payabvash S**, Tihan T, Cha S. Volumetric voxelwise apparent diffusion coefficient histogram analysis for differentiation of the fourth ventricular tumors. *Neuroradiol J* 2018; **31**: 554-564 [PMID: 30230411 DOI: 10.1177/1971400918800803]

22 **Drevelegas K**, Nikiforaki K, Constantinides M, Papanikolaou N, Papalavrentios L, Stoikou I, Zarogoulidis P, Pitsiou G, Pataka A, Organtzis J, Papadaki E, Porpodis K, Kougioumtzi I, Kioumis I, Kouskouras C, Akriviadis E, Drevelegas A. Apparent Diffusion Coefficient Quantification in Determining the Histological Diagnosis of Malignant Liver Lesions. *J Cancer* 2016; **7**: 730-735 [PMID: 27076855 DOI: 10.7150/jca.14197]

Published By Baishideng Publishing Group Inc
7041 Koll Center Parkway, Suite 160, Pleasanton, CA 94566, USA
Telephone: +1-925-2238242
E-mail: bpgoffice@wjgnet.com
Help Desk: https://www.f6publishing.com/helpdesk
https://www.wjgnet.com

ISSN 1949-8470 (online)

World Journal of *Radiology*

World J Radiol 2019 December 28; 11(12): 144-148

Published by Baishideng Publishing Group Inc

World Journal of Radiology

Contents

Monthly Volume 11 Number 12 December 28, 2019

CASE REPORT

Contents

World Journal of Radiology

Volume 11 Number 12 December 28, 2019

ABOUT COVER

Editorial Board Member of *World Journal of Radiology*, Yongxia Zhou, PhD, Senior Scientist, Department of Radiology, New York University, New York, NY 10012-1126, United States.

AIMS AND SCOPE

The primary aim of *World Journal of Radiology* (*WJR*, *World J Radiol*) is to provide scholars and readers from various fields of radiology with a platform to publish high-quality basic and clinical research articles and communicate their research findings online.

WJR mainly publishes articles reporting research results and findings obtained in the field of radiology and covering a wide range of topics including state of the art information on cardiopulmonary imaging, gastrointestinal imaging, genitourinary imaging, musculoskeletal imaging, neuroradiology/head and neck imaging, nuclear medicine and molecular imaging, pediatric imaging, vascular and interventional radiology, and women's imaging.

INDEXING/ABSTRACTING

The *WJR* is now abstracted and indexed in Emerging Sources Citation Index (Web of Science), PubMed, PubMed Central, China National Knowledge Infrastructure (CNKI), China Science and Technology Journal Database (CSTJ), and Superstar Journals Database.

RESPONSIBLE EDITORS FOR THIS ISSUE

NAME OF JOURNAL
World Journal of Radiology

ISSN
ISSN 1949-8470 (online)

LAUNCH DATE
January 31, 2009

FREQUENCY
Monthly

EDITORS-IN-CHIEF
Venkatesh Mani

EDITORIAL BOARD MEMBERS
https://www.wjgnet.com/1949-8470/editorialboard.htm

EDITORIAL OFFICE
Ruo-Yu Ma, Director

PUBLICATION DATE
December 28, 2019

INSTRUCTIONS TO AUTHORS
https://www.wjgnet.com/bpg/gerinfo/204

GUIDELINES FOR ETHICS DOCUMENTS
https://www.wjgnet.com/bpg/GerInfo/287

GUIDELINES FOR NON-NATIVE SPEAKERS OF ENGLISH
https://www.wjgnet.com/bpg/gerinfo/240

PUBLICATION MISCONDUCT
https://www.wjgnet.com/bpg/gerinfo/208

ARTICLE PROCESSING CHARGE
https://www.wjgnet.com/bpg/gerinfo/242

STEPS FOR SUBMITTING MANUSCRIPTS
https://www.wjgnet.com/bpg/GerInfo/239

ONLINE SUBMISSION
https://www.f6publishing.com

World Journal of Radiology

Submit a Manuscript: https://www.f6publishing.com

World J Radiol 2019 December 28; 11(12): 144-148

DOI: 10.4329/wjr.v11.i12.144

ISSN 1949-8470 (online)

CASE REPORT

Chest pain without a clue-ultrasound to rescue occult multiple myeloma: A case report

Gopal Chawla, Naveen Dutt, Kunal Deokar, Virender Kumar Meena

ORCID number: Gopal Chawla (0000-0002-8735-9774); Naveen Dutt (0000-0002-9517-4999); Kunal Deokar (0000-0003-2603-1633); Virendra Kumar Meena (0000-0002-1824-3671).

Author contributions: All authors conceived the idea; Chawla G, Deokar K, Meena VK collected the data; Chawla G, and Dutt N performed the literature search; Chawla G, and Deokar K wrote the manuscript; Deokar K, Dutt N, Meena VK critically reviewed the manuscript.

Informed consent statement: Informed consent was obtained from the patient.

Conflict-of-interest statement: The authors state they have no conflicts of interest.

CARE Checklist (2016) statement: Guidelines of the CARE checklist (2016) have been adopted.

Manuscript source: Unsolicited

Gopal Chawla, Naveen Dutt, Kunal Deokar, Pulmonary, Critical Care and Sleep Medicine, All India Institute of Medical Sciences, Jodhpur 342008, Rajasthan, India

Virender Kumar Meena, Department of Radiodiagnosis, Geetanjali Medical College and Hospital, Udaipur 342005, India

Corresponding author: Gopal Chawla, DNB, FCCP, MBBS, MD, Academic Fellow, DM Fellow, Pulmonary, Critical Care and Sleep Medicine, All India Institute of Medical Sciences, Jodhpur 342005, Rajasthan, India. dr.gopalchawla@gmail.com
Telephone: +91-7982283553

Abstract

BACKGROUND

Chest pain is one of the most common symptoms with which a patient presents to a doctor. Differentials include, but are not limited to, cardiac pulmonary, gastrointestinal, psychosomatic and musculoskeletal causes. In our case, ultrasound of the chest wall paved the way for the diagnosis of multiple myeloma, which occultly presented with chronic chest pain.

CASE SUMMARY

Here we report a case of 50-year-old man with chronic chest pain without anemia or renal failure who was diagnosed with multiple myeloma, despite negative bence jones protein and M band electrophoresis. An ultrasound of the chest wall showed cortical irregularities along with a hypoechoic mass in the sternum and left 5th rib, which helped us in clinching the diagnosis.

CONCLUSION

Ultrasound of bone can often aid in reaching a diagnosis indirectly if not directly.

Key words: Case report; Ultrasound; Multiple myeloma; Chest pain

Core tip: Multiple myeloma is notorious for presenting in atypical ways, and one should have a high index of suspicion for the same. Ultrasounds of bone can often aid in reaching a diagnosis indirectly if not directly.

Citation: Chawla G, Dutt N, Deokar K, Meena VK. Chest pain without a clue-ultrasound to rescue occult multiple myeloma: A case report. *World J Radiol* 2019; 11(12): 144-148

manuscript

Received: July 3, 2019
Peer-review started: July 16, 2019
First decision: September 21, 2019
Revised: October 11, 2019
Accepted: November 7, 2019
Article in press: November 7, 2019
Published online: December 28, 2019

P-Reviewer: Armellini E, Iovino P, Li CH
S-Editor: Yan JP
L-Editor: Filipodia
E-Editor: Li X

URL: https://www.wjgnet.com/1949-8470/full/v11/i12/144.htm
DOI: https://dx.doi.org/10.4329/wjr.v11.i12.144

INTRODUCTION

Chest pain is one of the most common symptoms with which a patient presents to a doctor. Etiology is wide, and ranges from acute and life-threatening diseases like acute coronary syndrome and pulmonary embolism to conditions with favorable prognosis like myalgia and costochondritis[1]. It is important to know the relevant etiologies and their respective frequencies.

Bone pain is one of the most common presentations of multiple myeloma (70%-80%), and 90% of cases will present with lumbar spine or rib pain. Plain films are only 80%-90% sensitive at detecting lytic bone lesions, due to an inability to detect lesions with less than 30%-50% trabecular bone loss. By the time this degree of sternal/rib bone loss occurs, patients are at high risk for fracture, which can result in serious complications such as flail chest and acute hypoxic respiratory failure[2].

Since early treatment with chemotherapy and zoledronic acid reduces vertebral fractures and skeletal events, multiple myeloma is an important disease to keep on a differential for persistent atypical chest pain, especially when anemia and renal injury is present.

CASE PRESENTATION

Chief complaints

A 50-year-old banker presented with complaints of chest pain for 2 mo.

History of present illness

Chest pain was parasternal, non-radiating and continuous in nature. There was no history of trauma, cough, breathlessness, loss of weight, loss of appetite or fever.

History of past illness

There was no major medical or surgical illness in the past.

Physical examination

Results of chest examination were within normal limits, apart from left parasternal tenderness.

Laboratory examinations

The patient had normal hemogram, and erythrocyte sedimentation rate was 35 mm in the first hour. He was worked up for metabolic causes of chest pain, his vitamin D level was within normal limits, and serum calcium was 10.42 mg/dL. Urine examination showed trace proteins. Urine for Bence jones proteins and blood electrophoresis were found to be negative for multiple myeloma.

Imaging examinations

The chest X-ray was within normal limits. The electrocardiograph, 2D echocardiography and treadmill test were also within normal limits. The patient even underwent coronary angiography due to the troublesome nature of his chest pain, which was also normal. Upper gastrointestinal endoscopy was done to rule out reflux disease and gastroesophageal ulcers, which was once again normal. The patient was referred to psychiatry, and underwent cognitive behavior therapy, however this too was of no avail. He was also being worked up for musculoskeletal causes and was started on non-steroidal anti-inflammatory drugs suspecting costochondritis, but he remained uncomfortable (Table 1).

To rule out sternal and rib lesions, he was screened with an ultrasound of the chest wall, which showed cortical irregularities along with a hypoechoic mass in the sternum and left 5th rib (Figure 1). Considering the cortical irregularities, differential of bone neoplasms, metastasis and multiple myeloma were kept in consideration. He underwent magnetic resonance imaging (MRI) of the spine, which showed multiple well-defined T1/T2 hypointense lesions of varying sizes in the dorso lumber vertebra at multiple levels, including the body of the sternum and posterior aspect of the left 4th rib. A whole body positron emission tomogram (PET scan) was done to rule out any primary, which showed multiple fluorodeoxyglucose avid lesions in the axial and

Table 1 Timeline

Presentation, day 0-2 mo	3rd month	4th month	4th month	5th month
Worked up for various causes of chest pain	Tread mill test, coronary angiography, upper gastrointestinal endoscopy	Metabolic causes ruled out	Ultrasonography chest, clue to Bone lesion	Magnetic resonance imaging, positron emission technology, bone marrow biopsy

appendicular skeleton (Figure 2). To confirm the diagnosis, bone marrow aspiration and biopsy were performed, which showed increased immature and mature plasma cells. Marrow was slightly hypercellular for age and showed all hematopoietic components. There was a marked interstitial prominence of plasma cells along with a definitive presence of sheets of plasma cells.

This is a very rare case where chest pain was the only initial symptom of multiple myeloma, and shows how screening ultrasonography helped in leading us to the diagnosis. There is no evidence reported in the literature of any such case where multiple myeloma was diagnosed using ultrasonography.

FINAL DIAGNOSIS

Multiple myeloma.

TREATMENT

He was started on bortezomib, leflunomide and dexamethasone.

OUTCOME AND FOLLOW-UP

After a mere two cycles of chemotherapy, he showed drastic improvement in pain wherein his Visual Analogue Score dropped from 7/10 to 2/10.

DISCUSSION

Chronic chest pain has been broadly classified as cardiogenic and non-cardiogenic chest pain (NCP). The etiology of NCP can be pulmonary, gastrointestinal, musculoskeletal or psychosomatic. At times it becomes very difficult to search the etiology of chest pain[3,4].

Multiple myeloma is a clonal condition of B cells that involves uncontrolled proliferation of abnormal plasma cells. Clinical features can either be directly due to proliferation or indirectly due to substances released by these cells. It results in suppression of erythropoiesis along with multiple osteolytic lesions, which results in hypercalcemia, skeletal pain and pathological fractures. It also causes the accumulation of monoclonal immunoglobulins (Igs) along with other regulating substances. These circulating monoclonal Igs or their subunits are the reason behind proteinuria, renal tubular damage and amyloid deposition[5].

They have varied presentation, 10%-40% are asymptomatic and 50%-70% have bone pain due to lytic lesions and pathological fractures. About 1%-5% cases may not demonstrate Igs or their subunits in serum or urine (non-secretory multiple myeloma)[6].

This is a unique case where initial work-up, consisting of a complete hemogram, serum calcium, erythrocyte sedimentation rate, chest radiology, urine bence jones proteins and serum electrophoresis, was normal. This misguided us to search for other causes of chest pain. However, during later ultrasound screening for a musculoskeletal cause, we came across multiple cortical irregularities over the ribs that helped us in clinching the diagnosis.

Ultrasound of bone has not been frequently used in the past. It has been used as a diagnostic tool in the evaluation of costochondral cartilage deformities in children of the anterior chest wall mass where there was negative radiography[7], and has been used in bone tumors like chondrosarcoma and fractures where a painful area shows fragmented cortical bone and at times subperiosteal hematoma[8].

The chest wall is known to get involved either by direct extension of a tumor mass, metastases or hematologic malignancy like multiple myeloma. In this region,

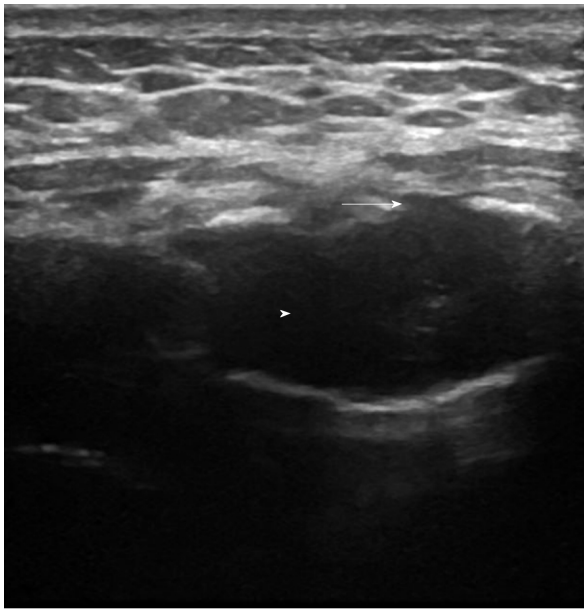

Figure 1 Ultrasound of sternum showing cortical irregularities (arrow) with central hypoechoic area (arrow head).

metastases are mainly from breast, thyroid, kidney, lung and prostate cancer along with plasma cell myeloma. The vast majority of such tumors are osteolytic. Ultrasound detection of osseous defects is possible only after the damage of the anterior compact substance[9].

Paik *et al*[10] has shown ultrasonography to be better than conventional radiography (39%) for the diagnosis of such tumors. These were characterized by cortical defects or an irregular cortical edge or a mass invading local soft tissues, including pleura in some cases. Lee *et al*[11] compared a group of patients with rib metastases from renal cancer and prostate cancer metastases, and they showed that the irregular surface of the costal cortex in the absence of fracture or the presence of masses within the soft tissue represented the only sonographic feature of osteoblastic foci of prostate cancer.

While for multiple myeloma it has never been used in the literature, we found cortical irregularities along with focal bone destruction (Figure 1), which was later confirmed with MRI by the presence of multiple osteolytic lesions. PET computed tomography ruled out any contribution from the kidney, thyroid or lung and also helped in assessing disease burden and the identification of extramedullary involvement. Bone marrow biopsy sealed the diagnosis. Apart from atypical presentation and an unconventional way of diagnosing, our case was unique as the patient had normal hemoglobin, absent bence jones proteins and a negative M band on electrophoresis, *i.e*. the patient was having non-secretory multiple myeloma, which is even difficult to diagnose.

CONCLUSION

Multiple myeloma is notorious to present in atypical ways, and therefore one should have a high index of suspicion for the same. Ultrasound of bone can often help in reaching the diagnosis indirectly if not directly. As a non-invasive, bedside and easily available investigation, it is truly a patient-friendly approach to finding clues in difficult cases.

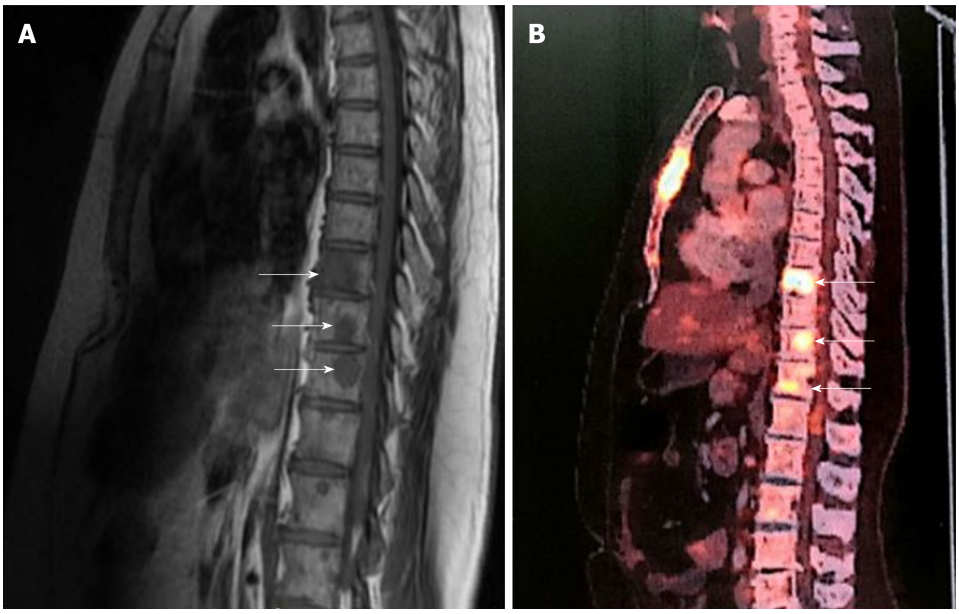

Figure 2 Magnetic resonance imaging and positron emission technology scan. A: Magnetic resonance imaging showing multiple osteolytic lesions (arrows); B: Positron emission technology scan showing multiple osteolytic lesions with high fluorodeoxyglucose avidity (arrows).

ACKNOWLEDGEMENTS

I would like to thank Dr. Govind Patel from Clinical Hematology for his valuable inputs and Dr. Nupur Abrol for Pain and Palliative care.

REFERENCES

1 **Hurst JW**, Morris DC. Chest pain. Armonk, NY, United States: Futura Pub, 2001.
2 **Dimopoulos M**, Terpos E, Comenzo RL, Tosi P, Beksac M, Sezer O, Siegel D, Lokhorst H, Kumar S, Rajkumar SV, Niesvizky R, Moulopoulos LA, Durie BG; IMWG. International myeloma working group consensus statement and guidelines regarding the current role of imaging techniques in the diagnosis and monitoring of multiple Myeloma. *Leukemia* 2009; **23**: 1545-1556 [PMID: 19421229 DOI: 10.1038/leu.2009.89]
3 **Campbell KA**, Madva EN, Villegas AC, Beale EE, Beach SR, Wasfy JH, Albanese AM, Huffman JC. Non-cardiac Chest Pain: A Review for the Consultation-Liaison Psychiatrist. *Psychosomatics* 2017; **58**: 252-265 [PMID: 28196622 DOI: 10.1016/j.psym.2016.12.003]
4 **Fass R**, Achem SR. Noncardiac chest pain: epidemiology, natural course and pathogenesis. *J Neurogastroenterol Motil* 2011; **17**: 110-123 [PMID: 21602987 DOI: 10.5056/jnm.2011.17.2.110]
5 **Dash NR**, Mohanty B. Multiple myeloma: a case of atypical presentation on protein electrophoresis. *Indian J Clin Biochem* 2012; **27**: 100-102 [PMID: 23277721 DOI: 10.1007/s12291-011-0178-3]
6 **Middela S**, Kanse P. Nonsecretory multiple myeloma. *Indian J Orthop* 2009; **43**: 408-411 [PMID: 19838394 DOI: 10.4103/0019-5413.55979]
7 **Supakul N**, Karmazyn B. Ultrasound evaluation of costochondral abnormalities in children presenting with anterior chest wall mass. *AJR Am J Roentgenol* 2013; **201**: W336-W341 [PMID: 23883250 DOI: 10.2214/AJR.12.9792]
8 **Zarqane H**, Viala P, Dallaudière B, Vernhet H, Cyteval C, Larbi A. Tumors of the rib. *Diagn Interv Imaging* 2013; **94**: 1095-1108 [PMID: 24007770 DOI: 10.1016/j.diii.2013.05.006]
9 **Smereczyński A**, Kołaczyk K, Bernatowicz E. Chest wall - a structure underestimated in ultrasonography. Part III: Neoplastic lesions. *J Ultrason* 2017; **17**: 281-288 [PMID: 29375904 DOI: 10.15557/JoU.2017.0041]
10 **Paik SH**, Chung MJ, Park JS, Goo JM, Im JG. High-resolution sonography of the rib: can fracture and metastasis be differentiated? *AJR Am J Roentgenol* 2005; **184**: 969-974 [PMID: 15728626 DOI: 10.2214/ajr.184.3.01840969]
11 **Lee KS**, De Smet AA, Liu G, Staab MJ. High resolution ultrasound features of prostatic rib metastasis: a prospective feasibility study with implication in the high-risk prostate cancer patient. *Urol Oncol* 2014; **32**: 24.e7-24.11 [PMID: 23481369 DOI: 10.1016/j.urolonc.2012.08.014]

Published By Baishideng Publishing Group Inc
7041 Koll Center Parkway, Suite 160, Pleasanton, CA 94566, USA
Telephone: +1-925-2238242
E-mail: bpgoffice@wjgnet.com
Help Desk: https://www.f6publishing.com/helpdesk
https://www.wjgnet.com

ISSN 1949-8470 (online)

World Journal of *Radiology*

World J Radiol 2019 February 28; 11(2): 19-26

Published by Baishideng Publishing Group Inc

WJR

World Journal of Radiology

Contents

Monthly Volume 11 Number 2 February 28, 2019

MINIREVIEWS

Contents

World Journal of Radiology

Volume 11 Number 2 February 28, 2019

ABOUT COVER

Editorial Board Member of *World Journal of Radiology*, Fernando R Santiago, PhD, Doctor, Professor, Teacher, Department of Radiology, Santiago, FR (reprint author), Hosp Traumatol Ciudad Sanitaria Virgen de las Nie, Dept Radiol, Carretera Jaen SN, Granada 18013, Spain., Granada 18003, Granada, Spain

AIMS AND SCOPE

World Journal of Radiology (*World J Radiol*, *WJR*, online ISSN 1949-8470, DOI: 10.4329) is a peer-reviewed open access academic journal that aims to guide clinical practice and improve diagnostic and therapeutic skills of clinicians.

WJR covers topics concerning diagnostic radiology, radiation oncology, radiologic physics, neuroradiology, nuclear radiology, pediatric radiology, vascular/interventional radiology, medical imaging achieved by various modalities and related methods analysis. The current columns of *WJR* include editorial, frontier, mini-reviews, review, medical ethics, original articles, case report, *etc*.

We encourage authors to submit their manuscripts to *WJR*. We will give priority to manuscripts that are supported by major national and international foundations and those that are of great basic and clinical significance.

INDEXING/ABSTRACTING

The *WJR* is now abstracted and indexed in Emerging Sources Citation Index (Web of Science), PubMed, PubMed Central, China National Knowledge Infrastructure (CNKI), China Science and Technology Journal Database (CSTJ), and Superstar Journals Database.

RESPONSIBLE EDITORS FOR THIS ISSUE

Responsible Electronic Editor: *Han Song* **Proofing Editorial Office Director:** *Jin-Lei Wang*

NAME OF JOURNAL
World Journal of Radiology

ISSN
ISSN 1949-8470 (online)

LAUNCH DATE
January 31, 2009

FREQUENCY
Monthly

EDITORS-IN-CHIEF
Venkatesh Mani

EDITORIAL BOARD MEMBERS
https://www.wjgnet.com/1949-8470/editorialboard.htm

EDITORIAL OFFICE
Jin-Lei Wang, Director

PUBLICATION DATE
February 28, 2019

INSTRUCTIONS TO AUTHORS
https://www.wjgnet.com/bpg/gerinfo/204

GUIDELINES FOR ETHICS DOCUMENTS
https://www.wjgnet.com/bpg/GerInfo/287

GUIDELINES FOR NON-NATIVE SPEAKERS OF ENGLISH
https://www.wjgnet.com/bpg/gerinfo/240

PUBLICATION MISCONDUCT
https://www.wjgnet.com/bpg/gerinfo/208

ARTICLE PROCESSING CHARGE
https://www.wjgnet.com/bpg/gerinfo/242

STEPS FOR SUBMITTING MANUSCRIPTS
https://www.wjgnet.com/bpg/GerInfo/239

ONLINE SUBMISSION
https://www.f6publishing.com

World Journal of Radiology

Submit a Manuscript: https://www.f6publishing.com

World J Radiol 2019 February 28; 11(2): 19-26

DOI: 10.4329/wjr.v11.i2.19

ISSN 1949-8470 (online)

MINIREVIEWS

Artificial intelligence in breast ultrasound

Ge-Ge Wu, Li-Qiang Zhou, Jian-Wei Xu, Jia-Yu Wang, Qi Wei, You-Bin Deng, Xin-Wu Cui, Christoph F Dietrich

ORCID number: Ge-Ge Wu (0000-0002-7159-2483); Li-Qiang Zhou (0000-0002-6025-2694); Jia-Yu Wang (0000-0001-9902-0666); Qi Wei (0000-0002-7955-406X); You-Bin Deng (0000-0001-8002-5109); Xin-Wu Cui (0000-0003-3890-6660); Christoph F Dietrich (0000-0001-6015-6347).

Author contributions: Cui XW established the design and conception of the paper; Wu GG, Zhou LQ, Xu JW, Wang JY, Wei Q, Deng YB, Cui XW, and Dietrich CF explored the literature data; Wu GG provided the first draft of the manuscript, which was discussed and revised critically for intellectual content by Wu GG, Zhou LQ, Xu JW, Wang JY, Wei Q, Deng YB, Cui XW, and Dietrich CF; all authors discussed the statement and conclusions and approved the final version to be published.

Conflict-of-interest statement: We declare that we do not have anything to disclose regarding funding or conflict of interest with respect to this manuscript.

Ge-Ge Wu, Li-Qiang Zhou, Jia-Yu Wang, Qi Wei, You-Bin Deng, Xin-Wu Cui, Christoph F Dietrich, Sino-German Tongji-Caritas Research Center of Ultrasound in Medicine, Department of Medical Ultrasound, Tongji Hospital, Tongji Medical College, Huazhong University of Science and Technology, Wuhan 430030, Hubei Province, China

Jian-Wei Xu, Department of Ultrasound, The First Affiliated Hospital of Zhengzhou University, Zhengzhou 450052, Henan Province, China

Christoph F Dietrich, Medical Clinic 2, Caritas-Krankenhaus Bad Mergentheim, Academic Teaching Hospital of the University of Würzburg, Würzburg 97980, Germany

Corresponding author: Xin-Wu Cui, MD, PhD, Professor, Deputy Director, Sino-German Tongji-Caritas Research Center of Ultrasound in Medicine, Department of Medical Ultrasound, Tongji Hospital, Tongji Medical College, Huazhong University of Science and Technology, No. 1095, Jiefang Avenue, Wuhan 430030, Hubei Province, China.
cuixinwu@live.cn
Telephone: +86-27-83663754
Fax: +86-27-83663754

Abstract

Artificial intelligence (AI) is gaining extensive attention for its excellent performance in image-recognition tasks and increasingly applied in breast ultrasound. AI can conduct a quantitative assessment by recognizing imaging information automatically and make more accurate and reproductive imaging diagnosis. Breast cancer is the most commonly diagnosed cancer in women, severely threatening women's health, the early screening of which is closely related to the prognosis of patients. Therefore, utilization of AI in breast cancer screening and detection is of great significance, which can not only save time for radiologists, but also make up for experience and skill deficiency on some beginners. This article illustrates the basic technical knowledge regarding AI in breast ultrasound, including early machine learning algorithms and deep learning algorithms, and their application in the differential diagnosis of benign and malignant masses. At last, we talk about the future perspectives of AI in breast ultrasound.

Key words: Breast; Ultrasound; Artificial intelligence; Machine learning; Deep learning

Core tip: Artificial intelligence (AI) is gaining extensive attention for its excellent performance in image-recognition tasks and increasingly applied in breast ultrasound. In this review, we summarize the current knowledge of AI in breast ultrasound, including

Manuscript source: Invited manuscript

Received: November 29, 2018
Peer-review started: November 30, 2018
First decision: January 4, 2019
Revised: January 14, 2019
Accepted: January 26, 2019
Article in press: January 27, 2019
Published online: February 28, 2019

the technical aspects, and its applications in the differentiation between benign and malignant breast masses. In the meanwhile, we also discuss the future perspectives, such as combining with elastography and contrast-enhanced ultrasound, to improve the performance of AI in breast ultrasound.

Citation: Wu GG, Zhou LQ, Xu JW, Wang JY, Wei Q, Deng YB, Cui XW, Dietrich CF. Artificial intelligence in breast ultrasound. *World J Radiol* 2019; 11(2): 19-26
URL: https://www.wjgnet.com/1949-8470/full/v11/i2/19.htm
DOI: https://dx.doi.org/10.4329/wjr.v11.i2.19

INTRODUCTION

Breast cancer is the most common malignant tumor and the second leading cause of cancer death among women in the United States[1]. In recent years, the incidence and mortality of breast cancer have increased year by year[2,3]. Mortality can be reduced by early detection and timely therapy. Therefore, its early and correct diagnosis has received significant attention. There are several predominant diagnostic methods for breast cancer, such as X-ray mammography, ultrasound, and magnetic resonance imaging (MRI).

Ultrasound is a first-line imaging tool for breast lesion characterization for its high availability, cost-effectiveness, acceptable diagnostic performance, and noninvasive and real-time capabilities. In addition to B-mode ultrasound, new techniques such as color Doppler, spectral Doppler, contrast-enhanced ultrasound, and elastography can also help ultrasound doctors obtain more accurate information. However, it suffers from operator dependence[4].

In recent years, artificial intelligence (AI), particularly deep learning (DL) algorithms, is gaining extensive attention for its extremely excellent performance in image-recognition tasks. AI can make a quantitative assessment by recognizing imaging information automatically so as to improve ultrasound performance in imaging breast lesions[5].

The use of AI in breast ultrasound has also been combined with other novel technology, such as ultrasound radiofrequency (RF) time series analysis[6], multimodality GPU-based computer-assisted diagnosis of breast cancer using ultrasound and digital mammography image[7], optical breast imaging[8,9], QT-based breast tissue volume imaging[10], and automated breast volume scanning (ABVS)[11].

So far, most studies on the use of AI in breast ultrasound focus on the differentiation of benign and malignant breast masses based on the B-mode ultrasound features of the masses. There is a need of a review to summarize the current status and future perspectives of the use of AI in breast ultrasound. In this paper, we introduce the applications of AI for breast mass detection and diagnosis with ultrasound.

EARLY AI

Early AI mainly refers to traditional machine learning. It solves problems with two steps: object detection and object recognition. First, the machine uses a bounding box detection algorithm to scan the entire image to find the possible area of the object; second, the object recognition algorithm identifies and recognizes the object based on the previous step.

In the identification process, experts need to determine certain features and encode them into a data type. The machine extracts such features through images, performs quantitative analysis processing and then gives a judgment. It will be able to assist the radiologist to discover and analyze the lesions and improve the accuracy and efficiency of the diagnosis.

In the 1980s, computer-aided diagnosis (CAD) technology developed rapidly in medical imaging diagnosis. The workflow of the CAD system is roughly divided into several processes: data preprocessing, image segmentation-feature, extraction, selection and classification recognition, and result output (Figure 1).

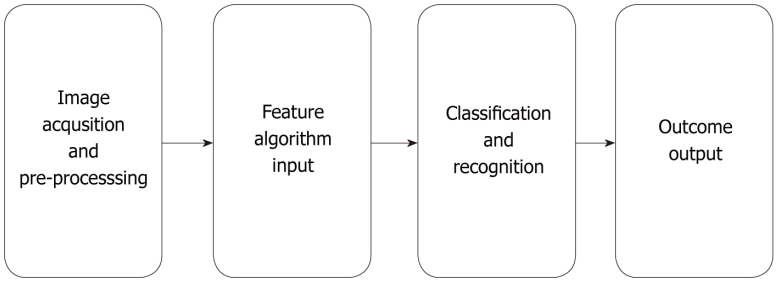

Figure 1 Workflow of machine learining algorithm.

FEATURE EXTRACTION

In traditional machine learning, most applied features of a breast mass on ultrasound, including shape, texture, location, orientation and so on, require experts to identify and encode each as a data type. Therefore, the performance of machine learning algorithms depends on the accuracy of the extracted features of benign and malignant breast masses.

Identifying effective computable features from the Breast Imaging Reporting and Data System (BI-RADS) can help distinguish between benign and potential malignant lesions by different machine learning methods. Lesion margin and orientation were optimum features in almost all of the different machine learning methods[12].

CAD model can also be used to classify benign and metastatic lymph nodes in patients with breast tumor. Zhang *et al*[13] proposed a computer-assisted method through dual-modal features extracted from real-time elastography (RTE) and B-mode ultrasound. With the assistance of computer, five morphological features describing the hilum, size, shape, and echogenic uniformity of a lymph node were extracted from B-mode ultrasound, and three elastic features consisting of hard area ratio, strain ratio, and coecient of variance were extracted from RTE. This computer-assisted method is proved to be valuable for the identification of benign and metastatic lymph nodes.

SEGMENTATION

Recently, great progress has been made in processing and segmentation of images and selection of regions of interest (ROIs) in CAD. Feng *et al*[14] proposed a method of adaptively utilizing neighboring information, which can effectively improve the breast tumor segmentation performance on ultrasound images. Cai *et al*[15] proposed a phased congruency-based binary pattern texture descriptor, which is effective and robust to segament and classify B-mode ultrasound images regardless of image grey-scale variation.

CLASSIFICATION AND RECOGNITION

According to the similarity of algorithm functions and forms, machine learning generally includes support vector machine, fuzzy logic, artificial neural network, *etc*., and each has its own advantages and disadvantages. Bing *et al*[16] proposed a novel method based on sparse representation for breast ultrasound image classification under the framework of multi-instance learning (MIL). Compared with state-of-the-art MIL method, this method achieved its obvious superiority in classification accuracy.

Lee *et al*[17] studied a novel Fourier-based shape feature extraction technique and proved that this technique provides higher classification accuracy for breast tumors in computer-aided B-mode ultrasound diagnosis system.

Otherwise, more features extracted and trained may benefit the recognition effciency. De *et al*[18] questioned the claim that training of machines with a simplified set of features would have a better effect on recognition. They conducted related experiments, and the results showed that the performance obtained with all 22 features in this experiment was slightly better than that obtained with a reduced set of features.

DL ALGORITHMS

In contrast to traditional machine learning algorithms, DL algorithms do not rely on the features and ROIs that humans set in advance[19,20]. On the contrary, it prefers carrying out all the task processions on its own. Taking the convolutional neural networks (CNNs), the most popular architecture in DL for medical imaging, as an example, input layers, hidden layers, and output layers constitute the whole model, among which hidden layers are the key determinant of accomplishing the recognition. Hidden layers consist of quantities of convolutional layers and the fully connected layer. Convolutional layers handle different and massive problems that the machine raise itself on the basis of the input task, and the fully connected layer then connects them to be a complex system so as to output the outcome easily[21]. It has been proved that DL won an overwhelming victory over other architectures in computer vision completion despite its excessive data and hardware dependencies[22]. In medical imaging, besides ultrasound[23], studies have found that DL methods also perform perfectly on computed tomography[24] and MRI[25] (Figure 2).

CLASSIFICATION AND RECOGNITION

Becker *et al*[26] conducted a retrospective study to evaluate the performance of generic DL software (DLS) in classifying breast cancer based on ultrasound images. They found that the accuracy of DLS to diagnose breast cancer is comparable to that of radiologists, and DLS can learn better and faster than a human reader without prior experience.

Zhang *et al*[27] established a DL architecture that could automatically extract image features from shear-wave elastography and evaluated the DL architecture in differentiation between benign and malignant breast tumors. The results showed that DL achieved better classification performance with an accuracy of 93.4%, a sensitivity of 88.6%, a specificity of 97.1%, and an area under the receiver operating characteristic curve (AUC) of 0.947.

Han *et al*[28] used CNN DL framework to differentiate the distinctive types of lesions and nodules on breast images acquired by ultrasound. The networks showed an accuracy of about 0.9, a sensitivity of 0.86, and a specificity of 0.96. This method shows promising results to classify malignant lesions in a short time and supports the diagnosis of radiologists in discriminating malignant lesions. Therefore, the proposed method can work in tandem with human radiologists to improve performance.

TRANSFERRED DEEP NEURAL NETWORKS

CNN has proven to be an effective task classifier, while it requires a large amount of training data, which can be a difficult task. Transferred deep neural networks are powerful tools for training deeper networks without overfitting and they may have better performance than CNN. Xiao *et al*[29] compared the performance of three transferred models, a CNN model, and a traditional machine learning-based model to differentiate benign and malignant tumors from breast ultrasound data and found that the transfer learning method outperformed the traditional machine learning model and the CNN model, where the transferred InceptionV3 achieved the best performance with an accuracy of 85.13% and an AUC of 0.91. Moreover, they built the model with combined features extracted from all three transferred models, which achieved the best performance with an accuracy of 89.44% and an AUC of 0.93 on an independent test set.

Yap *et al*[30] studied the use of three DL methods (patch-based LeNet, U-Net, and a transfer learning approach with a pretrained FCN-AlexNet) for breast ultrasound lesion detection and compared their performance against four state-of-the-art lesion detection algorithms. The results demonstrate that the transfer learning method showed the best performance over the other two DL approaches when assessed on two datasets in terms of true positive fraction, false positives per image, and F-measure.

AI EQUIPPED IN ULTRASOUND SYSTEM

Images are usually uploaded from the ultrasonic machine to the workstation for image re-processing, while a DL technique (S-detect) can directly identify and mark breast masses on the ultrasound system. S-detect is a tool equipped in the Samsung

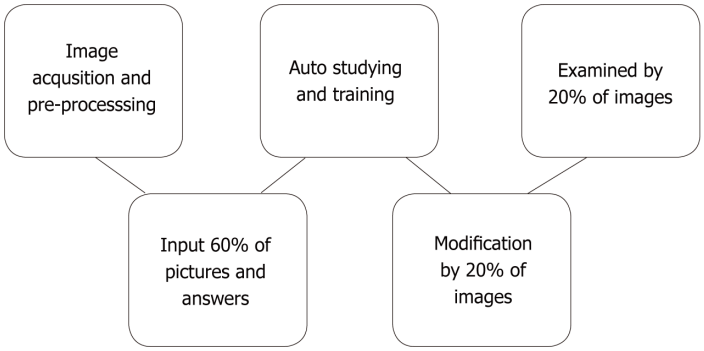

Figure 2 Workflow of deep learining algorithm.

RS80A ultrasound system, and based on the DL algorithm, it performs lesion segmentation, feature analysis, and descriptions according to the BI-RADS 2003 or BI-RADS 2013 lexicon. It can give immediate judgment of benignity or malignancy in the freezd images on the ultrasound machine after choosing ROI automatically or manually (Figure 3). Kim *et al*[31] evaluated the diagnostic performance of S-detect for the differentiation of benign from malignant breast lesions. When the cutoff was set at category 4a in BI-RADS, the specificity, PPV, and accuracy were significantly higher in S-detect compared to the radiologist ($P < 0.05$ for all), and the AUC was 0.725 compared to 0.653 ($P = 0.038$).

Di Segni *et al*[32] also evaluated the diagnostic performance of S-detect in the assessment of focal breast lesions. S-detect showed a sensitivity > 90% and a 70.8% specificity, with inter-rater agreement ranging from moderate to good. S-detect may be a feasible tool for the characterization of breast lesions and assist physicians in making clinical decisions.

CONCLUSION

AI has been increasingly applied in ultrasound and proved to be a powerful tool to provide a reliable diagnosis with higher accuracy and efficiency and reduce the workload of pyhsicians. It is roughly divided into early machine learning controlled by manual input algorithms, and DL, with which software can self-study. There is still no guidelines to recommend the application of AI with ultrasound in clinical practice, and more studies are required to explore more advanced methods and to prove their usefulness.

In the near future, we believe that AI in breast ultrasound can not only distinguish between benign and malignant breast masses, but also further classify specific benign diseases, such as inflammative breast mass and fibroplasia. In addition, AI in ultrasound may also predict Tumor Node Metastasis classification[33], prognosis, and the treatment response for patients with breast cancer. Last but not the least, the accuracy of AI on ultrasound to differentiate benign from malignant breast lesions may not only be based on B-mode ultrasound images, but also could combine images from other advanced techniqes, such as ABVS, elastography, and contrast-enhanced ultrasound.

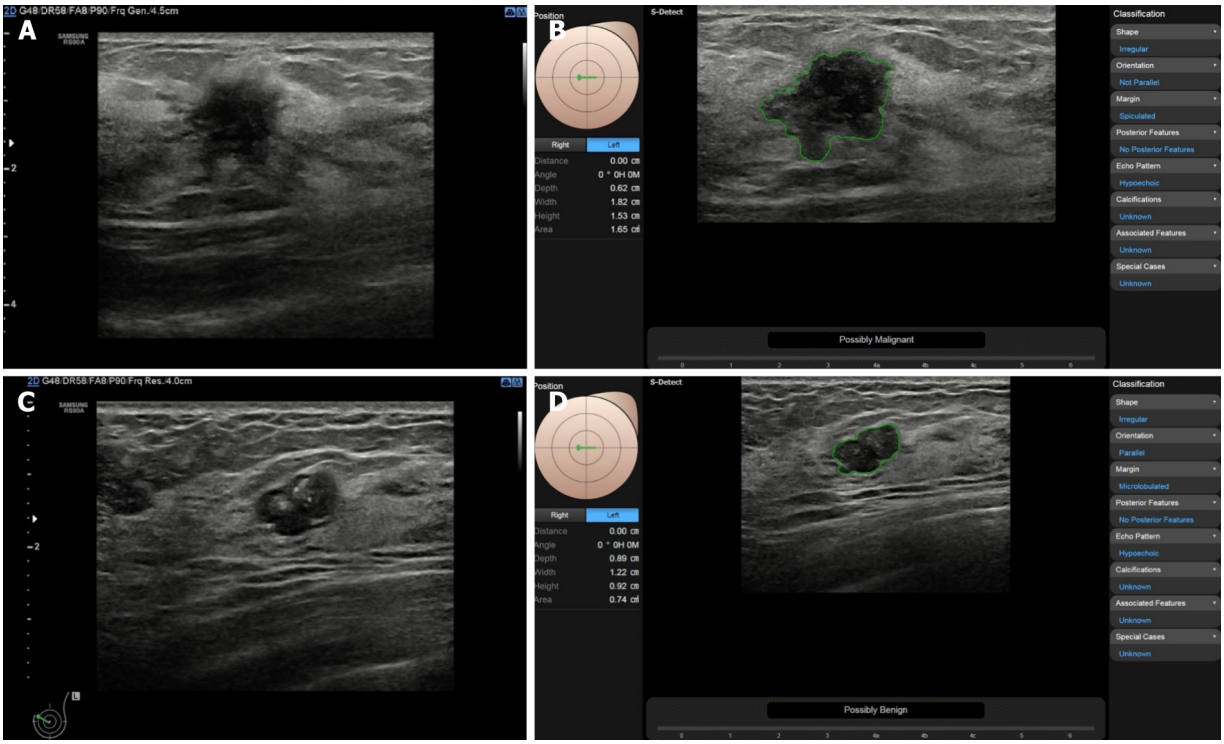

Figure 3 S-detect technique in the Samsung RS80A ultrasound system. A and B: In a 47-year-old woman with left invasive breast cancer on B-mode ultrasound (A), S-detect correctly concluded that it is "Possibly Malignant" based on the lesion features listed on the right column (B); C and D: In a 55-year-old woman with fibroadenoma of left breast on B-mode ultrasound (C), S-detect correctly concluded that it is "Possibly Benign" based on the lesion features listed on the right column (D).

REFERENCES

1 **Siegel RL**, Miller KD, Jemal A. Cancer Statistics, 2017. *CA Cancer J Clin* 2017; **67**: 7-30 [PMID: 28055103 DOI: 10.3322/caac.21387]

2 **Ferlay J**, Soerjomataram I, Dikshit R, Eser S, Mathers C, Rebelo M, Parkin DM, Forman D, Bray F. Cancer incidence and mortality worldwide: sources, methods and major patterns in GLOBOCAN 2012. *Int J Cancer* 2015; **136**: E359-E386 [PMID: 25220842 DOI: 10.1002/ijc.29210]

3 **Global Burden of Disease Cancer Collaboration**; Fitzmaurice C, Dicker D, Pain A, Hamavid H, Moradi-Lakeh M, MacIntyre MF, Allen C, Hansen G, Woodbrook R, Wolfe C, Hamadeh RR, Moore A, Werdecker A, Gessner BD, Te Ao B, McMahon B, Karimkhani C, Yu C, Cooke GS, Schwebel DC, Carpenter DO, Pereira DM, Nash D, Kazi DS, De Leo D, Plass D, Ukwaja KN, Thurston GD, Yun Jin K, Simard EP, Mills E, Park EK, Catalá-López F, deVeber G, Gotay C, Khan G, Hosgood HD 3rd, Santos IS, Leasher JL, Singh J, Leigh J, Jonas JB, Sanabria J, Beardsley J, Jacobsen KH, Takahashi K, Franklin RC, Ronfani L, Montico M, Naldi L, Tonelli M, Geleijnse J, Petzold M, Shrime MG, Younis M, Yonemoto N, Breitborde N, Yip P, Pourmalek F, Lotufo PA, Esteghamati A, Hankey GJ, Ali R, Lunevicius R, Malekzadeh R, Dellavalle R, Weintraub R, Lucas R, Hay R, Rojas-Rueda D, Westerman R, Sepanlou SG, Nolte S, Patten S, Weichenthal S, Abera SF, Fereshtehnejad SM, Shiue I, Driscoll T, Vasankari T, Alsharif U, Rahimi-Movaghar V, Vlassov VV, Marcenes WS, Mekonnen W, Melaku YA, Yano Y, Artaman A, Campos I, MacLachlan J, Mueller U, Kim D, Trillini M, Eshrati B, Williams HC, Shibuya K, Dandona R, Murthy K, Cowie B, Amare AT, Antonio CA, Castañeda-Orjuela C, van Gool CH, Violante F, Oh IH, Deribe K, Soreide K, Knibbs L, Kereselidze M, Green M, Cardenas R, Roy N, Tillmann T, Li Y, Krueger H, Monasta L, Dey S, Sheikhbahaei S, Hafezi-Nejad N, Kumar GA, Sreeramareddy CT, Dandona L, Wang H, Vollset SE, Mokdad A, Salomon JA, Lozano R, Vos T, Forouzanfar M, Lopez A, Murray C, Naghavi M. The Global Burden of Cancer 2013. *JAMA Oncol* 2015; **1**: 505-527 [PMID: 26181261 DOI: 10.1001/jamaoncol.2015.0735]

4 **Hooley RJ**, Scoutt LM, Philpotts LE. Breast ultrasonography: state of the art. *Radiology* 2013; **268**: 642-659 [PMID: 23970509 DOI: 10.1148/radiol.13121606]

5 **Hosny A**, Parmar C, Quackenbush J, Schwartz LH, Aerts HJWL. Artificial intelligence in radiology. *Nat Rev Cancer* 2018; **18**: 500-510 [PMID: 29777175 DOI: 10.1038/s41568-018-0016-5]

6 **Uniyal N**, Eskandari H, Abolmaesumi P, Sojoudi S, Gordon P, Warren L, Rohling RN, Salcudean SE, Moradi M. Ultrasound RF time series for classification of breast lesions. *IEEE Trans Med Imaging* 2015; **34**: 652-661 [PMID: 25350925 DOI: 10.1109/TMI.2014.2365030]

7 **Sidiropoulos KP**, Kostopoulos SA, Glotsos DT, Athanasiadis EI, Dimitropoulos ND, Stonham JT, Cavouras DA. Multimodality GPU-based computer-assisted diagnosis of breast cancer using ultrasound and digital mammography images. *Int J Comput Assist Radiol Surg* 2013; **8**: 547-560 [PMID: 23354971 DOI: 10.1007/s11548-013-0813-y]

8 **Pearlman PC**, Adams A, Elias SG, Mali WP, Viergever MA, Pluim JP. Mono- and multimodal registration of optical breast images. *J Biomed Opt* 2012; **17**: 080901-080901 [PMID: 23224161 DOI: 10.1117/1.JBO.17.8.080901]

9 **Lee JH**, Kim YN, Park HJ. Bio-optics based sensation imaging for breast tumor detection using tissue

characterization. *Sensors (Basel)* 2015; **15**: 6306-6323 [PMID: 25785306 DOI: 10.3390/s150306306]
10 **Malik B**, Klock J, Wiskin J, Lenox M. Objective breast tissue image classification using Quantitative Transmission ultrasound tomography. *Sci Rep* 2016; **6**: 38857 [PMID: 27934955 DOI: 10.1038/srep38857]
11 **Wang HY**, Jiang YX, Zhu QL, Zhang J, Xiao MS, Liu H, Dai Q, Li JC, Sun Q. Automated Breast Volume Scanning: Identifying 3-D Coronal Plane Imaging Features May Help Categorize Complex Cysts. *Ultrasound Med Biol* 2016; **42**: 689-698 [PMID: 26742895 DOI: 10.1016/j.ultrasmedbio.2015.11.019]
12 **Shen WC**, Chang RF, Moon WK, Chou YH, Huang CS. Breast ultrasound computer-aided diagnosis using BI-RADS features. *Acad Radiol* 2007; **14**: 928-939 [PMID: 17659238 DOI: 10.1016/j.acra.2007.04.016]
13 **Zhang Q**, Suo J, Chang W, Shi J, Chen M. Dual-modal computer-assisted evaluation of axillary lymph node metastasis in breast cancer patients on both real-time elastography and B-mode ultrasound. *Eur J Radiol* 2017; **95**: 66-74 [PMID: 28987700 DOI: 10.1016/j.ejrad.2017.07.027]
14 **Feng Y**, Dong F, Xia X, Hu CH, Fan Q, Hu Y, Gao M, Mutic S. An adaptive Fuzzy C-means method utilizing neighboring information for breast tumor segmentation in ultrasound images. *Med Phys* 2017; **44**: 3752-3760 [PMID: 28513858 DOI: 10.1002/mp.12350]
15 **Cai L**, Wang X, Wang Y, Guo Y, Yu J, Wang Y. Robust phase-based texture descriptor for classification of breast ultrasound images. *Biomed Eng Online* 2015; **14**: 26 [PMID: 25889570 DOI: 10.1186/s12938-015-0022-8]
16 **Bing L**, Wang W. Sparse Representation Based Multi-Instance Learning for Breast Ultrasound Image Classification. *Comput Math Methods Med* 2017; **2017**: 7894705 [PMID: 28690670 DOI: 10.1155/2017/7894705]
17 **Lee JH**, Seong YK, Chang CH, Park J, Park M, Woo KG, Ko EY. Fourier-based shape feature extraction technique for computer-aided B-Mode ultrasound diagnosis of breast tumor. *Conf Proc IEEE Eng Med Biol Soc* 2012; **2012**: 6551-6554 [PMID: 23367430 DOI: 10.1109/EMBC.2012.6347495]
18 **de S Silva SD**, Costa MG, de A Pereira WC, Costa Filho CF. Breast tumor classification in ultrasound images using neural networks with improved generalization methods. *Conf Proc IEEE Eng Med Biol Soc* 2015; **2015**: 6321-6325 [PMID: 26737738 DOI: 10.1109/EMBC.2015.7319838]
19 **Miotto R**, Wang F, Wang S, Jiang X, Dudley JT. Deep learning for healthcare: review, opportunities and challenges. *Brief Bioinform* 2018; **19**: 1236-1246 [PMID: 28481991 DOI: 10.1093/bib/bbx044]
20 **Shen D**, Wu G, Suk HI. Deep Learning in Medical Image Analysis. *Annu Rev Biomed Eng* 2017; **19**: 221-248 [PMID: 28301734 DOI: 10.1146/annurev-bioeng-071516-044442]
21 **Suzuki K**. Overview of deep learning in medical imaging. *Radiol Phys Technol* 2017; **10**: 257-273 [PMID: 28689314 DOI: 10.1007/s12194-017-0406-5]
22 **Erickson BJ**, Korfiatis P, Akkus Z, Kline TL. Machine Learning for Medical Imaging. *Radiographics* 2017; **37**: 505-515 [PMID: 28212054 DOI: 10.1148/rg.2017160130]
23 **Metaxas D**, Axel L, Fichtinger G, Szekely G. Medical image computing and computer-assisted intervention--MICCAI2008. Preface. *Med Image Comput Comput Assist Interv* 2008; **11**: V-VII [PMID: 18979724 DOI: 10.1007/978-3-540-85988-8]
24 **González G**, Ash SY, Vegas-Sánchez-Ferrero G, Onieva Onieva J, Rahaghi FN, Ross JC, Díaz A, San José Estépar R, Washko GR; COPDGene and ECLIPSE Investigators. Disease Staging and Prognosis in Smokers Using Deep Learning in Chest Computed Tomography. *Am J Respir Crit Care Med* 2018; **197**: 193-203 [PMID: 28892454 DOI: 10.1164/rccm.201705-0860OC]
25 **Ghafoorian M**, Karssemeijer N, Heskes T, van Uden IWM, Sanchez CI, Litjens G, de Leeuw FE, van Ginneken B, Marchiori E, Platel B. Location Sensitive Deep Convolutional Neural Networks for Segmentation of White Matter Hyperintensities. *Sci Rep* 2017; **7**: 5110 [PMID: 28698556 DOI: 10.1038/s41598-017-05300-5]
26 **Becker AS**, Mueller M, Stoffel E, Marcon M, Ghafoor S, Boss A. Classification of breast cancer in ultrasound imaging using a generic deep learning analysis software: a pilot study. *Br J Radiol* 2018; **91**: 20170576 [PMID: 29215311 DOI: 10.1259/bjr.20170576]
27 **Zhang Q**, Xiao Y, Dai W, Suo J, Wang C, Shi J, Zheng H. Deep learning based classification of breast tumors with shear-wave elastography. *Ultrasonics* 2016; **72**: 150-157 [PMID: 27529139 DOI: 10.1016/j.ultras.2016.08.004]
28 **Han S**, Kang HK, Jeong JY, Park MH, Kim W, Bang WC, Seong YK. A deep learning framework for supporting the classification of breast lesions in ultrasound images. *Phys Med Biol* 2017; **62**: 7714-7728 [PMID: 28753132 DOI: 10.1088/1361-6560/aa82ec]
29 **Xiao T**, Liu L, Li K, Qin W, Yu S, Li Z. Comparison of Transferred Deep Neural Networks in Ultrasonic Breast Masses Discrimination. *Biomed Res Int* 2018; **2018**: 4605191 [PMID: 30035122 DOI: 10.1155/2018/4605191]
30 **Yap MH**, Pons G, Marti J, Ganau S, Sentis M, Zwiggelaar R, Davison AK, Marti R, Moi Hoon Yap, Pons G, Marti J, Ganau S, Sentis M, Zwiggelaar R, Davison AK, Marti R. Automated Breast Ultrasound Lesions Detection Using Convolutional Neural Networks. *IEEE J Biomed Health Inform* 2018; **22**: 1218-1226 [PMID: 28796627 DOI: 10.1109/JBHI.2017.2731873]
31 **Kim K**, Song MK, Kim EK, Yoon JH. Clinical application of S-Detect to breast masses on ultrasonography: a study evaluating the diagnostic performance and agreement with a dedicated breast radiologist. *Ultrasonography* 2017; **36**: 3-9 [PMID: 27184656 DOI: 10.14366/usg.16012]
32 **Di Segni M**, de Soccio V, Cantisani V, Bonito G, Rubini A, Di Segni G, Lamorte S, Magri V, De Vito C, Migliara G, Bartolotta TV, Metere A, Giacomelli L, de Felice C, D'Ambrosio F. Automated classification of focal breast lesions according to S-detect: validation and role as a clinical and teaching tool. *J Ultrasound* 2018; **21**: 105-118 [PMID: 29681007 DOI: 10.1007/s40477-018-0297-2]
33 **Plichta JK**, Ren Y, Thomas SM, Greenup RA, Fayanju OM, Rosenberger LH, Hyslop T, Hwang ES. Implications for Breast Cancer Restaging Based on the 8th Edition AJCC Staging Manual. *Ann Surg* 2018 [PMID: 30312199 DOI: 10.1097/SLA.0000000000003071]

P- Reviewer: Bazeed MF, Gao BL
S- Editor: Ji FF **L- Editor:** Wang TQ **E- Editor:** Song H

Published By Baishideng Publishing Group Inc
7901 Stoneridge Drive, Suite 501, Pleasanton, CA 94588, USA
Telephone: +1-925-2238242
Fax: +1-925-2238243
E-mail: bpgoffice@wjgnet.com
Help Desk: https://www.f6publishing.com/helpdesk
https://www.wjgnet.com

ISSN 1949-8470 (online)

World Journal of *Radiology*

World J Radiol 2019 March 28; 11(3): 27-54

Published by Baishideng Publishing Group Inc

World Journal of Radiology

Contents

Monthly Volume 11 Number 3 March 28, 2019

MINIREVIEWS

Contents

World Journal of Radiology

Volume 11 Number 3 March 28, 2019

ABOUT COVER

Editorial Board Member of *World Journal of Radiology*, SeyedReza Najafizadeh, MD, Associate Professor, Department of Rheumatology, Imam Khomeini Hospital, Tehran University of Medical Sciences, Tehran 1586814116, Iran

AIMS AND SCOPE

World Journal of Radiology (*World J Radiol*, *WJR*, online ISSN 1949-8470, DOI: 10.4329) is a peer-reviewed open access academic journal that aims to guide clinical practice and improve diagnostic and therapeutic skills of clinicians.

The *WJR* covers topics concerning diagnostic radiology, radiation oncology, radiologic physics, neuroradiology, nuclear radiology, pediatric radiology, vascular/interventional radiology, medical imaging achieved by various modalities and related methods analysis. The current columns of *WJR* include editorial, frontier, mini-reviews, review, medical ethics, original articles, case report, *etc*.

We encourage authors to submit their manuscripts to *WJR*. We will give priority to manuscripts that are supported by major national and international foundations and those that are of great basic and clinical significance.

INDEXING/ABSTRACTING

The *WJR* is now abstracted and indexed in Emerging Sources Citation Index (Web of Science), PubMed, PubMed Central, China National Knowledge Infrastructure (CNKI), China Science and Technology Journal Database (CSTJ), and Superstar Journals Database.

RESPONSIBLE EDITORS FOR THIS ISSUE

Responsible Electronic Editor: *Yun-Xiaojian Wu* **Proofing Editorial Office Director:** *Jin-Lei Wang*

NAME OF JOURNAL
World Journal of Radiology

ISSN
ISSN 1949-8470 (online)

LAUNCH DATE
January 31, 2009

FREQUENCY
Monthly

EDITORS-IN-CHIEF
Venkatesh Mani

EDITORIAL BOARD MEMBERS
https://www.wjgnet.com/1949-8470/editorialboard.htm

EDITORIAL OFFICE
Jin-Lei Wang, Director

PUBLICATION DATE
March 28, 2019

INSTRUCTIONS TO AUTHORS
https://www.wjgnet.com/bpg/gerinfo/204

GUIDELINES FOR ETHICS DOCUMENTS
https://www.wjgnet.com/bpg/GerInfo/287

GUIDELINES FOR NON-NATIVE SPEAKERS OF ENGLISH
https://www.wjgnet.com/bpg/gerinfo/240

PUBLICATION MISCONDUCT
https://www.wjgnet.com/bpg/gerinfo/208

ARTICLE PROCESSING CHARGE
https://www.wjgnet.com/bpg/gerinfo/242

STEPS FOR SUBMITTING MANUSCRIPTS
https://www.wjgnet.com/bpg/GerInfo/239

ONLINE SUBMISSION
https://www.f6publishing.com

World Journal of Radiology

Submit a Manuscript: https://www.f6publishing.com

World J Radiol 2019 March 28; 11(3): 27-45

DOI: 10.4329/wjr.v11.i3.27

ISSN 1949-8470 (online)

MINIREVIEWS

Role of advanced magnetic resonance imaging in the assessment of malignancies of the mediastinum

Jordi Broncano, Ana María Alvarado-Benavides, Sanjeev Bhalla, Antonio Álvarez-Kindelan, Constantine A Raptis, Antonio Luna

ORCID number: Jordi Broncano (0000-0002-0683-8061); Ana María Alvarado-Benavides (0000-0003-1856-0690); Sanjeev Bhalla (0000-0002-1262-8925); Antonio Álvarez-Kindelan (0000-0003-1531-9543); Constantine A Raptis (0000-0003-0924-2447); Antonio Luna (0000-0001-9358-3396).

Author contributions: All authors contributed to this article.

Conflict-of-interest statement: There is no conflict of interest associated with any of the senior author or other coauthors contributed their efforts in this manuscript.

Manuscript source: Invited manuscript

Received: November 21, 2018
Peer-review started: November 23, 2018
First decision: December 10, 2018

Jordi Broncano, Cardiothoracic Imaging Unit, Hospital San Juan de Dios, Health Time, Cordoba 14012, Spain

Ana María Alvarado-Benavides, Sanjeev Bhalla, Constantine A Raptis, Cardiothoracic Department, Mallinckrodt Institute of Radiology, Washington University in Saint Louis, Saint Louis, MO 63110, United States

Antonio Álvarez-Kindelan, Thoracic Surgery Department, Hospital Reina Sofía, Cordoba 14004, Spain

Antonio Luna, MR imaging Unit, Clínica Las Nieves, Jaen 23007, Spain

Corresponding author: Jordi Broncano, MD, Staff Physician, Cardiothoracic Imaging Unit, Hospital San Juan de Dios, Health Time, Avenida el Brillante, 106, Cordoba 14012, Spain.
jordibroncano@gmail.com
Telephone: +34-957277000
Fax: +34-957277179

Abstract

In the new era of functional magnetic resonance imaging (MRI), the utility of chest MRI is increasing exponentially due to several advances, including absence of ionizing radiation, excellent tissue contrast and high capability for lesion characterization and treatment monitoring. The application of several of these diagnostic weapons in a multiparametric fashion enables to better characterize thymic epithelial tumors and other mediastinal tumoral lesions, accurate assessment of the invasion of adjacent structures and detection of pathologic lymph nodes and metastasis. Also, "do not touch lesions" could be identified with the associated impact in the management of those patients. One of the hot-spots of the multiparametric chest MR is its ability to detect with acuity early response to treatment in patients with mediastinal malignant neoplasms. This has been related with higher rates of overall survival and progression free survival. Therefore, in this review we will analyze the current functional imaging techniques available (^{18}F-Fluorodeoxiglucose positron emission tomography/computed tomography, diffusion-weighted imaging, dynamic contrast-enhanced MRI, diffusion tensor imaging and MR spectroscopy) for the evaluation of mediastinal lesions, with a focus in their correct acquisition and post-processing. Also, to review the clinical applications of these techniques in the diagnostic approach of benign and malignant conditions of the mediastinum.

Revised: February 28, 2019
Accepted: March 12, 2019
Article in press: March 12, 2019
Published online: March 28, 2019

P-Reviewer: Battal B, Kumar J, Xiao EH, Yang L
S-Editor: Yan JP
L-Editor: A
E-Editor: Wu YXJ

Key words: Mediastinum; Magnetic resonance; Diffusion; Perfusion; ^{18}F-Fluorodeoxiglucose positron emission tomography/computed tomography; Advanced imaging

Core tip: With the past improvements on magnetic resonance hardware, gradients and advanced sequences, the interest of magnetic resonance application in the chest is exponentially growing. In this review, we show the evidence in the literature of its application in mediastinal malignancies. In addition, we explore the advantages of applying new imaging techniques for lesion characterization, helping to differentiate with acuity benign and malignant etiologies. The use of several advanced sequences together yields specificity in identifying false positives from ^{18}F-Fluorodeoxiglucose positron emission tomography/computed tomography. Also, due to its precision in defining invasion and variation in tissue properties through the time, magnetic resonance enhances accurate staging and treatment monitoring.

Citation: Broncano J, Alvarado-Benavides AM, Bhalla S, Álvarez-Kindelan A, Raptis CA, Luna A. Role of advanced magnetic resonance imaging in the assessment of malignancies of the mediastinum. *World J Radiol* 2019; 11(3): 27-45
URL: https://www.wjgnet.com/1949-8470/full/v11/i3/27.htm
DOI: https://dx.doi.org/10.4329/wjr.v11.i3.27

INTRODUCTION

Morphological evaluation of mediastinal tumors are traditionally performed using computed tomography (CT). Magnetic resonance (MR) is considered a second-line test. However, other imaging methods are used to study tumor ultrastructure characteristics. Of them, the most validated and widely used is ^{18}F-Fluorodeoxiglucose positron emission tomography/CT (^{18}F-FDG-PET/CT) for assessing cell metabolism. Functional MR sequences, such as diffusion-weighted imaging (DWI) and perfusion-weighted imaging (PWI), are gradually becoming more available in daily clinical practice for assessment of mediastinal tumors. In addition to the absence of ionizing radiation, one of its significant advantages is the possibility of studying several physiological characteristics of tumors in the same protocol. Therefore, although technically very demanding, chest MR imaging (MRI) allows an integral evaluation of tumor and accurate differentiation from the non-neoplastic tissue.

Although there is scarce evidence in the literature, DWI helps to differentiate non tumoral thymic entities from thymo-epithelial neoplasms[1-3]. Moreover, by means of apparent diffusion coefficient (ADC) values, it could identify well-differentiated from more aggressive thymomas. DWI has a great value in the diagnosis, characterization and staging of central lung cancer and lymphoma[4]. Also, helps to characterize thyroid nodules and neurogenic tumors. By contrast, PWI is useful to characterize anterior mediastinal neoplasms. When a threshold time to peak of more than 120 seconds is used, it could separate non-invasive thymomas from invasive thymo-epithelial tumors, lymphoma and germ cell neoplasms[5]. The combination of DWI and PWI has demonstrated and increased in the diagnostic performance of MR in lung neoplasms[6]. Also, increases the precision of lung cancer staging by means of better identification of local invasion, metastatic lymph nodes (LN) and distant metastasis. By acquiring PWI and real time steady state free precession real time cine sequences (RT-SSFP), a higher conspicuity of mediastinal, pleural, chest wall and diaphragmatic invasion is obtained[7]. Finally, current data suggests a promising role of functional MRI in treatment monitoring of some neoplasms, like lung and esophageal cancer. The identification of early response has been liked to higher overall and progression free survival rates[8].

IMAGING TECHNIQUES AND OPTIMIZATION

Different imaging methods can study several tumor ultrastructure characteristics. The most widely available and validated molecular method is ^{18}F-FDG-PET/CT for

evaluating mainly, but not only, tumor glucose metabolism. Using other radiotracers, hypoxia and proliferation of mediastinal tumors, as long as the total tumor burden, could be analyzed. Recently, chest MR has become more widely available, allowing the assessment of different functional and morphological neoplastic characteristics in a one – stop – shop examination, with the advantage of avoiding the use of ionizing radiation.

Diffusion-weighted imaging

DWI interrogates the Brownian motion of water molecules of the tissues and lesions, particularly in the extracellular-extravascular space. DWI is a consolidated oncological biomarker in clinical practice, indirectly representing the occupancy of the interstitial space. For that purpose, several motion probe gradients are placed surrounding a 180° radiofrequency pulse. At least, two *b* values are necessary for analyzing the signal intensity decay of the tissues and calculating its ADC, following a mono-exponential model of diffusion signal decay[9]. In this manner, the higher the magnitude of signal intensity decay, the higher the ADC would be, indicating no restriction of water molecules. But, when a tissue shows restricted movement of water molecules, the signal intensity decay is lower and, therefore, ADC has a smaller value[10].

Intra-voxel incoherent motion (IVIM) model of diffusion signal decay is better than mono-exponential analysis for assessment of well-vascularized organs such as kidney, liver, pancreas, and prostate. For this model, it is necessary to acquire several b values. The diffusion signal decay splits into two components. At low *b* values (< 100-150 s/mm^2) the slope of signal decay is higher due to the bulk motion of water molecules inside randomly oriented capillaries (perfusion related decay of diffusion signal). But at higher *b* values (> 150 s/mm^2) the diffusion signal decay curve is related to the true diffusion of water molecules inside the tissue being evaluated (Figure 1)[9].

At very high *b* values (*b* > 1500 s/mm^2), there is a deviation of the theoretically mono-exponential based signal decay of DWI, that does not follow any Gaussian distribution. Diffusion kurtosis imaging explains this decreased slope of signal decay following a non–Gaussian distribution and relates it to tissue heterogeneity (Figure 1). In addition, these advanced models of quantification of DWI provide several derived parameters (Table 1).

Some cellular structures impede the diffusion of water molecules in one preferential direction. By the application of at least 6 non-collinear DWI gradients, a 3D diffusion profile of motion of water molecules could be plotted (diffusion tensor model) at a given voxel, which is an ellipsoid[11]. Therefore, when water molecules in a specified tissue move freely in all directions, the diffusion is isotropic. Contrarily, when this motion occurs mainly in one axis or axes due to structural properties of the tissue, this diffusion is anisotropic. Two metric measurements are derived. Mean diffusivity constitute the average diffusion in all three directions. Fractional anisotropy (FA) measures the degree of non-uniform diffusion in the three orthogonal directions[12].

Perfusion-weighted imaging

Tumor angiogenesis is essential for the development and behavior of solid tumors. Vasculature formation, growth patterns and vascular permeability are affected by antiangiogenic factors. Therefore, they modulate host response and weights tumor invasion, metastasis and outcome[13]. PWI is a functional technique focused on the evaluation of tumor neoangiogenesis[14,15]. It is a non-invasive and sensitive technique to neoplastic perfusion parameters such as blood volume, blood flow and vascular permeability[16].

There are two main technical approaches in the evaluation of tumor perfusion with MRI. Dynamic contrast-enhanced MRI (DCE-MRI) uses 2D or 3D gradient echo dynamic acquisitions, acquired during breath-holding. The temporal resolution of each dynamic acquisition is low (13-15 s), but with an excellent spatial resolution. Contrarily, PWI is based on ultrafast (2 to 3 s) 2D or 3D gradient echo dynamic sequences acquired during free-breathing. In order to achieve this very high temporal resolution, it is necessary to employ acceleration techniques such as non-Cartesian parallel imaging and compressed sensing, with the shortest available echo time[17]. Both of them show limited coverage, being higher in DCE-MR compared to PWI. Movement and respiratory artifacts are significant limitations of these techniques requiring the use of motion correction during post-processing[14]. Subtraction images are useful for adjacent structures infiltration detection. Semi-quantitative analysis can be performed with both types of acquisition, which benefits of the use of parametric color-coded maps. Because, these sequences track the variation of signal intensity secondary to gadolinium infusion per second, time-intensity curves (TIC) could be

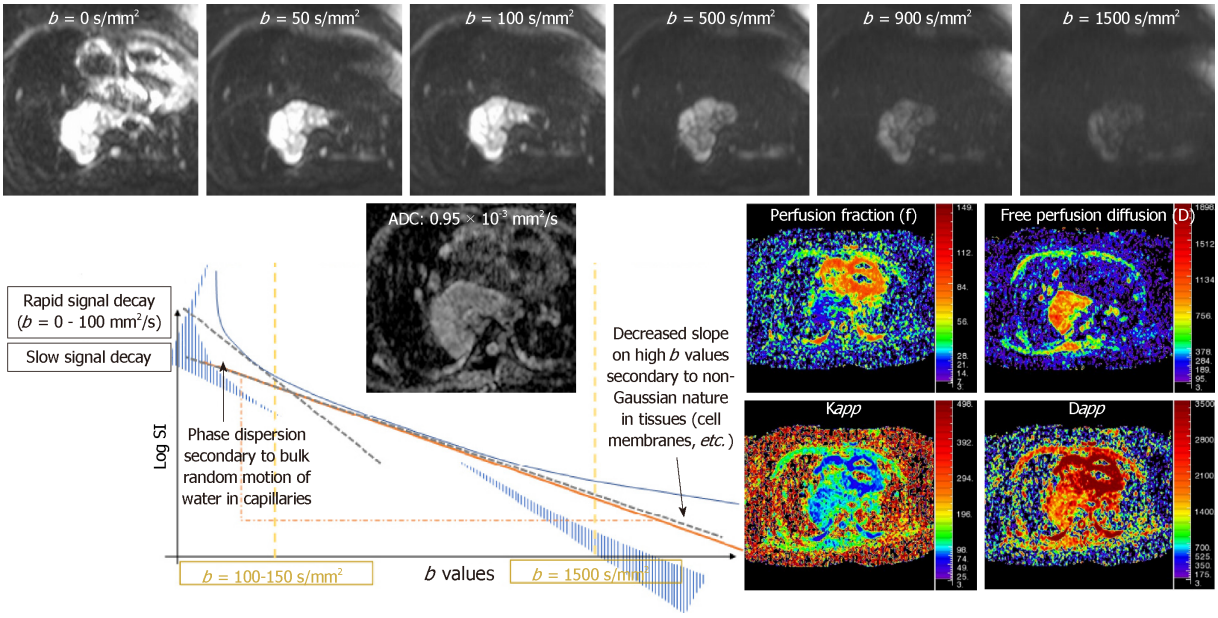

Figure 1 Different schemes on diffusion weighted imaging. Diagram represents the different diffusion weighted imaging models: Monoexponential, intravoxel incoherent motion and diffusion kurtosis imaging. Top images represent the behaviour of an esophageal leiomyosarcoma with different *b* values. Apparent diffusion coefficient and parametric maps of intravoxel incoherent motion -derived (perfusion fraction and free perfusion diffusion) and kurtosis-derived (K*app* and D*app*) biomarkers are also shown. IVIM: Intravoxel incoherent motion.

plotted (Figure 2).

PWI has the advantage to allow quantitative analysis using a mono-compartmental or bicompartmental approach. The mono-compartmental approach does not distinguish the intravascular and extravascular–extracellular compartments. Conversely, in the bicompartmental model, both spaces and the exchange of contrast agent between both of them are explored. For its quantification, a region of interest is placed in a principal artery, so the arterial input function is calculated. Additionally, it is possible to differentiate the transfer rates between both compartments. Mono and bicompartmental derived parameters are useful in tissue characterization and lesion management, and some of them have also demonstrated to be prognostic biomarkers of chest malignancies (Table 2)[16].

Other functional MR based techniques

Proton-based MR spectroscopy helps to depict the mi-croscopic metabolic microenvironment of tissues and lesions. The presence of a choline peak has been related to excessive cellular turnover in tumors outside the brain, helping to differentiate benign from malignant lesions[18]. To the best of our knowledge, there is no evidence in the literature about its utility in mediastinal tumors.

Blood oxygen level dependent imaging (BOLD) evaluates changes in the concentration of paramagnetic molecules, being a surrogate marker of tumor hypoxia, a well-known cause of radioresistance of malignancies. BOLD acquisition is based on a multi-echoT2*GE sequence, which is able to depict small reductions in T2* relaxation in tissues, secondary to increases in deoxyhemoglobin content during physiological gaseous exchange. Both, hyperoxia or hypercapnia challenges can be applied to depict changes in oxygen content within the tissues. Tissues with rising oxygen consumption would decrease T2* in those sequences. The rate of spin dephasing (R2* = 1/T2*) is related to the index of tissular oxygenation. Therefore, hypoxic tumors with high blood volume will show greater ΔR2* to physiological changes being, as a consequence, are less suitable to radiotherapy treatment[19].

ASSESSMENT OF MEDIASTINAL MASSES

The mediastinum is a complex segment of the chest, since it contains multiple vital structures in a reduced space. Traditional classification schemes have divided the mediastinum into three or four compartments. The 3-compartment models describe anterior, middle, and posterior divisions, and most 4-compartment models include superior, anterior, middle, and posterior divisions. The International Thymic Malignancy Interest Group (ITMIG) propose a 3-compartment model of the

Table 1 Diffusion weighted derived parameters of different model analysis

Mono-exponential model		
ADC	Apparent diffusion coefficient	Exponential signal decay of water molecules in a voxel by voxel basis.
IVIM-derived parameters		
D	True diffusion of H_2O molecules	Not influenced by movement of water molecules within capillaries
f	Perfusion contribution to diffusion signal	Fractional volume of flowing water molecules within capillaries
D	Perfusion contribution to diffusion signal decay	Amount of non-diffusional random movements of water molecules
DKI-derived parameters		
D*app*	Apparent diffusion	Estimation of diffusion coefficient in the direction parallel to the orientation of diffusion sensitizing agents
K*app*	Apparent diffusional kurtosis	Measures the deviation of the true diffusion from a Gaussian pattern.
DTI-derived parameters		
MD	Mean diffusivity	Reflects the average diffusion of water molecules in all three directions.
FA	Fractional anisotropy	Measures the extent to which diffusion is non-uniform in the three orthogonal directions.

ADC: Apparent diffusion coefficient; IVIM: Intravoxel incoherent motion; MD: Mean diffusivity; FA: Fractional anisotropy.

mediastinum based on boundaries identifiable on routine cross-sectional imaging. These segments include prevascular (anterior), visceral (middle), and paravertebral (posterior) compartments[20].

Prevascular (anterior) mediastinal lesions

Thymic hyperplasia: Thymic hyperplasia manifests as diffuse symmetric enlargement of the thymus. There are two histologic types of thymic hyperplasia: lymphofollicular hyperplasia and true thymic hyperplasia. Lymphofollicular hyperplasia refers to the presence of hyperplastic lymphoid germinal centers with lymphocytic and plasma cell infiltrate. It is most commonly associated with myasthenia gravis (50% of patients) and other autoimmune conditions such as thyrotoxicosis, systemic lupus erythematosus (SLE), rheumatoid arthritis, scleroderma, among others. True thymic hyperplasia is an enlargement of the thymus, without histologic abnormalities. Rebound hyperplasia occurs after chemotherapy, steroids, and radiotherapy[21].

In patients with diffuse thymic enlargement, it may be difficult to differentiate between hyperplasia and tumor. Fat infiltration is present within the normal thymus and thymic hyperplasia[22]. Chemical shift imaging (CSI) is a fat-suppression technique that enables the identification of microscopic or intravoxel fat[1]. It allows the detection of an intravoxel mixture of water and fat by showing a signal loss on the opposed-phase image relative to the in-phase image in the thymic tissue compared to paraspinal muscle. CSI can be used to distinguish thymo-epithelial tumor from thymic hyperplasia, by detecting microscopic fat in the latter. A chemical shift ratio (CSR) can be calculated for quantifying the signal suppression on opposed-phase divided by the signal intensity in-phase of the thymic tissue related to the paraspinal muscle. A CSR value of less than or equal to 0.7 is suggestive of thymic hyperplasia, depending on sex and age[23]. When the CSR is over 1.0, it is indicative of tumoral origin. Between 0.8 and 0.9 the lesion is unclear and a control examination is needed. It is essential to take into account that not all young thymus suppress fat in out of phase imaging[24]. Also, the thymus of young women had lower CSR than the thymus of young men[25]. On DWI, thymic hyperplasia shows no significant restriction of free water molecules, revealing higher ADC values compared to tumoral lesions. Also, on DCE-MRI, it shows minimal (type D) or no enhancement after gadolinium intake. Meanwhile, thymic tumors show increased perfusion.

Thymic epithelial neoplasms: Thymic epithelial neoplasms are rare malignant tumors, with a described prevalence of 0.13/100000 individual in the United States[3]. Thymic epithelial neoplasms include thymoma, thymic neuroendocrine tumors (NETs), and thymic carcinoma. Up to 15 different staging systems have been

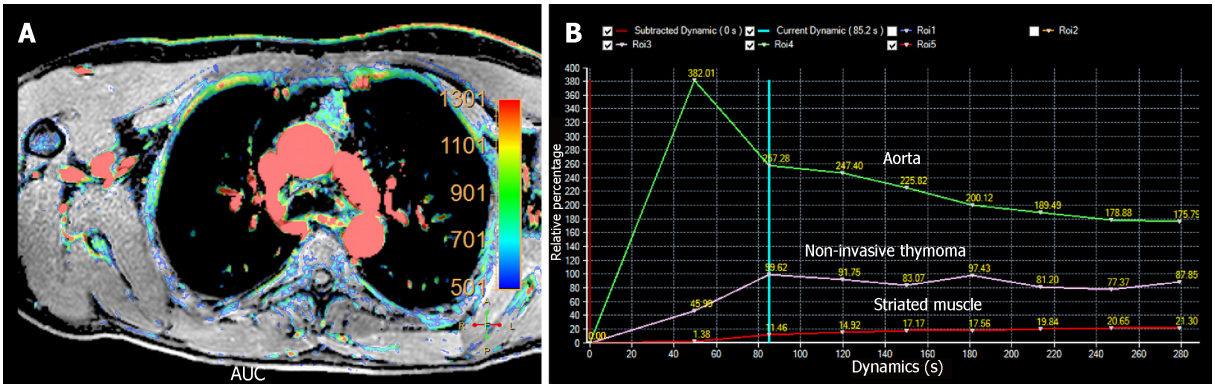

Figure 2 Perfusion weighted imaging of non-invasive thymoma. A 38 year - old male with an anterior mediastinal well-defined solid nodule, without signs of local infiltration of adjacent structures. A: Dynamic contrast-enhanced magnetic resonance (DCE-MR) derived area under the curve parametric map reveals a significant uptake of intravenous gadolinium based contrast (white arrow); B: DCE-MR derived time intensity curve shows a moderate initial slope of enhancement with a delayed plateau and with a time to peak less than 120 s (pink curve). This is in keeping with non–invasive thymoma (stage I Masaoka–Koga). AUC: Area under the curve; DCE-MR: Dynamic contrast-enhanced magnetic resonance.

described for thymo-epithelial neoplasms. The Masaoka system and its variant, the Masaoka–Koga staging system, are the most commonly used in clinical practice (Table 3). The radiologist has a crucial role in the staging, because the identification of advanced stages (III and IV) directs the patient towards neoadjuvant therapy[2]. In fact, the ITMIG recommended this staging system due to its correlation with patient survival[26]. Recently, the ITMIG in association with the International Association for the Study of Lung Cancer proposed a TNM staging system according to conclusions obtained from the retrospective inclusion of more than 10000 patients (Table 4)[27].

Thymoma is the most common histologic type of thymic epithelial neoplasms of the prevascular mediastinum. Men and women are affected equally. Has a peak incidence in middle age (40-60 years) and is rare in children and young adults[2]. About 20% of thymomas coexist with other neoplasms such as lymphoma, lung cancer, and thyroid cancer. Thymomas are slow-growing neoplasms and, although an aggressive behavior is rare, they may present pleural, pericardial, and more unusually, hematogenous spread[28]. The association of thymoma with myasthenia gravis is common. Between 30 to 50% of thymomas coexist with myasthenia gravis, being more frequent this relation in women, and up to 10% to 15% of patients with myasthenia gravis have a thymoma[1,2]. Other associated conditions are hypogammaglobulinemia (10%), pure red cell aplasia (5%), Good's syndrome (B and T cell immunodeficiency) and autoimmune disorders (SLE, polymyositis, and myocarditis)[29].

On MRI, thymomas have low to intermediate signal intensity on T1 and high signal intensity on T2-weighted sequences. They may present with cystic changes, necrosis, fibrous septa, nodules, and hemorrhage[4]. DWI is useful for differentiating between benign and malignant tumors by using ADC values. The study by Razek *et al*[4] showed ADC values of 2.38 ± 0.65 × 10^{-3} mm^2/s and 1.09 ± 0.25 × 10^{-3} mm^2/s, for benign and malignant tumors. They defined a threshold ADC value of 1.56 × 10^{-3} mm^2/s for differentiating malignant from benign mediastinal neoplasms, with a sensitivity, specificity, and accuracy of 96%, 94%, and 95%, respectively. Additionally, well-differentiated tumors showed higher ADC values (1.20 ± 0.22 × 10^{-3} mm^2/s) compared to poor differentiated tumors (0.98 ± 0.18 × 10^{-3} mm^2/s). Nevertheless, there was an overlap in the ADC values of invasive thymoma, lymphoma and lung cancer. Consequently, the solely use of ADC values cannot differentiate them with accuracy[4]. On the other hand, Yabuuchi *et al*[5] found no significant difference in ADC values between thymic epithelial tumors, lymphomas and malignant germ cell tumors. Furthermore, Carter *et al*[3] stated that ADC could not differentiate between low-grade thymomas, high-grade thymomas and thymic carcinomas.

DCE-MRI can be used to differentiate anterior mediastinal masses. Yabuuchi *et al*[5] described 3 types of time-signal intensity curves: (1) Persistent, with a time-to-peak (TTP) > 120 s; (2) Plateau, with a TTP < 120 s and a wash-out < 30%; and (3) Wash-out, with a TTP < 120 s and wash-out > 30%. In their population, the washout pattern was seen only in thymic epithelial tumors (Figure 2). Also, they added the use of ^{18}FDG-PET for this differentiation. The combination of TIC pattern (washout or persistent/plateau pattern), maximal diameter (< 6.8 cm *vs* ≥ 6.8 cm), and a maximum standardized uptake value (SUV_{max}) cut off value of 11.6 could help differentiate between thymoma (SUV_{max} < 11.6) and thymic carcinoma (SUV_{max} > 11.6). They proposed a flow diagram combining the TIC pattern, SUV_{max}, and maximal diameter

Table 2 Perfusion weighted imaging derived parameters

Semiquantitative parameters	
Initial area under the curve	Include information of blood flow, blood volume, permeability, extravascular–extracellular space volume and microvessel density.
Time to peak	Depends on tissue perfusion
Wash in	Represents velocity of enhancement
Wash out	Represents velocity of enhancement loss
Quantitative parameters	
K^{trans}	Influx volume transfer constant of a contrast agent from the vascular compartment to the interstitial space
V_e	Volume of extravascular–extracellular space per unit of tumor volume
V_p	Blood plasma volume
K^{ep}	Rate constant between extravascular-extracelular space and plasma

for characterization of anterior mediastinal solid tumors. With this scheme, they obtained a sensitivity and specificity of 93.9% and 77.8%, respectively, for differentiating anterior mediastinal tumors (Figure 3)[5].

On the other hand, Sakai *et al*[30] found a correlation between histologic grade and DCE-MRI parameters. Low-risk thymomas (Masaoka stage I/II) demonstrated rapid TTP with a mean time of 1.5 min; Masaoka stage III showed a TTP of 2.5 minutes, and other lesions such as thymic carcinoma, NETs, lymphoma, and malignant germ cell tumor demonstrated progressive enhancement, with a TTP of 3.2 min. The differentiation of thymoma from other mediastinal masses showed a sensitivity, specificity, and accuracy of 79%, 84%, and 81% respectively, when a cut-off value of TTP < 2 min was used (Figure 4).

NETs or thymic carcinoid are the least common type of thymic epithelial neoplasms (incidence 525 cases per 100000 people per year in the United States)[31]. Thymic NETs primarily affect males (male to female ratio of 3:1) in their sixth decade of life. The median age at presentation is approximately 57 years. Thymic NETs originate from neural crest cells and are associated with poor prognosis as they are aggressive, locally invasive with distant metastases and resistant to chemotherapy[32]. Nearly 25% of thymic NETs arise in patients with multiple endocrine neoplasia type 1, Cushing syndrome and inappropriate antidiuretic hormone secretion syndrome[33].

Imaging findings are similar to those of thymomas at CT and conventional MR, although, they tend to be larger, lobulated and locally invasive masses. As well as thymic carcinomas, suggestive findings include: (1) Irregular contour and cystic component; (2) metastasis and vascular invasion; and (3) heterogeneous enhancement and lymphadenopathy. They may present with low ADC values, which represents aggressiveness, hypercellularity, and poor differentiation. Additionally, a DCE-MRI with a TTP > 2 min suggests a high-grade tumor[4,5,30].

Thymic carcinomas are the second most common type of thymic epithelial neoplasms, representing up to 20% of those tumors[34]. Middle age men are more commonly affected. Thymic carcinomas are more aggressive and invasive than thymomas, with a larger size, lobulated contour, and invasion of adjacent structures. They may also present with cystic changes and necrosis. Poor prognosis is related with infiltrating tumor margin, the absence of a lobular growth pattern, high-grade atypia and necrosis, and more than ten mitoses per High-Power Field[35,36].

Thymic carcinomas present similar findings at CT and conventional MR as thymomas. Suggestive signs of thymic carcinomas are the presence of metastases, vascular invasion, irregular contour, cystic component, heterogeneous enhancement, and lymphadenopathy[35,36]. As well as thymic NETs, low ADC values suggest aggressiveness and poor differentiation, and DCE-MRI with a TTP > 2 min indicates a high-grade tumor (Figure 3). High ^{18}FDG uptake is another characteristic that may help differentiate between thymoma and thymic carcinoma, with the latter presenting with higher SUV_{max} values (Figure 4)[4,5,30].

Lymphoma: Lymphoma comprises a heterogeneous group of neoplasms involving the LN. Mediastinal involvement is frequently a part of the systemic disease. Primary mediastinal lymphomas are rare (10%). The majority of lymphomas affecting the mediastinum are Hodgkin lymphoma (HL)[37]. There were 66000 new cases of non-Hodgkin lymphoma (NHL) and 8800 new cases of HL diagnosed in the United States in 2011[38-40]. The value of imaging techniques relies on the capacity to differentiate reactive from malignant lymph node, but also to evaluate tumor extension, treatment

Table 3 Masaoka–Koga staging system

Stage	Degree of invasion	5 yr survival rate (%)
I	Tumor completely encapsulated	96-100
IIa	Microscopic tumor invasion into the capsule	86-95
IIb	Tumor invasion into the surrounding fat	
III	Tumor invasion into surrounding organ such as the pericardium, great vessel or lung	56-69
IVa	Pleural or pericardial dissemination	11-50
IVb	Lymphatic or hematogeneous metastasis	

response, and relapse. Additionally, the ability to discriminate lymphoma subtypes allows treatment assessment, outcome, and differentiation between indolent and aggressive NHL[41].

It usually presents as an anterior mediastinal soft-tissue mass or a conglomerate of LN with mild enhancement. The association of lymphadenopathy affecting different lymph node stations in the chest without mediastinal mass suggests a secondary involvement of NHL arising from other location[27]. When a mediastinal mass shows an infiltrative nature with encasement or encirclement of vascular structures without involving it, a lymphoma should be the first entity to keep in mind over thymo-epithelial or germ cell tumors[27].

^{18}FDG-PET/CT is better than ^{18}FDG-PET or CT alone for evaluating lymphoma as it helps to discriminate indolent from aggressive NHL. In 2016, the International Workshop on NHL approved the new response evaluation criteria in lymphoma (RECIL). RECIL criteria are aligned with response evaluation criteria in solid tumors, in as much as it suggests a uni-dimensional measurement method, but introduce tumor metabolic evaluation with ^{18}FDG-PET/CT. SUV_{max} is useful for evaluating treatment response and outcome in ^{18}FDG-avid lymphoma. There is an excellent correlation between high SUV_{mean} values and progression-free survival (PFS)[42].

DWI reveals inherent tissue properties, such as hypercellularity, nuclear hyperchromatism and an increase in the number of macromolecular proteins. Koşucu *et al*[43] described the utility of ADC values in the differentiation of malignant and benign mediastinal LN. They found the lowest ADC values in metastatic LN compared to benign LN ($1.02 \pm 0.19 \times 10^{-3}$ mm^2/s *vs* $1.51 \pm 0.07 \times 10^{-3}$ mm^2/s, for malignant and benign LN respectively). Also, an overlap in ADC values was present with invasive thymoma and bronchogenic carcinoma. The study by Mosavi *et al*[44] showed a difference in ADC values between indolent NHL, aggressive NHL and HL using whole-body DWI, with ADC values being lower in indolent NHL (597 ± 115 mm^2/s) rather than aggressive NHL (822 ± 266 mm^2/s) and HL (1020 ± 547 mm^2/s) (Figure 5). The explanation for lower values of ADC in indolent NHL could be explained by the higher cell density when compared to HL and aggressive NHL. Additionally, an increased ADC value has been related to longer overall survival (OS). Whole body DWI had a similar diagnostic performance to ^{18}FDG-^{18}FDG-PET/CT. Therefore, in the assessment of early treatment response, usually at after one week, could be an alternative radiation-free surveillance method. PET/MR could be a promising alternative method for staging and follow up of patients with lymphoma. In fact, ADCs and SUVs demonstrate to be independent biomarkers in lymphoma, with significant correlation between them in follicular lymphoma[17].

Germ cell tumors: They comprise neoplasms arising from primitive germ cells, miss-migrated along the urogenital ridge. There are two types, of seminomatous (seminoma and dysgerminoma) or non-seminomatous (NSGCT) origin (embryonal carcinoma, choriocarcinoma, Yolk-Salk tumor, and teratoma). Malignant germ cell tumors usually have a male predominance. Mature teratoma constitutes the most common mediastinal germ cell tumor, demostrating a varying amount of intralesional fluid, fat (present in up to 50% of cases), calcification or soft tissue components. Frequently, teratomas manifest as large unilocular or multilocular thin-walled cystic masses[3]. Occasionally, bones or tooth-like elements could be identified[45,46]. Fat-fluid levels are highly specific to this entity, which typically affect young patients, with a described prevalence of 25% of the prevascular masses in patients of 10-19 years-old, 10%-15% in individuals of 20-49 years old and less than 5% in subjects of more than 50 years-old[47]. Differential diagnosis includes other fat-containing anterior mediastinal lesions like thymolipoma, lipoma or liposarcoma.

Non-teratomatous germ cell tumors usually manifest as large soft-tissue prevascular mediastinal masses. Clinical and serological information is useful in the

Table 4 The tumor node metastasis staging system by International Thymic Malignancy Interest Group

		TNM staging					
Tumor (T) descriptor		**I**	**II**	**IIIA**	**IIIB**	**IVA**	**IVB**
T1a	Encapsulated or unencapsulated tumor, with or without extension into fat	X				X	X
T1b	Invasion of mediastinal pleura	X				X	X
T2	Invasion of pericardium		X			X	X
T3	Involvement of lung, chest wall, phrenic nerve, brachiocephalic vein, superior vena cava, or hilar (extrapericardial) pulmonary vessels			X		X	X
T4	Invasion of thoracic aorta, arch vessels, main pulmonary artery, trachea, esophagus, or myocardium				X	X	X
Node (N) descriptor		**I**	**II**	**IIIA**	**IIIB**	**IVA**	**IVB**
N0	No lymph node metastasis	X	X	X	X	X	X
N1	Involvement of anterior (perithymic) lymph nodes					X	X
N2	Involvement of deep intrathoracic or cervical lymph nodes						X
Metastasis (M) descriptor		**I**	**II**	**IIIA**	**IIIB**	**IVA**	**IVB**
M0	No Metastasis	X	X	X	X	X (N1)	X (N2)
M1a	Pleural or pericardial metastatic nodule or lesions					X (N0,1)	X (N2)
M1b	Pulmonary intraparenchymal metastastic nodule or distant organ metastasis						X (any T, N)

TNM: Tumor node metastasis staging system; ITMIG: International Thymic Malignancy Interest Group.

differentiation of these lesions with lymphoma. Seminomas generally affect patients between 10 to 39 years old. In up to 10% of patients, there is an elevation of serum levels of beta-human chorionic gonadotropin (b-HCG)[48]. Elevated levels of lactate dehydrogenase could be present in seminomas but also in lymphoma patients[49,50]. Contrarily, NSGCT present with high levels of serum b-HCG and alpha-fetoprotein in 90% of them[51,52]. Seminomatous tumors manifest as hypointense masses on T2-weighted images, with homogeneous enhancement after gadolinium uptake. By contrast, NSGCT are large and heterogeneous masses. Internal foci of hyperintensity on T1-weighted images are related to intralesional hemorrhage. Although, the presence of pleural effusion is rare, pulmonary metastasis may help to distinguish seminomatous germ cell tumors from lymphoma. An NSGCT is firstly suspected when a large and heterogeneous prevascular mass with pulmonary nodules is

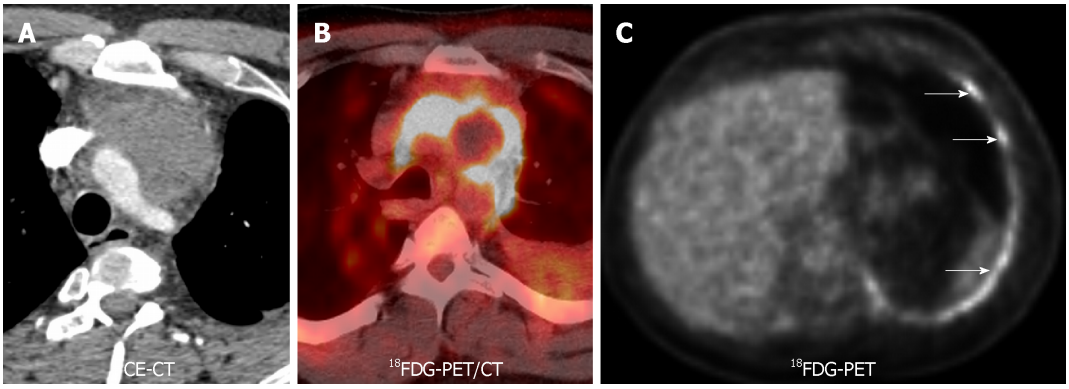

Figure 3 ^{18}F-Fluorodeoxiglucose positron emission tomography/computed tomography of a thymic carcinoma. A 34-year-old with chest pain, found to have infiltrative mass on pulmonary embolism protocol. Pathology revealed a thymic carcinoma. A and B: Contrast-enhanced computed tomography and fused ^{18}F-Fluorodeoxiglucose positron emission tomography/computed tomography showed an ^{18}F-Fluorodeoxiglucose avid anterior mediastinal mass infiltrating thoracic vascular vessels; C: Concentric increased ^{18}F-Fluorodeoxiglucose activity in the left pleura was proven to represent metastatic disease (white arrows). ^{18}F-FDG-PET/CT: ^{18}F-Fluorodeoxiglucose positron emission tomography/computed tomography; ^{18}FDG-PET: ^{18}F-Fluorodeoxiglucose positron emission tomography; CE-CT: Contrast-enhanced computed tomography.

identified on a male patient below 40 years-old[45,53]. DWI could help to differentiate a benign from a malignant origin, but also, may increase our specificity to detect mature fibrosis or cystic components. At DCE-MR, they usually show a persistent or plateau pattern of TIC, with a TTP over 120 s. On ^{18}FDG-PET/CT, they show a high radiotracer uptake, often with maximum SUVs higher than 11.6 (Figure 6). The combination of size, DCE-MR derived TIC, and ^{18}FDG-PET/CT along with serologic markers could help to differentiate germ cell tumors from other anterior mediastinal masses[5].

Mediastinal goiter: It has a described incidence of 1%-15% of patients undergoing thyroidectomy. On a CT exam, when a hyperattenuating (70-85 Hounsfield units) prevascular mediastinal mass with intense and sustained enhancement is identified in continuity with the cervical thyroid gland, a mediastinal goiter should be the most preferred diagnosis. Cystic changes and calcifications may be present. Additional findings favouring a malignant transformation are loss of mediastinal tissue planes and cervical or mediastinal lymphadenopathy[27,47].

DWI could help to differentiate benign from malignant thyroid nodules. Using a b value of 500 s/mm^2 and an ADC cut-off value of 1.704 × 10^{-3} mm^2/s, a sensitivity, specificity, and accuracy of 92%, 88%, and 87%, respectively has been described. Additionally, using a DW-sequence with a *b* value of 1000 s/mm^2, significant differences on ADC values have been described between benign and malignant nodules (2.75 ± 0.6 × 10^{-3} mm^2/s *vs* 0.69 ± 0.35 × 10^{-3} mm^2/s). The decrease in ADC values in malignant lesions is due to the presence of increased cell density and relatively severe desmoplastic response. Contrarily, the cause of elevated ADC in thyroid adenomas and hyperplastic nodular goiter is the predominance of abundant cellular follicles, extracellular fluid and reduced cell density[54]. Furthermore, the presence of a delayed wash-out pattern is also suggestive of thyroid carcinoma, with higher diagnostic performance compared to fine needle aspiration (sensitivity 100% *vs* 50%-85.7%; accuracy 90% *vs* 70% to 87.5%, respectively)[55].

Parathyroid adenoma: It usually presents in a patient with a history of primary hyperparathyroidism, hypercalcemia and/or elevated serum parathormone levels, with or without parathyrodectomy and a soft-tissue nodule in the anterior–prevascular mediastinum[56]. 20% of parathyroid adenomas are ectopic, and 80% of ectopic parathyroid adenomas showed an anterior mediastinal location. Possible ectopic locations include the thymus, tracheoesophageal groove, retrosternal region and posterosuperior mediastinum[36]. On imaging, they usually present as small (< 3 cm) rounded and well-defined nodules, with high radiotracer uptake at ^{99m}Tecnetium and ^{201}Talium scans[27]. Four dimensional (4D) CT provides both functional (perfusion) and highly detailed anatomic knowledge about parathyroid lesions. At 4D CT imaging, they present strong enhancement after intravenous contrast infusion with significant washout at the delayed phase[57,58]. Although there is no reference in the literature about the utility of DWI and DCE-MR in parathyroid adenoma, in the authors' experience, these lesions demonstrate high ADC values and, and on PWI, a TIC with a steep slope and significant washout, in a similar fashion to the findings described on 4D CT[27].

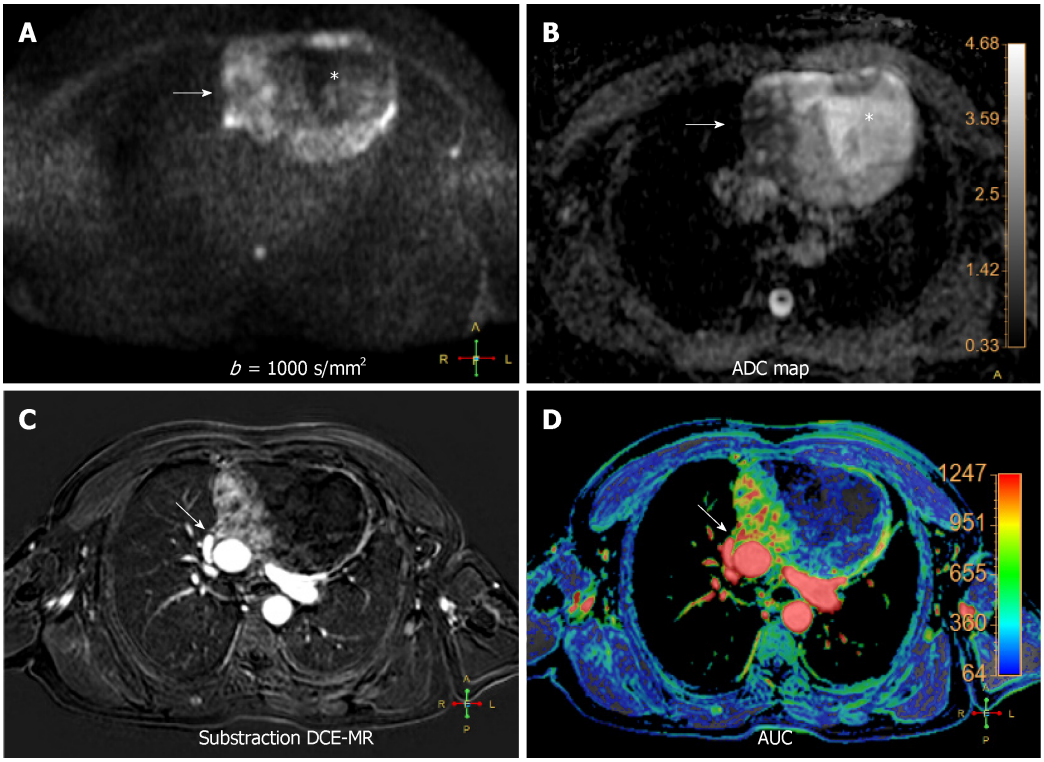

Figure 4 Multiparametric functional magnetic resonance imaging thymoepithelial mass. A 63 year-old male with a complex cystic anterior mediastinal mass. A and B: High *b* value diffusion-weighted imaging (DWI) (b = 1000 s/mm^2) (A) and corresponding apparent diffusion coefficient (ADC) map (B) revealing the complex behaviour of the lesion. In this case, DWI can differentiate the solid (white arrow on A and B) and cystic (white asterisk on A and B) components and also reveals heh restrictive behaviour of the solid part of the mass (ADC: 1.12-1.23 × 10^{-3} mm^2/s), related to hypercellularity; C and D: Substraction of dynamic contrast-enhanced magnetic resonance on the arterial phase (C) and area under the curve parametric map (D) showing the locally invasive behaviour of the lesion to the pericardium and adjacent ascending aorta (white arrows on C and D). The mass corresponded to an invasive thymoma stage III of Masaoka–Koga classification system. DWI: Diffusion-weighted imaging; ADC: Apparent diffusion coefficient; AUC: Area under the curve; DCE-MR: Dynamic contrast-enhanced magnetic resonance.

Visceral mediastinal lesions

Central lung cancer: Functional MR has shown great utility in patients with lung cancer, enabling to differentiate with accuracy benign from malignant nodules. The combination of DWI and DCE-MR showed similar sensitivity to ^{18}FDG-PET-CT but higher specificity and accuracy (up to 94%), thanks to the reduction of the number of false positives from the latter technique, such as active inflammatory and tuberculous nodules[6]. In addition, DWI has a potential impact on lung cancer differentiation. Well-differentiated adenocarcinomas display higher ADC values than aggressive adenocarcinomas, with certain overlap with small cell lung cancer and squamous cell lung cancer[59]. The amount of tumor cells and its distribution is related to signal intensity at high *b* value. A signal intensity lesion-to-spinal cord ratio (LSR) on high b value has been explored in the differentiation of malignant and benign ones. Malignant tumors demonstrated higher values, having more specificity and accuracy than ADC and IVIM derived values in this differentiation[60,61]. Furthermore, aggressive subtypes of adenocarcinoma showed higher signal intensity at high b value with a heterogeneous pattern. However, other authors did not show significant differences in the LSR of benign and malignant pulmonary lesions (Figure 7)[62].

Different patterns of enhancement have been described in primary mediastinal neoplasms, although some overlap is also present[63-66]. Some authors obtained higher relative signal enhancement and steeper slope in active inflammatory lesions[66]. Coolen *et al*[63] described a flowchart , where the use of DWI in lesions with TIC type B curves could distinguish benign (non-restrictive) from malignant (restrictive) entities (Figure 7). Therefore, functional multiparametric chest MRI constitutes a valuable one-stop-shop radiation-free diagnostic modality for lung cancer characterization.

Paravertebral mediastinal masses

Neurogenic tumors group a certain type of lesions that arise from peripheral nerves, sympathetic and parasympathetic ganglia. Correspond to 75% of all posterior mediastinal lesions, 20% of adult posterior mediastinal lesions and 25% of pediatric mediastinal lesions[3]. There are significant differences in the ADC of benign and malignant peripheral nerve tumors (1.848 ± 0.40 × 10^{-3} mm^2/s *vs* 0.900 ± 0.25 × 10^{-3}

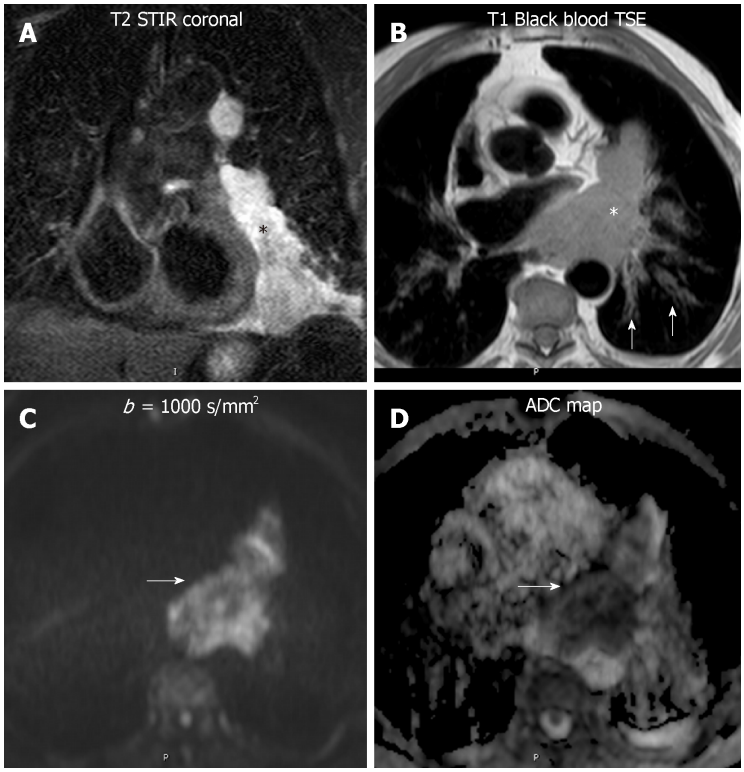

Figure 5 Diffusion weighted imaging of a lymphoma. An 82 year - old man with a paracardiac lymphomatous mass. A: The lesion is hyperintense in short tau inversion recovery (black asterisk); B: On black blood turbo spin echo T1-weighted image, the lesion is slightly hyperintense compared to striated muscle (white asterisk), with infiltration of the pericardium and hilar vessels. Secondary involvement of the left axial interstitium, bilaterally (white arrows on B); C and D: In high *b* value diffusion-weighted imaging (*b*: 1000 s/mm^2) the mass showed high signal intensity, with low apparent diffusion coefficient: 1.1 × 10^{-3} mm^2/s on the apparent diffusion coefficient map, in keeping with lymphoma (white arrows on C and D). STIR: Short tau inversion recovery; TSE: Turbo spin echo; ADC: Apparent diffusion coefficient.

mm^2/s; for benign and malignant tumors, respectively, $P < 0.001$)[67]. Also, the FA derived from diffusion tensor imaging of involved nerves was lower compared to normal ones[67]. There is limited evidence about the application of functional MRI in other mediastinal lesions.

FUNCTIONAL MR AND STAGING

Functional MR has shown great utility in the staging of lung cancer by allowing an accurate assessment of invasion of vascular, bronchial and other mediastinal and chest wall structures. DWI can differentiate, without the need for any radiotracer intake, central tumor (restrictive) from post-obstructive pneumonitis (non-restrictive), which is vital for cancer staging and radiotherapy planning. DCE-MR is superior to contrast enhanced CT and morphological MR in the identification of vascular and mediastinal invasion[12]. Free breathing RT-SSFP sequences can distinguish those peripheral tumors invading only the visceral pleura (mobile with respiratory motion) rather than those that invade parietal pleura and beyond (static with respiratory motion). Therefore, the combination of DCE-MR and RT-SSFP could be an optimized strategy for assessing pleural, mediastinal, diaphragmatic and chest wall invasion.

For nodal staging (N-staging) ^{18}FDG-PET/CT constitute the primary modality in lung cancer. The primary objective is to identify occult metastatic LN and distant lesions. It could discriminate N3 from M1 stages, which require neoadjuvant therapy. By contrast, DWI has also shown great utility in the differentiation of benign from malignant LN, distinguishing false positive ^{18}FDG-PET/CT targets due to reactive – inflammatory LN. In DWI, false positives are due to granulomatous LN, and false negatives are secondary to microscopic cancer deposits, mainly. Nomori *et al*[68] detected higher ADC values in benign lymph nodes compared to metastatic ones, using an ADC threshold value of 1.63 × 10^{-3} mm^2/s (accuracy: 89%, specificity: 99%). Finally, Chhabra *et al*[67] applied a semiquantitative approach. They referred that short tau inversion recovery was more sensitive and accurate for N staging compared to

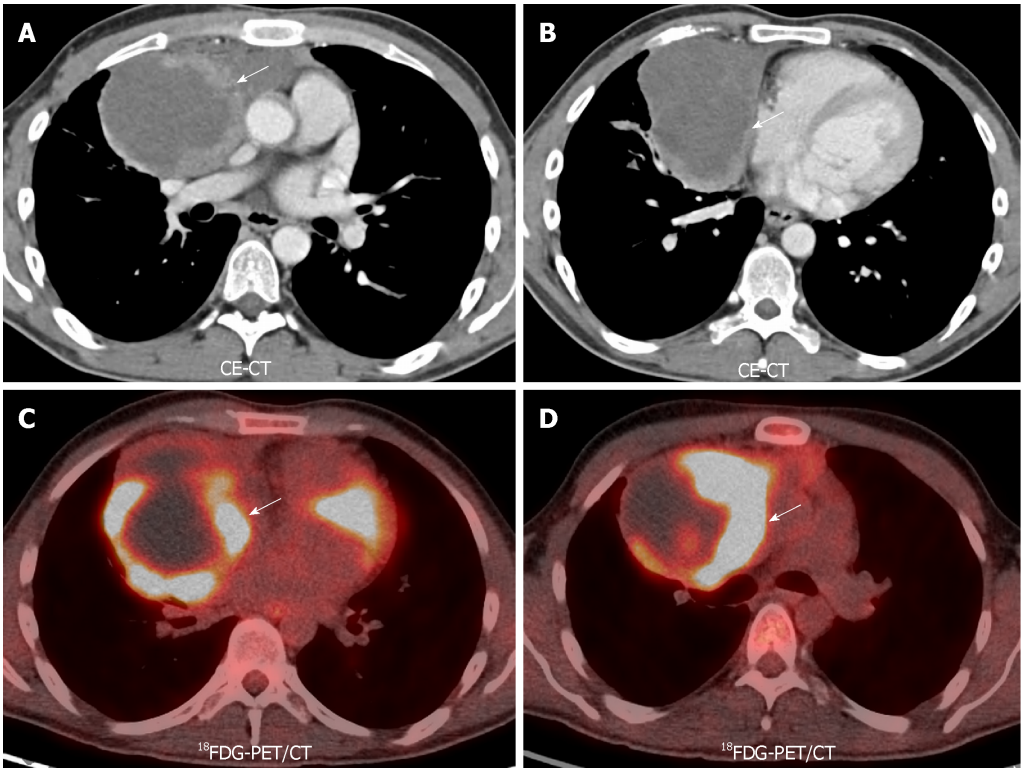

Figure 6 ^{18}F-Fluorodeoxiglucose positron emission tomography/computed tomography of a germ cell tumor. A 27-year-old man with back pain, found to have germ cell tumor on ^{18}F-Fluorodeoxiglucose positron emission tomography/computed tomography (^{18}FDG-PET/CT). A and B: Contrast-enhanced CT shows a cystic mass with enhancing solid border (white arrows on A and B); C and D: Note ^{18}FDG activity only within the solid portions of the lesion on fused ^{18}FDG-PET/CT acquisitions (white arrows on C-D). ^{18}FDG-PET/CT: ^{18}F-Fluorodeoxiglucose positron emission tomography/computed tomography; CE CT: Contrast-enhanced computed tomography.

DWI and ^{18}FDG-PET/CT.

^{18}FDG-PET/CT is the current standard technique for staging esophageal cancer, with an overall accuracy of 90%-92%. False negatives are due to early stage (T*in situ*, T1 and T2). False positives of this technique are secondary to leiomyomas and esophagitis (Figure 8). Another limitation is the poor spatial resolution, which explains its limited role in defining the depth of invasion. MRI has no role in current staging guidelines. MR also has poor detection rates in the early stages. The detection rates using a combination of high resolution T2 and DWI are 33%, 58%, 96% and 100% for T1, T2, T3, and T4 stages, respectively[69]. Contrarily to lung cancer LN, in esophageal carcinoma the ADC of malignant LN is higher than benign LN ($1.46 \pm 0.35 \times 10^{-3}$ mm^2/s *vs* $1.15 \pm 0.25 \times 10^{-3}$ mm^2/s, $P < 0.0001$), due to their mucinous content[70].

Whole body–DWI (WB-DWI) is a promising tool for M staging, which globally reflects similar results to ^{18}FDG-PET/CT. In detail, it is superior to bone scintigraphy, ^{18}FDG-PET/CT and CT in the identification of bone metastasis, and has substantial advantages in the detection of bone, liver, brain, and kidney metastasis[71]. Contrarily, compared to a WB-DWI scheme, ^{18}FDG-PET/CT has better results in LN and soft-tissue metastasis, probably due to the non-selective fat saturation technique applied for background signal suppression in WB-DWI[72,73].

CHEST MR IN EARLY RESPONSE AND TREATMENT MONITORING

One of the most promising applications of functional MR in the chest is treatment monitoring and detection of recurrence (Table 5). An increase in ADC in patients of non-small cell lung cancer during or after chemotherapy or radiotherapy has been related to good response, being associated to higher OS and PFS. This increase in ADC is due to cell death, necrosis, apoptosis, and cell lysis. DWI has better results for detection of early response than DCE-MR and ^{18}FDG-PET/CT. Also, a low ADC value at the pre-treatment stage has been predictive of proper response to chemotherapy[8,74,75].

Another important application of DWI is the treatment monitoring of new

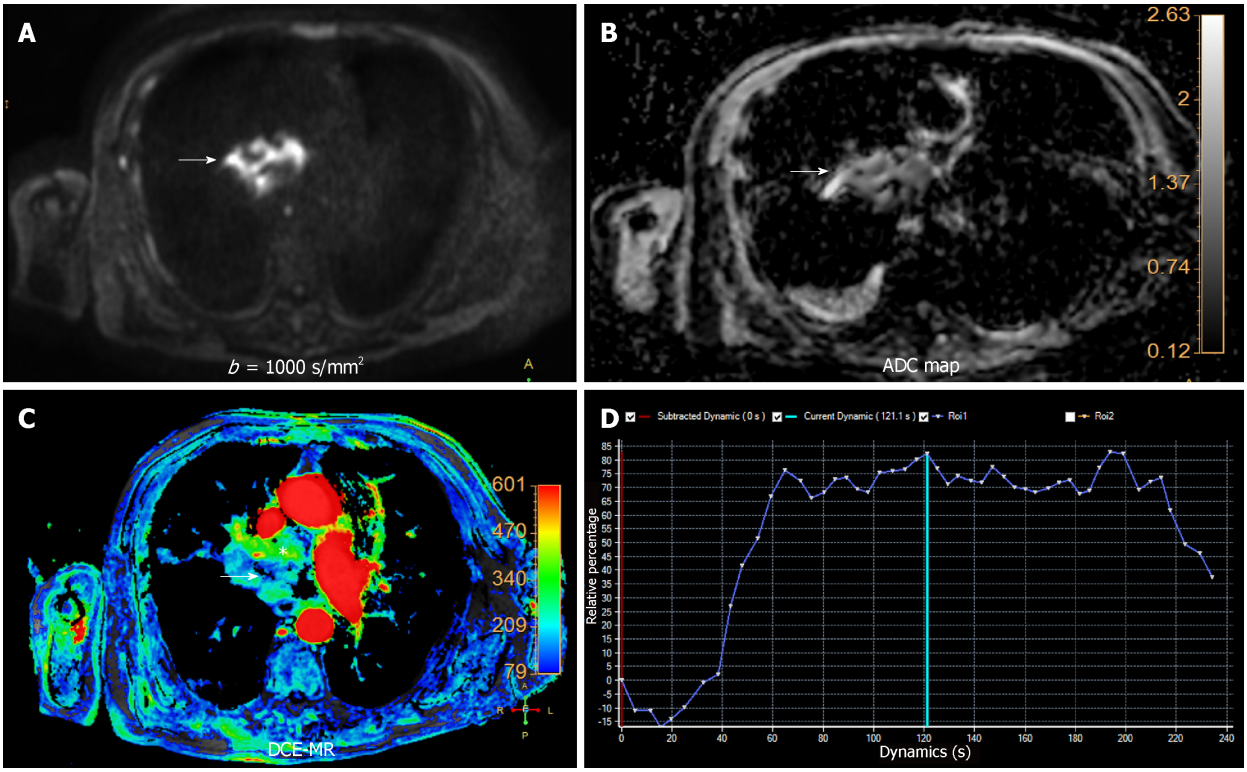

Figure 7 Multiparametric functional chest magnetic resonance of central lung cancer. A 78 year-old male with a central hilar mass in keeping with epidermoid type lung carcinoma. A and B: High *b* value (*b* = 1000 s/mm^2) and apparent diffusion coefficient (ADC) map (B) revealing a heterogeneous and restrictive behavior of the lesion, related to hypercellularity and aggressiveness (white arrows on A and B). The mean ADC was 0.97 × 10^{-3} mm^2/s, confirming a malignant origin; C: Dynamic contrast-enhanced magnetic resonance showing a significant uptake of gadolinium based contrast agent on area under the curve parametric map (white asterisk), with central necrosis (White arrow on C); D: Time intensity curve (TIC) plot revealing steep slope of enhancement with posterior plateau (type B TIC) also favoring a malignant etiology. DCE-MR: Dynamic contrast-enhanced magnetic resonance; ADC: Apparent diffusion coefficient; TIC: Time intensity curve.

therapeutic agents (vascular disrupting agents and immunotherapy). Because of the different mechanism of action in cancerous cells compared to conventional drugs, the radiologist must be conscious of the paradigmatic behavior of the lesions during treatment surveillance. Lung tumors with high ADC value are predictive of good response to vascular disrupting agents, and during the follow-up, a decrease of ADC is a sign of treatment effectiveness[8].

As well as in staging, the treatment response of esophageal cancer is made usually by ^{18}FDG-PET/CT. A decrease of more than 50% of the SUV_{max}/SUV_{mean} in the post-treatment follow-up compared to pre-treatment examination is in keeping with a good response. This method has low sensitivity and specificity (67%-70%), mainly due to chemotherapy and radiotherapy induced esophagitis. Also, the identification of a good response behavior precludes the detection of local recurrence, being present only in 42% of PET-based clinical responders[69]. On MRI, a difference in post-treatment ADC compared to pre-treatment value has been correlated with histopathological regression grade. This difference early on the treatment onset has a 100% predictive value on responders[76-78]. Therefore, the assessment of treatment effect with functional MR has a great potential utility in the differentiation of early response, with a possible impact in the prognosis of these patients (Figure 9).

CONCLUSION

Functional imaging of the mediastinum enhances an accurate assessment of mediastinal masses. It allows to distinguish with accuracy benign from malignant lesions. DWI and DCE-MRI are functional techniques which can be used in clinical protocols, providing an alternative to ^{18}FDG-PET/CT in the evaluation of mediastinal lesions. It allows a complete characterization of them in a one-stop-shop procedure, while avoiding the use of ionizing radiation. Functional techniques have a great potential impact in the staging of lung and esophageal cancers, increasing its precision, and in the therapy monitoring of mediastinal neoplasms. Quantitative functional MR-derived parameters provide unique information, which makes them authentic biomarkers with potential prognostic implications.

Table 5 Treatment monitoring and recurrence behavior

	Good response	Poor response
T2WI	No tumor ↑ SI in bone marrow	Residual/↑soft tissue mass ↑ extent bone marrow invasion
DWI	↑ ADC	↓ ADC
DCE-MRI	↓ slope/absent enhancement	Persistent / ↑ enhancement
MRS	↑ Choline peak	↓ Choline peak

T2WI: T2 weighted imaging; SI: Signal intensity; DWI: Diffusion weighted imaging; ADC: Apparent diffusion coefficient; DCE-MRI: Dynamic contrast enhanced magnetic resonance imaging; MRS: Magnetic resonance spectroscopy. Modified from Vilanova *et al*[18].

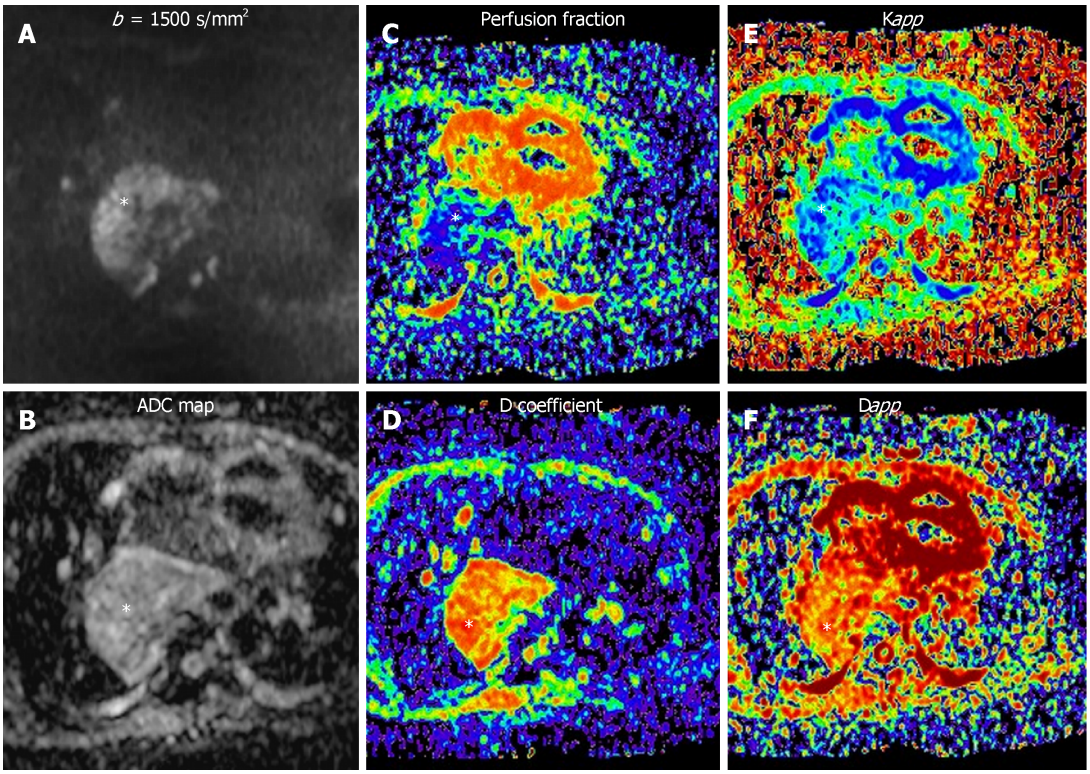

Figure 8 Different diffusion weighted imaging approaches to an aggressive middle mediastinal mass. A 56 year-old woman with esophageal leiomyosarcoma stage IV. A-F: Restrictive behavior of the mass could be seen [Apparent diffusion coefficient (ADC): 0.951 × 10^{-3} m^2/s; malignant origin]. Derived biomarkers of three different ways of quantification of diffusion-weighted imaging (white asterisk) of the mass are shown: A-B: Mono-exponential approach (A: High *b* value; B: ADC map); C-D: bi-exponential scheme (Intravoxel incoherent motion; C: Perfusion fraction map; D: Diffusion coefficient map); E-F: Diffusion kurtosis imaging (E: Apparent diffusional kurtosis map; F: Apparent diffusion map). ADC: Apparent diffusion coefficient.

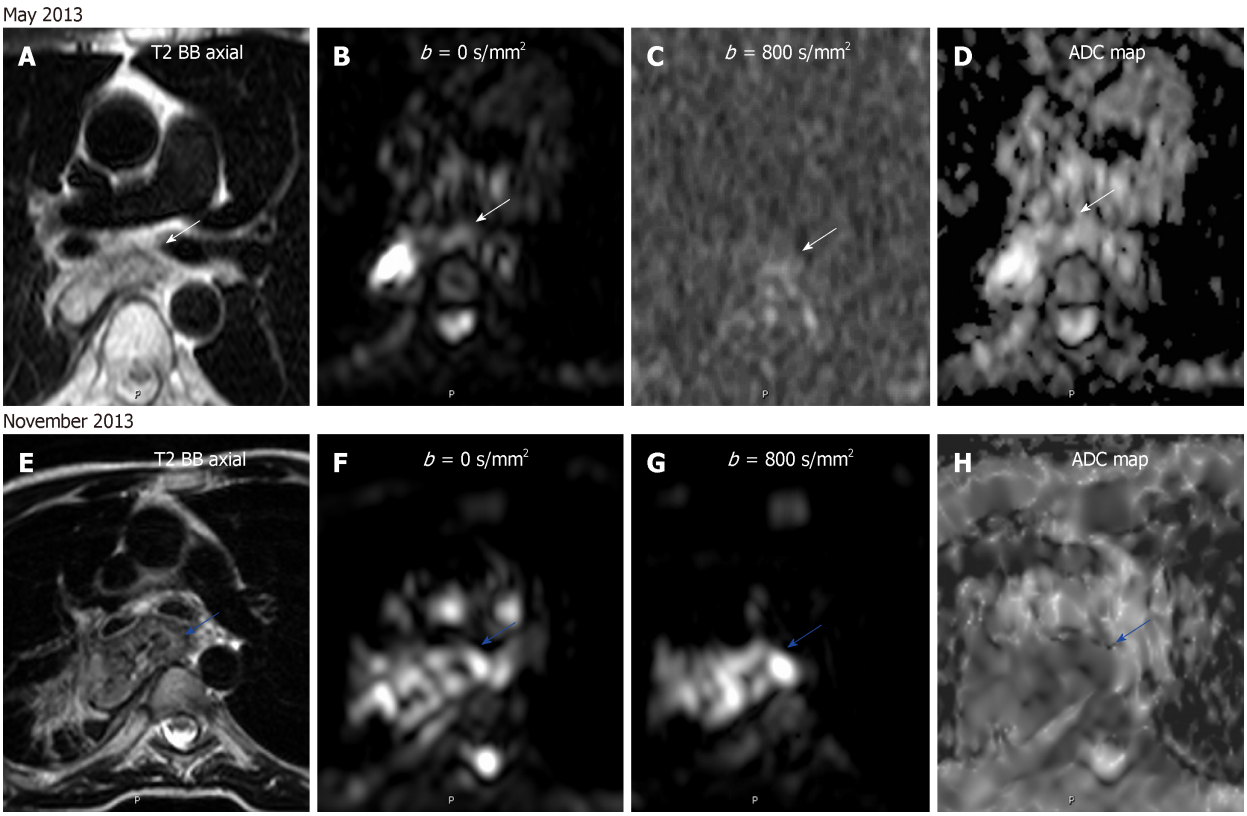

Figure 9 Treatment monitoring of an esophageal carcinoma by diffusion-weighted imaging. A 47 year-old male with esophageal carcinoma treated with esophagectomy and gastroplasty. A-D: Post-surgery surveillance magnetic resonance (MR) shows a normal appearing anastomosis on turbo spin echo (TSE) T2-weighted sequence and with no restriction on diffusion-weighted imaging and apparent diffusion coefficient (ADC) map (B-D; white arrows); D-G: Follow-up MR examination done 6 mo later revealing anastomotic thickening on TSE T2-weighted image and with restrictive behavior on diffusion-weighted whole-body imaging and ADC map (F-H), in keeping with relapse (blue arrows). ADC: Apparent diffusion coefficient.

REFERENCES

1 **Ackman JB**. MR Imaging of Mediastinal Masses. *Magn Reson Imaging Clin N Am* 2015; **23**: 141-164 [PMID: 25952512 DOI: 10.1016/j.mric.2015.01.002]
2 **Carter BW**, Benveniste MF, Truong MT, Marom EM. State of the Art: MR Imaging of Thymoma. *Magn Reson Imaging Clin N Am* 2015; **23**: 165-177 [PMID: 25952513 DOI: 10.1016/j.mric.2015.01.005]
3 **Carter BW**, Betancourt SL, Benveniste MF. MR Imaging of Mediastinal Masses. *Top Magn Reson Imaging* 2017; **26**: 153-165 [PMID: 28777164 DOI: 10.1097/RMR.0000000000000134]
4 **Razek AA**, Elmorsy A, Elshafey M, Elhadedy T, Hamza O. Assessment of mediastinal tumors with diffusion-weighted single-shot echo-planar MRI. *J Magn Reson Imaging* 2009; **30**: 535-540 [PMID: 19630080 DOI: 10.1002/jmri.21871]
5 **Yabuuchi H**, Matsuo Y, Abe K, Baba S, Sunami S, Kamitani T, Yonezawa M, Yamasaki Y, Kawanami S, Nagao M, Okamoto T, Nakamura K, Yamamoto H, Sasaki M, Honda H. Anterior mediastinal solid tumours in adults: Characterisation using dynamic contrast-enhanced MRI, diffusion-weighted MRI, and FDG-PET/CT. *Clin Radiol* 2015; **70**: 1289-1298 [PMID: 26272529 DOI: 10.1016/j.crad.2015.07.004]
6 **Broncano J**, Luna A, Sánchez-González J, Alvarez-Kindelan A, Bhalla S. Functional MR Imaging in Chest Malignancies. *Magn Reson Imaging Clin N Am* 2016; **24**: 135-155 [PMID: 26613879 DOI: 10.1016/j.mric.2015.08.004]
7 **Ciliberto M**, Kishida Y, Seki S, Yoshikawa T, Ohno Y. Update of MR Imaging for Evaluation of Lung Cancer. *Radiol Clin North Am* 2018; **56**: 437-469 [PMID: 29622078 DOI: 10.1016/j.rcl.2018.01.005]
8 **Bains LJ**, Zweifel M, Thoeny HC. Therapy response with diffusion MRI: An update. *Cancer Imaging* 2012; **12**: 395-402 [PMID: 23022595 DOI: 10.1102/1470-7330.2012.9047]
9 **Le Bihan D**. Apparent diffusion coefficient and beyond: What diffusion MR imaging can tell us about tissue structure. *Radiology* 2013; **268**: 318-322 [PMID: 23882093 DOI: 10.1148/radiol.13130420]
10 **Le Bihan D**, Breton E, Lallemand D, Aubin ML, Vignaud J, Laval-Jeantet M. Separation of diffusion and perfusion in intravoxel incoherent motion MR imaging. *Radiology* 1988; **168**: 497-505 [PMID: 3393671 DOI: 10.1148/radiology.168.2.3393671]
11 **Filippi M**, Agosta F. Diffusion tensor imaging and functional MRI. *Handb Clin Neurol* 2016; **136**: 1065-1087 [PMID: 27430459 DOI: 10.1016/B978-0-444-53486-6.00056-9]
12 **Huston JM**, Field AS. Clinical applications of diffusion tensor imaging. *Magn Reson Imaging Clin N Am* 2013; **21**: 279-298 [PMID: 23642554 DOI: 10.1016/j.mric.2012.12.003]
13 **Barrett T**, Brechbiel M, Bernardo M, Choyke PL. MRI of tumor angiogenesis. *J Magn Reson Imaging* 2007; **26**: 235-249 [PMID: 17623889 DOI: 10.1002/jmri.20991]
14 **Buonaccorsi GA**, Roberts C, Cheung S, Watson Y, O'Connor JP, Davies K, Jackson A, Jayson GC, Parker GJ. Comparison of the performance of tracer kinetic model-driven registration for dynamic contrast enhanced MRI using different models of contrast enhancement. *Acad Radiol* 2006; **13**: 1112-1123 [PMID:

16935723 DOI: 10.1016/j.acra.2006.05.016]
15 **Runge VM**, Clanton JA, Herzer WA, Gibbs SJ, Price AC, Partain CL, James AE. Intravascular contrast agents suitable for magnetic resonance imaging. *Radiology* 1984; **153**: 171-176 [PMID: 6433402 DOI: 10.1148/radiology.153.1.6433402]
16 **Rijpkema M**, Kaanders JH, Joosten FB, van der Kogel AJ, Heerschap A. Method for quantitative mapping of dynamic MRI contrast agent uptake in human tumors. *J Magn Reson Imaging* 2001; **14**: 457-463 [PMID: 11599071 DOI: 10.1002/jmri.1207]
17 **Luna A**, Pahwa S, Bonini C, Alcalá-Mata L, Wright KL, Gulani V. Multiparametric MR Imaging in Abdominal Malignancies. *Magn Reson Imaging Clin N Am* 2016; **24**: 157-186 [PMID: 26613880 DOI: 10.1016/j.mric.2015.08.005]
18 **Vilanova JC**, Baleato-Gonzalez S, Romero MJ, Carrascoso-Arranz J, Luna A. Assessment of Musculoskeletal Malignancies with Functional MR Imaging. *Magn Reson Imaging Clin N Am* 2016; **24**: 239-259 [PMID: 26613884 DOI: 10.1016/j.mric.2015.08.006]
19 **Vaupel P**, Mayer A. Hypoxia in cancer: Significance and impact on clinical outcome. *Cancer Metastasis Rev* 2007; **26**: 225-239 [PMID: 17440684 DOI: 10.1007/s10555-007-9055-1]
20 **Carter BW**, Tomiyama N, Bhora FY, Rosado de Christenson ML, Nakajima J, Boiselle PM, Detterbeck FC, Marom EM. A modern definition of mediastinal compartments. *J Thorac Oncol* 2014; **9**: S97-101 [PMID: 25396318 DOI: 10.1097/JTO.0000000000000292]
21 **Nishino M**, Ashiku SK, Kocher ON, Thurer RL, Boiselle PM, Hatabu H. The thymus: A comprehensive review. *Radiographics* 2006; **26**: 335-348 [PMID: 16549602 DOI: 10.1148/rg.262045213]
22 **Priola AM**, Priola SM, Ciccone G, Evangelista A, Cataldi A, Gned D, Pazè F, Ducco L, Moretti F, Brundu M, Veltri A. Differentiation of rebound and lymphoid thymic hyperplasia from anterior mediastinal tumors with dual-echo chemical-shift MR imaging in adulthood: Reliability of the chemical-shift ratio and signal intensity index. *Radiology* 2015; **274**: 238-249 [PMID: 25105246 DOI: 10.1148/radiol.14132665]
23 **Inaoka T**, Takahashi K, Mineta M, Yamada T, Shuke N, Okizaki A, Nagasawa K, Sugimori H, Aburano T. Thymic hyperplasia and thymus gland tumors: Differentiation with chemical shift MR imaging. *Radiology* 2007; **243**: 869-876 [PMID: 17463136 DOI: 10.1148/radiol.2433060797]
24 **Ackman JB**, Mino-Kenudson M, Morse CR. Nonsuppressing normal thymus on chemical shift magnetic resonance imaging in a young woman. *J Thorac Imaging* 2012; **27**: W196-W198 [PMID: 22487991 DOI: 10.1097/RTI.0b013e318249936a]
25 **Ackman JB**, Kovacina B, Carter BW, Wu CC, Sharma A, Shepard JA, Halpern EF. Sex difference in normal thymic appearance in adults 20-30 years of age. *Radiology* 2013; **268**: 245-253 [PMID: 23440318 DOI: 10.1148/radiol.13121104]
26 **Falkson CB**, Bezjak A, Darling G, Gregg R, Malthaner R, Maziak DE, Yu E, Smith CA, McNair S, Ung YC, Evans WK; Lung Cancer Disease Site Group of Cancer Care Ontario's Program in Evidence-Based Care. The management of thymoma: A systematic review and practice guideline. *J Thorac Oncol* 2009; **4**: 911-919 [PMID: 19557895 DOI: 10.1097/JTO.0b013e3181a4b8e0]
27 **Carter BW**, Benveniste MF, Madan R, Godoy MC, de Groot PM, Truong MT, Rosado-de-Christenson ML, Marom EM. ITMIG Classification of Mediastinal Compartments and Multidisciplinary Approach to Mediastinal Masses. *Radiographics* 2017; **37**: 413-436 [PMID: 28129068 DOI: 10.1148/rg.2017160095]
28 **Engels EA**. Epidemiology of thymoma and associated malignancies. *J Thorac Oncol* 2010; **5**: S260-S265 [PMID: 20859116 DOI: 10.1097/JTO.0b013e3181f1f62d]
29 **Levy Y**, Afek A, Sherer Y, Bar-Dayan Y, Shibi R, Kopolovic J, Shoenfeld Y. Malignant thymoma associated with autoimmune diseases: A retrospective study and review of the literature. *Semin Arthritis Rheum* 1998; **28**: 73-79 [PMID: 9806367 DOI: 10.1016/S0049-0172(98)80039-5]
30 **Sakai S**, Murayama S, Soeda H, Matsuo Y, Ono M, Masuda K. Differential diagnosis between thymoma and non-thymoma by dynamic MR imaging. *Acta Radiol* 2002; **43**: 262-268 [PMID: 12100322 DOI: 10.1080/j.1600-0455.2002.430306.x]
31 **Yao JC**, Hassan M, Phan A, Dagohoy C, Leary C, Mares JE, Abdalla EK, Fleming JB, Vauthey JN, Rashid A, Evans DB. One hundred years after "carcinoid": Epidemiology of and prognostic factors for neuroendocrine tumors in 35,825 cases in the United States. *J Clin Oncol* 2008; **26**: 3063-3072 [PMID: 18565894 DOI: 10.1200/JCO.2007.15.4377]
32 **Gaur P**, Leary C, Yao JC. Thymic neuroendocrine tumors: A SEER database analysis of 160 patients. *Ann Surg* 2010; **251**: 1117-1121 [PMID: 20485130 DOI: 10.1097/SLA.0b013e3181dd4ec4]
33 **Gibril F**, Chen YJ, Schrump DS, Vortmeyer A, Zhuang Z, Lubensky IA, Reynolds JC, Louie A, Entsuah LK, Huang K, Asgharian B, Jensen RT. Prospective study of thymic carcinoids in patients with multiple endocrine neoplasia type 1. *J Clin Endocrinol Metab* 2003; **88**: 1066-1081 [PMID: 12629087 DOI: 10.1210/jc.2002-021314]
34 **Nasseri F**, Eftekhari F. Clinical and radiologic review of the normal and abnormal thymus: Pearls and pitfalls. *Radiographics* 2010; **30**: 413-428 [PMID: 20228326 DOI: 10.1148/rg.302095131]
35 **Nishino M**, Ashiku SK, Kocher ON, Thurer RL, Boiselle PM, Hatabu H. The Thymus: A Comprehensive Review-Erratum. *Radiographics* 2017; **37**: 1004 [PMID: 28493794 DOI: 10.1148/rg.2017174002]
36 **Ried M**, Marx A, Götz A, Hamer O, Schalke B, Hofmann HS. State of the art: Diagnostic tools and innovative therapies for treatment of advanced thymoma and thymic carcinoma. *Eur J Cardiothorac Surg* 2016; **49**: 1545-1552 [PMID: 26670806 DOI: 10.1093/ejcts/ezv426]
37 **Duwe BV**, Sterman DH, Musani AI. Tumors of the mediastinum. *Chest* 2005; **128**: 2893-2909 [PMID: 16236967 DOI: 10.1378/chest.128.4.2893]
38 **Jemal A**, Siegel R, Ward E, Murray T, Xu J, Thun MJ. Cancer statistics, 2007. *CA Cancer J Clin* 2007; **57**: 43-66 [PMID: 17237035 DOI: 10.3322/canjclin.57.1.43]
39 **Siegel R**, Ward E, Brawley O, Jemal A. Cancer statistics, 2011: The impact of eliminating socioeconomic and racial disparities on premature cancer deaths. *CA Cancer J Clin* 2011; **61**: 212-236 [PMID: 21685461 DOI: 10.3322/caac.20121]
40 **Barrington SF**, Mikhaeel NG, Kostakoglu L, Meignan M, Hutchings M, Müeller SP, Schwartz LH, Zucca E, Fisher RI, Trotman J, Hoekstra OS, Hicks RJ, O'Doherty MJ, Hustinx R, Biggi A, Cheson BD. Role of imaging in the staging and response assessment of lymphoma: Consensus of the International Conference on Malignant Lymphomas Imaging Working Group. *J Clin Oncol* 2014; **32**: 3048-3058 [PMID: 25113771 DOI: 10.1200/JCO.2013.53.5229]
41 **Kulkarni NM**, Pinho DF, Narayanan S, Kambadakone AR, Abramson JS, Sahani DV. Imaging for Oncologic Response Assessment in Lymphoma. *AJR Am J Roentgenol* 2017; **208**: 18-31 [PMID: 27786547 DOI: 10.2214/AJR.16.16180]
42 **Younes A**, Hilden P, Coiffier B, Hagenbeek A, Salles G, Wilson W, Seymour JF, Kelly K, Gribben J,

Pfreunschuh M, Morschhauser F, Schoder H, Zelenetz AD, Rademaker J, Advani R, Valente N, Fortpied C, Witzig TE, Sehn LH, Engert A, Fisher RI, Zinzani PL, Federico M, Hutchings M, Bollard C, Trneny M, Elsayed YA, Tobinai K, Abramson JS, Fowler N, Goy A, Smith M, Ansell S, Kuruvilla J, Dreyling M, Thieblemont C, Little RF, Aurer I, Van Oers MHJ, Takeshita K, Gopal A, Rule S, de Vos S, Kloos I, Kaminski MS, Meignan M, Schwartz LH, Leonard JP, Schuster SJ, Seshan VE. International Working Group consensus response evaluation criteria in lymphoma (RECIL 2017). *Ann Oncol* 2017; **28**: 1436-1447 [PMID: 28379322 DOI: 10.1093/annonc/mdx097]

43 **Koşucu P**, Tekinbaş C, Erol M, Sari A, Kavgaci H, Oztuna F, Ersöz S. Mediastinal lymph nodes: Assessment with diffusion-weighted MR imaging. *J Magn Reson Imaging* 2009; **30**: 292-297 [PMID: 19629990 DOI: 10.1002/jmri.21850]

44 **Mosavi F**, Wassberg C, Selling J, Molin D, Ahlström H. Whole-body diffusion-weighted MRI and (18)F-FDG PET/CT can discriminate between different lymphoma subtypes. *Clin Radiol* 2015; **70**: 1229-1236 [PMID: 26208992 DOI: 10.1016/j.crad.2015.06.087]

45 **Rosado-de-Christenson ML**, Templeton PA, Moran CA. From the archives of the AFIP. Mediastinal germ cell tumors: Radiologic and pathologic correlation. *Radiographics* 1992; **12**: 1013-1030 [PMID: 1326777 DOI: 10.1148/radiographics.12.5.1326777]

46 **Molinari F**, Bankier AA, Eisenberg RL. Fat-containing lesions in adult thoracic imaging. *AJR Am J Roentgenol* 2011; **197**: W795-W813 [PMID: 22021525 DOI: 10.2214/AJR.11.6932]

47 **Carter BW**, Okumura M, Detterbeck FC, Marom EM. Approaching the patient with an anterior mediastinal mass: A guide for radiologists. *J Thorac Oncol* 2014; **9**: S110-S118 [PMID: 25396307 DOI: 10.1097/JTO.0000000000000295]

48 **Strollo DC**, Rosado-de-Christenson ML. Primary mediastinal malignant germ cell neoplasms: Imaging features. *Chest Surg Clin N Am* 2002; **12**: 645-658 [PMID: 12471868 DOI: 10.1016/S1052-3359(02)00026-1]

49 **Lemarié E**, Assouline PS, Diot P, Regnard JF, Levasseur P, Droz JP, Ruffié P. Primary mediastinal germ cell tumors. Results of a French retrospective study. *Chest* 1992; **102**: 1477-1483 [PMID: 1330448 DOI: 10.1378/chest.102.5.1477]

50 **Economou JS**, Trump DL, Holmes EC, Eggleston JE. Management of primary germ cell tumors of the mediastinum. *J Thorac Cardiovasc Surg* 1982; **83**: 643-649 [PMID: 7200560]

51 **Kesler KA**, Rieger KM, Ganjoo KN, Sharma M, Fineberg NS, Einhorn LH, Brown JW. Primary mediastinal nonseminomatous germ cell tumors: The influence of postchemotherapy pathology on long-term survival after surgery. *J Thorac Cardiovasc Surg* 1999; **118**: 692-700 [PMID: 10504636 DOI: 10.1016/S0022-5223(99)70015-2]

52 **Wright CD**, Kesler KA, Nichols CR, Mahomed Y, Einhorn LH, Miller ME, Brown JW. Primary mediastinal nonseminomatous germ cell tumors. Results of a multimodality approach. *J Thorac Cardiovasc Surg* 1990; **99**: 210-217 [PMID: 2153877 DOI: 10.1016/0022-4804(90)90209-K]

53 **Lee KS**, Im JG, Han CH, Han MC, Kim CW, Kim WS. Malignant primary germ cell tumors of the mediastinum: CT features. *AJR Am J Roentgenol* 1989; **153**: 947-951 [PMID: 2552783 DOI: 10.2214/ajr.153.5.947]

54 **Shi HF**, Feng Q, Qiang JW, Li RK, Wang L, Yu JP. Utility of diffusion-weighted imaging in differentiating malignant from benign thyroid nodules with magnetic resonance imaging and pathologic correlation. *J Comput Assist Tomogr* 2013; **37**: 505-510 [PMID: 23863524 DOI: 10.1097/RCT.0b013e31828d28f0]

55 **Schob S**, Voigt P, Bure L, Meyer HJ, Wickenhauser C, Behrmann C, Höhn A, Kachel P, Dralle H, Hoffmann KT, Surov A. Diffusion-Weighted Imaging Using a Readout-Segmented, Multishot EPI Sequence at 3 T Distinguishes between Morphologically Differentiated and Undifferentiated Subtypes of Thyroid Carcinoma-A Preliminary Study. *Transl Oncol* 2016; **9**: 403-410 [PMID: 27661405 DOI: 10.1016/j.tranon.2016.09.001]

56 **Juanpere S**, Cañete N, Ortuño P, Martínez S, Sanchez G, Bernado L. A diagnostic approach to the mediastinal masses. *Insights Imaging* 2013; **4**: 29-52 [PMID: 23225215 DOI: 10.1007/s13244-012-0201-0]

57 **Kukar M**, Platz TA, Schaffner TJ, Elmarzouky R, Groman A, Kumar S, Abdelhalim A, Cance WG. The use of modified four-dimensional computed tomography in patients with primary hyperparathyroidism: An argument for the abandonment of routine sestamibi single-positron emission computed tomography (SPECT). *Ann Surg Oncol* 2015; **22**: 139-145 [PMID: 25074663 DOI: 10.1245/s10434-014-3940-y]

58 **Rodgers SE**, Hunter GJ, Hamberg LM, Schellingerhout D, Doherty DB, Ayers GD, Shapiro SE, Edeiken BS, Truong MT, Evans DB, Lee JE, Perrier ND. Improved preoperative planning for directed parathyroidectomy with 4-dimensional computed tomography. *Surgery* 2006; **140**: 932-40; discussion 940-1 [PMID: 17188140 DOI: 10.1016/j.surg.2006.07.028]

59 **Matoba M**, Tonami H, Kondou T, Yokota H, Higashi K, Toga H, Sakuma T. Lung carcinoma: Diffusion-weighted mr imaging--preliminary evaluation with apparent diffusion coefficient. *Radiology* 2007; **243**: 570-577 [PMID: 17400757 DOI: 10.1148/radiol.2432060131]

60 **Koyama H**, Ohno Y, Seki S, Nishio M, Yoshikawa T, Matsumoto S, Maniwa Y, Itoh T, Nishimura Y, Sugimura K. Value of diffusion-weighted MR imaging using various parameters for assessment and characterization of solitary pulmonary nodules. *Eur J Radiol* 2015; **84**: 509-515 [PMID: 25554007 DOI: 10.1016/j.ejrad.2014.11.024]

61 **Gümüştaş S**, Inan N, Akansel G, Ciftçi E, Demirci A, Ozkara SK. Differentiation of malignant and benign lung lesions with diffusion-weighted MR imaging. *Radiol Oncol* 2012; **46**: 106-113 [PMID: 23077446 DOI: 10.2478/v10019-012-0021-3]

62 **Liu H**, Liu Y, Yu T, Ye N. Usefulness of diffusion-weighted MR imaging in the evaluation of pulmonary lesions. *Eur Radiol* 2010; **20**: 807-815 [PMID: 19862533 DOI: 10.1007/s00330-009-1629-6]

63 **Coolen J**, Vansteenkiste J, De Keyzer F, Decaluwé H, De Wever W, Deroose C, Dooms C, Verbeken E, De Leyn P, Vandecaveye V, Van Raemdonck D, Nackaerts K, Dymarkowski S, Verschakelen J. Characterisation of solitary pulmonary lesions combining visual perfusion and quantitative diffusion MR imaging. *Eur Radiol* 2014; **24**: 531-541 [PMID: 24173597 DOI: 10.1007/s00330-013-3053-1]

64 **Schaefer JF**, Vollmar J, Schick F, Vonthein R, Seemann MD, Aebert H, Dierkesmann R, Friedel G, Claussen CD. Solitary pulmonary nodules: Dynamic contrast-enhanced MR imaging--perfusion differences in malignant and benign lesions. *Radiology* 2004; **232**: 544-553 [PMID: 15215548 DOI: 10.1148/radiol.2322030515]

65 **Donmez FY**, Yekeler E, Saeidi V, Tunaci A, Tunaci M, Acunas G. Dynamic contrast enhancement patterns of solitary pulmonary nodules on 3D gradient-recalled echo MRI. *AJR Am J Roentgenol* 2007;

189: 1380-1386 [PMID: 18029874 DOI: 10.2214/AJR.07.2429]
66 **Kono R**, Fujimoto K, Terasaki H, Müller NL, Kato S, Sadohara J, Hayabuchi N, Takamori S. Dynamic MRI of solitary pulmonary nodules: Comparison of enhancement patterns of malignant and benign small peripheral lung lesions. *AJR Am J Roentgenol* 2007; **188**: 26-36 [PMID: 17179342 DOI: 10.2214/AJR.05.1446]
67 **Chhabra A**, Thakkar RS, Andreisek G, Chalian M, Belzberg AJ, Blakeley J, Hoke A, Thawait GK, Eng J, Carrino JA. Anatomic MR imaging and functional diffusion tensor imaging of peripheral nerve tumors and tumorlike conditions. *AJNR Am J Neuroradiol* 2013; **34**: 802-807 [PMID: 23124644 DOI: 10.3174/ajnr.A3316]
68 **Nomori H**, Mori T, Ikeda K, Kawanaka K, Shiraishi S, Katahira K, Yamashita Y. Diffusion-weighted magnetic resonance imaging can be used in place of positron emission tomography for N staging of non-small cell lung cancer with fewer false-positive results. *J Thorac Cardiovasc Surg* 2008; **135**: 816-822 [PMID: 18374761 DOI: 10.1016/j.jtcvs.2007.10.035]
69 **van Rossum PS**, van Lier AL, Lips IM, Meijer GJ, Reerink O, van Vulpen M, Lam MG, van Hillegersberg R, Ruurda JP. Imaging of oesophageal cancer with FDG-PET/CT and MRI. *Clin Radiol* 2015; **70**: 81-95 [PMID: 25172205 DOI: 10.1016/j.crad.2014.07.017]
70 **Sakurada A**, Takahara T, Kwee TC, Yamashita T, Nasu S, Horie T, Van Cauteren M, Imai Y. Diagnostic performance of diffusion-weighted magnetic resonance imaging in esophageal cancer. *Eur Radiol* 2009; **19**: 1461-1469 [PMID: 19172278 DOI: 10.1007/s00330-008-1291-4]
71 **Takenaka D**, Ohno Y, Matsumoto K, Aoyama N, Onishi Y, Koyama H, Nogami M, Yoshikawa T, Matsumoto S, Sugimura K. Detection of bone metastases in non-small cell lung cancer patients: Comparison of whole-body diffusion-weighted imaging (DWI), whole-body MR imaging without and with DWI, whole-body FDG-PET/CT, and bone scintigraphy. *J Magn Reson Imaging* 2009; **30**: 298-308 [PMID: 19629984 DOI: 10.1002/jmri.21858]
72 **Ohno Y**, Koyama H, Onishi Y, Takenaka D, Nogami M, Yoshikawa T, Matsumoto S, Kotani Y, Sugimura K. Non-small cell lung cancer: Whole-body MR examination for M-stage assessment--utility for whole-body diffusion-weighted imaging compared with integrated FDG PET/CT. *Radiology* 2008; **248**: 643-654 [PMID: 18539889 DOI: 10.1148/radiol.2482072039]
73 **Yi CA**, Shin KM, Lee KS, Kim BT, Kim H, Kwon OJ, Choi JY, Chung MJ. Non-small cell lung cancer staging: Efficacy comparison of integrated PET/CT versus 3.0-T whole-body MR imaging. *Radiology* 2008; **248**: 632-642 [PMID: 18552311 DOI: 10.1148/radiol.2482071822]
74 **Yabuuchi H**, Hatakenaka M, Takayama K, Matsuo Y, Sunami S, Kamitani T, Jinnouchi M, Sakai S, Nakanishi Y, Honda H. Non-small cell lung cancer: Detection of early response to chemotherapy by using contrast-enhanced dynamic and diffusion-weighted MR imaging. *Radiology* 2011; **261**: 598-604 [PMID: 21852569 DOI: 10.1148/radiol.11101503]
75 **Ohno Y**, Koyama H, Yoshikawa T, Matsumoto K, Aoyama N, Onishi Y, Sugimura K. Diffusion-weighted MRI versus 18F-FDG PET/CT: Performance as predictors of tumor treatment response and patient survival in patients with non-small cell lung cancer receiving chemoradiotherapy. *AJR Am J Roentgenol* 2012; **198**: 75-82 [PMID: 22194481 DOI: 10.2214/AJR.11.6525]
76 **van Rossum PS**, van Lier AL, van Vulpen M, Reerink O, Lagendijk JJ, Lin SH, van Hillegersberg R, Ruurda JP, Meijer GJ, Lips IM. Diffusion-weighted magnetic resonance imaging for the prediction of pathologic response to neoadjuvant chemoradiotherapy in esophageal cancer. *Radiother Oncol* 2015; **115**: 163-170 [PMID: 26002307 DOI: 10.1016/j.radonc.2015.04.027]
77 **Wang L**, Liu L, Han C, Liu S, Tian H, Li Z, Ren X, Shi G, Wang Q, Wang G. The diffusion-weighted magnetic resonance imaging (DWI) predicts the early response of esophageal squamous cell carcinoma to concurrent chemoradiotherapy. *Radiother Oncol* 2016; **121**: 246-251 [PMID: 27838148 DOI: 10.1016/j.radonc.2016.10.021]
78 **Giganti F**, Salerno A, Ambrosi A, Chiari D, Orsenigo E, Esposito A, Albarello L, Mazza E, Staudacher C, Del Maschio A, De Cobelli F. Prognostic utility of diffusion-weighted MRI in oesophageal cancer: Is apparent diffusion coefficient a potential marker of tumour aggressiveness? *Radiol Med* 2016; **121**: 173-180 [PMID: 26392393 DOI: 10.1007/s11547-015-0585-2]

World Journal of Radiology

Submit a Manuscript: https://www.f6publishing.com

World J Radiol 2019 March 28; 11(3): 46-54

DOI: 10.4329/wjr.v11.i3.46

ISSN 1949-8470 (online)

MINIREVIEWS

Progress in image-guided radiotherapy for the treatment of non-small cell lung cancer

Xiao-Cang Ren, Yue-E Liu, Jing Li, Qiang Lin

ORCID number: Xiao-Cang Ren (0000-0001-5632-1434); Yue-E Liu (0000-0002-4222-2061); Jing Li (0000-0003-1724-3490); Qiang Lin (0000-0001-9599-4121).

Author contributions: Ren XC wrote the manuscript; Liu YE and Li J contributed to the writing of the manuscript; Lin Q designed the editorial and wrote the manuscript.

Conflict-of-interest statement: There is no conflict of interest associated with any of the senior author or other coauthors contributed their efforts in this manuscript.

Manuscript source: Invited manuscript

Received: October 29, 2018
Peer-review started: October 29, 2018
First decision: November 29, 2018
Revised: January 27, 2019
Accepted: February 27, 2019
Article in press: March 28, 2019

Xiao-Cang Ren, Yue-E Liu, Jing Li, Qiang Lin, Department of Oncology, North China Petroleum Bureau General Hospital, Hebei Medical University, Renqiu 062552, Hebei Province, China

Corresponding author: Qiang Lin, MD, PhD, Professor, Department of Oncology, North China Petroleum Bureau General Hospital, Hebei Medical University, 8 Huizhan Avenue, Renqiu 062552, Hebei Province, China. zyy_lq@petrochina.com.cn
Telephone: +86-317-2721951
Fax: +86-317-2722381

Abstract

Lung cancer is one of the most common malignant tumors. It has the highest incidence and mortality rate of all cancers worldwide. Late diagnosis of non-small cell lung cancer (NSCLC) is very common in clinical practice, and most patients miss the chance for radical surgery. Thus, radiotherapy plays an indispensable role in the treatment of NSCLC. Radiotherapy technology has evolved from the classic two-dimensional approach to three-dimensional conformal and intensity-modulated radiotherapy. However, how to ensure delivery of an accurate dose to the tumor while minimizing the irradiation of normal tissues remains a huge challenge for radiation oncologists, especially due to the positioning error between fractions and the autonomous movement of organs. In recent years, image-guided radiotherapy (IGRT) has greatly increased the accuracy of tumor irradiation while reducing the irradiation dose delivered to healthy tissues and organs. This paper presents a brief review of the definition of IGRT and the various technologies and applications of IGRT. IGRT can help ensure accurate dosing of the target area and reduce radiation damage to the surrounding normal tissue. IGRT may increase the local control rate of tumors and reduce the incidence of radio-therapeutic complications.

Key words: Non-small cell lung cancer; Radiotherapy; Image-guided radiotherapy; Intensity-modulated radiotherapy; Positioning error

Core tip: Lung cancer is one of the most common malignant tumors. Radiotherapy plays an indispensable role in the treatment of non-small cell lung cancer. How to ensure delivery of an accurate dose to the tumor while minimizing the irradiation of normal tissues remains a huge challenge. In this brief review, we summarize the methods of radiotherapy technology, especially for the image-guided radiotherapy (IGRT). We believe that IGRT can help ensure accurate dosing of the target area and reduce radiation

Published online: March 28, 2019

P-Reviewer: Bazeed MF, Engin G, Liang Y, Neninger E, Peitsidis P
S-Editor: Ji FF
L-Editor: A
E-Editor: Wu YXJ

damage to the surrounding normal tissue.

Citation: Ren XC, Liu YE, Li J, Lin Q. Progress in image-guided radiotherapy for the treatment of non-small cell lung cancer. *World J Radiology* 2019; 11(3): 46-54
URL: https://www.wjgnet.com/1949-8470/full/v11/i3/46.htm
DOI: https://dx.doi.org/10.4329/wjr.v11.i3.46

INTRODUCTION

Lung cancer is one of the most common malignant tumors, and it ranks first in both incidence and mortality worldwide. Non-small cell lung cancer (NSCLC) accounts for 80%-85% of all lung cancers[1]. Late diagnosis of NSCLC is very common in clinical practice, and most patients miss the chance for radical surgery. Thus, radiotherapy is one of major treatment modalities for NSCLC[1]. In recent years, continuous advancements in image-guided radiotherapy (IGRT) technology have enabled more accurate positioning and precise radiotherapy. IGRT can decrease errors during treatment, increase the local radiation dose, and reduce the dose of radiation delivered to the normal surrounding tissue to optimize the local tumor control rate and significantly improve patient quality of life[2,3]. This paper presents a brief review of the technical developments and application of IGRT in recent years.

STATUS OF RADIOTHERAPY

Lung cancer has increased globally in both incidence and mortality. It ranks first among malignant tumors in both incidence and mortality worldwide and is a threat to human health. NSCLC account for 80%-85% of all lung cancers, and early diagnosis is limited. Approximately 85% of patients are in advanced stages at the time of diagnosis. The efficacy of surgical treatment is not ideal, and the 5-year survival rate is only about 16%[4]. According to statistics radiotherapy was widely utilized as high as 55% in all new cancer cases[5]. In traditional two-dimensional radiotherapy, an oncologist must control the treatment based on his experience because the imaging diagnosis and positioning system operate on a two-dimensional plane. Irradiating a large area can easily destroy normal cells around the tumor but not the tumor itself. Therefore, the treatment efficacy is poor, with obvious side effects and many complications[6]. The ideal radiotherapy technique is to deliver a lethal dose to the target area according to the shape of the tumor without irradiating the normal tissue around the target area. In 1959, Dr. Takahashi from Japan first proposed and outlined the concept of conformal radiation therapy. The development and application of technologies such as computed tomography (CT), magnetic resonance imaging, three-dimensional treatment planning systems and multi-leaf collimators have made three-dimensional conformal radiotherapy possible and facilitated the transition from the 2-dimensional era to the 3-dimensional era. In recent years, many new technologies and new methods for improving the accuracy of treatment have been developed. Technologies such as three-dimensional conformal radiation therapy (3DCRT) and intensity-modulated radiation therapy (IMRT) have solved the problem of dose conformation in stationary target areas. However, the position and shape of the tumor and the positional relationship between the tumor and its surrounding organs can change over the course of treatment. The proactive treatment method uses a certain technique to detect the positioning error and/or movement of the target area and to improve the delivery of radiation to the tumor while correcting the error to better protect the surrounding normal tissues. Methods to ensure and control the quality of radiation therapy are still under active investigation.

DEFINITION OF IGRT

Compared to traditional radiotherapy, IGRT enhances the biological effects of radiotherapy and is considered an extension of 3DCRT and IMRT. It integrates respiratory movement over time during treatment and positioning error between fractions. It is the most advanced four-dimensional radiotherapy technology in the field of tumor treatment, featuring accurate positioning, plan design and control of

the accelerators. IGRT can correct the patient's positioning error, aid in planning subsequent radiotherapy, guide real-time beam irradiation, and collect images and/or other signals during treatment in order to ensure the accuracy of radiation delivery. The collected images and/or signals are used to guide and deliver the dose of radiation to the target area and ultimately improve the rate of local control rate and long-term survival in patients with advanced NSCLC[7-9]. IGRT technology can correct the error between the lesions and the markers and modify the changes in the radiation dose between the tumor and normal tissues. It can reasonably adjust the dose to protect normal tissue while reducing the safe marginal region and increasing dose delivery to the tumor area[10]. IGRT can be achieved using the following technologies: online correction, adaptive radiotherapy, breath-holding and respiratory gating control, four-dimensional radiotherapy and real-time tracking technology[11].

IMPLEMENTATION OF IGRT IN NSCLC RADIOTHERAPY

Online correction technology

During the course of fractional treatments, two-dimensional or three-dimensional images of the patient are acquired and compared to the planned image (preplaced markers) after positioning to determine the positioning error or the error of the radiation field, which are corrected immediately to obtain the appropriate position of the target area. The optimal radiation dose can then be delivered. In recent years, online correction has evolved from earlier film to current electro phoretic image display technology, which increases the degree of automation and shortens the additional treatment time. Moreover, the X-ray source for imaging has evolved from MV imaging to KV-MV combination imaging or KV imaging alone, and the technology for the calibration image has also evolved from two-dimensional to three-dimensional imaging such as spiral CT or cone beam CT (CBCT)[10,11].

Adaptive radiotherapy

Due to individual differences, the actual appropriate width of the marginal region around the target areas different for each patient. Therefore, it is necessary to set an individualized width of the marginal region according to the individual's positioning error and organ movement data and then to adjust the margins of the planned target volume (PTV) and the clinical target volume. The plan and mode of adaptive radiation therapy can be modified using a systematic feedback of measurements during treatment[12,13].

CBCT-guided adaptive radiotherapy: Conventional radiotherapy plans are designed based on CT images obtained before radiotherapy. However, changes in the patient's body mass index, tumor deformation, and movement of the surrounding organs can cause displacement of the target and consequent deformation[14]. CBCT-guided adaptive radiotherapy is a new extension of IGRT technology that allows for feedback of the target tumor volume and position changes during treatment to analyze the difference between the original plan and the treatment and to obtain real-time anatomical images in order to re-design the treatment plan. This technique can ensure appropriate dose delivery to the target area and reduce unnecessary irradiation of normal tissue, thus minimizing the side effects of radiotherapy[15,16]. A study by Zhao *et al*[17] described how to delineate the target area using the anatomical images collected by CBCT and how to form an outline of the new target area using deformation registration software. Under the guidance of CBCT, the treatment plan can be re-optimized. CBCT also allows for updated calculations of the actual dose accumulation in the target area and surrounding organs and an accurate final determination of the radiation dose for further treatments in order to reduce damage to normal tissues and increase dose delivery to the target area. Buckley *et al*[18] proposed CBCT-guided helical tomotherapy (HT) as a replacement for IMRT to achieve adaptive contour delineation, planning, and fractional dose accumulation. Currently, studies of CBCT-guided radiotherapy for NSCLC mainly focus on respiratory movement and shrinkage of the target area. Interference of respiratory movement can be improved by techniques such as respiratory gating, real-time tracking and 4D-CT, while the effect of target shrinkage can be effectively addressed by the timely modification of radiotherapy plans[19]. Adaptive radiotherapy technology based on CBCT image guidance could be comparable to adaptive HT with further optimization of the time required for adaptive radiotherapy planning. De *et al*[20] reported that HT and IGRT are effective and safe treatment modalities for anal cancer and are considered standard of care for these conditions in our department. A study by Elsayad *et al*[17] demonstrated 83% tumor regression and 13% progression in patients with small cell lung cancer (13 patients) or NSCLC (59 patients) undergoing

fractional CBCT-guided radiation. Moreover, the decrease in gross tumor volume was associated with the number of CBCT scans (r = 0.313, P = 0.046) and the time of chemotherapy administration (r = 0.385, P = 0.013). Weekly CBCT to monitor changes in the tumor offers the advantage of adaptive treatment for patients with lung cancer.

Breath-holding and respiratory gating technology

If the target area is affected by respiratory movement, breath-holding can temporarily eliminate such movement, allowing for a small marginal region. Before treatment, the patient should perform appropriate breathing exercises to increase the duration of breath-holding during treatment and to reduce the volume of lung radiation exposure[21,22]. Active respiratory gating technology and deep inspiration breath hold techniques are the two options available to minimize the influence of respiratory movement. Respiratory gating is a technique that collects images from different respiratory phases in NSCLC patients and reconstructs images by using four-dimensional computed tomography (4D-CT). It can be used to calculate and reconstruct doses at different respiratory phases to better eliminate movement artifacts, adjust the radiation plan, and monitor the effects of the patient's respiratory movement on the organ and target tumor area during treatment. Ultimately, this technique allows for control of the intensity of the radiation beam to the linear accelerator and matches the specific phase of the respiratory cycle of NSCLC patients with the controlled radiation beam[23-25]. Respiratory gating technology can reduce the influence of respiratory movement on radiotherapy. For instance, patients with stage I to II lung cancer who are affected by respiratory movements and patients with sub-phrenic tumors are better suited to respiratory gating technology with hypo-fractionated radiation therapy.

During radiotherapy, respiratory and organ movement in NSCLC patients causes movement of the tumor target area and displacement of the tumor's position in the lung, resulting in differences in anatomical position between the planned design and actual treatment. Moreover, changes in the volume and density of the lung tissue result in beam penumbra changes in the field and a lower dose of radiation delivery to the tumor target in lung tissue. Therefore, during IGLFRT, in addition to expansion of the radiation target area, assisted respiratory gating technology can help reduce the scope of treatment while increasing dose delivery to the tumor target area. This can effectively avert the possibility of mistargeted dose delivery and the consequent excessive exposure of normal tissue to radiation due to individual differences in respiratory movement[26].

Radiotherapy techniques accounting for time

Three-dimensional radiotherapy technology can be further enhanced by accounting for time using a technique that accounts for changes in anatomical structure during imaging positioning, planning, and therapeutic implementation. Three key factors must be taken into consideration: four-dimensional image localization (collecting the time sequence of four-dimensional images throughout all phases in one respiratory cycle), four-dimensional plan design (determination of time-marked field parameters from four-dimensional image data), and four-dimensional treatment implementation (monitoring of the patient's breathing using the same respiratory monitoring device used in the four-dimensional imaging system)[27,28].

Personalized delineation of the target range based on 4D-CT: During the course of routine spiral CT scanning, movement artifacts can cause up to 90% volumetric deviation in the 3D reconstruction of the target area. Therefore, it is very important to individualize the target range of movement in NSCLC patients[29]. The development of 4D-CT technology not only effectively eliminates movement artifacts to accurately and reliably reproduce the target area receiving radiotherapy but also can reflect the dynamic characteristics of radiotherapy in the target area with respect to respiratory movements and perform precise, individualized delineation of the target area[30]. 4D-CT takes advantage of three-dimensional reconstruction technology and integrates a time factor during image positioning, planning and treatment implementation stages. It also incorporates changes in anatomical structure over time, individualized target volume (ITV) changes and respiratory cycle. A study by Tan *et al*[31] has shown that 4D-CBCT is superior to 3D-CBCT in image guidance in small lung tumors because 4D-CBCT can reduce the uncertainty of the tumor location caused by internal respiratory movement, thereby increasing the accuracy of image guidance. Ehrbar *et al*[32] used 4D-CT to delineate ITV and design a radiotherapy plan for patients with lung cancer. Their results show that ITV ensured tumor coverage but that the lung tissue was exposed to higher doses of radiation. Significantly reduced ITV can improve tumor control while protecting normal tissues. In addition, Jurkovic *et al*[33] used the average intensity projection and maximum intensity projection techniques to

quickly and accurately delineate ITV. These techniques can significantly reduce the physical effort involved in target delineation. ITV delineation based on 4D-CT can increase the target dose and reduce the marginal region, thus reducing the radiation dose delivered to normal lung tissue.

Real-time tracking with stereotactic body radiotherapy

Because human respiratory movement is not strictly identical between two consecutive cycles, and treatment time is often longer than the image positioning time, especially when using hypofractional techniques (such as stereotactic radiotherapy), involuntary movements cannot be predicted. Real-time X-ray tracking treatment techniques have been developed to address this problem.

Image-guided hypofractionated stereotactic radiotherapy after accurate positioning in NSCLC patients can deliver large doses to the tumor target area, whereas the dose of radiation delivered to surrounding normal lung tissue is decreased[7,34]. The tumor control rate of conventional radiotherapy is low in some patients with early NSCLC who are not candidates for surgical treatment. IGRT treatment can reduce the uncertainty of the positioning error and the movement of the target area, thereby reducing the irradiation volume, which can allow for increased daily treatment doses, shortened treatment time, and improved local control[35]. For patients undergoing hypofractionated stereotactic radiotherapy, during the course of treatment, image guidance techniques are used to correct positioning errors and to monitor changes in tumor volume and location, thus ensuring coverage of the target area and reducing the dose absorbed by surrounding tissues[36,37]. A study by Ehrbar *et al*[32] showed that the control rate and overall survival of patients undergoing hypofractionated stereotactic treatment are superior to those of patients receiving conventional radiotherapy. Moreover, side effects were less common with hypofractionated radiotherapy. Verma *et al*[38] evaluated 92 patients from 12 institutions and found from their multi-institutional study that the toxicity of stereotactic body radiotherapy (SBRT) in patients with NSCLC tumors ≥ 5 cm was acceptable. Daily treatment are associated with a high toxicity rate. Vivek *et al*[39] reported that the 1- and 2-year actuarial local control rates in patients with NSCLC tumors ≥ 5 cm were 95.7% and 73.2%, respectively, and the 1-year and 2-year disease-free survival rates were 72.1% and 53.5%, respectively; the 1- and 2-year disease-specific survival rates were 95.5% and 78.6%, respectively. Their study indicates that SBRT is a safe and effective treatment when combined with IGRT technology (Figure 1 and Table 1).

CONCLUSION

In summary, image-guided hypofractionated radiotherapy has several advantages in the treatment of NSCLC. Functional imaging allows for the differentiation of normal tissue from tumor tissue. By ensuring radiotherapy accuracy and appropriate dosing, these technologies can lower the radiation dose delivered to normal surrounding tissue while improving the local tumor control rate of the tumor and reducing the chance of radiation complications. This results in improved the quality of life of patients after treatment. Treatment that is based on advanced image guidance technology and computer-assisted adaptive radiotherapy is likely to become the most common approach for NSCLC radiotherapy in the future.

Table 1 Summary of important data of advantage of image-guided radiotherapy in radiotherapy

Ref.	Published date	Authors	Highlights of detailed data
[21]	2003	Remouchamps *et al*	The use of mDIBH reduced the mean percentage of both lungs receiving more than 20 Gy from 20.4% to 15.2% ($P < 0.00007$)
[22]	2015	Muralidhar *et al*	The mean difference of right lung volume receiving more than 20 Gy of the dose was from 1% to -98 % (IGRT < 0.24556)
[26]	2003	Hof *et al*	In the craniocaudal direction the mean tumor movement was 5.1 mm , in the ventrodorsal direction 3.1 mm, and in the lateraldirection 2.6 mm
[31]	2017	Tan *et al*	The errors of image-guided registration using 4D-CBCT and 3D-CBCT on the X, Y, Z axes, and 3D space were 0.80 ± 0.21 mm and 1.08 ± 0.25 mm, 2.02 ± 0.46 mm and 3.30 ± 0.53 mm, 0.52 ± 0.16 mm and 0.85 ± 0.24 mm, and 2.25 ± 0.44 mm and 3.59 ± 0.48 mm (all $P < 0.001$), respectively
[32]	2017	Ehrbar *et al*	Compared with the 4D dose calculations, the mid-ventilation and single-phase tracking overestimated the target mean dose (2.3% and 1.3%), respectively
[34]	2016	Garibaldi	The PTV margins used to compensate for residual tumor localization errors were 3.1, 3.5 and 3.3 mm in the LR, SI and AP directions, respectively
[7]	2016	Wang *et al*	Position errors after correction in Left–right, Anterior–posterior and Cranial–caudal were 0.22 cm, 0.16 cm and 0.19 cm, respectively
[36]	2016	Ariyaratne *et al*	Under the use of IGRT, the population mean setup error was 0.01 cm (left–right), 0.05 cm (supero-inferior) and 0.13 cm (antero-posterior)

mDIBH: Moderate deep inspiration breath hold; IGRT: Image-guided radiotherapy; PTV: Planned target volume.

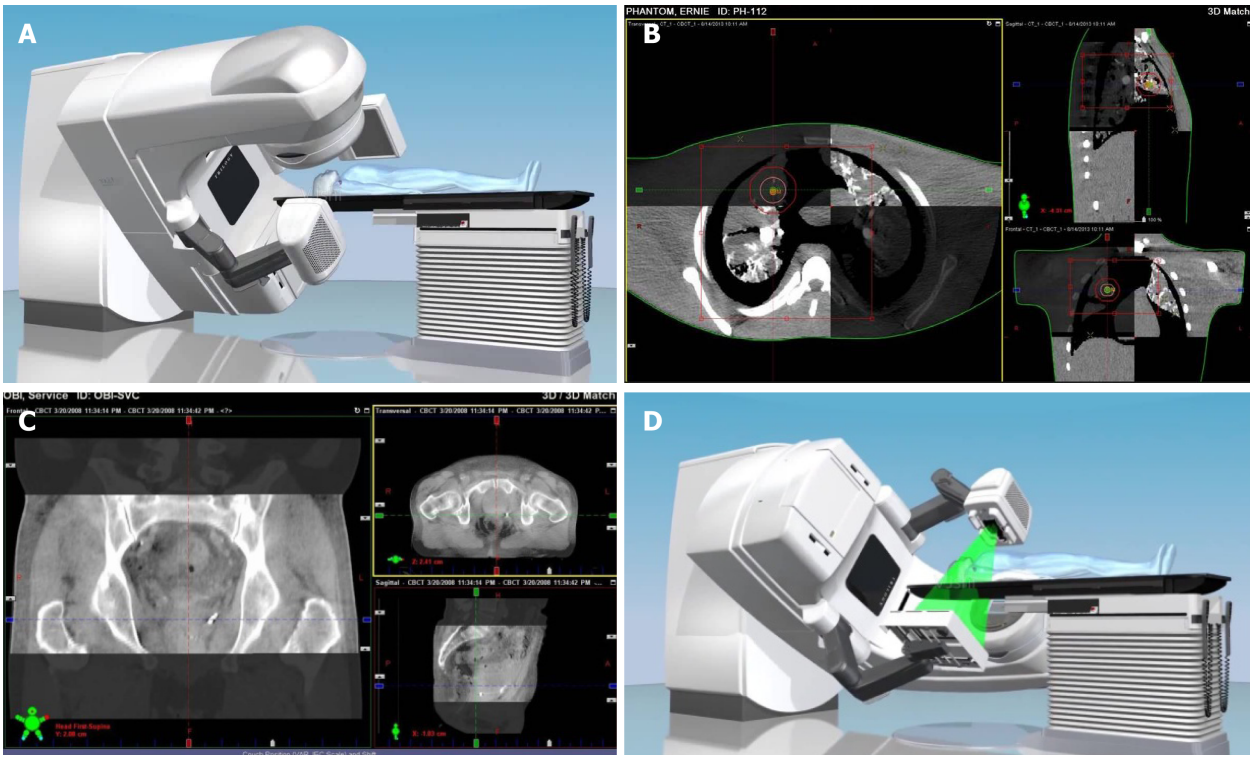

Figure 1 Images of computed tomography. A: The placement of cone beam computed tomography; B: Chest image fusion; C: Pelvic image fusion; D: Radiotherapy after correction with image-guided radiotherapy.

REFERENCES

1 **Glatzer M**, Elicin O, Ramella S, Nestle U, Putora PM. Radio(chemo)therapy in locally advanced nonsmall cell lung cancer. *Eur Respir Rev* 2016; **25**: 65-70 [PMID: 26929423 DOI: 10.1183/16000617.0053-2015]

2 **Holmes T**. *Image-Guided Radiotherapy (IGRT)*. In: Speer TW, Knowlton CA, Mackay MK. Encyclopedia of Radiation Oncology. Springer Berlin Heidelberg 2013; 364-364

3 **Vilotte F**, Antoine M, Bobin M, Latorzeff I, Supiot S, Richaud P, Thomas L, Leduc N, Guérif S, Iriondo-Alberdi J, de Crevoisier R, Sargos P. Post-Prostatectomy Image-Guided Radiotherapy: The Invisible Target Concept. *Front Oncol* 2017; **7**: 34 [PMID: 28337425 DOI: 10.3389/fonc.2017.00034]

4 **Siegel R**, Naishadham D, Jemal A. Cancer statistics, 2012. *CA Cancer J Clin* 2012; **62**: 10-29 [PMID: 22237781 DOI: 10.3322/caac.20138]

5 **Delaney G**, Jacob S, Featherstone C, Barton M. The role of radiotherapy in cancer treatment: estimating optimal utilization from a review of evidence-based clinical guidelines. *Cancer* 2005; **104**: 1129-1137 [PMID: 16080176 DOI: 10.1002/cncr.21324]

6 **Moon SH**, Cho KH, Lee CG, Keum KC, Kim YS, Wu HG, Kim JH, Ahn YC, Oh D, Lee JH. IMRT vs. 2D-radiotherapy or 3D-conformal radiotherapy of nasopharyngeal carcinoma: Survival outcome in a Korean multi-institutional retrospective study (KROG 11-06). *Strahlenther Onkol* 2016; **192**: 377-385 [PMID: 26972085 DOI: 10.1007/s00066-016-0959-y]

7 **Wang SW**, Ren J, Yan YL, Xue CF, Tan L, Ma XW. Effect of image-guided hypofractionated stereotactic radiotherapy on peripheral non-small-cell lung cancer. *Onco Targets Ther* 2016; **9**: 4993-5003 [PMID: 27574441 DOI: 10.2147/OTT.S101125]

8 **De Los Santos J**, Popple R, Agazaryan N, Bayouth JE, Bissonnette JP, Bucci MK, Dieterich S, Dong L, Forster KM, Indelicato D, Langen K, Lehmann J, Mayr N, Parsai I, Salter W, Tomblyn M, Yuh WT, Chetty IJ. Image guided radiation therapy (IGRT) technologies for radiation therapy localization and delivery. *Int J Radiat Oncol Biol Phys* 2013; **87**: 33-45 [PMID: 23664076 DOI: 10.1016/j.ijrobp.2013.02.021]

9 **Arcangeli S**, Falcinelli L, Bracci S, Greco A, Monaco A, Dognini J, Chiostrini C, Bellavita R, Aristei C, Donato V. Treatment outcomes and patterns of radiologic appearance after hypofractionated image-guided radiotherapy delivered with helical tomotherapy (HHT) for lung tumours. *Br J Radiol* 2017; **90**: 20160853 [PMID: 28256158 DOI: 10.1259/bjr.20160853]

10 **Mao W**, Speiser M, Medin P, Papiez L, Solberg T, Xing L. Initial application of a geometric QA tool for integrated MV and kV imaging systems on three image guided radiotherapy systems. *Med Phys* 2011; **38**: 2335-2341 [PMID: 21776767 DOI: 10.1118/1.3570768]

11 **Arns A**, Blessing M, Fleckenstein J, Stsepankou D, Boda-Heggemann J, Simeonova-Chergou A, Hesser J, Lohr F, Wenz F, Wertz H. Towards clinical implementation of ultrafast combined kV-MV CBCT for IGRT of lung cancer : Evaluation of registration accuracy based on phantom study. *Strahlenther Onkol* 2016; **192**: 312-321 [PMID: 26864049 DOI: 10.1007/s00066-016-0947-2]

12 **Wang ZQ**, Li RQ, Zhang Y. Progress in Research of Adaptive Radiation Therapy for Head and Neck Cancer. Zhongguo Aizheng Zazhi. 2016; 131-134 [DOI: 10.3969/j.issn.1007-3969.2014.12.012]

13 **Wang D**, Sha XY, Lin HL. Evaluations of set-up errors and target margins for super and middle part of esophageal carcinoma in image guided radiotherapy. *Zhongguo Fangshe Yixue Yu Fanghu Zazhi* 2014; **34**: 610-612 [DOI: 10.3760/cma.j.issn.0254-5098.2014.08.012]

14 **Li Q**, Kim J, Balagurunathan Y, Liu Y, Latifi K, Stringfield O, Garcia A, Moros EG, Dilling TJ, Schabath MB, Ye Z, Gillies RJ. Imaging features from pretreatment CT scans are associated with clinical outcomes in nonsmall-cell lung cancer patients treated with stereotactic body radiotherapy. *Med Phys* 2017; **44**: 4341-4349 [PMID: 28464316 DOI: 10.1002/mp.12309]

15 **Buckley JG**, Wilkinson D, Malaroda A, Metcalfe P. Investigation of the radiation dose from cone-beam CT for image-guided radiotherapy: A comparison of methodologies. *J Appl Clin Med Phys* 2018; **19**: 174-183 [PMID: 29265684 DOI: 10.1002/acm2.12239]

16 **Rotolo N**, Floridi C, Imperatori A, Fontana F, Ierardi AM, Mangini M, Arlant V, De Marchi G, Novario R, Dominioni L, Fugazzola C, Carrafiello G. Comparison of cone-beam CT-guided and CT fluoroscopy-guided transthoracic needle biopsy of lung nodules. *Eur Radiol* 2016; **26**: 381-389 [PMID: 26045345 DOI: 10.1007/s00330-015-3861-6]

17 **Elsayad K**, Kriz J, Reinartz G, Scobioala S, Ernst I, Haverkamp U, Eich HT. Cone-beam CT-guided radiotherapy in the management of lung cancer: Diagnostic and therapeutic value. *Strahlenther Onkol* 2016; **192**: 83-91 [PMID: 26630946 DOI: 10.1007/s00066-015-0927-y]

18 **Cui QL**, Sun Y, Zhong W, Chen YZ, Zhao YX. Meta-analysis of dosemetriccomparision between helical tomotherapy and intensity-modulated radiotherapy for early-stage postoperative breast cancer. *Cancer Res Clin* 2016; **28**: 828-832 [DOI: 10.3760/cma.j.issn.1006-9801.2016.12.009]

19 **Zhang SX**, Lin SQ. New progress in radiotherapy of NSCLC guided by multimodality medical imaging. *Oncology Progress* 2013; **11**: 520-524

20 **De Bari B**, Jumeau R, Bouchaab H, Vallet V, Matzinger O, Troussier I, Mirimanoff RO, Wagner AD, Hanhloser D, Bourhis J, Ozsahin EM. Efficacy and safety of helical tomotherapy with daily image guidance in anal canal cancer patients. *Acta Oncol* 2016; **55**: 767-773 [PMID: 27034083 DOI: 10.3109/0284186X.2015.1120886]

21 **Remouchamps VM**, Vicini FA, Sharpe MB, Kestin LL, Martinez AA, Wong JW. Significant reductions in heart and lung doses using deep inspiration breath hold with active breathing control and intensity-modulated radiation therapy for patients treated with locoregional breast irradiation. *Int J Radiat Oncol Biol Phys* 2003; **55**: 392-406 [PMID: 12527053 DOI: 10.1016/S0360-3016(02)04143-3]

22 **Muralidhar KR**, Sha RL, Rout BK, Murthy PN. Advantage of using deep inspiration breath hold with active breathing control and image-guided radiation therapy for patients treated with lung cancers. *Int J Cancer Ther Oncol* 2015; **3**: 1-7 [DOI: 10.14319/ijcto.0302.1]

23 **Chang Q**, Lin MZ, Wang XH. Advances in radiotherapy for non-small cell lung cancer guided by image. *Zhongliu Jichu Yu Linchuang* 2014; **27**: 183-184

24 **Jiang SB**, Wolfgang J, Mageras GS. Quality assurance challenges for motion-adaptive radiation therapy: gating, breath holding, and four-dimensional computed tomography. *Int J Radiat Oncol Biol Phys* 2008; **71**: S103-S107 [PMID: 18406905 DOI: 10.1016/j.ijrobp.2007.07.2386]

25 **Bernatowicz K**, Keall P, Mishra P, Knopf A, Lomax A, Kipritidis J. Quantifying the impact of respiratory-gated 4D CT acquisition on thoracic image quality: a digital phantom study. *Med Phys* 2015; **42**: 324-334 [PMID: 25563272 DOI: 10.1118/1.4903936]

26 **Hof H**, Herfarth KK, Münter M, Essig M, Wannenmacher M, Debus J. The use of the multislice CT for the determination of respiratory lung tumor movement in stereotactic single-dose irradiation. *Strahlenther Onkol* 2003; **179**: 542-547 [PMID: 14509953 DOI: 10.1007/s00066-003-1070-8]

27 **Moorees J**, Bezak E. Four dimensional CT imaging: a review of current technologies and modalities. *Australas Phys Eng Sci Med* 2012; **35**: 9-23 [PMID: 22302463 DOI: 10.1007/s13246-012-0124-6]

28 **Liu Q**, Li N, Sun B. Effect of 4D-CT reconstruction technique in accurate radiotherapy for hepatocellular carcinoma. *Weichang Bingxue He Ganbingxue Zazhi* 2016; **25**: 885-888

29 **Zhang SX**, Chen GJ, Zhou LH, Yang KC, Lin SQ. Influences of Motion Artifacts on Three-Dimensional Reconstruction Volume and Conformal Radiotherapy Planning. *Zhongguo Shengwu Yixue Gongcheng Xuebao* 2007; **16**: 123-130

30 **Lu XG**, Ohtani H. The research of respiratory movement induced hepatic tumor motion in radiotherapy by use of a cone-beam CT under the fluoroscopic mode. *Riben Weisheng Kexueyuan Yuanbao* 2017; **16**: 133-139 [DOI: 10.24531/jhsaiih.16.3_133]

31 **Tan Z**, Liu C, Zhou Y, Shen W. Preliminary comparison of the registration effect of 4D-CBCT and 3D-CBCT in image-guided radiotherapy of Stage IA non-small-cell lung cancer. *J Radiat Res* 2017; **58**: 854-861 [PMID: 28992047 DOI: 10.1093/jrr/rrx040]

32 **Ehrbar S**, Jöhl A, Tartas A, Stark LS, Riesterer O, Klöck S, Guckenberger M, Tanadini-Lang S. ITV, mid-ventilation, gating or couch tracking - A comparison of respiratory motion-management techniques based on 4D dose calculations. *Radiother Oncol* 2017; **124**: 80-88 [PMID: 28587761 DOI: 10.1016/j.radonc.2017.05.016]

33 **Jurkovic I**, Stathakis S, Li Y, Patel A, Vincent J, Papanikolaou N, Mavroidis P. SU-E-J-79: Internal Tumor Volume Motion and Volume Size Assessment Using 4D CT Lung Data. *Med Phys* 2014; **41** (6 Part 7): 173-173 [DOI: 10.1118/1.4888131]

34 **Garibaldi C**, Piperno G, Ferrari A, Surgo A, Muto M, Ronchi S, Bazani A, Pansini F, Cremonesi M, Jereczek-Fossa BA, Orecchia R. Translational and rotational localization errors in cone-beam CT based image-guided lung stereotactic radiotherapy. *Phys Med* 2016; **32**: 859-865 [PMID: 27289354 DOI: 10.1016/j.ejmp.2016.05.055]

35 **Nguyen NP**, Kratz S, Chi A, Vock J, Vos P, Shen W, Vincent VH, Ewell L, Jang S, Altdorfer G, Karlsson U, Godinez J, Woods W, Dutta S, Ampil F; International Geriatric Radiotherapy Group. Feasibility of image-guided radiotherapy and concurrent chemotherapy for locally advanced nonsmall cell lung cancer. *Cancer Invest* 2015; **33**: 53-60 [PMID: 25634242 DOI: 10.3109/07357907.2014.1001896]

36 **Ariyaratne H**, Chesham H, Pettingell J, Alonzi R. Image-guided radiotherapy for prostate cancer with cone beam CT: dosimetric effects of imaging frequency and PTV margin. *Radiother Oncol* 2016; **121**: 103-108 [PMID: 27576431 DOI: 10.1016/j.radonc.2016.07.018]

37 **Rudat V**, Nour A, Hammoud M, Alaradi A, Mohammed A. Image-guided intensity-modulated radiotherapy of prostate cancer: Analysis of interfractional errors and acute toxicity. *Strahlenther Onkol* 2016; **192**: 109-117 [PMID: 26545764 DOI: 10.1007/s00066-015-0919-y]

38 **Verma V**, Shostrom VK, Zhen W, Zhang M, Braunstein SE, Holland J, Hallemeier CL, Harkenrider MM, Iskhanian A, Jabbour SK, Attia A, Lee P, Wang K, Decker RH, McGarry RC, Simone CB 2nd. Influence of Fractionation Scheme and Tumor Location on Toxicities After Stereotactic Body Radiation Therapy for Large (≥ 5 cm) Non-Small Cell Lung Cancer: A Multi-institutional Analysis. *Int J Radiat Oncol Biol Phys* 2017; **97**: 778-785 [PMID: 28244414 DOI: 10.1016/j.ijrobp.2016.11.049]

39 **Verma V**, Shostrom VK, Kumar SS, Zhen W, Hallemeier CL, Braunstein SE, Holland J, Harkenrider

MM, S Iskhanian A, Neboori HJ, Jabbour SK, Attia A, Lee P, Alite F, Walker JM, Stahl JM, Wang K, Bingham BS, Hadzitheodorou C, Decker RH, McGarry RC, Simone CB 2nd. Multi-institutional experience of stereotactic body radiotherapy for large (≥5 centimeters) non-small cell lung tumors. *Cancer* 2017; **123**: 688-696 [PMID: 27741355 DOI: 10.1002/cncr.30375]

Published By Baishideng Publishing Group Inc
7041 Koll Center Parkway, Suite 160, Pleasanton, CA 94566, USA
Telephone: +1-925-2238242
Fax: +1-925-2238243
E-mail: bpgoffice@wjgnet.com
Help Desk: https://www.f6publishing.com/helpdesk
https://www.wjgnet.com

ISSN 1949-8470 (online)

World Journal of *Radiology*

World J Radiol 2019 April 28; 11(4): 55-61

Published by Baishideng Publishing Group Inc

WJR World Journal of Radiology

Contents

Monthly Volume 11 Number 4 April 28, 2019

EDITORIAL

Contents

World Journal of Radiology

Volume 11 Number 4 April 28, 2019

ABOUT COVER

Editorial Board Member of *World Journal of Radiology*, Carlo N De Cecco, MD, PhD, Assistant Professor, Department of Radiology and Radiological Sciences, Medical University of South Carolina, Charleston, SC 29401, United States

AIMS AND SCOPE

World Journal of Radiology (*World J Radiol*, *WJR*, online ISSN 1949-8470, DOI: 10.4329) is a peer-reviewed open access academic journal that aims to guide clinical practice and improve diagnostic and therapeutic skills of clinicians.

The *WJR* covers topics concerning diagnostic radiology, radiation oncology, radiologic physics, neuroradiology, nuclear radiology, pediatric radiology, vascular/interventional radiology, medical imaging achieved by various modalities and related methods analysis. The current columns of *WJR* include editorial, frontier, mini-reviews, review, medical ethics, original articles, case report, *etc*.

We encourage authors to submit their manuscripts to *WJR*. We will give priority to manuscripts that are supported by major national and international foundations and those that are of great basic and clinical significance.

INDEXING/ABSTRACTING

The *WJR* is now abstracted and indexed in Emerging Sources Citation Index (Web of Science), PubMed, PubMed Central, China National Knowledge Infrastructure (CNKI), China Science and Technology Journal Database (CSTJ), and Superstar Journals Database.

RESPONSIBLE EDITORS FOR THIS ISSUE

Responsible Electronic Editor: *Yun-Xiaojian Wu* **Proofing Editorial Office Director:** *Jin-Lei Wang*

NAME OF JOURNAL
World Journal of Radiology

ISSN
ISSN 1949-8470 (online)

LAUNCH DATE
January 31, 2009

FREQUENCY
Monthly

EDITORS-IN-CHIEF
Venkatesh Mani

EDITORIAL BOARD MEMBERS
https://www.wjgnet.com/1949-8470/editorialboard.htm

EDITORIAL OFFICE
Jin-Lei Wang, Director

PUBLICATION DATE
April 28, 2019

INSTRUCTIONS TO AUTHORS
https://www.wjgnet.com/bpg/gerinfo/204

GUIDELINES FOR ETHICS DOCUMENTS
https://www.wjgnet.com/bpg/GerInfo/287

GUIDELINES FOR NON-NATIVE SPEAKERS OF ENGLISH
https://www.wjgnet.com/bpg/gerinfo/240

PUBLICATION MISCONDUCT
https://www.wjgnet.com/bpg/gerinfo/208

ARTICLE PROCESSING CHARGE
https://www.wjgnet.com/bpg/gerinfo/242

STEPS FOR SUBMITTING MANUSCRIPTS
https://www.wjgnet.com/bpg/GerInfo/239

ONLINE SUBMISSION
https://www.f6publishing.com

World Journal of Radiology

Submit a Manuscript: https://www.f6publishing.com

World J Radiol 2019 April 28; 11(4): 55-61

DOI: 10.4329/wjr.v11.i4.55

ISSN 1949-8470 (online)

EDITORIAL

Imaging of the spine: Where do we stand?

Mohamed R Nouh

ORCID number: Mohamed R Nouh (0000-0003-2843-1120).

Author contributions: Mohamed R Nouh wrote the manuscript.

Conflict-of-interest statement: The author declares no conflictofinterest.

Manuscript source: Invited manuscript

Received: September 4, 2018
Peer-review started: September 4, 2018
First decision: October 26, 2018
Revised: March 11, 2019
Accepted: March 16, 2019
Article in press: March 16, 2019
Published online: April 28, 2019

P-Reviewer: Vahedi P, Velnar T
S-Editor: Dou Y
L-Editor: Filipodia
E-Editor: Wu YXJ

Mohamed R Nouh, Faculty of Medicine, Alexandria University, Alexandria 21521, Egypt

Corresponding author: Mohamed R Nouh, MD, Assistant Professor, Faculty of Medicine, Alexandria University, Alexandria 21521, Egypt. mragab73@yahoo.com
Telephone: +966-53-7476313

Abstract

The number of patients presenting with spine-related problems has globally increased, with an enormous growing demand for the use of medical imaging to address this problem. The last three decades witnessed great leaps for diagnostic imaging modalities, including those exploited for imaging the spine. These developments improved our diagnostic capabilities in different spinal pathologies, especially with multi-detector computed tomography and magnetic resonance imaging, *via* both hardware and software improvisations. Nowadays, imaging may depict subtle spinal instability caused by various osseous and ligamentous failures, and could elucidate dynamic instabilities. Consequently, recent diagnostic modalities can discern clinically relevant spinal canal stenosis. Likewise, improvement in diagnostic imaging capabilities revolutionized our understanding of spinal degenerative diseases *via* quantitative biomarkers rather than mere subjective perspectives. Furthermore, prognostication of spinal cord injury has become feasible, and this is expected to be translated into better effective patient tailoring to management plans with better clinical outcomes. Meanwhile, our confidence in diagnosing spinal infections and assessing the different spinal instrumentation has greatly improved over the past few last decades. Overall, revolutions in diagnostic imaging over the past few decades have upgraded spinal imaging from simple subjective and qualitative indices into a more sophisticated yet precise era of objective metrics *via* deploying quantitative imaging biomarkers.

Key words: Spine; Radiography; Multi-detector computed tomography; Magnetic resonance Imaging

Core tip: Advancements in diagnostic imaging over the last few decades have developed spinal imaging from simple subjective and qualitative indices into a more sophisticated yet precise era of objective metrics *via* deploying quantitative imaging biomarkers. These have revolutionized our understanding of the patho-physiological basis of a lot of spinal pathologies and spinal biomechanics that were not previously available. This is projected to improve patient care from both diagnostic and prognostic perspectives in the near future.

Citation: Nouh MR. Imaging of the spine: Where do we stand? *World J Radiol* 2019; 11(4): 55-61
URL: https://www.wjgnet.com/1949-8470/full/v11/i4/55.htm
DOI: https://dx.doi.org/10.4329/wjr.v11.i4.55

INTRODUCTION

Over the last few decades, the number of patients presenting with spine-related problems has globally increased across all age groups with variable etiologic factors, of which degenerative diseases constitute the major bulk[1,2]. Subsequently, more imaging modalities are exploited to address these health problems, with a rise of the total health expenditure[1,2]. Furthermore, our understanding of spinal biomechanics has been evolved over the last 25 years[3]. This imposed a great demand for more qualitative indices of the different imaging modalities, which have grown enormously over that time. Meanwhile, the efficient use of these new diagnostic tools in different clinical scenarios requires judicial deployment for improved cost-effective and patient-tailored management plans[4].

Spinal imaging is complicated by the complex anatomy, different osseous, and soft tissue components and biomechanics of the spines[3]. Since the early days of radiology, the spine was assessed by plain radiography that was limited to assessment of osseous elements and its projections. By the mid-1970s, computed tomography (CT) started to reproduce clinically useful two- and three-dimensional images of the spine. A few years later, a major breakthrough of spinal imaging has been achieved thanks to the introduction of magnetic resonance imaging (MRI) that enabled non-invasive visualization of the spine anatomy. Since then, continual technological improvements in CT and MRI have continued. Consequently, progressive improvement in health care of patients with spine-related disorders has followed[5].

SPINAL INSTABILITY

With regards to spinal instability, dynamic upright radiographs have been the cornerstone for assessing spinal motion segmental instability for decades. However, they are inconvenient in trauma, and suffer from both measurement errors as well as dimensional limitations[6]. More importantly, radiographs miss the soft tissue factors associated with instabilities[6]. Besides, subtle spinal instabilities may not be recognized on conventional non-weight-bearing CT and MRI in the recumbent position where they might be self-reduced[7].By the current millennium, axial loading on both CT and MR imaging were visionary tools in the work-up of spinal instability[8,9]. However, some argued that the parameters assessed differ from those measured in the upright position and dismiss the actual variable effects of body weight, gravity and neuromuscular factors working on the spine in the erect posture that may be clinically relevant[9,10].

On the other hand, volumetric isotropic high resolution CT imaging, achieved by the introduction of multi-detector CT (MDCT) in clinical practice during the last 15years, made identification of subtle instabilities caused by osseous failure amenable, especially in trauma settings[11]. In parallel, technologic advances in MRI (hard- and soft-wares); including the availability of vertical gap open MRI systems and functional devices that can be applied on high-field units; allowed the investigation of spinal instabilities in a feasibly functional way with acceptable reproducibility[12]. Thus, MRI may nowadays depict subtle spinal instability caused by various ligamentous failures, and could elucidate dynamic instabilities caused by movements using novel dynamic MRI with the advantage of non-ionizing radiation exposure.

ADOLESCENT SPINAL DEFORMITIES

Upright serial radiography of the spine has been the gold standard for evaluating adolescent spinal deformities, with subsequent deriving of quantitative indices of angular deformities, as well as judgment of curve structure and spine flexibility for optimized management[13]. However, it is disadvantaged for repeated exposure to ionizing radiation[14,15]. Besides, the development of 3D rendering of adolescent spinal deformities and the various interplaying factors in adolescent spinal deformities, such

as spino-pelvic relationship, diurnal variations, and the effect of different groups of acting muscles, questioned the reliability of 2D radiographic imaging[16,17].

By the year 2000, EOS Imaging® had been introduced as low radiation dose equipment that produce both 2D and 3D images of the whole spine comparable to those acquired by CT and similarly reproducible measurements[18,19].

Furthermore, ultrasound has been explored for the evaluation of spinal scoliotic curves, vertebral rotation deformities and skeletal maturity, with the goal to reduce radiation exposure to a minimum with encouraging results[20,21].

On the other hand, medical imaging using real-time image guidance and computerized navigational systems has revolutionized the spinal surgical procedures for better surgical planning, minimal invasiveness, and optimized outcomes[22]. However, discussion of these advancements is beyond the scope of this editorial.

SPINAL DEGENERATIVE DISEASE

Currently, MRI is the benchmark for imaging spinal degenerative disorders, thanks to its exquisite soft tissue contrast and the superb identification of intervertebral disk zonal anatomy. In addition, it is capable of addressing degenerative marrow changes of the spine, as well as inflammatory changes induced by degenerative disc disease that are largely responsible for patient symptoms[23]. Promisingly, emerging functional MR techniques, such as T2/T2* mapping, T1ρ calculation, T2 relaxation time measurement, diffusion quantitative imaging, chemical exchange saturation transfer and MR spectroscopy, have shown the potential to quantitatively address the disk's zonal chemical composition with a greater ability to discern painful spines that warrant different clinical interventions[24-28]. A recent frontier is the study of stiffness of the intervertebral discs *via* MR elastography shear propagation[29]. Walter *et al*[29]found significant developments in intervertebral discs stiffness in the higher grades of disc degenerations, and this showed significant correlation with the classic Pfirrmann's scoring system. These advances are projected to be clinically implemented in the forthcoming years as non-invasive mechanical biomarkers of spinal degeneration. This may result in a revolution in patient-tailored management strategies by using targeted novel minimally-invasive interventions[30].

SPINAL CANAL STENOSIS

In the spectrum of degenerative spinal disease, spinal canal stenosis is an increasingly recognized reason for spinal imaging, especially in the elderly. It results from a myriad of spinal pathologic entities, of which degenerative processes prevail[31]. CT and/or myelography have been employed to elucidate morphologic changes associated with neural compromise in the central neural canal, lateral recess or at foramen levels. However, MRI surpassed these modalities thanks to the lack of ionizing radiation and invasiveness, as well as its surplus soft tissue contrast[32].

There are many considerations to be accounted for when imaging spinal canal stenosis. Firstly, the imaging diagnosis of spinal stenosis relies mainly on arguable subjective and objective imaging indices to suspect the existence of neurovascular compromise[33,34]. Among these variables, antero-posterior dimensions of the spinal canal, its cross-sectional area and spinal cord-CSF congruity were the most agreed parameters for diagnosing central stenosis[33]. Notably, the compression of the nerve root at the lateral recess was the most acceptable index of lateral recess stenosis[33]. Furthermore, nerve root impingement and foraminal zone compromise were the most consensual parameters for diagnosis of foraminal stenosis[34]. Secondly, not all imaging of spinal stenosis is clinically symptomatic[35]. A judicial clinical assessment is crucial for evaluating the relevance of the imaging findings in view of the proper clinical settings[36]. Thirdly, and to add complexity, spinal canal stenosis should be perceived as a dynamic phenomenon. A lot of spinal canal stenosis subjects report position-dependent symptoms due to postural changes in the dimensions of the spinal canal[12,37].

Taking the aforementioned points into account, further functional imaging workup became of immense importance to discern clinically-relevant canal stenosis. Nowadays, axial-loaded MR and MDCT cross-sectional studies, as well as upright and dynamic MR systems, may be deployed to elucidate the cause of radicular pain in symptomatic spinal stenosis subjects with routine imaging studies with equivocal results[8,10,12,37]. Despite this, logistics as well as economic factors and clinical consensus are limiting the widespread clinical adoption of these tools, especially in developing countries.

Another remarkable achievement for MR imaging of the spine is the wide availability of newer MR techniques. As an example, 3D volumetric T2-high resolution sequences, whether those employing the steady-state precession principle *e.g.*, CISS (constructive interference in steady state) or those based on fast-spin imaging *e.g.*, SPACE (Sampling Perfection with Application optimized Contrast Evolution), combine high resolution, clear T2 contrast and non-distorted visualization in different orthogonal planes due to their isotropic sampling[38]. These tools yield better signal-to-noise ratios of different spinal structures in a clinically-relevant shorter acquisition time. Furthermore, they accurately depicted spinal cord lesions, as well as the spinal nerve roots and those based on fast spin imaging that advantageously resist motion and susceptibility artifacts[38,39]. These advances allowed a robust rapid screening for vague cervical and low back pain causes, including spinal degenerative disease and spinal stenosis, which subsequently increases the radiology departments' potency and lessens MRI abuse in an economically compromised health system[40,41].

SPINAL TRAUMA

Spinal trauma and its devastating sequels are considered a major cause for emergency room admissions and rehabilitation program admissions worldwide, respectively[42,43]. Over the last decade, MDCT has been considered the benchmark for clearance of spinal trauma patients as a result of robust data acquisition and provided spatial resolution[44]. Though further MR imaging may not be warranted, the utility of MRI in assessing the severity of soft tissue injuries may affect clinical outcomes and should not be underestimated, especially in spinal cord injury (SCI) patients[45]. Over the years, conventional MR sequences like TSE and STIR depicted the presence and extent of subtle vertebral fractures and spinal cord edema. Nevertheless, it remains limited due to its inability to address degenerative and regenerative processes at the microstructural level of the spinal cord. Currently, a novel array of MR techniques such as susceptibility weighted (SW), diffusion weighted (DW) and diffusion tensor imaging (DTI) are revolutionizing SCI imaging, with improved clinical decision making and clinical outcome. For instance, SW is able to assess spinal cord petechial hemorrhages an important neural recovery prognostication index[46]. Furthermore, DW and DTI are becoming more handy clinical tools that show promise in addressing the spinal cord micro-architecture[47]. They can non-invasively provide quantitative probing of directional diffusivities of cord tracts, as well as assess SCI, its recovery, and remyelination[48]. Another potential for MR imaging is functional MRI, which is based on neural activation-induced changes resulting from oxygen and water molecules shifts between the intra- and extra-vascular spaces[49]. Clinical trials showed its ability to reveal spinal cord injuries and monitor results of rehabilitation[50].

SPINAL INFECTION

Spinal infection continues to be a challenge to both clinician and radiologists alike. Though infectious spondylitis and spondylodiskitis are uncommon, they remain as increasingly recognized health problems worldwide. This may be due to growing life expectancy across most communities, prevalence of chronic diseases, outbreaks of immune-suppression, and increased spinal instrumentation procedures[51].

MR imaging exhibited the highest sensitivity and specificity of all imaging modalities to diagnose spinal infections because of its superb soft tissue contrast, lack of ionizing radiation and different image weights that depict early pathologic changes in marrow, disc and soft tissues[52]. Dynamic contrast-enhanced magnetic resonance proved to be useful supplements in differentiating spinal infection when conventional MR sequences are equivocal[53]. The use of DW may be an excellent alternative where contrast use is not advocated[54]. Recently,[18]F-FDG-PET has offered a promising comparable sensitivity and specificity to MR in the diagnosis of spinal infection and its anatomic extents when MRI use is unlikely, as in the case of spinal instrumentations[55].

On the other hand, CT can diagnose spinal infection by documenting bony changes in established spinal infections and depicting soft tissue calcifications in TB spondylitis. Interestingly, CT perfusion parameters showed the potential to non-invasively differentiate neoplastic and inflammatory paraspinal masses, a fairly common arduous diagnostic task[56]. Furthermore, it has carved its niche as a widely acceptable handy tool for guiding MSK biopsies and drainage procedures for spinal infections[57].

SPINAL INSTRUMENTATION

Over the last few decades, there was an escalating trend in the number of spinal instrumentation deployed to manage different spinal pathological entities[2,58]. Subsequently, there has been robust growth in the requested imaging procedures that assess outcomes and instrument-related complications. Radiography used to be the convenient imaging tool employed for this purpose. In contrast, the use of CT and MR was hampered by beam-hardening and magnetic susceptibility artifacts; respectively[58]. Over the last two decades, synchronous advances in MDCT and MR technologies, coupled with similar developments in spinal hardware materials have revolutionized imaging of those patients.

The reduction of metallic artifacts in MDCT has been achieved via the use of anti-scatter grids and collimation, along with improved post-processing reconstruction algorithms, especially when dual energy (DE) CT is exploited[59]. Likewise, new MR techniques such as view angle tilting, slice encoding for metal artifact correction, and multi-acquisition variable-resonance image combination, used solely or in hybrid, have been clinically exploited to overcome susceptibility artifacts produced by implanted spinal hardware[60]. These improvements have been translated into enhanced diagnostic imaging quality, thus enabling better chances for fruitful clinical outcomes.

CONCLUSION

In conclusion, significant improvements in diagnostic imaging over the last few decades have upgraded spinal imaging from simple subjective and qualitative indices into a more sophisticated yet precise era of objective metrics via deploying quantitative imaging biomarkers. These have revolutionized our understanding of the patho-physiological basis of many spinal pathologies and spinal biomechanics that were not available previously. Consequently, these developments are projected to improve patient care from both diagnostic and prognostic perspectives in the near future.

REFERENCES

1 **Dieleman JL**, Baral R, Birger M, Bui AL, Bulchis A, Chapin A, Hamavid H, Horst C, Johnson EK, Joseph J, Lavado R, Lomsadze L, Reynolds A, Squires E, Campbell M, DeCenso B, Dicker D, Flaxman AD, Gabert R, Highfill T, Naghavi M, Nightingale N, Templin T, Tobias MI, Vos T, Murray CJ. US Spending on Personal Health Care and Public Health, 1996-2013. *JAMA* 2016; **316**: 2627-2646 [PMID: 28027366 DOI: 10.1001/jama.2016.16885]

2 **Andersson G**, Watkins-Castillo SI. Spinal Fusion. BMUS: The Burden of Musculoskeletal Diseases in the United States. Available from: http://www.boneandjointburden.org/2014-report/iie1/spinal-fusion

3 **Oxland TR**. Fundamental biomechanics of the spine--What we have learned in the past 25 years and future directions. *J Biomech* 2016; **49**: 817-832 [PMID: 26706717 DOI: 10.1016/j.jbiomech.2015.10.035]

4 **Chou R**, Qaseem A, Owens DK, Shekelle P; Clinical Guidelines Committee of the American College of Physicians. Diagnostic imaging for low back pain: advice for high-value health care from the American College of Physicians. *Ann Intern Med* 2011; **154**: 181-189 [PMID: 21282698 DOI: 10.7326/0003-4819-154-3-201102010-00008]

5 **Hoeffner EG**, Mukherji SK, Srinivasan A, Quint DJ. Neuroradiology back to the future: spine imaging. *AJNR Am J Neuroradiol* 2012; **33**: 999-1006 [PMID: 22576888 DOI: 10.3174/ajnr.A3129]

6 **Leone A**, Guglielmi G, Cassar-Pullicino VN, Bonomo L. Lumbar intervertebral instability: a review. *Radiology* 2007; **245**: 62-77 [PMID: 17885181 DOI: 10.1148/radiol.2451051359]

7 **Even JL**, Chen AF, Lee JY. Imaging characteristics of "dynamic" versus "static" spondylolisthesis: analysis using magnetic resonance imaging and flexion/extension films. *Spine J* 2014; **14**: 1965-1969 [PMID: 24361349 DOI: 10.1016/j.spinee.2013.11.057]

8 **Cartolari R**. Axial loaded imaging of the lumbar spine 18 years later. Is it still a valuable examination? *Neuroradiol J* 2011; **24**: 519-534 [PMID: 24059708 DOI: 10.1177/197140091102400406]

9 **Kanno H**, Ozawa H, Koizumi Y, Morozumi N, Aizawa T, Ishii Y, Itoi E. Changes in lumbar spondylolisthesis on axial-loaded MRI: do they reproduce the positional changes in the degree of olisthesis observed on X-ray images in the standing position? *Spine J* 2015; **15**: 1255-1262 [PMID: 25684062 DOI: 10.1016/j.spinee.2015.02.016]

10 **Hioki A**, Miyamoto K, Sakai H, Shimizu K. Lumbar axial loading device alters lumbar sagittal alignment differently from upright standing position: a computed tomography study. *Spine (Phila Pa 1976)* 2010; **35**: 995-1001 [PMID: 20139804 DOI: 10.1097/BRS.0b013e3181bb8188]

11 **Munera F**, Rivas LA, Nunez DB, Quencer RM. Imaging evaluation of adult spinal injuries: emphasis on multidetector CT in cervical spine trauma. *Radiology* 2012; **263**: 645-660 [PMID: 22623691 DOI: 10.1148/radiol.12110526]

12 **Hansen BB**, Hansen P, Christensen AF, Trampedach C, Rasti Z, Bliddal H, Boesen M. Reliability of standing weight-bearing (0.25T) MR imaging findings and positional changes in the lumbar spine. *Skeletal Radiol* 2018; **47**: 25-35 [PMID: 28812185 DOI: 10.1007/s00256-017-2746-y]

13 **Raso VJ**, Lou E, Hill DL, Mahood JK, Moreau MJ, Durdle NG. Trunk distortion in adolescent idiopathic scoliosis. *J Pediatr Orthop* 1998; **18**: 222-226 [PMID: 9531406]

14 **Simony A**, Hansen EJ, Christensen SB, Carreon LY, Andersen MO. Incidence of cancer in adolescent idiopathic scoliosis patients treated 25 years previously. *Eur Spine J* 2016; **25**: 3366-3370 [PMID: 27592106 DOI: 10.1007/s00586-016-4747-2]
15 **Law M**, Ma WK, Lau D, Chan E, Yip L, Lam W. Cumulative radiation exposure and associated cancer risk estimates for scoliosis patients: Impact of repetitive full spine radiography. *Eur J Radiol* 2016; **85**: 625-628 [PMID: 26860676 DOI: 10.1016/j.ejrad.2015.12.032]
16 **Labelle H**, Aubin CE, Jackson R, Lenke L, Newton P, Parent S. Seeing the spine in 3D: how will it change what we do? *J Pediatr Orthop* 2011; **31**: S37-S45 [PMID: 21173617 DOI: 10.1097/BPO.0b013e3181fd8801]
17 **Lafage V**, Schwab F, Patel A, Hawkinson N, Farcy JP. Pelvic tilt and truncal inclination: two key radiographic parameters in the setting of adults with spinal deformity. *Spine (Phila Pa 1976)* 2009; **34**: E599-E606 [PMID: 19644319 DOI: 10.1097/BRS.0b013e3181aad219]
18 **Deschênes S**, Charron G, Beaudoin G, Labelle H, Dubois J, Miron MC, Parent S. Diagnostic imaging of spinal deformities: reducing patients radiation dose with a new slot-scanning X-ray imager. *Spine (Phila Pa 1976)* 2010; **35**: 989-994 [PMID: 20228703 DOI: 10.1097/BRS.0b013e3181bdcaa4]
19 **Somoskeöy S**, Tunyogi-Csapó M, Bogyó C, Illés T. Accuracy and reliability of coronal and sagittal spinal curvature data based on patient-specific three-dimensional models created by the EOS 2D/3D imaging system. *Spine J* 2012; **12**: 1052-1059 [PMID: 23102842 DOI: 10.1016/j.spinee.2012.10.002]
20 **Ungi T**, King F, Kempston M, Keri Z, Lasso A, Mousavi P, Rudan J, Borschneck DP, Fichtinger G. Spinal curvature measurement by tracked ultrasound snapshots. *Ultrasound Med Biol* 2014; **40**: 447-454 [PMID: 24268452 DOI: 10.1016/j.ultrasmedbio.2013.09.021]
21 **Young M**, Hill DL, Zheng R, Lou E. Reliability and accuracy of ultrasound measurements with and without the aid of previous radiographs in adolescent idiopathic scoliosis (AIS). *Eur Spine J* 2015; **24**: 1427-1433 [PMID: 25753005 DOI: 10.1007/s00586-015-3855-8]
22 **Helm PA**, Teichman R, Hartmann SL, Simon D. Spinal Navigation and Imaging: History, Trends, and Future. *IEEE Trans Med Imaging* 2015; **34**: 1738-1746 [PMID: 25594965 DOI: 10.1109/TMI.2015.2391200]
23 **Li Y**, Fredrickson V, Resnick DK. How should we grade lumbar disc herniation and nerve root compression? A systematic review. *Clin Orthop Relat Res* 2015; **473**: 1896-1902 [PMID: 24825130 DOI: 10.1007/s11999-014-3674-y]
24 **Schleich C**, Müller-Lutz A, Matuschke F, Sewerin P, Sengewein R, Schmitt B, Ostendorf B, Wittsack HJ, Stanke K, Antoch G, Miese F. Glycosaminoglycan chemical exchange saturation transfer of lumbar intervertebral discs in patients with spondyloarthritis. *J Magn Reson Imaging* 2015; **42**: 1057-1063 [PMID: 25758361 DOI: 10.1002/jmri.24877]
25 **Mulligan KR**, Ferland CE, Gawri R, Borthakur A, Haglund L, Ouellet JA. Axial T1ρ MRI as a diagnostic imaging modality to quantify proteoglycan concentration in degenerative disc disease. *Eur Spine J* 2015; **24**: 2395-2401 [PMID: 25236594 DOI: 10.1007/s00586-014-3582-6]
26 **Xie R**, Ruan L, Chen L, Zhou K, Yuan J, Ji W, Jing G, Huang X, Shi Q, Chen C. T2 relaxation time for intervertebral disc degeneration in patients with upper back pain: initial results on the clinical use of 3.0 Tesla MRI. *BMC Med Imaging* 2017; **17**: 9 [PMID: 28143419 DOI: 10.1186/s12880-017-0182-z]
27 **Xiong X**, Zhou Z, Figini M, Shangguan J, Zhang Z, Chen W. Multi-parameter evaluation of lumbar intervertebral disc degeneration using quantitative magnetic resonance imaging techniques. *Am J Transl Res* 2018; **10**: 444-454 [PMID: 29511438]
28 **Wang YX**, Zhao F, Griffith JF, Mok GS, Leung JC, Ahuja AT, Yuan J. T1rho and T2 relaxation times for lumbar disc degeneration: an in vivo comparative study at 3.0-Tesla MRI. *Eur Radiol* 2013; **23**: 228-234 [PMID: 22865227 DOI: 10.1007/s00330-012-2591-2]
29 **Walter BA**, Mageswaran P, Mo X, Boulter DJ, Mashaly H, Nguyen XV, Prevedello LM, Thoman W, Raterman BD, Kalra P, Mendel E, Marras WS, Kolipaka A. MR Elastography-derived Stiffness: A Biomarker for Intervertebral Disc Degeneration. *Radiology* 2017; **285**: 167-175 [PMID: 28471737 DOI: 10.1148/radiol.2017162287]
30 **Fernandez-Moure J**, Moore CA, Kim K, Karim A, Smith K, Barbosa Z, Van Eps J, Rameshwar P, Weiner B. Novel therapeutic strategies for degenerative disc disease: Review of cell biology and intervertebral disc cell therapy. *SAGE Open Med* 2018; **6**: 2050312118761674 [PMID: 29568524 DOI: 10.1177/2050312118761674]
31 **Kalichman L**, Cole R, Kim DH, Li L, Suri P, Guermazi A, Hunter DJ. Spinal stenosis prevalence and association with symptoms: the Framingham Study. *Spine J* 2009; **9**: 545-550 [PMID: 19398386 DOI: 10.1016/j.spinee.2009.03.005]
32 **Kent DL**, Haynor DR, Larson EB, Deyo RA. Diagnosis of lumbar spinal stenosis in adults: a metaanalysis of the accuracy of CT, MR, and myelography. *AJR Am J Roentgenol* 1992; **158**: 1135-1144 [PMID: 1533084 DOI: 10.2214/ajr.158.5.1533084]
33 **Mamisch N**, Brumann M, Hodler J, Held U, Brunner F, Steurer J; Lumbar Spinal Stenosis Outcome Study Working Group Zurich. Radiologic criteria for the diagnosis of spinal stenosis: results of a Delphi survey. *Radiology* 2012; **264**: 174-179 [PMID: 22550311 DOI: 10.1148/radiol.12111930]
34 **Andreisek G**, Deyo RA, Jarvik JG, Porchet F, Winklhofer SF, Steurer J; LSOS working group. Consensus conference on core radiological parameters to describe lumbar stenosis - an initiative for structured reporting. *Eur Radiol* 2014; **24**: 3224-3232 [PMID: 25079488 DOI: 10.1007/s00330-014-3346-z]
35 **Ishimoto Y**, Yoshimura N, Muraki S, Yamada H, Nagata K, Hashizume H, Takiguchi N, Minamide A, Oka H, Kawaguchi H, Nakamura K, Akune T, Yoshida M. Associations between radiographic lumbar spinal stenosis and clinical symptoms in the general population: the Wakayama Spine Study. *Osteoarthritis Cartilage* 2013; **21**: 783-788 [PMID: 23473979 DOI: 10.1016/j.joca.2013.02.656]
36 **Splettstößer A**, Khan MF, Zimmermann B, Vogl TJ, Ackermann H, Middendorp M, Maataoui A. Correlation of lumbar lateral recess stenosis in magnetic resonance imaging and clinical symptoms. *World J Radiol* 2017; **9**: 223-229 [PMID: 28634513 DOI: 10.4329/wjr.v9.i5.223]
37 **Kanbara S**, Yukawa Y, Ito K, Machino M, Kato F. Dynamic changes in the dural sac of patients with lumbar canal stenosis evaluated by multidetector-row computed tomography after myelography. *Eur Spine J* 2014; **23**: 74-79 [PMID: 23817960 DOI: 10.1007/s00586-013-2873-7]
38 **Vargas MI**, Delattre BMA, Boto J, Gariani J, Dhouib A, Fitsiori A, Dietemann JL. Advanced magnetic resonance imaging (MRI) techniques of the spine and spinal cord in children and adults. *Insights Imaging* 2018; **9**: 549-557 [PMID: 29858818 DOI: 10.1007/s13244-018-0626-1]
39 **Dietemann JL**, Bogorin A, Abu Eid M, Sanda R, Mourao Soares I, Draghici S, Rotaru N, Koob M. Tips and traps in neurological imaging: imaging the perimedullary spaces. *Diagn Interv Imaging* 2012; **93**: 985-

992 [PMID: 23164638 DOI: 10.1016/j.diii.2012.08.005]
40 **Swami VG**, Katlariwala M, Dhillon S, Jibri Z, Jaremko JL. Magnetic Resonance Imaging in Patients With Mechanical Low Back Pain Using a Novel Rapid-Acquisition Three-Dimensional SPACE Sequence at 1.5-T: A Pilot Study Comparing Lumbar Stenosis Assessment With Routine Two-Dimensional Magnetic Resonance Sequences. *Can Assoc Radiol J* 2016; **67**: 368-378 [PMID: 27245289 DOI: 10.1016/j.carj.2015.11.005]
41 **Koontz NA**, Wiggins RH, Mills MK, McLaughlin MS, Pigman EC, Anzai Y, Shah LM. Less Is More: Efficacy of Rapid 3D-T2 SPACE in ED Patients with Acute Atypical Low Back Pain. *Acad Radiol* 2017; **24**: 988-994 [PMID: 28385420 DOI: 10.1016/j.acra.2017.02.011]
42 **Liu P**, Yao Y, Liu MY, Fan WL, Chao R, Wang ZG, Liu YC, Zhou JH, Zhao JH. Spinal trauma in mainland China from 2001 to 2007: an epidemiological study based on a nationwide database. *Spine (Phila Pa 1976)* 2012; **37**: 1310-1315 [PMID: 22744399 DOI: 10.1097/BRS.0b013e3182474d8b]
43 **Ten Brinke JG**, Saltzherr TP, Panneman MJM, Hogervorst M, Goslings JC. Incidence of spinal fractures in the Netherlands 1997-2012. *J Clin Orthop Trauma* 2017; **8**: S67-S70 [PMID: 29339845 DOI: 10.1016/j.jcot.2017.03.011]
44 **Raza M**, Elkhodair S, Zaheer A, Yousaf S. Safe cervical spine clearance in adult obtunded blunt trauma patients on the basis of a normal multidetector CT scan--a meta-analysis and cohort study. *Injury* 2013; **44**: 1589-1595 [PMID: 23856632 DOI: 10.1016/j.injury.2013.06.005]
45 **Martínez-Pérez R**, Paredes I, Cepeda S, Ramos A, Castaño-León AM, García-Fuentes C, Lobato RD, Gómez PA, Lagares A. Spinal cord injury after blunt cervical spine trauma: correlation of soft-tissue damage and extension of lesion. *AJNR Am J Neuroradiol* 2014; **35**: 1029-1034 [PMID: 24335539 DOI: 10.3174/ajnr.A3812]
46 **Wang M**, Dai Y, Han Y, Haacke EM, Dai J, Shi D. Susceptibility weighted imaging in detecting hemorrhage in acute cervical spinal cord injury. *Magn Reson Imaging* 2011; **29**: 365-373 [PMID: 21232894 DOI: 10.1016/j.mri.2010.10.016]
47 **Vedantam A**, Jirjis MB, Schmit BD, Wang MC, Ulmer JL, Kurpad SN. Characterization and limitations of diffusion tensor imaging metrics in the cervical spinal cord in neurologically intact subjects. *J Magn Reson Imaging* 2013; **38**: 861-867 [PMID: 23389869 DOI: 10.1002/jmri.24039]
48 **Cheran S**, Shanmuganathan K, Zhuo J, Mirvis SE, Aarabi B, Alexander MT, Gullapalli RP. Correlation of MR diffusion tensor imaging parameters with ASIA motor scores in hemorrhagic and nonhemorrhagic acute spinal cord injury. *J Neurotrauma* 2011; **28**: 1881-1892 [PMID: 21875333 DOI: 10.1089/neu.2010.1741]
49 **Figley CR**, Leitch JK, Stroman PW. In contrast to BOLD: signal enhancement by extravascular water protons as an alternative mechanism of endogenous fMRI signal change. *Magn Reson Imaging* 2010; **28**: 1234-1243 [PMID: 20299173 DOI: 10.1016/j.mri.2010.01.005]
50 **Cadotte DW**, Bosma R, Mikulis D, Nugaeva N, Smith K, Pokrupa R, Islam O, Stroman PW, Fehlings MG. Plasticity of the injured human spinal cord: insights revealed by spinal cord functional MRI. *PLoS One* 2012; **7**: e45560 [PMID: 23029097 DOI: 10.1371/journal.pone.0045560]
51 **Fantoni M**, Trecarichi EM, Rossi B, Mazzotta V, Di Giacomo G, Nasto LA, Di Meco E, Pola E. Epidemiological and clinical features of pyogenic spondylodiscitis. *Eur Rev Med Pharmacol Sci* 2012; **16** Suppl 2: 2-7 [PMID: 22655478]
52 **Hong SH**, Choi JY, Lee JW, Kim NR, Choi JA, Kang HS. MR imaging assessment of the spine: infection or an imitation? *Radiographics* 2009; **29**: 599-612 [PMID: 19325068 DOI: 10.1148/rg.292085137]
53 **Lang N**, Su MY, Yu HJ, Yuan H. Differentiation of tuberculosis and metastatic cancer in the spine using dynamic contrast-enhanced MRI. *Eur Spine J* 2015; **24**: 1729-1737 [PMID: 25749725 DOI: 10.1007/s00586-015-3851-z]
54 **Daghighi MH**, Poureisa M, Safarpour M, Behzadmehr R, Fouladi DF, Meshkini A, Varshochi M, Kiani Nazarlou A. Diffusion-weighted magnetic resonance imaging in differentiating acute infectious spondylitis from degenerative Modic type 1 change; the role of b-value, apparent diffusion coefficient, claw sign and amorphous increased signal. *Br J Radiol* 2016; **89**: 20150152 [PMID: 27452260 DOI: 10.1259/bjr.20150152]
55 **Smids C**, Kouijzer IJ, Vos FJ, Sprong T, Hosman AJ, de Rooy JW, Aarntzen EH, de Geus-Oei LF, Oyen WJ, Bleeker-Rovers CP. A comparison of the diagnostic value of MRI and ¹⁸F-FDG-PET/CT in suspected spondylodiscitis. *Infection* 2017; **45**: 41-49 [PMID: 27317050 DOI: 10.1007/s15010-016-0914-y]
56 **Shankar J**, Jayakumar P, Vasudev M, Ravishankar S, Sinha N. The usefulness of CT perfusion in differentiation between neoplastic and tuberculous disease of the spine. *J Neuroimaging* 2009; **19**: 132-138 [PMID: 19021840 DOI: 10.1111/j.1552-6569.2008.00265.x]
57 **Chang CY**, Simeone FJ, Nelson SB, Taneja AK, Huang AJ. Is Biopsying the Paravertebral Soft Tissue as Effective as Biopsying the Disk or Vertebral Endplate? 10-Year Retrospective Review of CT-Guided Biopsy of Diskitis-Osteomyelitis. *AJR Am J Roentgenol* 2015; **205**: 123-129 [PMID: 26102390 DOI: 10.2214/AJR.14.13545]
58 **Nouh MR**. Spinal fusion-hardware construct: Basic concepts and imaging review. *World J Radiol* 2012; **4**: 193-207 [PMID: 22761979 DOI: 10.4329/wjr.v4.i5.193]
59 **Coupal TM**, Mallinson PI, McLaughlin P, Nicolaou S, Munk PL, Ouellette H. Peering through the glare: using dual-energy CT to overcome the problem of metal artefacts in bone radiology. *Skeletal Radiol* 2014; **43**: 567-575 [PMID: 24435711 DOI: 10.1007/s00256-013-1802-5]
60 **den Harder JC**, van Yperen GH, Blume UA, Bos C. Off-resonance suppression for multispectral MR imaging near metallic implants. *Magn Reson Med* 2015; **73**: 233-243 [PMID: 24488684 DOI: 10.1002/mrm.25126]

Published By Baishideng Publishing Group Inc
7041 Koll Center Parkway, Suite 160, Pleasanton, CA 94566, USA
Telephone: +1-925-2238242
Fax: +1-925-2238243
E-mail: bpgoffice@wjgnet.com
Help Desk: https://www.f6publishing.com/helpdesk
https://www.wjgnet.com

ISSN 1949-8470 (online)

World Journal of *Radiology*

World J Radiol 2019 May 28; 11(5): 62-80

Published by Baishideng Publishing Group Inc

WJR

World Journal of Radiology

Contents

Monthly Volume 11 Number 5 May 28, 2019

ORIGINAL ARTICLE

Observational Study

CASE REPORT

Contents

World Journal of Radiology

Volume 11 Number 5 May 28, 2019

ABOUT COVER

Editorial Board Member of *World Journal of Radiology*, Chirag Kamal Ahuja, MBBS, MD, Assistant Professor, Department of Radiodiagnosis and Imaging, Postgraduate Institute of Medical Education and Research, Chandigarh 160012, India

AIMS AND SCOPE

World Journal of Radiology (*World J Radiol*, *WJR*, online ISSN 1949-8470, DOI: 10.4329) is a peer-reviewed open access academic journal that aims to guide clinical practice and improve diagnostic and therapeutic skills of clinicians.

The *WJR* covers topics concerning diagnostic radiology, radiation oncology, radiologic physics, neuroradiology, nuclear radiology, pediatric radiology, vascular/interventional radiology, medical imaging achieved by various modalities and related methods analysis. The current columns of *WJR* include editorial, frontier, mini-reviews, review, medical ethics, original articles, case report, *etc*.

We encourage authors to submit their manuscripts to *WJR*. We will give priority to manuscripts that are supported by major national and international foundations and those that are of great basic and clinical significance.

INDEXING/ABSTRACTING

The *WJR* is now abstracted and indexed in Emerging Sources Citation Index (Web of Science), PubMed, PubMed Central, China National Knowledge Infrastructure (CNKI), China Science and Technology Journal Database (CSTJ), and Superstar Journals Database.

RESPONSIBLE EDITORS FOR THIS ISSUE

Responsible Electronic Editor: *Yan-Xia Xing* **Proofing Editorial Office Director:** *Jin-Lei Wang*

NAME OF JOURNAL
World Journal of Radiology

ISSN
ISSN 1949-8470 (online)

LAUNCH DATE
January 31, 2009

FREQUENCY
Monthly

EDITORS-IN-CHIEF
Venkatesh Mani

EDITORIAL BOARD MEMBERS
https://www.wjgnet.com/1949-8470/editorialboard.htm

EDITORIAL OFFICE
Jin-Lei Wang, Director

PUBLICATION DATE
May 28, 2019

INSTRUCTIONS TO AUTHORS
https://www.wjgnet.com/bpg/gerinfo/204

GUIDELINES FOR ETHICS DOCUMENTS
https://www.wjgnet.com/bpg/GerInfo/287

GUIDELINES FOR NON-NATIVE SPEAKERS OF ENGLISH
https://www.wjgnet.com/bpg/gerinfo/240

PUBLICATION MISCONDUCT
https://www.wjgnet.com/bpg/gerinfo/208

ARTICLE PROCESSING CHARGE
https://www.wjgnet.com/bpg/gerinfo/242

STEPS FOR SUBMITTING MANUSCRIPTS
https://www.wjgnet.com/bpg/GerInfo/239

ONLINE SUBMISSION
https://www.f6publishing.com

World Journal of Radiology

Submit a Manuscript: https://www.f6publishing.com

World J Radiol 2019 May 28; 11(5): 62-73

DOI: 10.4329/wjr.v11.i5.62

ISSN 1949-8470 (online)

ORIGINAL ARTICLE

Observational Study

Imaging plaque inflammation in asymptomatic cocaine addicted individuals with simultaneous positron emission tomography/magnetic resonance imaging

Keren Bachi, Venkatesh Mani, Audrey E Kaufman, Nadia Alie, Rita Z Goldstein, Zahi A Fayad, Nelly Alia-Klein

ORCID number: Keren Bachi (0000-0001-9817-5957); Venkatesh Mani (0000-0002-0432-2918); Audrey E Kaufman (0000-0002-9221-9004); Nadia Alie (0000-0002-0626-7393); Rita Z Goldstein (0000-0002-1127-028X); Zahi A Fayad (0000-0002-3439-7347); Nelly Alia-Klein (0000-0003-1876-8133).

Author contributions: Mani V, Goldstein RZ, Fayad ZA and Alia-Klein N designed the research; Bachi K reviewed literature and collected drug use data; Mani V and Fayad ZA performed vascular imaging; Mani V, Kaufman AE and Alie N analyzed imaging data; Bachi K performed statistical analyses; Bachi K, Mani V, Goldstein RZ, Fayad ZA and Alia-Klein N provided interpretation; Mani V, Kaufman AE, Goldstein RZ and Fayad ZA provided commentary and manuscript editing; and Bachi K and Alia-Klein N wrote the paper.

Supported by NIDA, No. K23DA045928-01 (to Bachi K) and No. R01DA041528 (to Goldstein RZ); NIH/NHLBI, No. R01 HL071021; Translational and Molecular Imaging Institute internal funding (to Fayad ZAF); and American Heart Association Grant in Aid, No. 17GRNT33420119 (to Mani VM).

Institutional review board statement: The study protocol was reviewed and conducted with approval by the Institutional Review Board of the Icahn School of Medicine at Mount Sinai (Study

Keren Bachi, Rita Z Goldstein, Nelly Alia-Klein, Department of Psychiatry, Icahn School of Medicine at Mount Sinai, One Gustave L. Levy Place, New York, NY 10029, United States

Keren Bachi, Department of Environmental Medicine and Public Health, Icahn School of Medicine at Mount Sinai, One Gustave L. Levy Place, New York, NY 10029, United States

Venkatesh Mani, Audrey E Kaufman, Nadia Alie, Zahi A Fayad, Translational and Molecular Imaging Institute, Icahn School of Medicine at Mount Sinai, One Gustave L. Levy Place, New York, NY 10029, United States

Nadia Alie, Children's Hospital of Philadelphia, 3401 Civic Center Blvd, Philadelphia, PA 19104, United States

Rita Z Goldstein, Nelly Alia-Klein, Department of Neuroscience, Icahn School of Medicine at Mount Sinai, One Gustave L. Levy Place, New York, NY 10029, United States

Corresponding author: Nelly Alia-Klein, PhD, Associate Professor, Departments of Psychiatry and Neuroscience, Icahn School of Medicine at Mount Sinai, One Gustave Levy, 1470 Madison Ave., New York, NY 10029, United States. nelly.alia-klein@mssm.edu
Telephone: +1-212-8249311

Abstract

BACKGROUND

Chronic cocaine use is associated with stroke, coronary artery disease and myocardial infarction, resulting in severe impairments or sudden mortality. In the absence of clear cardiovascular symptoms, individuals with cocaine use disorder (iCUD) seeking addiction treatment receive mostly psychotherapy and psychiatric pharmacotherapy, with no attention to vascular disease (*i.e.*, atherosclerosis). Little is known about the pre-clinical signs of cardiovascular risk in iCUD and early signs of vascular disease are undetected in this underserved population.

AIM

To assess inflammation, plaque burden and plaque composition in iCUD aiming to detect markers of atherosclerosis and vascular disease.

METHODS

The bilateral carotid arteries were imaged with positron emission tomography/magnetic resonance imaging (PET/MRI) in iCUD asymptomatic for

ID: GCO#01-1032).

Informed consent statement: All participants in the study cohort have signed an informed consent form prior to study enrollment as required by the Institutional Review Board of the Icahn School of Medicine at Mount Sinai.

Conflict-of-interest statement: All authors declare that they have no conflict of interest.

Manuscript source: Invited manuscript

Received: February 16, 2019
Peer-review started: February 18, 2019
First decision: March 15, 2019
Revised: April 5, 2019
Accepted: May 21, 2019
Article in press: May 22, 2019
Published online: May 28, 2019

P-Reviewer: Kwok WE, Nouh MR
S-Editor: Wang JL
L-Editor: A
E-Editor: Xing YX

cardiovascular disease, healthy controls, and individuals with cardiovascular risk. PET with 18F-fluorodeoxyglucose (^{18}F-FDG) evaluated vascular inflammation and 3-D dark-blood MRI assessed plaque burden including wall area and thickness. Drug use and severity of addiction were assessed with standardized instruments.

RESULTS

The majority of iCUD and controls had carotid FDG-PET signal greater than 1.6 but lower than 3, indicating the presence of mild to moderate inflammation. However, the MRI measure of wall structure was thicker in iCUD as compared to the controls and cardiovascular risk group, indicating greater carotid plaque burden. iCUD had larger wall area as compared to the healthy controls but not as compared to the cardiovascular risk group, indicating structural wall similarities between the non-control study groups. In iCUD, wall area correlated with greater cocaine withdrawal and craving.

CONCLUSION

These preliminary results show markers of carotid artery disease burden in cardiovascular disease-asymptomatic iCUD. Broader trials are warranted to develop protocols for early detection of cardiovascular risk and preventive intervention in iCUD.

Key words: 3-D dark-blood magnetic resonance imaging; 18F-fluorodeoxyglucose positron emission tomography; Simultaneous positron emission tomography; Magnetic resonance; Substance use disorder; Cocaine addiction; Atherosclerosis; Plaque burden; Vascular inflammation

Core tip: Despite undetected clinical signs, cocaine use increases risk of stroke, coronary artery disease and myocardial infarction. Simultaneous carotid positron emission tomography/magnetic resonance imaging can effectively evaluate vascular inflammation and plaque burden in individuals with cocaine use disorder. Cocaine users had increased wall area, comparable to individuals with cardiovascular risk and significantly higher than healthy controls. Wall area in cocaine users positively correlated with greater cocaine withdrawal and craving. Broader trials are warranted to develop protocols for early detection of cardiovascular risk and preventive intervention in individuals with cocaine use disorder.

Citation: Bachi K, Mani V, Kaufman AE, Alie N, Goldstein RZ, Fayad ZA, Alia-Klein N. Imaging plaque inflammation in asymptomatic cocaine addicted individuals with simultaneous positron emission tomography/magnetic resonance imaging. *World J Radiol* 2019; 11(5): 62-73
URL: https://www.wjgnet.com/1949-8470/full/v11/i5/62.htm
DOI: https://dx.doi.org/10.4329/wjr.v11.i5.62

INTRODUCTION

Cocaine use disorder (CUD), chronic brain disease, imparts multiple cardiovascular effects. The phenomenology of cocaine addiction involves decades of chronic cocaine and other drug use as well as an unhealthy lifestyle (*e.g.*, poor sleep and nutrition) that affect cardiovascular health. Furthermore, cocaine's main vasoactive metabolite benzoylmethylecgonine, a tropane alkaloid, is associated with hematological effects on the vessel and the loss of the endothelium's protective functions[1-3]. Cocaine creates an elevated immune system inflammatory state with increased pro-inflammatory cytokines, and brain-derived neurotrophic factor levels, all contributing to vascular disease[4,5]. These effects are expressed by activation of cells in the endothelium (interior surface of blood vessels) leading to macrophage proliferation and vascular inflammation, with subsequent formation of complex plaque that manifests as structural abnormalities and progresses to atherosclerotic disease[6,7]. Atherosclerosis

reflects a long-term inflammatory process, where, in medium to large arteries (*e.g.*, the carotid arteries), it may be present even before it becomes susceptible to rupture, without overt clinical symptoms[8]. However, once symptoms occur, the artery is severely damaged and cerebral ischemia can ensue, a common fatal outcome in CUD[1,9].

Significant advances in multi-modal imaging for early detection of atherosclerosis in asymptomatic populations who are at increased risk for vascular disease (*e.g.*, individuals with high cholesterol, Type II diabetes mellitus) have proven efficacy for preventive treatment[10,11]. Thus, characterizing the atherosclerotic cascade with magnetic resonance imaging (MRI) and positron emission tomography (PET) in asymptomatic individuals at cardiovascular risk can help delineate disease stage and inform on medication choices and follow-up[10,11]. The presence of inflammation captured by PET- with 18F-fluorodeoxyglucose (^{18}F-FDG) is an important indicator of early stage disease progression and validation that the cause of vascular pathology is indeed atherosclerosis. For the purpose of imaging vascular inflammation, FDG is internalized (but not metabolized as in brain FDG) by tissues with active anaerobic metabolism, such as inflamed areas. ^{18}F-FDG PET can quantify inflammation in atherosclerotic plaques[12-14] and has been correlated consistently with plaque macrophage content (white blood cells that increase inflammation and stimulate the immune system) in atherosclerotic rabbits[15] and patients[12,16,17]. An important indication of atherosclerosis overall burden is assessed using MR, an excellent modality for evaluating the blood vessel wall. The MR sequence uses black (or dark) blood techniques, in which the blood appears black and the arterial wall can be seen, accurately depicting plaque presence, size, and morphology with sub-millimeter resolution and high reproducibility, providing new indices of atherosclerotic burden that can be applied in large scale studies to varied populations[6].

Thus, PET with FDG can detect early disease stages and simultaneous MR is used to quantify atherosclerosis burden. Such simultaneous PET/MRI[10,11] has never been used for early detection of vascular pathology in asymptomatic drug addicted individuals. Targeting this population for early detection is of urgency now that the "Crack generation" of the mid 1980s is aging[18]. Owing to decades of cocaine and comorbid tobacco and alcohol use, these individuals with CUD (iCUD) are at particularly high risk for vascular disease and atherosclerosis. Hence, the characterization of atherosclerosis by multimodal imaging can help to detect early signs of disease and inform treatment trials with non-invasive end-points. We applied imaging protocols with PET/MRI of the bilateral carotids for measuring markers of cardiovascular risk for the first time in iCUD. We hypothesize that iCUD will have elevated inflammation and carotid plaque burden as compared to non-addicted controls and even as compared to non-addicted individuals with established cardiovascular risk who are a decade older.

MATERIALS AND METHODS

iCUD and healthy controls

We studied a group of iCUD (n = 14), a group of non-addicted healthy controls (n = 10), and a group of non-addicted individuals with cardiovascular risk (n = 62). Individuals with CUD and non-addicted healthy controls were recruited using advertisement in websites, local newspapers, bulletin boards, and by word-of-mouth with calls for imaging in individuals with cocaine problems or healthy controls. Subjects were given a complete physical examination that included electrocardiography and laboratory tests of renal, hepatic, pancreatic, hematopoietic, and thyroid functions to ensure good physical health. Drug use was assessed with urine tests in all subjects on screening day and pregnancy was tested in women on screening as well as on imaging visits. In addition, on screening day alcohol use was measured with a breathalyzer and tobacco use was measured by levels of nicotine and cotinine in blood. An in-depth interview included the following instruments for assessing inclusion/exclusion criteria: The Structured Clinical Interview for the Diagnostic and Statistical Manual-IV of Axis I Disorders (research version[19,20]) for psychiatric diagnostics. Addiction Severity Index[21], a semi-structured interview provided an estimate of the years of drug/alcohol and severity of use and a detailed assessment for recent and lifetime history of use of various drugs including alcohol. We supplement this interview with brief, well-validated, instruments of addiction severity to assess potential covariates: Cocaine Selective Severity Assessment Scale[22] evaluated cocaine withdrawal symptoms occurring over the past 24 h, Cocaine Craving Questionnaire assessed cocaine craving symptoms over the past 24 h[23], and Severity of Dependence Scale[24,25] examined the severity of addiction during the past

12 mo.

Inclusion criteria: (1) Ability to understand and give informed consent; (2) age 35-65 years; (3) Primary current diagnosis of CUD for the iCUD group; diagnoses for tobacco and alcohol use disorders were allowed; (4) Framingham score of < 10%-20% in iCUD and controls; and (5) right-handed. Exclusion criteria: (1) Urine positive for any psychoactive drugs (except cocaine in iCUD) or their metabolites tested on the day of screening; (2) Psychiatric disorders with psychosis and pervasive developmental disorders such as autism; (3) Head trauma with loss of consciousness > 30 min; (4) Present or past history of neurological disease of central origin (including seizures); (5) Any cardiovascular disease or abnormal vital signs; (6) Any other medical condition (*e.g.*, diabetes mellitus) that may alter cerebral function, endocrinological, oncological or autoimmune diseases; (7) Pregnant or breast feeding; and (8) Counter-indications to PET scanning and metal implants or other counter-indicators to MRI.

Non-addicted individuals with cardiovascular risk

In addition to our healthy control comparison group, MRI values in iCUD were compared with values of existing data[11] from 62 non-addicted individuals (age 64.6 ± 7.8, 83% males), with the following inclusion criteria: (1) Ability to understand and give informed consent; (2) Men and women aged 18–75 years; (3) Previous known coronary heart disease or at high risk of coronary heart disease (diabetes or a 10-year risk of coronary heart disease events > 20% by Framingham Risk scoring), triglyceride concentrations of 400 mg/dL or lower (≤ 4.5 mmol/L), and carotid or aortic arterial wall (target) to background (blood) ratio (TBR) of 1.6 or higher, as identified by ^{18}F-FDG uptake measured by PET/CT during the screening period; and (4) Clinically stable and receiving appropriate and stable treatment with a statin or other low-density lipoprotein (LDL)-C lowering drugs with LDL-C concentrations of 100 mg/dL or lower (< 2.6 mmol/L) unless receiving maximum tolerated doses of therapy or intolerant to statins. Exclusion criteria included: (1) Concomitant treatment with fibrates or nicotinic acid; (2) Presence of uncontrolled blood pressure or diabetes (HbA_{1c} >10%); and (3) Recent (< 3 mo) clinically significant coronary or cerebral vascular event, diagnosis of familial hypercholesterolaemia, or a glomerular filtration rate lower than 30 mL/min. Other reasons for exclusion were standard for this type of trial, as previously described[11].

Imaging

Carotid PET/MR image acquisition: ^{18}F-FDG PET was used to evaluate arterial inflammation within the right and left carotid of the subjects[10,11,26]. Participants were imaged at rest in supine position 90 min after injection of 10mCi of 18-FDG[13]. MRI sequences for PET attenuation correction were acquired while the FDG was still circulating. 3-D dark-blood MRI imaging of the internal carotid arteries extending 3 cm below and above the carotid bifurcations using a 4-channel carotid coil was conducted. After localization with gradient echo sequences, time-of-flight images were acquired to delineate vessel lumen (interior of the vessel). Then, dark blood images were obtained using 3D SPACE with multiple contrast weightings. Proton density weighted, T1 and T2 weighted images were acquired[27-29], during free breathing[30,31], un-triggered with fat suppression, with template based attenuation correction as previously validated[26]. PET data for one subject, right and left carotid MRI data of one subject, and right carotid MRI data of a third subject were not analyzable for iCUD.

Analysis of inflammation by PET: Image analysis of PET/MRI data was performed using OsiriX MD (Pixmeo, Geneva, Switzerland). T2 TSE MRI images of the head and neck were fused with PET images of the same region and analyzed in the axial plane. The technique employed has been previously described in other studies[10,32]. The common carotid artery was assessed where it was well delineated from its most caudal extent up to the level of the carotid bifurcation. Using the closed polygon drawing tool, the common carotid artery was traced on the fused images. MRI signal differences between the target and adjacent tissue were used as guidelines to best mark the region of interest (ROI). The right and left carotid arteries were analyzed separately, as the bifurcation is often not at the same level when comparing the two sides. The mean and maximum standardized uptake values (SUV) of the target vessel were measured for each slice.

Background was measured within the jugular veins using an oval drawing tool to acquire five measurements of at least 10 mm^2 on both the right and left sides for a total of 10 measurements. The lowest fused image SUVmean-slice within each slice of the jugular vein was chosen for background ROI placement. The SUVmean-background represents the average of the SUVmean-slice values acquired from the 10

background slices. TBR mean and maximum were then calculated by dividing respectively the target SUVmean of a slice and the target SUVmax of a slice by the SUVmean-background. The TBRmean-overall and TBRmax-overall represent the average of the metric's values when considering all slices evaluated for each artery. The most diseased segment (MDS) is defined as the highest TBRmax-slice and that of its two adjacent slices and the TBR of the MDS (TBR-MDS) is the average of the TBRmax-slice of this three level segment. Calculations were made using Excel (Microsoft, Washington, USA).

Analysis of atherosclerotic burden by MRI: 3D-SPACE MRI images of the neck were obtained and reformatted into the axial plane prior to analysis. Using these reformatted 'black blood' MRI images, the carotid arteries were analyzed at a dedicated workstation running the software program VesselMASS, (VesselMASS, Division of Image Processing, Department of Radiology, Leiden University Medical Center, Leiden, Netherlands). The technique used has been previously described in other studies[33,34]. As with the MR/PET analysis, the common carotid artery was assessed separately and bilaterally in the slices where each vessel was well delineated, from its most caudal extent up to the level of the carotid bifurcation. The metrics acquired for each vessel included: lumen area, wall area, total vessel area, wall thickness and wall thickness SD. A normalized wall index was also calculated to account for arterial wall size differences that are found within each subject.

Statistical analyses

Statistical analysis was conducted in SPSS (IBM Corp., Version 23.0. Armonk, NY) to compare between the iCUD and the healthy control group on demographics and drug use by a two samples *t*-tests (two-tailed). Comparisons of PET/MR measurements between the iCUD and the healthy controls groups were conducted by univariate analysis of covariance (ANCOVA) while controlling for age. Comparisons of MRI measurements between the iCUD and the group of individuals with cardiovascular risk were conducted by one sample *t*-tests (two-tailed) using the mean values of the group of individuals with cardiovascular risk (since only mean values were available for this group). Associations between the findings that differed between the iCUD and the healthy control group and drug use measures were examined by partial correlations with age and nicotine lifetime use (which differed significantly between the groups) as covariates. A familywise correction for multiple correlations at significance level of $P = 0.05$ was applied.

RESULTS

Participants

Cocaine addicted individuals were slightly older than non-addicted healthy controls and about a decade younger than those with cardiovascular risk. The race distribution was unequal, with more African Americans in the iCUD group. There were no differences between the iCUD and non-addicted healthy controls in gender, education, body mass index, and resting heart rate. Framingham risk scores were available only for a limited number of participants (3 iCUD scored 8.7 ± 3.6 *vs* 6 healthy controls 2.7 ± 2.1, $P < 0.05$). iCUD were chronic users with 21.9 ± 7.9 years of cocaine use, 20.8 ± 11.8 years of alcohol use, and 9.1 ± 10.5 years of cannabis use; 64% were current smokers whereas in the healthy controls 10.0% were current and 20.0% were past smokers (groups differences on lifetime use of cocaine, cannabis, and nicotine smoking, $P < 0.001$; alcohol lifetime use did not differ between the iCUD and healthy control groups) (Table 1).

Imaging results

According to norms established in clinical research studies of risk detection[35,36], TBR ≥ 1.6 is indicative of inflamed plaque. The PET FDG results showed that both iCUD (85%) and the healthy controls (90%) had slightly inflamed plaque in one or both carotid arteries. There were no significant differences in plaque inflammation between the iCUD and the non-addicted healthy controls measured by maximum target-to-background ratios and measures of most diseased segment (Table 2).

The MRI measures demonstrated that the iCUD had significantly elevated carotid plaque burden as compared to the non-addicted healthy controls and the group of individuals with cardiovascular risk (Figure 1 and Figure 2, Table 2). The ANCOVA results showed that, as compared to the healthy controls, the iCUD group had significantly increased wall thickness and wall area. Notably, in one sample *t*-tests using the individuals with cardiovascular risk comparison group's mean values, a similar pattern of elevated plaque in iCUD was observed as follows: iCUD had

Table 1 Sample characteristics: Demographics, cardiovascular risk, and drug use

	Group 1: Cardiovascular risk[15] (n = 62)	Group 2: Healthy controls (n = 10)	Group 3: Cocaine users (n = 14)
Demographics			
Race	62 white (94%); 4 other	5 black (50%); 4 white; 1 other	13 black (93%); 1 white
Gender	55 men (83%)	8 men (80%)	10 men (71%)
Age[ad]	64.6 ± 7.8	46.2 ± 5.3	50.8 ± 4.1
Education	NA	15.0 ± 2.0	13.6 ± 1.8
Cardiovascular risk			
BMI	NA	29.1 ± 5.0	28.3 ± 3.7[1]
Heart rate	NA	74.9 ± 11.9	79.1 ± 10.9
Total cholesterol	NA	182.7 ± 28.2[2]	163.3 ± 28.9[3]
HDL cholesterol	NA	55.8 ± 16.1[4]	42.3 ± 9.1[5]
Drug use			
Alcohol lifetime	NA	18.9 ± 13.4	20.8 ± 11.8
Cocaine lifetime	NA	NA	21.9 ± 7.9
Nicotine lifetime[f]	12% current	10.0% current; 20.0% past; 70.0% never; 3.5 ± 8.1	64.3% current; 28.6% past; 7.1% never; 26.4 ± 10.1
THC lifetime[e]	NA	0.5 ± 1.3	9.1 ± 10.5
Cocaine withdrawal[22]	NA	NA	18.6 ± 11.9
Cocaine craving[23]	NA	NA	14.7 ± 14.5
Severity of drug dependence[24]	NA	NA	3.2 ± 3.6

[1]n = 13.
[2]n = 7.
[3]n = 4.
[4]n = 6.
[5]n = 3. Cardiovascular risk > cocaine users:
[a]P < 0.001. Healthy controls < cocaine users:
[d]P < 0.05,
[e]P < 0.01,
[f]P < 0.001. Cocaine Selective Severity Assessment Scale[22] (range: 0-126). Cocaine Craving Questionnaire[23] (range: 0-45). Severity of Dependence Scale[24] (range: 0-15). NA: Not available; BMI: Body Mass index; THC: Tetrahydrocannabinol.

significantly thicker wall, whereas the cardiovascular risk group and healthy controls did not differ on this measure indicating the presence of more plaque and worse structural disease state in the carotids of iCUD than the much older symptomatic comparison sample, who has been identified for risk for cardiovascular events. Using the cardiovascular risk comparison group's mean values for wall area, significant differences were detected when compared with healthy controls but differences did not reach significance when compared with iCUD.

Testing whether these elevated inflammation markers in iCUD correlated with addiction symptoms, we found that plaque burden (wall area) was positively associated with the degree of cocaine withdrawal and craving even after controlling for age and nicotine use and also familywise error correcting for multiple analyses. The greater the cocaine withdrawal symptoms (r = 0.838, P_{uncorr} = 0.003, $P_{corr.}$ = 0.021) and the greater the cocaine craving (r = 0.787, $P_{uncorr.}$ = 0.007, $P_{corr.}$ = 0.049) the larger the wall area in iCUD (Figure 3). No correlations with PET inflammation markers were found.

DISCUSSION

In this study, we conducted noninvasive vascular PET/MR imaging of the bilateral carotid arteries in iCUD and two control groups. Elevated markers of carotid artery atherosclerotic disease burden were found in iCUD as compared to non-addicted healthy controls and even as compared to older non-addicted individuals with high risk for cardiovascular disease. Specifically, the MRI measure of carotid wall structure showed higher thickness in the iCUD as compared to the healthy controls and cardiovascular risk group, indicating greater carotid plaque burden. The iCUD also had larger wall area as compared to the healthy controls (a difference that did not reach significance when compared to the cardiovascular risk group), indicating

Table 2 Positron emission tomography/magnetic resonance imaging results by group

	Group 1: Cardiovascular risk[15] (*n* = 62)	Group 2: Cocaine users (*n* = 13)	Group 3: Healthy controls (*n* = 10)	Group 2 and 3 difference [Sig. (ANCOVA)]
PET results				
Target-to-Background ratios (TBR max)				
Left	NA	1.77 ± 0.10	1.77 ± 0.07	F (1, 20) = 0.3, P = 0.619
Right	NA	1.93 ± 0.09	1.76 ± 0.04	F (1, 20) = 1.9, P = 0.178
R+L	NA	1.85 ± 0.09	1.76 ± 0.05	F (1, 20)= -0.2, P = 0.687
Most diseased segment				
Left	NA	2.05 ± 0.15	1.99 ± 0.09	F (1, 20) = 0.0, P = 0.914
Right	NA	2.10 ± 0.10	1.93 ± 0.07	F (1, 20) = 1.3, P = 0.259
R+L	NA	2.07 ± 0.11	1.96 ± 0.08	F (1, 20) = 0.4, P = 0.560
MR results				
Wall thickness (mm; mean, SE)				
Left	NA	1.53 ± 0.06	1.25 ± 0.04	F (1, 20) = 7.6, P = 0.012
Right	NA	1.50 ± 0.07 [1]	1.20 ± 0.05	F (1, 19) = 8.3, P = 0.009
R+L	1.27 ± 0.04; t(12)[2] = 4.12, P = 0.001	1.51 ± 0.06[2]	1.22 ± 0.04 [3]	F (1, 20) = 100, P = 0.005
Wall area (mm^2)				
Left	NA	35.67 ± 2.25	29.02 ± 1.54	F (1, 20) = 3.3, P = 0.086
Right	NA	34.51 ± 2.06[1]	27.37 ± 1.43	F (1, 19) = 4.9, P = 0.039
R + L	32.28 ± 1.43; t(9)[4] = -3.13, P = 0.012	35.18 ± 1.95 [5]	28.19 ± 1.31[4]	F (1, 20) = 4.9, P = 0.039

[1]n = 12.
[2]Cocaine users > Cardiovascular risk: P < 0.001.
[3]Cardiovascular disease risk and healthy controls group difference: t(9) = -1.12, P = 0.294.
[4]Cardiovascular risk > healthy controls: P < 0.05.
[5]Cocaine users and Cardiovascular risk group difference: t(12) = 1.49, P = 0.163. NA: Not available.

structural wall abnormalities that reached levels of those in the cardiovascular risk group. These elevated cardiovascular disease markers were associated with elevated degree of cocaine withdrawal and craving in iCUD, indicating a relationship between the extent of substance use disorder and the development of atherosclerosis.

The carotid FDG-PET images indicating the presence of inflammation did not differ between the iCUD and non-addicted healthy controls, as most of these individuals had inflammatory presence in one side or bilaterally in the carotid arteries. This result may indicate the beginning of an atherosclerosis process in all subjects with inflammation levels (*i.e.*, TBR) over 1.6[35,36], yet, overall the detected inflammatory levels in both samples were mild to moderate.

A most intriguing aspect of this study is the comparison with the cardiovascular risk group, whereby the iCUD group showed the most severe elevations in wall thickness (with similar results that did not reach significance also for the wall area). The thickening of the arterial wall to form an atherosclerotic plaque is a process in which cholesterol deposition, inflammation, extracellular-matrix formation and thrombosis have important roles[6,37]. Thus, although many of the healthy control participants showed some inflammation in the carotids (PET results), only iCUD showed a statistically significant elevation as compared with the cardiovascular risk group in the indices of plaque burden. Atherosclerosis and progression to cardiovascular disease are characterized by a slow and "silent" disease accumulation that occurs over decades and progress from a chronic inflammatory condition that can be converted into an acute clinical event by plaque rupture and thrombosis[38]. Since iCUD in this study had over 20 years of lifetime cocaine use as well as nicotine and alcohol it is possible that they passed the inflammatory disease stage and have progressed into an atherosclerosis disease state with a clear vascular structural impact (*i.e.*, the formation of plaques). Interestingly, iCUD who had increased carotid plaque burden also had greater withdrawal and craving, which have been implicated with negative outcomes of cocaine dependence[22,23].

Caveats and future studies

These preliminary results should be considered in light of several caveats which limit the generalizability of the findings, including small sample size, the limited number of

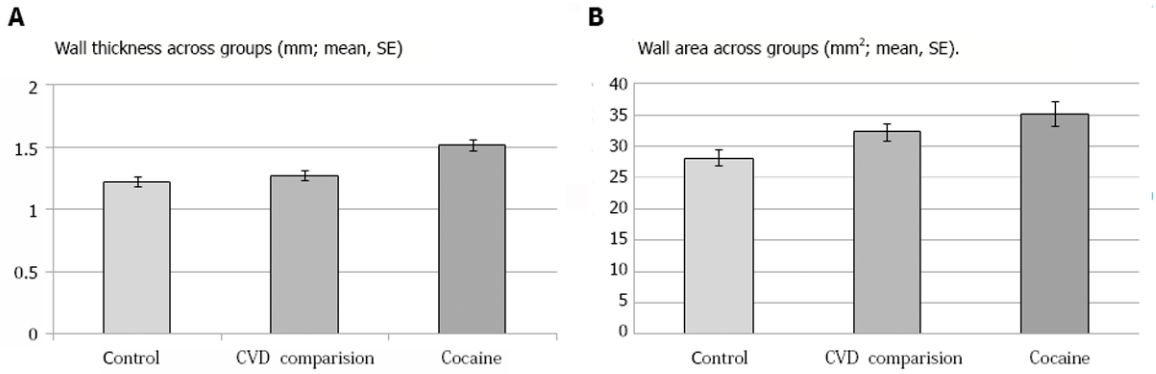

Figure 1 Positron emission tomography/magnetic resonance imaging results by group. A: Wall thickness across groups; B: Wall area across groups. CVD: Cardiovascular disease.

women, and the absence of a match on race. Race is very important for cardiovascular disease with African-American individuals showing greater progression of coronary atherosclerosis as compared to Caucasians[39]. Notably, among African-American men, cocaine was the largest contributor to overdose deaths[40]. Therefore, close matching on race in similar future studies could reduce potential bias in results. Despite considerable efforts, recruitment of healthy control individuals who match the iCUD group on years of nicotine smoking was also a challenge. While nicotine smoking, which is part of the phenomenology of CUD (frequently concomitant with multiple substance use), was accounted for in analyses, matching between groups on nicotine use could provide a better approximation of the vascular effects of cocaine use. Data for PET-^{18}FDG in the cardiovascular risk group and data for calculating Framingham Risk Scores for the full sample were not available. The cross sectional design of the study further limited tracking of disease progression as should be done in future studies. Thus, examining iCUD with less years of lifetime cocaine use and those in earlier stages of the addiction disease could provide opportunities for further stratification of the progression of atherosclerosis disease, even prior to structural narrowing of the arteries. In addition, longitudinal studies should explore whether preventive cardiovascular measures will combat disease progression and may also reduce addiction symptoms. Early detection and preventive intervention protocols will thus await the results of a broader trial.

Conclusion

Given the known vascular toxicity induced by cocaine[1,41] and the progressing age of the crack generation, there is a public health imperative for early detection of the preclinical markers of atherosclerosis in iCUD[42-44]. Once pathology is identified, and especially if identified at an early stage, timely intervention can be deployed to prevent the progression into severe impairments, emergency cardiovascular events and premature mortality.

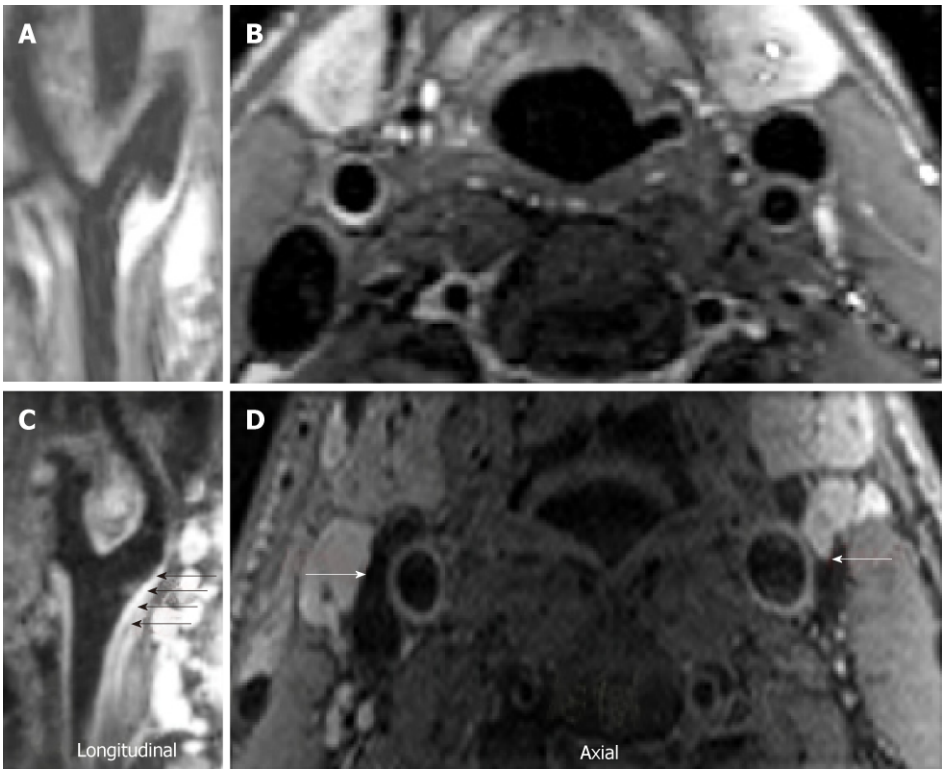

Figure 2 Dark blood magnetic resonance imaging images. A, B: Healthy vessel in a control subject; C, D: Increased carotid wall thickness (arrows) and area in a cocaine addicted individual. A and C show longitudinal images of the left carotid bifurcation. B and D show axial images of the lateral carotid.

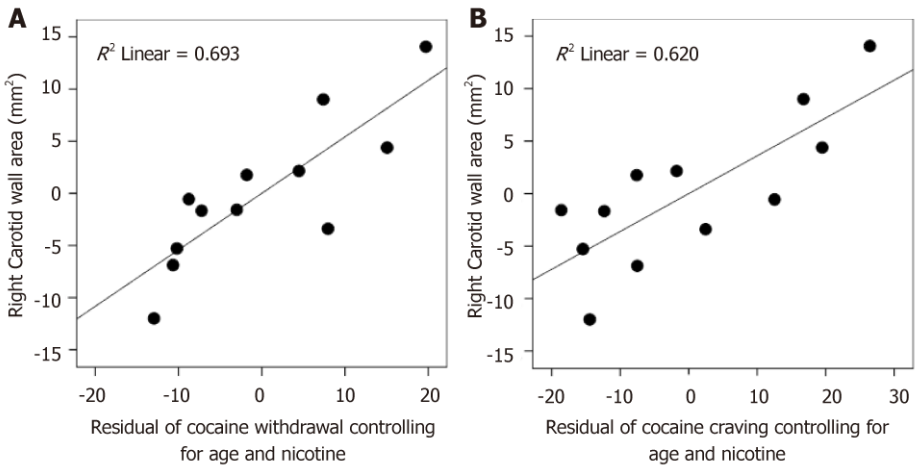

Figure 3 Partial correlation plot. A: Wall area associations with Cocaine withdrawal symptoms, controlled for age and nicotine; B: Wall area associations with Cocaine craving, controlled for age and nicotine.

ARTICLE HIGHLIGHTS

Research background

Cocaine is one of the most commonly illicit drugs involved in emergency department visits, amounting to a vast social and economic burden. Cocaine use disorder (CUD), a chronic relapsing condition, frequently leads to life-threatening vascular disease including stroke, coronary artery disease and myocardial infarction. Cocaine's main vasoactive metabolite benzoylmethylecgonine, a tropane alkaloid, is associated with hematological effects on the vessel and the loss of the endothelium's protective functions leading to elevated immune state including macrophage proliferation, atherosclerosis, and ischemic vascular disease. The life-style associated with chronic cocaine use (poor sleep and nutrition) further affects cardiovascular health.

Research motivation
Despite the known vascular toxicity associated with cocaine use, individuals with (iCUD) seeking addiction treatment receive mostly psychotherapy and psychiatric pharmacotherapy with no attention to vascular disease in the absence of clear symptoms. Little is known about the pre-clinical signs of cardiovascular risk in iCUD and early signs of vascular disease are undetected in this underserved population.

Research objectives
We aim to assess inflammation composition and plaque burden in individuals with cocaine use disorder aiming to quantify markers of atherosclerosis and vascular disease. The characterization of vascular disease in iCUD with no pre-clinical cardiovascular symptoms can inform development of future preventive and treatment protocols.

Research methods
Advancements in multi-modal imaging technologies have been efficacious in early detection of atherosclerosis in asymptomatic populations who are at heightened risk for vascular disease. Simultaneous magnetic resonance imaging (MRI) and positron emission tomography (PET) allows for the precise quantification of inflammatory composition and plaque burden during a single non-operator dependent scan.

The bilateral carotid arteries were imaged with PET/MRI in iCUD asymptomatic for cardiovascular disease, healthy controls, and MRI in individuals with cardiovascular risk. PET with 18F-fluorodeoxyglucose evaluated vascular inflammation and 3-D dark-blood MRI assessed plaque burden including wall area and thickness. Addiction questionnaires assessed drug use and severity of addiction.

Research results
The MRI measure of wall structure was thicker in iCUD as compared to the controls and even as compared with the cardiovascular risk group, indicating greater carotid plaque burden. iCUD had also statistically significant larger wall area as compared to the healthy controls but not as compared to the cardiovascular risk group (the later results did not reach significance). These findings indicate structural wall similarities between the iCUD and cardiovascular risk study groups.

The majority of iCUD and controls had carotid FDG-PET signal greater than Target-to-Background ratios (TBR max) 1.6, indicating the presence of inflammation, yet, overall the observed inflammatory levels in both groups were mild (TBR max level under 3). In iCUD, wall area correlated with greater cocaine withdrawal and craving.

Research conclusions
For the first time in cocaine addiction, this preliminary study used noninvasive simulations PET/MRI vascular imaging of the bilateral carotid arteries in cardiovascular disease-asymptomatic iCUD and two control groups, including healthy individuals and those with cardiovascular disease risk. Aligned with study hypothesis, we observed markers of elevated carotid artery plaque burden in iCUD, reaching similar (wall area) and even exceeding (wall thickness) levels of those in cardiovascular risk group. This plaque burden in iCUD was positively associated with extent of cocaine withdrawal and craving symptoms, indicative of a relationship between the severity of addiction and vascular disease state.

Several caveats limit generalizability of findings, including a small sample size, the limited number of women, and variance between groups in race and nicotine smoking. These factors were covaried in the current analyses, nonetheless, matching between groups in future studies would provide a better approximation of cardiovascular disease in iCUD.

Research perspectives
This PET/MRI investigation showed that markers of cardiovascular disease abnormalities were detected in iCUD with no presenting clinical symptoms. Expanding this line of research to examination of iCUD with fewer years of lifetime cocaine use could provide further stratification of cardiovascular disease progression in this population. Broader trials are warranted to develop protocols for early detection of cardiovascular risk and preventive intervention in individuals with cocaine use disorder.

REFERENCES

1 **Schwartz BG**, Rezkalla S, Kloner RA. Cardiovascular effects of cocaine. *Circulation* 2010; **122**: 2558-2569 [PMID: 21156654 DOI: 10.1161/CIRCULATIONAHA.110.940569]

2 **Afonso L**, Mohammad T, Thatai D. Crack whips the heart: a review of the cardiovascular toxicity of cocaine. *Am J Cardiol* 2007; **100**: 1040-1043 [PMID: 17826394 DOI: 10.1016/j.amjcard.2007.04.049]

3 **Bachi K**, Mani V, Jeyachandran D, Fayad ZA, Goldstein RZ, Alia-Klein N. Vascular disease in cocaine addiction. *Atherosclerosis* 2017; **262**: 154-162 [PMID: 28363516 DOI: 10.1016/j.atherosclerosis.2017.03.019]

4 **Narvaez JC**, Magalhães PV, Fries GR, Colpo GD, Czepielewski LS, Vianna P, Chies JA, Rosa AR, Von Diemen L, Vieta E, Pechansky F, Kapczinski F. Peripheral toxicity in crack cocaine use disorders. *Neurosci Lett* 2013; **544**: 80-84 [PMID: 23597759 DOI: 10.1016/j.neulet.2013.03.045]

5 **Fox HC**, D'Sa C, Kimmerling A, Siedlarz KM, Tuit KL, Stowe R, Sinha R. Immune system inflammation in cocaine dependent individuals: implications for medications development. *Hum Psychopharmacol* 2012; **27**: 156-166 [PMID: 22389080 DOI: 10.1002/hup.1251]

6 **Sanz J**, Fayad ZA. Imaging of atherosclerotic cardiovascular disease. *Nature* 2008; **451**: 953-957 [PMID: 18288186 DOI: 10.1038/nature06803]

7 **Shirai T**, Hilhorst M, Harrison DG, Goronzy JJ, Weyand CM. Macrophages in vascular inflammation--From atherosclerosis to vasculitis. *Autoimmunity* 2015; **48**: 139-151 [PMID: 25811915 DOI: 10.3109/08916934.2015.1027815]

8 **Fleg JL**, Stone GW, Fayad ZA, Granada JF, Hatsukami TS, Kolodgie FD, Ohayon J, Pettigrew R, Sabatine MS, Tearney GJ, Waxman S, Domanski MJ, Srinivas PR, Narula J. Detection of high-risk atherosclerotic plaque: report of the NHLBI Working Group on current status and future directions. *JACC Cardiovasc Imaging* 2012; **5**: 941-955 [PMID: 22974808 DOI: 10.1016/j.jcmg.2012.07.007]

9 **De Giorgi A**, Fabbian F, Pala M, Bonetti F, Babini I, Bagnaresi I, Manfredini F, Portaluppi F, Mikhailidis DP, Manfredini R. Cocaine and acute vascular diseases. *Curr Drug Abuse Rev* 2012; **5**: 129-134 [PMID: 22455504 DOI: 10.2174/1874473711205020129]

10 **Fayad ZA**, Mani V, Woodward M, Kallend D, Bansilal S, Pozza J, Burgess T, Fuster V, Rudd JH, Tawakol A, Farkouh ME. Rationale and design of dal-PLAQUE: a study assessing efficacy and safety of dalcetrapib on progression or regression of atherosclerosis using magnetic resonance imaging and 18F-fluorodeoxyglucose positron emission tomography/computed tomography. *Am Heart J* 2011; **162**: 214-221.e2 [PMID: 21835280 DOI: 10.1016/j.ahj.2011.05.006]

11 **Fayad ZA**, Mani V, Woodward M, Kallend D, Abt M, Burgess T, Fuster V, Ballantyne CM, Stein EA, Tardif JC, Rudd JH, Farkouh ME, Tawakol A; dal-PLAQUE Investigators. Safety and efficacy of dalcetrapib on atherosclerotic disease using novel non-invasive multimodality imaging (dal-PLAQUE): a randomised clinical trial. *Lancet* 2011; **378**: 1547-1559 [PMID: 21908036 DOI: 10.1016/S0140-6736(11)61383-4]

12 **Davies JR**, Izquierdo-Garcia D, Rudd JH, Figg N, Richards HK, Bird JL, Aigbirhio FI, Davenport AP, Weissberg PL, Fryer TD, Warburton EA. FDG-PET can distinguish inflamed from non-inflamed plaque in an animal model of atherosclerosis. *Int J Cardiovasc Imaging* 2010; **26**: 41-48 [PMID: 19784796 DOI: 10.1007/s10554-009-9506-6]

13 **Rudd JH**, Elkhawad M, Fayad ZA. Vascular imaging with 18F-FDG PET/CT: optimal 18F-FDG circulation time? *J Nucl Med* 2009; **50**: 1560; author reply 1560-1560; author reply 1561 [PMID: 19690022 DOI: 10.2967/jnumed.109.066456]

14 **Rudd JH**, Myers KS, Bansilal S, Machac J, Pinto CA, Tong C, Rafique A, Hargeaves R, Farkouh M, Fuster V, Fayad ZA. Atherosclerosis inflammation imaging with 18F-FDG PET: carotid, iliac, and femoral uptake reproducibility, quantification methods, and recommendations. *J Nucl Med* 2008; **49**: 871-878 [PMID: 18483100 DOI: 10.2967/jnumed.107.050294]

15 **Zhang Z**, Machac J, Helft G, Worthley SG, Tang C, Zaman AG, Rodriguez OJ, Buchsbaum MS, Fuster V, Badimon JJ. Non-invasive imaging of atherosclerotic plaque macrophage in a rabbit model with F-18 FDG PET: a histopathological correlation. *BMC Nucl Med* 2006; **6**: 3 [PMID: 16725052 DOI: 10.1186/1471-2385-6-3]

16 **Rudd JH**, Myers KS, Bansilal S, Machac J, Rafique A, Farkouh M, Fuster V, Fayad ZA. (18)Fluorodeoxyglucose positron emission tomography imaging of atherosclerotic plaque inflammation is highly reproducible: implications for atherosclerosis therapy trials. *J Am Coll Cardiol* 2007; **50**: 892-896 [PMID: 17719477 DOI: 10.1016/j.jacc.2007.05.024]

17 **Rudd JH**, Narula J, Strauss HW, Virmani R, Machac J, Klimas M, Tahara N, Fuster V, Warburton EA, Fayad ZA, Tawakol AA. Imaging atherosclerotic plaque inflammation by fluorodeoxyglucose with positron emission tomography: ready for prime time? *J Am Coll Cardiol* 2010; **55**: 2527-2535 [PMID: 20513592 DOI: 10.1016/j.jacc.2009.12.061]

18 **Bachi K**, Sierra S, Volkow ND, Goldstein RZ, Alia-Klein N. Is biological aging accelerated in drug addiction? *Curr Opin Behav Sci* 2017; **13**: 34-39 [PMID: 27774503 DOI: 10.1016/j.cobeha.2016.09.007]

19 **First MB**, Gibbon M, Williams J. Structured Clinical Interview for DSM-IV Axis I disorders - Patient Edition (SCID-I/P, Version 2.0). New York: Biometrics Research Department, New York State Psychiatric Institute 1996;

20 **Ventura J**, Liberman RP, Green MF, Shaner A, Mintz J. Training and quality assurance with the Structured Clinical Interview for DSM-IV (SCID-I/P). *Psychiatry Res* 1998; **79**: 163-173 [PMID: 9705054 DOI: 10.1016/S0165-1781(98)00038-9]

21 **McLellan AT**, Kushner H, Metzger D, Peters R, Smith I, Grissom G, Pettinati H, Argeriou M. The Fifth Edition of the Addiction Severity Index. *J Subst Abuse Treat* 1992; **9**: 199-213 [PMID: 1334156 DOI: 10.1016/0740-5472(92)90062-S]

22 **Kampman KM**, Volpicelli JR, McGinnis DE, Alterman AI, Weinrieb RM, D'Angelo L, Epperson LE. Reliability and validity of the Cocaine Selective Severity Assessment. *Addict Behav* 1998; **23**: 449-461 [PMID: 9698974 DOI: 10.1016/S0306-4603(98)00011-2]

23 **Tiffany ST**, Singleton E, Haertzen CA, Henningfield JE. The development of a cocaine craving questionnaire. *Drug Alcohol Depend* 1993; **34**: 19-28 [PMID: 8174499 DOI: 10.1016/0376-8716(93)90042-O]

24 **Gossop M**, Griffiths P, Powis B, Strang J. Severity of dependence and route of administration of heroin, cocaine and amphetamines. *Br J Addict* 1992; **87**: 1527-1536 [PMID: 1458032 DOI: 10.1111/j.1360-0443.1992.tb02660.x]

25 **Gossop M**, Darke S, Griffiths P, Hando J, Powis B, Hall W, Strang J. The Severity of Dependence Scale (SDS): psychometric properties of the SDS in English and Australian samples of heroin, cocaine and amphetamine users. *Addiction* 1995; **90**: 607-614 [PMID: 7795497 DOI: 10.1046/j.1360-0443.1995.9056072.x]

26 **Zaidi H**, Ojha N, Morich M, Griesmer J, Hu Z, Maniawski P, Ratib O, Izquierdo-Garcia D, Fayad ZA, Shao L. Design and performance evaluation of a whole-body Ingenuity TF PET-MRI system. *Phys Med Biol* 2011; **56**: 3091-3106 [PMID: 21508443 DOI: 10.1088/0031-9155/56/10/013]

27 **Itskovich VV**, Samber DD, Mani V, Aguinaldo JG, Fallon JT, Tang CY, Fuster V, Fayad ZA. Quantification of human atherosclerotic plaques using spatially enhanced cluster analysis of multicontrast-weighted magnetic resonance images. *Magn Reson Med* 2004; **52**: 515-523 [PMID: 15334569 DOI: 10.1002/mrm.20154]

28 **Yuan C**, Hatsukami TS, Cai J. MRI plaque tissue characterization and assessment of plaque stability. *Stud Health Technol Inform* 2005; **113**: 55-74 [PMID: 15923737 DOI: N/A]

29 **Yuan C**, Mitsumori LM, Ferguson MS, Polissar NL, Echelard D, Ortiz G, Small R, Davies JW, Kerwin WS, Hatsukami TS. In vivo accuracy of multispectral magnetic resonance imaging for identifying lipid-rich necrotic cores and intraplaque hemorrhage in advanced human carotid plaques. *Circulation* 2001; **104**:

2051-2056 [PMID: 11673345 DOI: doi:10.1161/hc4201.097839]
30 **Mani V**, Itskovich VV, Aguiar SH, Mizsei G, Aguinaldo JG, Samber DD, Macaluso FM, Fayad ZA. Comparison of gated and non-gated fast multislice black-blood carotid imaging using rapid extended coverage and inflow/outflow saturation techniques. *J Magn Reson Imaging* 2005; **22**: 628-633 [PMID: 16215965 DOI: 10.1002/jmri.20428]
31 **Mani V**, Itskovich VV, Szimtenings M, Aguinaldo JG, Samber DD, Mizsei G, Fayad ZA. Rapid extended coverage simultaneous multisection black-blood vessel wall MR imaging. *Radiology* 2004; **232**: 281-288 [PMID: 15220509 DOI: 10.1148/radiol.2321031022]
32 **Mani V**, Woodward M, Samber D, Bucerius J, Tawakol A, Kallend D, Rudd JH, Abt M, Fayad ZA. Predictors of change in carotid atherosclerotic plaque inflammation and burden as measured by 18-FDG-PET and MRI, respectively, in the dal-PLAQUE study. *Int J Cardiovasc Imaging* 2014; **30**: 571-582 [PMID: 24458953 DOI: 10.1007/s10554-014-0370-7]
33 **Mani V**, Muntner P, Gidding SS, Aguiar SH, El Aidi H, Weinshelbaum KB, Taniguchi H, van der Geest R, Reiber JH, Bansilal S, Farkouh M, Fuster V, Postley JE, Woodward M, Fayad ZA. Cardiovascular magnetic resonance parameters of atherosclerotic plaque burden improve discrimination of prior major adverse cardiovascular events. *J Cardiovasc Magn Reson* 2009; **11**: 10 [PMID: 19393089 DOI: 10.1186/1532-429X-11-10]
34 **Wong SK**, Mobolaji-Iawal M, Arama L, Cambe J, Biso S, Alie N, Fayad ZA, Mani V. Atherosclerosis imaging using 3D black blood TSE SPACE vs 2D TSE. *World J Radiol* 2014; **6**: 192-202 [PMID: 24876923 DOI: 10.4329/wjr.v6.i5.192]
35 **Abdelbaky A**, Tawakol A. Noninvasive Positron Emission Tomography Imaging of Coronary Arterial Inflammation. *Curr Cardiovasc Imaging Rep* 2011; **4**: 41-49 [PMID: 21379370 DOI: 10.1007/s12410-010-9062-4]
36 **Tawakol A**, Migrino RQ, Bashian GG, Bedri S, Vermylen D, Cury RC, Yates D, LaMuraglia GM, Furie K, Houser S, Gewirtz H, Muller JE, Brady TJ, Fischman AJ. In vivo 18F-fluorodeoxyglucose positron emission tomography imaging provides a noninvasive measure of carotid plaque inflammation in patients. *J Am Coll Cardiol* 2006; **48**: 1818-1824 [PMID: 17084256 DOI: 10.1016/j.jacc.2006.05.076]
37 **Fernández-Ortiz A**, Jiménez-Borreguero LJ, Peñalvo JL, Ordovás JM, Mocoroa A, Fernández-Friera L, Laclaustra M, García L, Molina J, Mendiguren JM, López-Melgar B, de Vega VM, Alonso-Farto JC, Guallar E, Sillesen H, Rudd JH, Fayad ZA, Ibañez B, Sanz G, Fuster V. The Progression and Early detection of Subclinical Atherosclerosis (PESA) study: rationale and design. *Am Heart J* 2013; **166**: 990-998 [PMID: 24268213 DOI: 10.1016/j.ahj.2013.08.024]
38 **Lusis AJ**. Atherosclerosis. *Nature* 2000; **407**: 233-241 [PMID: 11001066 DOI: 10.1038/35025203]
39 **Kataoka Y**, Hsu A, Wolski K, Uno K, Puri R, Tuzcu EM, Nissen SE, Nicholls SJ. Progression of coronary atherosclerosis in African-American patients. *Cardiovasc Diagn Ther* 2013; **3**: 161-169 [PMID: 24282765 DOI: 10.3978/j.issn.2223-3652.2013.08.05]
40 **Shiels MS**, Freedman ND, Thomas D, Berrington de Gonzalez A. Trends in U.S. Drug Overdose Deaths in Non-Hispanic Black, Hispanic, and Non-Hispanic White Persons, 2000-2015. *Ann Intern Med* 2018; **168**: 453-455 [PMID: 29204603 DOI: 10.7326/M17-1812]
41 **Finkel JB**, Marhefka GD. Rethinking cocaine-associated chest pain and acute coronary syndromes. *Mayo Clin Proc* 2011; **86**: 1198-1207 [PMID: 22134939 DOI: 10.4065/mcp.2011.0338]
42 **Aquaro GD**, Gabutti A, Meini M, Prontera C, Pasanisi E, Passino C, Emdin M, Lombardi M. Silent myocardial damage in cocaine addicts. *Heart* 2011; **97**: 2056-2062 [PMID: 21690608 DOI: 10.1136/hrt.2011.226977]
43 **D'Agostino RB**, Russell MW, Huse DM, Ellison RC, Silbershatz H, Wilson PW, Hartz SC. Primary and subsequent coronary risk appraisal: new results from the Framingham study. *Am Heart J* 2000; **139**: 272-281 [PMID: 10650300 DOI: 10.1016/S0002-8703(00)90236-9]
44 **Farooq MU**, Bhatt A, Patel M. Neurotoxic and cardiotoxic effects of cocaine and ethanol. *J Med Toxicol* 2009; **5**: 134-138 [PMID: 19655286 DOI: 10.1007/BF03161224]

World Journal of Radiology

Submit a Manuscript: https://www.f6publishing.com

World J Radiol 2019 May 28; 11(5): 74-80

DOI: 10.4329/wjr.v11.i5.74

ISSN 1949-8470 (online)

CASE REPORT

Malignant epidermoid arising from the third ventricle: A case report

Samadhan Pawar, Chaitanya Borde, Atul Patil, Rajnish Nagarkar

ORCID number: Samadhan Pawar (0000-0001-5057-158X); Chaitanya Borde (0000-0002-6627-6048); Atul Patil (0000-0002-5007-0993); Rajnish Nagarkar (0000-0002-8045-842X).

Author contributions: All authors contributed to this paper.

Informed consent statement: Written signed informed consent was obtained from the patient.

Conflict-of-interest statement: All authors have no conflicts of interest to report.

CARE Checklist (2016) statement: Guidelines of the CARE Checklist (2016) have been adopted while writing this manuscript.

Manuscript source: Unsolicited manuscript

Received: February 20, 2019
Peer-review started: February 22, 2019
First decision: March 14, 2019
Revised: April 4, 2019
Accepted: May 14, 2019
Article in press: May 15, 2019

Samadhan Pawar, Chaitanya Borde, Atul Patil, Rajnish Nagarkar, Department of Radiodiagnosis, HCG Manavata Cancer Centre, Nashik 422011, Maharashtra, India

Corresponding author: Samadhan Pawar, MD, Doctor, Consultant Radiologist, Department of Radiodiagnosis, HCG Manavata Cancer Centre, Off Nashik Expresswa, Near Mylan Circle, Nashik 422011, Maharashtra, India. academics@manavatacancercentre.com
Telephone: +91-98-19021567

Abstract

BACKGROUND

Third epidermoid tumors are a rare finding. The appearance of these tumors often makes them difficult to diagnose, and thus they require multimodality imaging.

CASE SUMMARY

A 48-year-old male patient reported to our hospital with complaints of vomiting and severe headache. The patient also complained of involuntary micturition for the past five days. We used a combination of computed tomography (CT) and magnetic resonance imaging (MRI) imaging modalities to confirm the presence of a malignant epidermoid cyst arising from the third ventricle. A contrast-enhanced CT of the head demonstrated minimal perilesional enhancement while an MRI revealed a large, lobulated and septated T2 hyperintense mass arising from the third ventricle. The maximum size of the lesion measured 73 mm × 65 mm × 64 mm in size.

CONCLUSION

Malignant epidermoid arising from the third ventricle in an adult male was reported using a combination of CT, MRI, and MR spectroscopy.

Key words: Epidermoid; Third ventricle; Magnetic resonance imaging; Case report

Core tip: The use of multi-modality imaging can help radiologist diagnose uncommon tumors in unusual sites. The combination of computed tomography, magnetic resonance imaging, and MR spectroscopy was useful in confirming the diagnosis of malignant epidermoid arising from the third ventricle, an unusual site in routine practice.

Citation: Pawar S, Borde C, Patil A, Nagarkar R. Malignant epidermoid arising from the third ventricle: A case report. *World J Radiol* 2019; 11(5): 74-80

Published online: May 28, 2019

P-Reviewer: Tang GH, Wasnik AP
S-Editor: Ji FF
L-Editor: A
E-Editor: Xing YX

URL: https://www.wjgnet.com/1949-8470/full/v11/i5/74.htm
DOI: https://dx.doi.org/10.4329/wjr.v11.i5.74

INTRODUCTION

Epidermoid cysts are an uncommon finding in routine clinical settings. They are slow-growing, benign tumors that grow in the extra-axial areas. Epidermoid cysts account for less than 1% of all intracranial tumors[1]. Intracranial dermoid cysts are often observed in the cranial midline, sub-frontal areas, posterior fossa, and suprasellar cistern[2]. Intraventricular dermoid cysts are extremely rare and have been reported in the fourth ventricle[2]. Current imaging modalities have made it possible to recognize intracranial tumors[3]. The use of radiologic diagnosis for third ventricle epidermoid cysts is almost always possible.

We present a case of epidermoid cysts in the third ventricle in an adult male.

CASE PRESENTATION

Chief complaints

A 48-year-old male presented to our outpatient department with vomiting, headache, and involuntary micturition.

History of present illness

The above-mentioned symptoms had been present for five days.

History of past illness

The patient had no history of major illness.

Personal and family history

The patient had no relevant family history.

Physical examination upon admission

The patient had no pallor. General condition of the patient was normal.

Laboratory examinations

The patient's routine laboratory investigations were within normal limits.

Imaging examinations

A non-contrast computed tomography scan of the head revealed a mass arising from the third ventricle appearing hypodense and showing coarse nodular as well as curvilinear calcifications (Figure 1).

A contrast-enhanced computed tomography (CT) of the head demonstrated minimal perilesional enhancement. The lesion obstructed the hydrocephalus of the lateral ventricles (Figure 2). No dilatation of the fourth ventricle was observed. The lesion measured 8-10 Hounsfield units. The maximum size of the lesion measured 77x57 mm on CT scan.

Magnetic resonance imaging (MRI) of the lesion revealed a large, lobulated, septated T2 hyperintense mass arising from the third ventricle (Figure 3B). It was hypointense on T1-weighted imaging with few cystic areas (Figure 3A). Few calcifications were observed within the cystic areas. On diffusion-weighted magnetic resonance imaging, the lesion showed increased restricted diffusion (Figure 3D). The lesion obstructed the hydrocephalus and caused moderate dilatation of the bilateral lateral ventricles. No dilation of the fourth ventricle was observed. On contrast-enhanced CT scan, the lesion showed minimal peripheral enhancement without any demonstrable solid enhancing component. The maximum size of the lesion measured 73 mm × 65 mm × 64 mm in size (Figure 4).

On MR spectroscopy, there was high lipid/lactate peak with comparatively lower N-acetylaspartate (NAA) and choline levels. The maximum choline (Cho)/creatine ratio was 2.85 within the lesion and CHO/NAA ratio was 0.766 (Figure 5). MR perfusion derived relative cerebral blood volume (rCBV) maps demonstrating heterogeneous perfusion abnormalities. Mild higher normalized rCBV ratios in comparison with white matter were noted in the peripheral region of the cyst, which corresponded to malignant transformation (Figure 6).

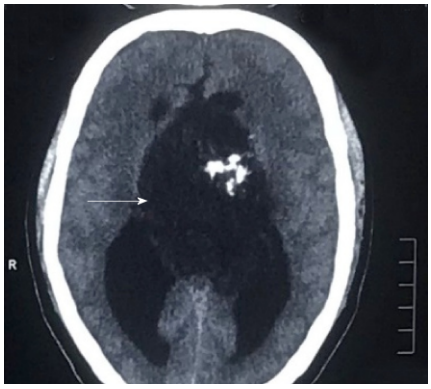

Figure 1 A non-contrast computed tomography scan of the head showing a mass arising from the third ventricle appearing hypodense and showing coarse nodular as well as curvilinear calcifications.

FINAL DIAGNOSIS

Considering the imaging findings, we suspected the lesion to be an epidermoid, dermoid, or an arachnoid cyst. However, we ruled out the diagnosis of a dermoid or arachnoid cyst considering the presence of a restricted diffusion on diffusion-weighted imaging (DWI). A combination of T1WI, T2WI, T2 axial FLAIR, and DW imaging techniques helped us diagnose an epidermoid cyst. However, the use of MR spectroscopy helped in making the probable diagnosis of a malignant epidermoid cyst arising from the third ventricle.

TREATMENT

The patient underwent craniotomy coupled with intra-hemisphere excision of the tumor. The patient was given levetiracetam 500 mg twice a day.

OUTCOME AND FOLLOW-UP

The patient is stable and currently doing well.

DISCUSSION

Epidermoid cysts are slow-growing and often benign congenital tumors that comprise 0.2%-1.8% of primary intracranial neoplasms[4]. The first epidermoid cysts were described by an artist in 1807 in a French medical school[5]. The French pathologist Cruveilhier gave the first full description of epidermoid cysts[6]. From a histological point of view, epidermoid cysts often resemble the linear growth rate of the skin[5]. They are made up of a thin epithelium lining that appears pearly white and smooth macroscopically. Epidermoid tumors often have a high content of cholesterol and an internal core composed of desquamated epithelial keratin that is distinctive on MR imaging and allied radiological modalities[5].

To the best of our knowledge, intracranial epidermoid cysts are located off the midline. The most common location of epidermoids includes the region within the cerebellopontine angle (CPA)[7]. Intracranial epidermoids account for the third most common tumor in the CPA region followed by vestibular schwannoma and meningioma[7].

There have been more than 100 cases of epidermoids reported in the fourth ventricle, followed by the parasellar and sellar regions[8]. However, epidermoids may also be found in the lobes of the cerebral hemisphere, spine, and brainstem[8].

To the best of our knowledge, third ventricular epidermoid tumors are extremely rare. Patients with epidermoid tumors often present with signs and symptoms such as headache, seizures, cranial nerve defects, raised intracranial pressure, and cerebral signs[8]. Our patient presented with headache and vomiting.

Epidermoids appear as well-defined lobulated, round hypoattenuated masses on CT imaging. However, there have been reports where uniformly hyperdense epidermoids have been reported on CT imaging, which are associated with a calcium

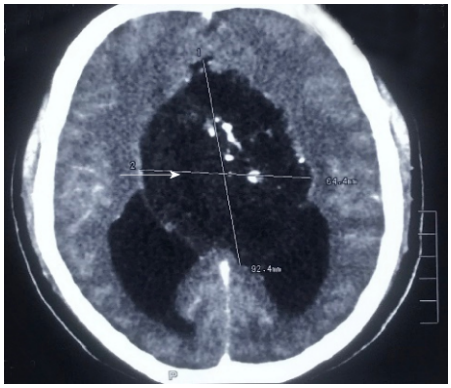

Figure 2 A contrast-enhanced computed tomography of the head demonstrates minimal perilesional enhancement. The lesion obstructs the hydrocephalus of lateral ventricles (Figure 2). The maximum size of lesion measures 77 mm × 57 mm on computed tomography scan.

constitution or high protein content[9,10]. Epidermoids appear hyperintense on T2 weighted and hypointense on T1 weighted MRI imaging[7]. In our case, we observed a hyperintense T2 weighted mass on MRI imaging. Lastly, MR spectroscopy showed an increase in the lactate peak, which was indicative of anaerobic metabolism. There was an increase in the Cho/NAA ratio, which is generally observed in neoplasms. The Cho/Cr ratio increased to 2.85.

As per current evidence, the major differential diagnosis for a third ventricle includes arachnoid cyst, cystic neoplasm, and dermoid cyst. The differential diagnosis of different third ventricle masses based on different sequences has been mentioned in Table 1. Arachnoid cysts often appear less lobulated and follow a signal intensity patterns similar to those of cerebrospinal fluid with all MR pulse sequences including DWI and FLAIR[11]. Cystic neoplasms, such as cystic ependymoma and cystic medulloblastoma, have a varied appearance on imaging due to the varying degrees of necrosis, calcification, and hemorrhage. The solid component of these lesions often shows heterogeneous contrast enhancement and restriction on DWI[11]. Dermoid cysts are similar to epidermoid cysts, as both are lined by stratified squamous epithelium. In the context of imaging, dermoid cysts show a hyperintense signal on T1-weighted images while they appear as well-defined low attenuating (fat density) lobulated masses on CT scan[11].

The patient underwent craniotomy coupled with intra-hemisphere excision of the tumor. The procedure was uneventful. The patient was administered levetiracetam 500 mg twice a day. The patient is currently doing well. The diagnosis of malignant transformation of an epidermoid cyst arising from the third ventricle is challenging. Our key strengths involved our multidisciplinary approach in diagnosing, treating, and managing the patient. Non-invasive imaging modalities such as MR spectroscopy helped us confirm the diagnosis of a malignant epidermoid cyst from the third ventricle.

CONCLUSION

We have presented a rare case of a third ventricular lesion presumed to be an epidermoid tumor as seen on MRI. The use of multimodality imaging can help radiologists diagnose uncommon tumors in unusual sites. The combination of CT, MRI, and MR spectroscopy was useful in confirming the diagnosis of a malignant epidermoid cyst arising from the third ventricle, an unusual site in routine practice.

Table 1 Differential imaging considerations

Sequences	Epidermoid	Dermoid	Arachnoid cyst	Cystic lesions medulloblastoma	Cystic lesions ependymoma
T1WI	Hypointense	Hyperintense	Hypointense	Hypointense	Hypointense (Solid part)
T2WI	Iso-hyperintense	Hypo-hyperintense	Hyperintense	Heterogenous due to calcification, necrosis, and cyst formation	Foci of blooming (hemorrhage/calcification)
FLAIR	Heterogenous signal higher than CSF	Hyperintense	Hypointense	Heterogeneous signal higher than CSF	Heterogeneous signal higher than CSF
DWI	Restricted diffusion	No restriction	No restriction	Restricted diffusion	Restricted diffusion (Solid part)
Contrast	Non enhancement (in malignant transformation it enhances)	Non-enhancement	Non-enhancement	Heterogeneous enhancement	Heterogeneous enhancement
MR spectroscopy	Choline: + NAA: - Cho/Crt: +	Choline: + NAA: - Cho/Crt: +	Choline: + NAA: - Cho/Crt: +	Choline: ++ NAA: - Cho/Crt: ++ Lipid: + Lactate: +	Choline: ++ NAA: - Cho/Crt ++ Lipid: + Lactate: +
MR perfusion	-	-	-	+++ (solid part)	+++

T1WI: T1 weighted image; T2WI: T2 weighted image; FLAIR: Fluid-attenuated inversion recovery; DWI: Diffusion weighted image; NAA: N-acetylaspartate.

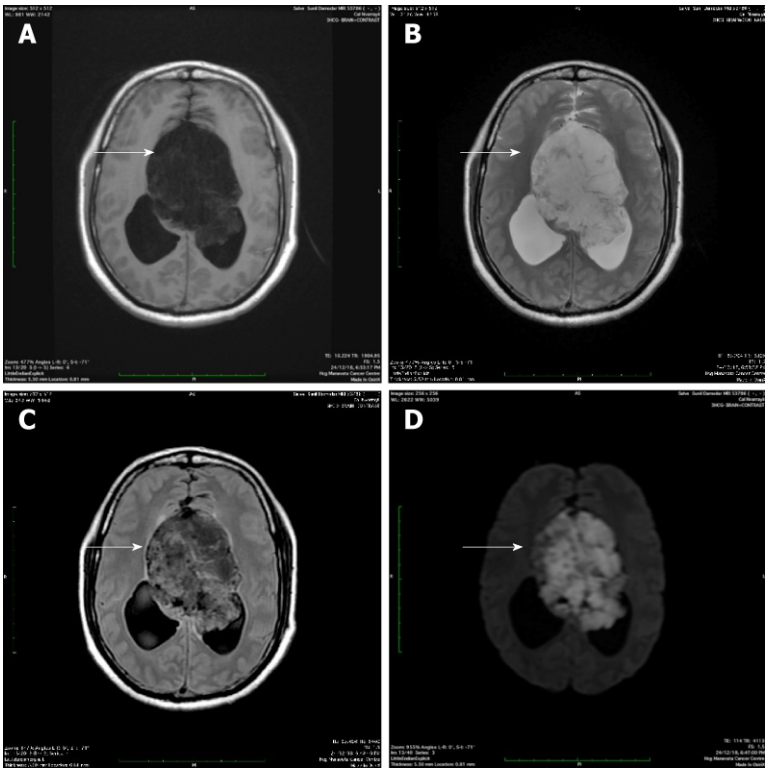

Figure 3 Magnetic resonance imaging. Magnetic resonance imaging revealed a large, lobulated and septated lesion arising from the third ventricle that was: A: Hypointense on T1 weighted imaging; B: Hyperintense on T2 weighted imaging; C: Heterogeneously hyperintense on T2 axial FLAIR imaging; D: Appeared diffusely restricted on diffusion weighted imaging.

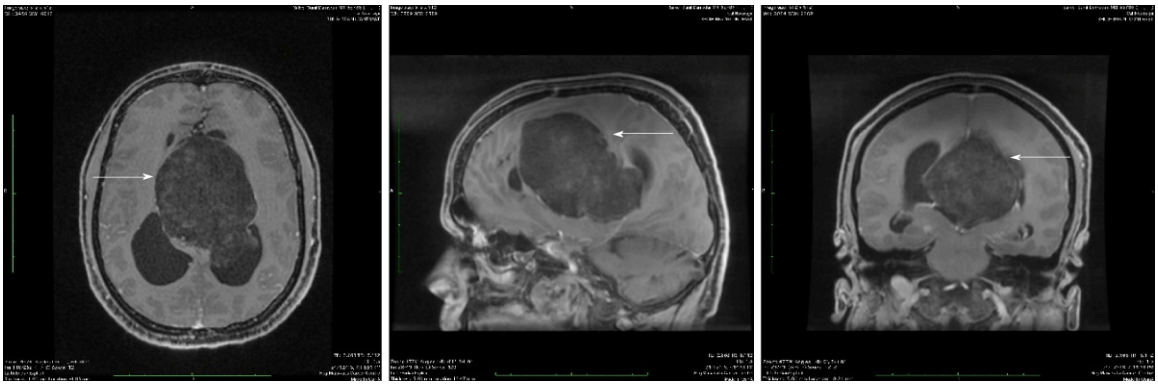

Figure 4 Minimal peripheral enhancement without any demonstrable solid enhancing component. The maximum size of the lesion measures 73 mm × 65 mm × 64 mm in size.

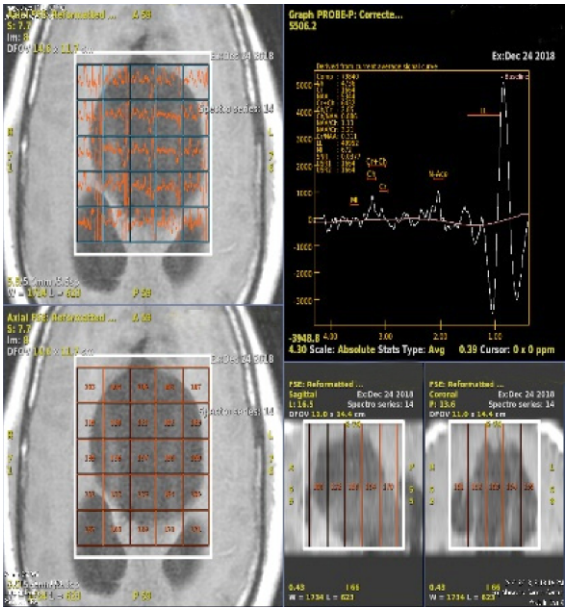

Figure 5 MR spectroscopy. High lipid/lactate peak with comparatively lower N-acetylaspartate and choline levels. Maximum choline/creatine ratio was 2.85 within the lesion and choline/N-acetylaspartate ratio being 0.766.

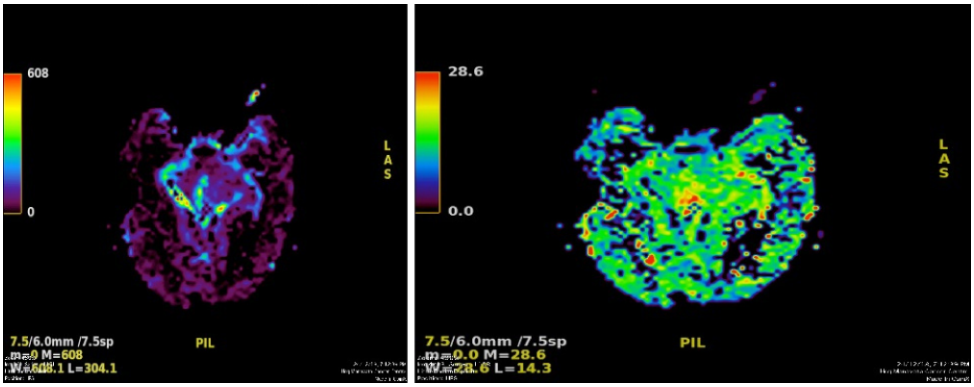

Figure 6 MR perfusion derived relative cerebral blood volume maps demonstrate heterogeneous perfusion abnormalities. Mild higher normalized relative cerebral blood volume ratios in comparison with white matter are noted in the peripheral region of the cyst, which corresponds to malignant transformation.

ACKNOWLEDGEMENTS

We would like to thank Mr. Lyndon Fernandes for his medical writing assistance.

REFERENCES

1 **Law EK**, Lee RK, Ng AW, Siu DY, Ng HK. Atypical intracranial epidermoid cysts: rare anomalies with unique radiological features. *Case Rep Radiol* 2015; **2015**: 528632 [PMID: 25667778 DOI: 10.1155/2015/528632]

2 **Iyer VR**, Sanghvi DA. Third ventricular dermoid: an unusual tumor at an unusual site. *Neurol India* 2008; **56**: 209-210 [PMID: 18688156 DOI: 10.4103/0028-3886.42009]

3 **Ozutemiz C**, Ada E, Ersen A, Ozer E. Imaging Findings of an Epidermoid Cyst with Malignant Transformation to Squamous Cell Carcinoma. *Turk Neurosurg* 2017; **27**: 312-315 [PMID: 27349393 DOI: 10.5137/1019-5149.JTN.12722-14.0]

4 **Patil A**, Kulkarni V, Singh G, Sehrawat P. Fourth ventricle epidermoid tumor: Radiologic findings. *Med J DY Patil Univ* 2016; **9**: 136-139 [DOI: 10.4103/0975-2870.168001]

5 **Kaido T**, Okazaki A, Kurokawa S, Tsukamoto M. Pathogenesis of intraparenchymal epidermoid cyst in the brain: a case report and review of the literature. *Surg Neurol* 2003; **59**: 211-216 [PMID: 12681557 DOI: 10.1016/S0090-3019(02)01042-X]

6 **Kachhara R**, Bhattacharya RN, Radhakrishnan VV. Epidermoid cyst involving the brain stem. *Acta Neurochir (Wien)* 2000; **142**: 97-100 [PMID: 10664382 DOI: 10.1007/s007010050013]

7 **Kallmes DF**, Provenzale JM, Cloft HJ, McClendon RE. Typical and atypical MR imaging features of intracranial epidermoid tumors. *AJR Am J Roentgenol* 1997; **169**: 883-887 [PMID: 9275916 DOI: 10.2214/ajr.169.3.9275916]

8 **Man XR**, Kanodia A, Nicholas R, Main G. A rare case of third ventricular epidermoid cyst as seen by newer MRI sequences. *Int Neuropsychiatr Dis J* 2014; **2**: 68-77 [DOI: 10.9734/INDJ/2014/7009]

9 **Giannotta SL**, Pauli F, Farhat SM. Epidermoid cyst of the third ventricle. *Surg Neurol* 1976; **5**: 164-166 [PMID: 1257889 DOI: 10.1111/j.1600-0404.1967.tb05556.x]

10 **Aribandi M**, Wilson NJ. CT and MR imaging features of intracerebral epidermoid--a rare lesion. *Br J Radiol* 2008; **81**: e97-e99 [PMID: 18270293 DOI: 10.1259/bjr/42146967]

11 **Osborn AG**, Preece MT. Intracranial cysts: radiologic-pathologic correlation and imaging approach. *Radiology* 2006; **239**: 650-664 [PMID: 16714456 DOI: 10.1148/radiol.2393050823]

Published By Baishideng Publishing Group Inc
7041 Koll Center Parkway, Suite 160, Pleasanton, CA 94566, USA
Telephone: +1-925-2238242
Fax: +1-925-2238243
E-mail: bpgoffice@wjgnet.com
Help Desk: https://www.f6publishing.com/helpdesk
https://www.wjgnet.com

ISSN 1949-8470 (online)

World Journal of *Radiology*

World J Radiol 2019 June 28; 11(6): 81-93

Published by Baishideng Publishing Group Inc

WJR World Journal of Radiology

Contents

Monthly Volume 11 Number 6 June 28, 2019

ORIGINAL ARTICLE

Retrospective Cohort Study

Contents

World Journal of Radiology

Volume 11 Number 6 June 28, 2019

ABOUT COVER

Editorial Board Member of *World Journal of Radiology*, Jyoti Kumar, DNB, MD, Professor, Department of Radiodiagnosis, Maulana Azad Medical College, New Delhi 110002, India

AIMS AND SCOPE

World Journal of Radiology (*World J Radiol*, *WJR*, online ISSN 1949-8470, DOI: 10.4329) is a peer-reviewed open access academic journal that aims to guide clinical practice and improve diagnostic and therapeutic skills of clinicians.

The *WJR* covers topics concerning diagnostic radiology, radiation oncology, radiologic physics, neuroradiology, nuclear radiology, pediatric radiology, vascular/interventional radiology, medical imaging achieved by various modalities and related methods analysis. The current columns of *WJR* include editorial, frontier, mini-reviews, review, medical ethics, original articles, case report, *etc*.

We encourage authors to submit their manuscripts to *WJR*. We will give priority to manuscripts that are supported by major national and international foundations and those that are of great basic and clinical significance.

INDEXING/ABSTRACTING

The *WJR* is now abstracted and indexed in Emerging Sources Citation Index (Web of Science), PubMed, PubMed Central, China National Knowledge Infrastructure (CNKI), China Science and Technology Journal Database (CSTJ), and Superstar Journals Database.

RESPONSIBLE EDITORS FOR THIS ISSUE

Responsible Electronic Editor: *Yu-Jie Ma*

Proofing Production Department Director: *Yun-Xiaojian Wu*

NAME OF JOURNAL
World Journal of Radiology

ISSN
ISSN 1949-8470 (online)

LAUNCH DATE
January 31, 2009

FREQUENCY
Monthly

EDITORS-IN-CHIEF
Venkatesh Mani

EDITORIAL BOARD MEMBERS
https://www.wjgnet.com/1949-8470/editorialboard.htm

EDITORIAL OFFICE
Jin-Lei Wang, Director

PUBLICATION DATE
June 28, 2019

INSTRUCTIONS TO AUTHORS
https://www.wjgnet.com/bpg/gerinfo/204

GUIDELINES FOR ETHICS DOCUMENTS
https://www.wjgnet.com/bpg/GerInfo/287

GUIDELINES FOR NON-NATIVE SPEAKERS OF ENGLISH
https://www.wjgnet.com/bpg/gerinfo/240

PUBLICATION MISCONDUCT
https://www.wjgnet.com/bpg/gerinfo/208

ARTICLE PROCESSING CHARGE
https://www.wjgnet.com/bpg/gerinfo/242

STEPS FOR SUBMITTING MANUSCRIPTS
https://www.wjgnet.com/bpg/GerInfo/239

ONLINE SUBMISSION
https://www.f6publishing.com

World Journal of Radiology

Submit a Manuscript: https://www.f6publishing.com

World J Radiol 2019 June 28; 11(6): 81-93

DOI: 10.4329/wjr.v11.i6.81

ISSN 1949-8470 (online)

ORIGINAL ARTICLE

Retrospective Cohort Study

Positron emission tomography/computed tomography imaging appearance of benign and classic "do not touch" osseous lesions

Stacey M Elangovan, Ronnie Sebro

ORCID number: Stacey M Elangovan (0000-0001-5359-9115); Ronnie Sebro (0000-0001-7232-4416).

Author contributions: Elangovan SM and Sebro R designed and performed the research and wrote the paper; Sebro R analyzed the data.

Institutional review board statement: The study was reviewed and approved by the local institutional review board and the need for signed informed consent for each participant was waived.

Informed consent statement: The study was reviewed and approved by the local institutional review board and the need for signed informed consent for each participant was waived.

Conflict-of-interest statement: The authors declare no conflicts of interest

Data sharing statement: Data available upon request from the senior author.

STROBE statement: The manuscript was prepared and revised according to the STROBE Statement-checklist of items.

Stacey M Elangovan, Ronnie Sebro, Department of Radiology, University of Pennsylvania, Philadelphia, PA 19104, United States

Ronnie Sebro, Department of Orthopedic Surgery, University of Pennsylvania, Philadelphia, PA 19104, United States

Ronnie Sebro, Department of Genetics, University of Pennsylvania, Philadelphia, PA 19104, United States

Ronnie Sebro, Department of Biostatistics, Epidemiology and Informatics, University of Pennsylvania, Philadelphia, PA 19104, United States

Corresponding author: Ronnie Sebro, MD, PhD, Assistant Professor, Department of Radiology, University of Pennsylvania, 3400 Spruce Street, Philadelphia, PA 19104, United States. ronnie.sebro@uphs.upenn.edu
Telephone: +1-215-2949512
Fax: +1-215-6153316

Abstract

BACKGROUND

Classic "do not touch" and benign osseous lesions are sometimes detected on ^{18}-F-fluorodeoxyglucose (^{18}F-FDG) positron emission tomography/computed tomography (PET/CT) studies. These lesions are often referred for biopsy because the physician interpreting the PET/CT may not be familiar with the spectrum of ^{18}F-FDG uptake patterns that these lesions display.

AIM

To show that "do not touch" and benign osseous lesions can have increased ^{18}F-FDG uptake above blood-pool on PET/CT; therefore, the CT appearance of these lesions should dictate management rather than the standardized uptake values (SUV).

METHODS

This retrospective study evaluated 287 independent patients with 287 classic "do not touch" (benign cystic lesions, insufficiency fractures, bone islands, bone infarcts) or benign osseous lesions (hemangiomas, enchondromas, osteochondromas, fibrous dysplasia, Paget's disease, osteomyelitis) who underwent ^{18}F-FDG positron emission tomography/computed tomography (PET/CT) at a tertiary academic healthcare institution between 01/01/2006 and 12/1/2018. The maximum and mean SUV, and the ratio of the maximum SUV to mean blood pool were calculated. Pearson's correlations between lesion size and

Manuscript source: Unsolicited manuscript

Received: March 7, 2019
Peer-review started: March 11, 2019
First decision: April 16, 2019
Revised: May 11, 2019
Accepted: June 20, 2019
Article in press: June 21, 2019
Published online: June 28, 2019

P-Reviewer: Bazeed M, Gao BL
S-Editor: Dou Y
L-Editor: A
E-Editor: Ma YJ

maximum SUV were calculated.

RESULTS

The ranges of the maximum SUV were as follows: For hemangiomas (0.95-2.99), bone infarcts (0.37-3.44), bone islands (0.26-3.29), enchondromas (0.46-2.69), fibrous dysplasia (0.78-18.63), osteochondromas (1.11-2.56), Paget's disease of bone (0.93-5.65), insufficiency fractures (1.06-12.97) and for osteomyelitis (2.57-12.64). The range of the maximum SUV was lowest for osteochondromas (maximum SUV 2.56) and was highest for fibrous dysplasia (maximum SUV of 18.63). There was at least one lesion that demonstrated greater ^{18}F-FDG avidity than the blood pool amongst each lesion type, with the highest maximum SUV ranging from 9.34 times blood pool mean (osteomyelitis) to 1.42 times blood pool mean (hemangiomas). There was no correlation between the maximum SUV and the lesion size except for enchondromas. Larger enchondromas had higher maximum SUV (r = 0.36, P = 0.02).

CONCLUSION

The classic "do not touch" lesions and classic benign lesions can be ^{18}F-FDG avid. The CT appearance of these lesions should dictate clinical management rather than the maximum SUV.

Key words: Positron emission tomography/computed tomography; Skeletal-axial; Skeletal-appendicular; "Do not touch" lesions

Core tip: Several benign and "do not touch" osseous lesions have ^{18}F-FDG uptake above blood pool. Clinical management should be based on the CT appearance of these lesions rather than the maximum SUV uptake from PET/CT.

Citation: Elangovan SM, Sebro R. Positron emission tomography/computed tomography imaging appearance of benign and classic "do not touch" osseous lesions. *World J Radiol* 2019; 11(6): 81-93
URL: https://www.wjgnet.com/1949-8470/full/v11/i6/81.htm
DOI: https://dx.doi.org/10.4329/wjr.v11.i6.81

INTRODUCTION

^{18}F-Fluorodeoxyglucose (^{18}F-FDG) positron emission tomography/computed tomography (PET/CT) is increasingly utilized for staging and surveillance of many common malignancies[1,2]. Approximately 1.9 million ^{18}F-FDG PET/CT studies were performed in the United States in 2017, a 13% increase compared to 2015[3]. Cancer cells often switch from oxidative to glucose metabolism, even in the presence of oxygen, resulting in aerobic glycolysis[4], first described by Warburg[5,6]. This change in cancer cell metabolism is easily detected and measured in vivo using ^{18}F-FDG PET/CT[3]. The rapid rise in the number of ^{18}F-FDG PET/CT scans performed annually has the potential to increase the number of incidental findings[7-9]. Simultaneously, there has been increased specialization of radiology with most physicians that interpret ^{18}F-FDG PET/CT not being simultaneously fellowship-trained in musculoskeletal radiology[10-14].

As a result, incidentally detected ^{18}F-FDG-avid osseous lesions are often subject to sometimes inappropriate clinical management. A previous meta-analysis showed that although a general approach to ^{18}F-FDG-avid incidental lesions may be recommended for selected organ systems, osseous lesions remain less amenable to blanket recommendations for or against biopsy, for incidentally noted ^{18}F-FDG-avid osseous lesions[15]. Anecdotally, we have noted a concomitant increase in request for biopsies of incidentally noted ^{18}F-FDG-avid osseous lesions in clinical practice, that, on review by a fellowship musculoskeletal trained radiologist, do not warrant biopsy because these lesions are classic "do not touch lesions" including non-ossifying fibromas, bone islands/enostoses, unicameral bone cysts, bone infarcts, and geodes/subchondral cysts)[16] or have a classic computed tomography (CT) imaging appearance including

fibrous dysplasia, Paget's disease and enchondromas. The "do not touch" osseous lesions are mostly benign osseous lesions; however, some may rarely undergo malignant degeneration. The term "do not touch" was coined by Clyde Helms, and refers to lesions that the radiographic/CT appearance is pathognomic, and additional diagnostic tests, biopsies and surgery involving these lesions may be misleading, potentially harming the patient[16]. Numerous case reports exist in the literature demonstrating that several of these benign lesions have resulted in ^{18}F-FDG-avid osseous lesions and were confirmed histologically by subsequent biopsy[17-22].

While image-guided percutaneous core needle biopsy of osseous lesions is generally regarded as a low-risk procedure, potential complications exist, including patient discomfort and anxiety, infection, bleeding, and the possibility of a non-diagnostic specimen. Non-diagnostic biopsies may occur in 5-29% of cases and may lead to repeat percutaneous or subsequent open biopsy[23,24]. Although the CT imaging characteristics of an osseous lesion may indicate its non-aggressive etiology, clinicians may persistently request biopsies of ^{18}F-FDG-avid osseous lesions in patients that have a primary malignancy elsewhere due to concerns of under-staging or clinical concerns centered around missing osseous metastases.

To date, despite multiple case reports of ^{18}F-FDG-avid benign osseous lesions in the literature, to the best of our knowledge a descriptive analysis of the ^{18}F-FDG uptake of common benign osseous lesions in the musculoskeletal system has not been performed. There are no prior reports demonstrating the spectrum of ^{18}F-FDG uptake patterns of several common benign skeletal osseous lesions with identifiable CT imaging characteristics. If this data existed, then it could be used as a guide for physicians that primarily interpret ^{18}F-FDG PET/CTs and to eliminate referral of these benign lesions for biopsies. The aim of the study is to show that "do not touch" and benign osseous lesions can have increased ^{18}F-FDG uptake above blood-pool, therefore the CT appearance of these osseous lesions should dictate management rather than the PET/CT standardized uptake values (SUV).

MATERIALS AND METHODS

Patient population

This retrospective study included patients who had PET/CT imaging at our institution between January 1, 2006, and December 1, 2018. PET/CT studies were performed for staging or surveillance of malignancies or for the evaluation of a solitary pulmonary nodule. Lesions were identified by retrospective review of radiology text reports using Nuance mPower powered by Montage software (Burlington, MA) to identify potential PET/CT cases by searching for each of the following terms: "bone infarct"; "bone island"; "enchondroma"; "fibrous dysplasia"; "bone cyst or geode or herniation pit or subchondral cyst"; "myositis ossificans"; "osteochondroma"; "Paget's disease"; "hemangioma"; "non-ossifying fibroma"; "insufficiency fracture" and "osteomyelitis".

A sequential search was performed in which radiology text reports were searched first for the lesion of interest regardless of modality using the same search terms described above and then filtered by patients for which a PET/CT was available in the system within 3000 days prior to (excluding insufficiency fractures and infections) or following the study identifying the lesion. Lesions had to be stable in size and appearance for 2 years to confirm their non-aggressive nature. The imaging studies were each reviewed and the final lesion diagnosis was made/confirmed by a musculoskeletal radiologist with 6 years of experience and a musculoskeletal fellow in consensus. Imaging criteria used to classify each bone lesion will be discussed in detail in the discussion.

Non-ossifying fibromas (NOFs) were excluded because there were less than 5 patients with NOFs that had PET/CT imaging of the NOFs in our database, since NOFs typically occur in the extremities and were often excluded using the limited whole body (skull base to upper thigh)[25] field of view (FOV) and because most NOFs involute in early-adulthood.

Myositis ossificans was also excluded because analysis of the small number of cases identified by searching radiology reports.

PET/CT examination acquisition parameters

Lesions were evaluated using one of the following PET/CT units: Philips Ingenuity TF PET/CT (Philips Medical Systems, Patient Port (Bore): 70 cm, Axial FOV: 18 cm, Detector Design: 4 × 4 × 22 mm LYSO crystals, Spatial Resolution: 4.7 mm full width at half maximum (FWHM); Philips Gemini TF small bore (Philips Medical Systems, Patient Port Bore: 70 cm, Reconstructed FOV: 25.6, 57.6, or 67.6 cm, Axial FOV: 18 cm,

Detector Design: 4 × 4 × 22 mm LYSO crystals, Spatial Resolution: 4.7 mm FWHM); or Phillips Gemini TF large bore (Philips Medical Systems, Patient Port Bore: 85 cm, Reconstructed FOV: 25.6, 57.6, or 67.6 cm, Axial FOV: 18 cm, Detector Design: 4 × 4 × 22 mm LYSO crystals, Spatial Resolution: 4.7 mm FWHM).

Patients underwent PET/CT examination according to institutional standard protocol, including fasting for 6 h prior to injection, followed by intravenous injection of 8-20 mCi (296-740 MBq) ^{18}F-FDG, depending on body habitus. Blood glucose levels had to be less than 200 mg/dL (< 11.1 mmol/L) prior to injection. Approximately 225 mL of dilute barium oral contrast was administered before and thirty minutes after the administration of ^{18}F-FDG if included in the imaging protocol. Images were acquired approximately 60 min (+/- 10 min) after the intravenous administration of ^{18}F-FDG with the patient positioned supine on the scan table. Images were acquired from skull-base to thigh or from head to toe according to the imaging protocol, with low-dose CT images followed by PET images. Low-dose CT images were obtained with a slice thickness of 4 mm, pitch of 0.8, tube voltage of 120 kVp, and tube current of 70 mAs.

SUV measurements

SUV measurements were obtained using MIM (version 6.7.10, Mim Software Inc.). A region of interest was drawn around each lesion using the SUV tool and the maximum and mean SUV recorded. Subsequently, the mean and max SUV were also measured for the liver, and for the blood pool, which was measured in the mediastinum at the level of the aorta and main pulmonary artery. The mean (standard deviation) and maximum SUV for each lesion was measured and reported both independently and in relation to the mean blood pool SUV on the examination, measured at the level of the great vessels in the mediastinum, to correct for slight variations in technique that affect SUV measurement [26].

Statistics

Descriptive statistics were calculated using R v3.5 (https://www.r-project.org/). Pearson's correlations between the size of lesions and the maximum SUV were calculated.

Research ethics standards compliance

This retrospective Health Insurance Portability and Accountability Act (HIPAA) compliant study was approved by the local institutional review board (IRB) (Protocol Number: 828078, Confirmation #: Cefchdfh), and the need for signed informed consent was waived.

RESULTS

There were 287 patients with either classic "do not touch" lesions or classic benign lesions. Patient characteristics are summarized in Table 1. Figure 1 shows the ^{18}F-FDG avidity of each lesion type. Benign cystic lesions included subchondral cysts, bone cysts, herniation pits, and geodes. The maximum SUV detected was lowest for osteochondromas (maximum SUV 2.56), enchondromas (maximum SUV 2.69), and hemangiomas (maximum SUV of 2.88). The maximum SUV was highest for Paget's disease of bone (maximum SUV of 5.65), benign cystic lesions (maximum SUV of 6.5), osteomyelitis (maximum SUV of 12.64), insufficiency fractures (maximum SUV of 12.97), and fibrous dysplasia (maximum SUV of 18.63) (Table 2). There was at least one lesion amongst each lesion type evaluated that demonstrated greater ^{18}F-FDG avidity than the blood pool, with the highest maximum SUV ranging from 9.34 times blood pool mean (osteomyelitis) to 1.42 times blood pool mean (hemangioma) (Table 2, Figure 1A and 1B).

There was no correlation between the maximum SUV and the size of benign cystic lesions (r = 0.08, P = 0.60), hemangiomas (r = 0.15, P = 0.44), bone infarcts (r = 0.12, P = 0.37), fibrous dysplasia (r = 0.13, P = 0.48), osteochondromas (r = 0.04, P = 0.95), Paget's disease of bone (r = 0.16, P = 0.50), insufficiency fractures (r = 0.01, P = 0.96) and osteomyelitis (r = 0.15, P = 0.60). However, the size of enchondromas was associated with the maximum SUV (r = 0.36, P = 0.02).

DISCUSSION

The "do not touch" and benign lesions evaluated demonstrated a range of SUV values. All evaluated "do not touch" and benign lesions had at least one lesion with

Table 1 Patient characteristics by lesion type

Lesion type	Mean patient age (yr)	Range patient age (yr)	Male (%)
Benign cystic lesions (n = 42)	63.2	36-92	69.0
Hemangioma (n = 29)	68.5	47-88	55.2
Bone infarct (n = 16)	58.7	33-74	62.5
Bone island (n = 56)	63.0	37-90	50.0
Enchondroma (n = 45)	64.6	52-84	46.7%
Fibrous dysplasia (n = 26)	56.1	28-86	76.9
Osteochondroma (n = 6)	61.3	43-80	100.0
Paget's disease of bone (n = 20)	73.4	59-86	80.0
Insufficiency fracture (n = 32)	69.1	47-89	6.3
Osteomyelitis (n = 15)	62.8	32-83	73.3

Benign cystic lesions: Subchondral cysts, bone cysts, herniation pits, and geodes.

maximum SUV that was greater than and at least one lesion with maximum SUV that was less than the mean blood pool SUV. For this reason, the results suggest that the maximum SUV is not a reliable tool for the characterization of osseous lesions, particularly as benign lesions such as fibrous dysplasia can demonstrate a maximum SUV up to 8.87 times the average blood pool SUV.

These findings are consistent with multiple case reports in the literature that have described pathology-proven benign lesions with high ^{18}F-FDG avidity prompting surgical excision on the basis of the ^{18}F-FDG uptake[7,17-22]. Our results reaffirm that, when specific, the CT characteristics of such lesions need not be accompanied by an SUV at or below that of the blood pool to confidently diagnose a lesion as benign. In fact, SUV values may be misleading, and over-reliance on ^{18}F-FDG uptake to characterize a lesion as benign or malignant may lead to over-diagnosis and unnecessary procedures such as biopsies, which although low-risk, are not risk-free.

Benign cystic lesions, including bone cysts, geodes, and herniation pits, have in common a well circumscribed, lytic appearance [27-30]. All may have a sclerotic rim, although such a rim is only occasionally present in simple bone cysts [27]. The terms geode and herniation pit both describe lesions arising in the setting of reactive changes at the surface of bone, although herniation pits have classically been described in the femoral neck, remote from the articular surface, whereas geodes are subarticular in location and regarded as synonymous with subchondral cysts (Figure 2), although these lesions lack an epithelial lining and are not true cysts[31]. Subchondral cysts/geodes are often accompanied by other signs of joint degeneration including subchondral sclerosis and eburnation as well as marginal osteophyte formation. Subchondral cysts are more common in the elderly. These lesions are lytic on CT and may show increased ^{18}F-FDG uptake on PET.

Osseous hemangiomas are most commonly seen in the vertebral bodies, but may occur in the calvarium, calcaneus, and long bones [28]. Vertebral body hemangiomas have a characteristic striated appearance on radiographs and a corresponding "polka dot" appearance on axial CT images (Figure 3A)[28]. On MRI, hemangiomas typically have high signal on both T1- and T2-weighted images[32] and commonly show loss of signal on in- and out-of-phase gradient sequences[33]. The PET/CT appearance is similar to the CT appearance, with some lesions showing increased ^{18}F-FDG uptake on PET.

The term "bone infarct" is commonly used to refer to osteonecrosis seen in the metaphyses and diaphyses of bones [34], whereas osteonecrosis occurring in the epiphysis is commonly referred to as avascular necrosis. On CT, these lesions may demonstrate a serpentine rim of sclerosis (Figure 3B), although this may not be seen early in the disease course [32]. Bone infarcts have a similar appearance on PET/CT to CT, but may show variable amounts of ^{18}F-FDG uptake on PET. On MRI, these lesions demonstrate a characteristic serpentine rim of low signal with variable internal signal [34]. Bone infarcts rarely undergo malignant degeneration, most commonly into osteosarcoma, pleomorphic sarcoma and fibrosarcoma, but here malignant degeneration is characterized by development of a soft tissue mass, cortical destruction and in some cases development of a pathological fracture [35].

Bone islands, or enostoses, are benign osteoblastic lesions consisting of dense intramedullary lamellar bone that appear on CT as hyperdense oval lesions with spiculated margins and are classically periarticular (Figure 4A)[28]. The data presented

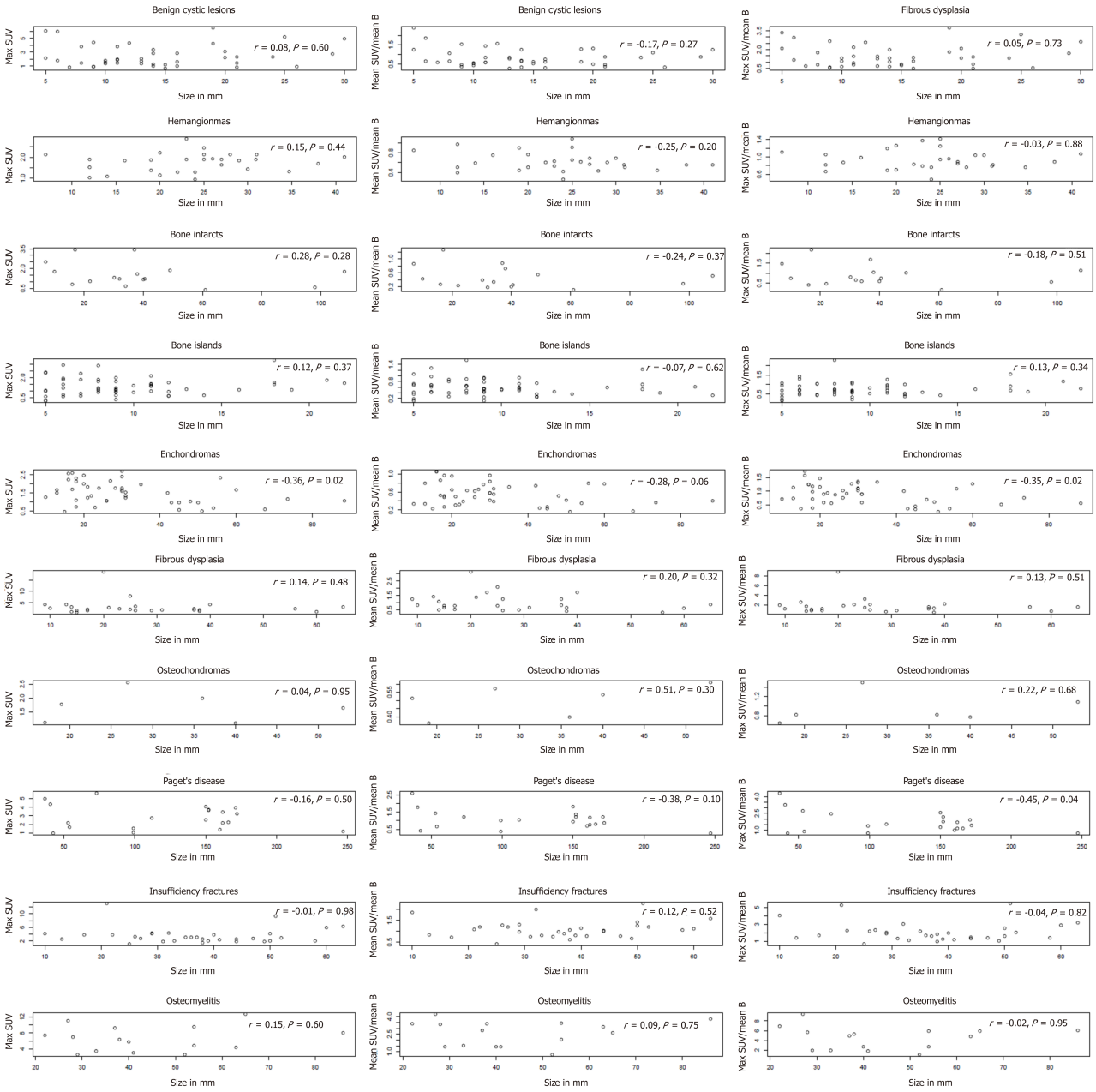

Figure 1 Plots of maximum standardized uptake value values, mean standardized uptake value/mean blood pool, and maximum standardized uptake value/blood pool by lesion size for each lesion type. SUV: Standardized uptake value; Max SUV: Maximum standardized uptake value; Mean SUV/Mean B: Mean standardized uptake value divided by the mean blood pool uptake; Max SUV/Mean B: Maximum standardized uptake value divided by the mean blood pool uptake.

show that enostoses appear similar on PET/CT to CT and may show ^{18}F-FDG uptake on PET above background. Although osteoblastic metastatic lesions may have a similar appearance, bone islands can be identified with high sensitivity and specificity by their higher attenuation value on CT[36]. On MRI, osteoblastic metastases may also show a halo of surrounding bone marrow edema, which may help distinguish these lesions from bone islands[28].

Enchondromas are benign lesions that typically occur within long bones. Enchondromas histologically represent rests of hyaline cartilage within medullary bone. Radiographically, enchondromas are expansile lucent lesions with a narrow zone of transition and varying degrees of ring-and-arc mineralization (Figure 4B)[28], although mineralization may be absent when these lesions are seen in the hands and feet. Enchondromas are almost never seen involving the flat bones (ribs, pelvis, scapula) or spine. Distinguishing between enchondromas and chondrosarcomas can be challenging, both by imaging features and by histology[37]. Malignant degeneration may be seen and is more common (20%-50%) in patients with Ollier disease or Maffucci syndrome[28]. Malignant degeneration is characterized by increase in size of lesion after skeletal maturity and pain[37,38]. A prior report suggested that a maximum

Table 2 18-F-fluorodeoxyglucose positron emission tomography/computed tomography standardized uptake value by lesion type

Lesion type	Range of the max SUV	Median (interquartile range) of the max SUV	Mean SUV (SD)	Proportion with max SUV > 3.0 (%)	Maximum SUV/mean blood Pool SUV range	Maximum SUV /mean blood pool SUV median (interquartile range)	Proportion of lesions with maximum SUV > mean blood pool (maximum SUV/mean blood pool SUV > 1.0) (%)
Benign cystic lesions (*n* = 42)	0.68-6.5	1.90 (1.34-3.27)	1.38 (0.86)	28.6	0.5-3.74	1.29 (0.76-1.94)	64.3
Hemangioma (*n* = 29)	0.95-2.88	1.86 (1.38-2.00)	1.14 (0.30)	0	0.49-1.42	0.88 (0.78-1.05)	34.5
Bone infarct (*n* = 16)	0.37-3.44	1.27 (0.95-1.80)	0.80 (0.54)	12.5	0.15-2.18	0.75 (0.57-1.08)	37.5
Bone island (*n* = 56)	0.26-3.29	1.18 (0.91-1.73)	1.04 (0.52)	1.8	0.13-2.28	0.69 (0.53-0.98)	25.0
Enchondroma (*n* = 45)	0.46-2.69	1.49 (1.05-1.98)	0.93 (0.43)	0.0	0.25-1.72	0.90 (0.58-1.15)	42.2
Fibrous dysplasia (*n* = 26)	0.78-18.63	2.07 (1.56-3.04)	1.80 (1.40)	30.8	0.49-8.87	1.35 (0.89-1.93)	69.2
Osteochondroma (*n* = 6)	1.11-2.56	1.71 (1.25-1.93)	0.89 (0.09)	0	0.64-1.50	0.82 (0.78-1.02)	33.3
Paget's disease of bone (*n* = 20)	0.93-5.65	2.59 (1.66-3.79)	1.77 (0.82)	45.0	0.70-4.30	1.45 (1.10-2.23)	75.0
Insufficiency fracture (*n* = 32)	1.06-12.97	2.95 (2.05-4.09)	1.82 (0.68)	46.9	0.64-5.43	1.76 (1.33-2.25)	90.6
Osteomyelitis (*n* = 15)	2.57-12.64	6.40 (3.99-8.63)	3.77 (1.31)	80.0	1.07-9.34	4.88 (2.34-5.88)	100

Benign cystic lesions: Subchondral cysts, bone cysts, herniation pits, and geodes. SUV: Standardized uptake value.

SUV > 4.4 was 99% specific for grade 2/3 chondrosarcoma[39]. Biopsy of low-grade chondroid matrix lesions, such as enchondromas, is of limited utility because enchondromas may be histologically mistaken for low-grade chondrosarcomas and vice versa. Enchondromas have a similar appearance on PET/CT to CT and radiographs, but may show variable amounts of ^{18}F-FDG uptake on PET. The data suggest that the size of the enchondroma is associated with higher maximum SUV; however, it is unclear whether this confers a potentially higher risk for chondrosarcoma. Development of a soft tissue mass with cortical destruction is highly suspicious for malignant degeneration.

Fibrous dysplasia is due to a post-natal sporadic mutation in the G-nucleotide binding protein alpha sub unit (GNAS) and results in development of fibrous tissue with ground-glass matrix on radiographs and CT studies[40]. Fibrous dysplasia may have areas of cystic change on CT. The PET/CT appearance of fibrous dysplasia is identical to its appearance on CT; however, fibrous dysplasia may be metabolically active and show increased ^{18}F-FDG uptake. Fibrous dysplasia may be monostotic or polyostotic. McCune-Albright syndrome is associated with polyostotic fibrous dysplasia, café au lait macules and hyperfunctioning endocrinopathies, which may include precocious puberty, hyperthyroidism or Cushing's syndrome. Mazabraud syndrome is characterized by fibrous dysplasia with intramuscular myxomas. Fibrous dysplasia typically affects ribs and long bones (femur, tibia, and humerus), and may result in a Shepherd's crook deformity of the femurs. Fibrous dysplasia may involve the bones of the face/jaw and result in disfigurement, or involve the spine and result in scoliosis. Approximately 1% of patients will have a lesion that undergoes malignant degeneration, most commonly into osteosarcoma, fibrosarcoma or undifferentiated pleomorphic sarcoma[40,41]. Malignant degeneration is characterized by development of an osteolytic component with cortical destruction[41].

Osteochondromas are tumors of the bone that may be sporadic or inherited. These are bony exostoses that show contiguity with the intramedullary canal on CT studies (Figure 5A). These exostoses have a cartilage cap that may be along various stages of ossification. Osteochondromas should not grow after skeletal maturity. Osteochondromas may be sessile or pedunculated, and if pedunculated point away from

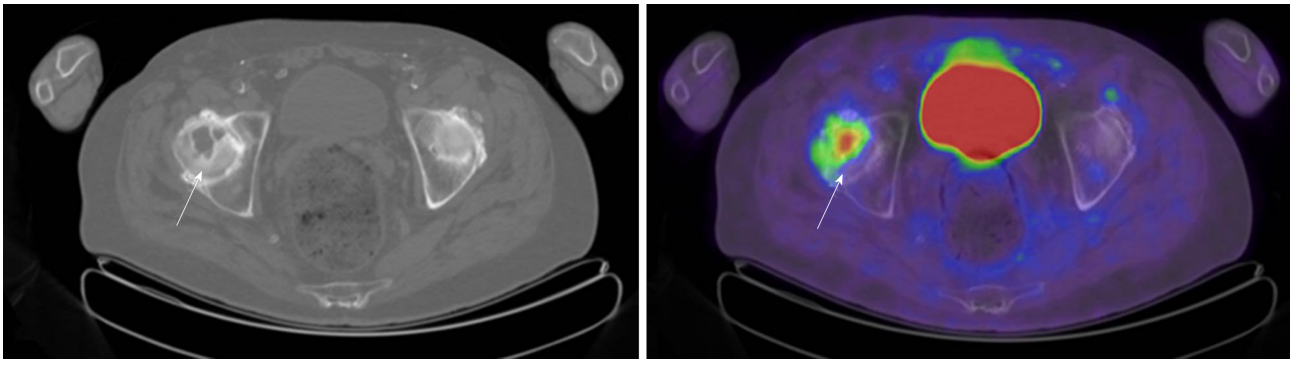

Figure 2 Axial computed tomography and axial fused positron emission tomography/computed tomography of the pelvis in an 82-year-old male with history of colon and parotid gland cancer with subchondral cyst in the right femoral head (arrows) (maximum standardized uptake value 5.2).

the nearest joint. Osteochondromas are benign tumors, but may rarely undergo malignant degeneration into a chondrosarcoma. Malignant degeneration is more common in patients with multiple hereditary exostoses (MHE). A thickened cartilage cap on CT, greater than 2.0 cm, has been reported as 100% sensitive and 95% specific for degeneration into chondrosarcoma[42]. The communication of the bony excrescence with the intramedullary space on PET/CT is pathognomic; however, osteochondromas should not be confused with tubercles/muscle insertion sites. Osteochondromas may show increased ^{18}F-FDG uptake on PET/CT.

Paget's disease of the bone is a disorder of normal bone homeostasis with abnormal osteoblastic and osteoclastic activity. The exact etiology of Paget's disease is unknown; however, Paget's disease may present in a mixture of three phases: the osteolytic phase, the intermediate phase, and the quiescent phase. Pagetic bone in osteolytic phase may show osteolytic lesions, like osteoporosis circumscripta cranii; however, Pagetic bone in the intermediate and quiescent phase shows cortical and trabecular thickening on CT (Figure 5B). The PET/CT appearance of Paget's disease is identical to that noted on CT; however, Paget's disease may show variable ^{18}F-FDG uptake, likely depending on the phase of Paget's disease. A proximal femur shepherd's crook deformity may be present. Paget's disease tends to be localized affecting adjacent bones. The cotton wool spots/patchy areas of sclerosis of Paget's disease are often mistaken for osteoblastic metastases, in particular metastases related to prostate or breast cancer. While Paget's disease is benign, Pagetic bone may rarely undergo malignant degeneration into undifferentiated pleomorphic sarcoma, fibrosarcoma, or osteosarcoma amongst other sarcomas[43]. Development of a soft tissue mass with cortical destruction should be considered highly suspicious for malignant degeneration of Paget's disease.

Insufficiency fractures can occur in patients after radiation, after chemotherapy, or after hormonal-altering therapy for some cancers including breast and prostate cancer, or be related to diminished bone mineral density related to senescent changes. Insufficiency fractures are more common in women. Acute sacral insufficiency fractures appear as unilateral or bilateral para-median linear lucencies with adjacent sclerosis oriented anterior-posterior along the sacral ala on CT (Figure 6A); however, a transverse component may be present, resulting in a "Honda" or "H" sign on Tc99m-MDP bone scans and PET/CT. Insufficiency fractures may also be noted involving the iliac wing, medial ilium, supraacetabular region, parasymphyseal region, and involving the pubic rami[44]. Proximal femoral insufficiency fractures are more common along the compression than tension side of the hip; however, insufficiency fractures related to bisphosphonate therapy are more common along the tension side of the sub-trochanteric proximal femur.

Osteomyelitis is an infection of the intramedullary canal and cortex of the bone. Signs of osteomyelitis may include elevated white blood cell counts (WBC), erythrocyte sedimentation rate (ESR) and C-reactive protein (CRP). Clinical history and physical examination are often required because the yield for bone biopsies for osteomyelitis is generally less than 50%. CT findings of osteomyelitis include periosteal reaction, sclerosis, osseous erosion/destruction, surrounding soft tissue inflammatory changes and reactive lymphadenopathy (Figure 6B). These areas of destruction may show increased ^{18}F-FDG uptake depending on chronicity on PET/CT. Longstanding chronic ulcers (Marjolin's ulcers) related to chronic infection, burns, injuries, or venous stasis and chronic osteomyelitis may undergo malignant degeneration into squamous cell or basal cell carcinoma [44,45]. Signs of malignant degeneration include development of bone destruction, soft tissue mass and per-

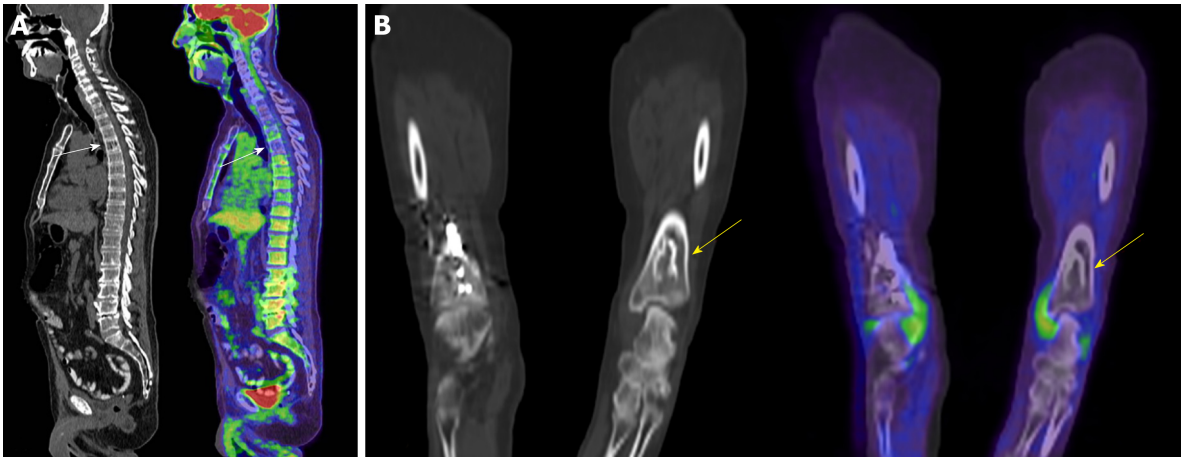

Figure 3 Computed tomography and fused positron emission tomography/computed tomography of two patients. A: Sagittal computed tomography (CT) and sagittal fused positron emission tomography (PET)/CT of the spine in a 73-year-old male with history of lymphoma and a hemangioma in the T5 vertebral body (arrows) [maximum standardized uptake value (SUV) 2.86]; B: Coronal CT and coronal fused PET/CT of the distal tibia in a 54-year-old female with history of a neuroendocrine lung tumor demonstrating a bone infarct (arrows) in the distal tibia (maximum SUV 0.37).

iosteal reaction[44,45].

These findings are clinically important for radiologists and clinicians, because we have described the key CT imaging features of these "do not touch" and benign lesions, which can be gleaned from the CT component of the PET/CT. We anticipate that this will decrease the number of times the PET/CT interpreting physician and the bone biopsy proceduralist have differing opinions and reduce the number of unnecessary bone biopsies.

This study has a few limitations. The data are obtained from a single center tertiary care academic healthcare center, and therefore subject to ascertainment bias since our institution primarily treats adult patients. Lesions that are more common in the pediatric population including cortical desmoids and avulsion fractures were not described. SUV measurements, while standardized by weight, acquisition time, and injected dose, may be affected by body mass index, scanner calibration, and imaging artifacts, among other factors[26]. To address this limitation, blood pool mean SUV was included as an internal control to better characterize the FDG uptake of the target lesions. Several lesions were not histologically confirmed – this was because these lesions had the classic imaging appearance of a benign lesion or a "do not touch" lesion[16], and biopsies of these lesions are generally thought to be unnecessary since characterization by a trained musculoskeletal radiologist is pathognomic. The sample size was limited, but these are rare lesions, and prior publications referencing these lesions are almost all are restricted to case-reports. Nonetheless, this work clearly shows the spectrum of ^{18}F-FDG uptake in several known "do not touch" and benign osseous lesions, which can be used to help in clinical decision making.

In conclusion, among benign lesions for which CT imaging findings are diagnostic, SUV values may vary, and these lesions may demonstrate ^{18}F-FDG uptake above that of the blood pool. For this reason, ^{18}F-FDG uptake above background should not be misconstrued to indicate the presence of malignancy for all osseous lesions.

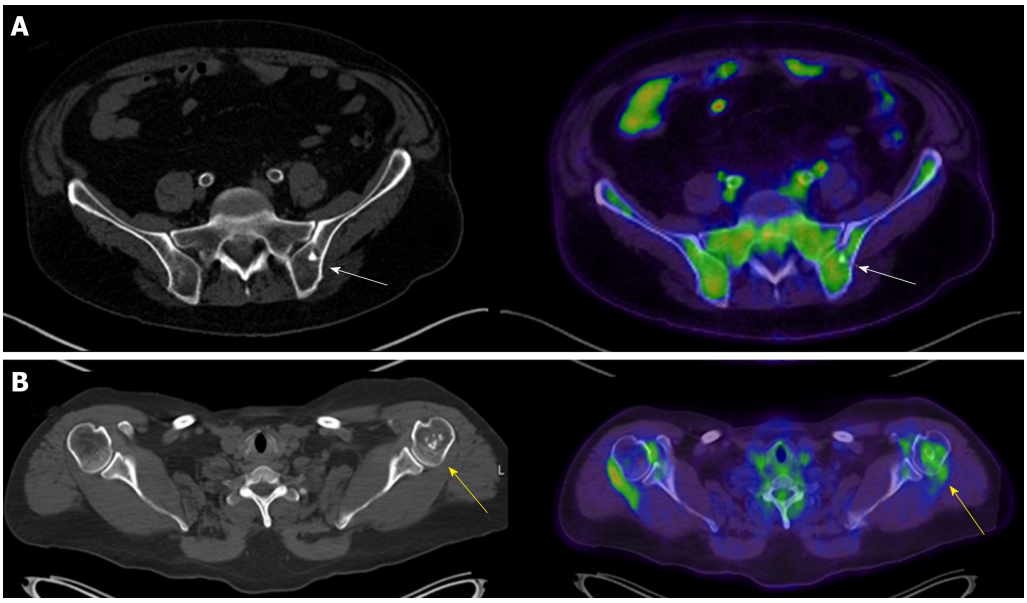

Figure 4 Axial computed tomography and axial fused positron emission tomography/computed tomography of two patients. A: Axial computed tomography (CT) and axial fused positron emission tomography (PET)/CT of the pelvis in a 76-year-old male with a history of a solitary pulmonary nodule and a bone island in his left ilium (arrows); B: Axial CT and axial fused PET/CT of the chest in a 52-year-old female with a history of melanoma and an enchondroma in the left proximal humerus (arrows) (maximum standardized uptake value 2.33).

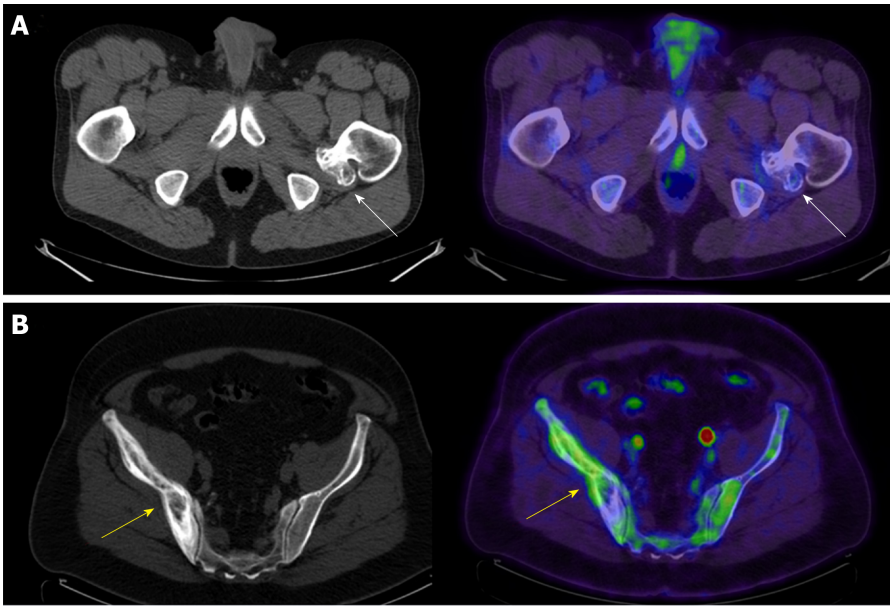

Figure 5 Axial computed tomography and axial fused positron emission tomography/computed tomography of two patients. A: Axial computed tomography (CT) and axial fused positron emission tomography (PET)/CT of the pelvis in a 51-year-old male with diffuse large B-cell lymphoma and a sessile osteochondroma arising from the proximal left femur (arrows) [maximum standardized uptake value (SUV) 1.64]; B: Axial CT and axial fused PET/CT of the pelvis in a 61-year-old male with a history of a follicular lymphoma and Paget's disease of the bone involving the right ilium (arrows) (maximum SUV 3.92).

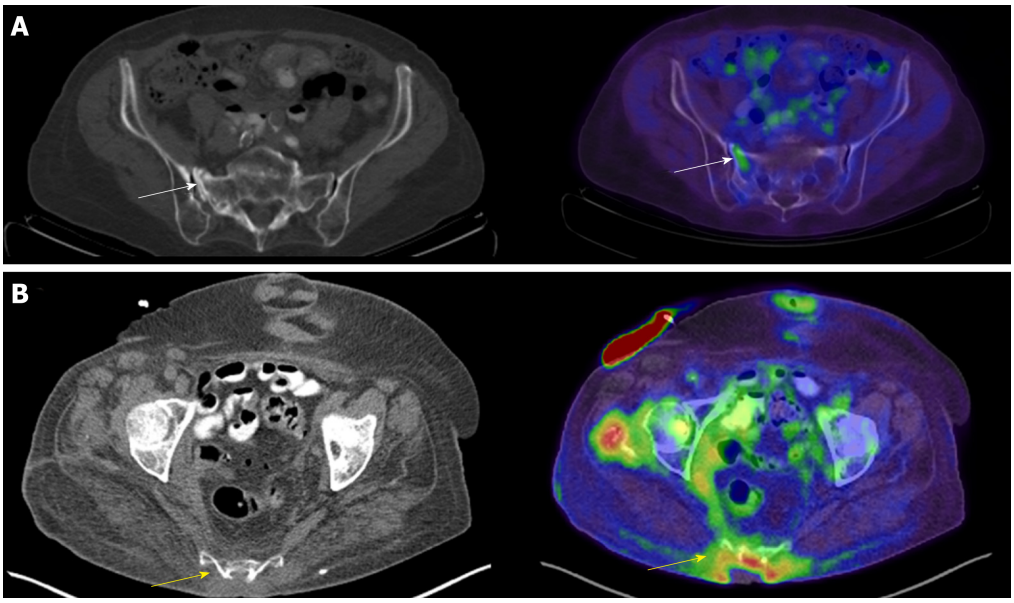

Figure 6 Axial computed tomography and axial fused positron emission tomography/computed tomography of two patients. A: Axial computed tomography (CT) and axial fused positron emission tomography (PET)/CT of the pelvis in an 84-year-old female with a history of non-Hodgkin's lymphoma and an insufficiency fracture of the right sacral ala (arrows) [maximum standardized uptake value (SUV) 1.99]; B: Axial CT and axial fused PET/CT of the pelvis in an 82-year-old female with a sacral decubitus ulcer and osteomyelitis (arrows).

ARTICLE HIGHLIGHTS

Research background

18-F-fluorodeoxyglucose (^{18}F-FDG) positron emission tomography/computed tomography (PET/CT) is increasingly used for staging and monitoring of many common malignancies. Classical "do not touch" and benign bone lesions are sometimes detected in ^{18}F-FDG PET/CT studies. These lesions may be referred for biopsy because the PET/CT interpreting physician may be unfamiliar with the spectrum of the ^{18}F-FDG PET/CT uptake pattern exhibited by these lesions.

Research motivation

There is no descriptive analysis of ^{18}F-FDG uptake of "do not touch" and benign osseous lesions.

Research objectives

This study evaluates the spectrum of ^{18}F-FDG PET/CT uptake patterns in several "do not touch" and benign osseous lesions to provide a reference for physicians interpreting ^{18}F-FDG PET/CTs .

Research methods

This study evaluated 287 independent patients, of whom 287 were classic "do not touch" (benign cystic lesions, insufficiency fractures, bone islands, bone infarcts) or benign osseous lesions (hemangiomas, enchondromas, osteochondromas, fibrous dysplasia, Paget's disease, osteomyelitis) ^{18}F-FDG PET/CT from January 1, 2006 to December 1, 2018 at a single academic institution. The maximum and mean standardized uptake values (SUV), and the ratio of the maximum SUV to mean blood pool were calculated. Pearson's correlations between lesion size and maximum SUV were calculated.

Research results

The maximum SUV range was as follows: hemangiomas (0.95-2.99), bone infarcts (0.37-3.44), bone islands (0.26-3.29), enchondromas (0.46-2.69), fibrous dysplasia (0.78-18.63), osteochondromas (1.11-2.56), Paget's disease of bone (0.93-5.65), insufficiency fractures (1.06-12.97) and for osteomyelitis (2.57-12.64). The upper range of the maximum SUV was lowest for Osteochondromas (maximum SUV 2.56). The upper range of the maximum SUV was highest for fibrous dysplasia (maximum SUV of 18.63). In each lesion type, at least one lesion showed greater ^{18}F-FDG activity than the blood pool, with the highest maximum SUV up to 9.34 times the blood pool average (osteomyelitis) to the blood pool average (hemangioma) 1.42 times. Except for enchondromas, there was no correlation between the maximum SUV and the size of the lesion. Larger enchondromas have a higher maximum SUV (r = 0.36, P = 0.02).

Research conclusions

"Do not touch" and benign osseous lesions may exhibit ^{18}F-FDG uptake higher than in the blood pool on PET/CT. Therefore, ^{18}F-FDG uptake above blood pool should not be misunderstood to indicate the presence of malignancy. The CT appearance, if pathognomic should be used to guide management rather than the maximum SUV.

Research perspectives

The data comes from an academic tertiary health care center that primarily treats adult patients. More common lesions in the pediatric population, including cortical desmoids and avulsion fractures, were not described. Although SUV measurements were normalized by weight, acquisition time and injection dose, they may be affected by factors such as body mass index, scanner calibration and imaging artifacts.

REFERENCES

1 **Valk PE**, Pounds TR, Tesar RD, Hopkins DM, Haseman MK. Cost-effectiveness of PET imaging in clinical oncology. *Nucl Med Biol* 1996; **23**: 737-743 [PMID: 8940715 DOI: 10.1016/0969-8051(96)00080-7]

2 **Hicks RJ**. Should positron emission tomography/computed tomography be the first rather than the last test performed in the assessment of cancer? *Cancer Imaging* 2012; **12**: 315-323 [PMID: 23022990 DOI: 10.1102/1470-7330.2012.9005]

3 Available from: https://imvinfo.com/product/pet-imaging-market-summary-report-2018/

4 **Czernin J**, Allen-Auerbach M, Nathanson D, Herrmann K. PET/CT in Oncology: Current Status and Perspectives. *Curr Radiol Rep* 2013; **1**: 177-190 [PMID: 24883234 DOI: 10.1007/s40134-013-0016-x]

5 **Warburg O**, Posener K, Negelein E. The metabolism of cancer cells. *Biochem Zeitschr* 1924; **152**: 129–169

6 **Warburg O**, Wind F, Negelein E. The metabolism of tumors in the body. *J Gen Physiol* 1927; **8**: 519-530 [PMID: 19872213 DOI: 10.1085/jgp.8.6.519]

7 **Wang G**, Lau EW, Shakher R, Rischin D, Ware RE, Hong E, Binns DS, Hogg A, Drummond E, Hicks RJ. How do oncologists deal with incidental abnormalities on whole-body fluorine-18 fluorodeoxyglucose PET/CT? *Cancer* 2007; **109**: 117-124 [PMID: 17133406 DOI: 10.1002/cncr.22370]

8 **Beatty JS**, Williams HT, Aldridge BA, Hughes MP, Vasudeva VS, Gucwa AL, David GS, Lind DS, Kruse EJ, McLoughlin JM. Incidental PET/CT findings in the cancer patient: how should they be managed? *Surgery* 2009; **146**: 274-281 [PMID: 19628085 DOI: 10.1016/j.surg.2009.04.024]

9 **Sebro R**, Aparici CM, Pampaloni MH. Frequency and clinical implications of incidental new primary cancers detected on true whole-body 18F-FDG PET/CT studies. *Nucl Med Commun* 2013; **34**: 333-339 [PMID: 23407371 DOI: 10.1097/MNM.0b013e32835f163f]

10 **European Society of Radiology 2009**. The future role of radiology in healthcare. *Insights Imaging* 2010; **1**: 2-11 [PMID: 22347897 DOI: 10.1007/s13244-009-0007-x]

11 **Mohan C**. Subspecialization in radiology - Is it time to hatch out of the cocoon? *Indian J Radiol Imaging* 2017; **27**: 261-262 [PMID: 29089669 DOI: 10.4103/ijri.IJRI_345_17]

12 **Thrall JH**, Wittenberg J. Radiology summit 1990: specialization in radiology--trends, implications, and recommendations. *AJR Am J Roentgenol* 1991; **156**: 1273-1276 [PMID: 2028877 DOI: 10.2214/ajr.156.6.2028877]

13 **Bluth EI**, Truong H, Nsiah E, Hughes D, Short BW. The 2013 ACR Commission on Human Resources workforce survey. *J Am Coll Radiol* 2013; **10**: 750-756 [PMID: 24091045 DOI: 10.1016/j.jacr.2013.06.010]

14 **Atlas SW**. Embracing subspecialization: the key to the survival of radiology. *J Am Coll Radiol* 2007; **4**: 752-753 [PMID: 17964496 DOI: 10.1016/j.jacr.2007.04.003]

15 **Pencharz D**, Nathan M, Wagner TL. Evidence-based management of incidental focal uptake of fluorodeoxyglucose on PET-CT. *Br J Radiol* 2018; **91**: 20170774 [PMID: 29243502 DOI: 10.1259/bjr.20170774]

16 **Brant WE**, Helms C. Fundamentals of Diagnostic Radiology. Lippincott Williams and Wilkins. 2012

17 **Döbert N**, Menzel C, Ludwig R, Berner U, Diehl M, Hamscho N, Grünwald F. Enchondroma: a benign osseous lesion with high F-18 FDG uptake. *Clin Nucl Med* 2002; **27**: 695-697 [PMID: 12352108 DOI: 10.1097/00003072-200210000-00001]

18 **Nakayama M**, Okizaki A, Ishitoya S, Aburano T. "Hot" vertebra on (18)F-FDG PET scan: a case of vertebral hemangioma. *Clin Nucl Med* 2012; **37**: 1190-1193 [PMID: 23154481 DOI: 10.1097/RLU.0b013e3182708628]

19 **Tripathi M**, Kumar R, Mohapatra T, Nadig M, Bal C, Malhotra A. Intense F-18 FDG uptake noted in a benign bone cyst. *Clin Nucl Med* 2007; **32**: 255-257 [PMID: 17314616 DOI: 10.1097/01.rlu.0000255272.96243.06]

20 **Charest M**, Singnurkar A, Hickeson M, Novales JA, Derbekyan V. Intensity of FDG uptake is not everything: synchronous liposarcoma and fibrous dysplasia in the same patient on FDG PET-CT imaging. *Clin Nucl Med* 2008; **33**: 455-458 [PMID: 18580228 DOI: 10.1097/RLU.0b013e31817793bb]

21 **Strobel K**, Merwald M, Huellner M, Zenklusen HR, Kuttenberger J. Osteoblastoma of the mandible mimicking osteosarcoma in FDG PET/CT imaging. *Clin Nucl Med* 2013; **38**: 143-144 [PMID: 23334133 DOI: 10.1097/RLU.0b013e318279f131]

22 **Mahmood S**, Martinez de Llano SR. Paget disease of the humerus mimicking metastatic disease in a patient with metastatic malignant mesothelioma on whole body F-18 FDG PET/CT. *Clin Nucl Med* 2008; **33**: 510-512 [PMID: 18580246 DOI: 10.1097/RLU.0b013e318177928a]

23 **Li J**, Weissberg Z, Bevilacqua TA, Yu G, Weber K, Sebro R. Concordance between fine-needle aspiration and core biopsies for osseous lesions by lesion imaging appearance and CT attenuation. *Radiol Med* 2018; **123**: 254-259 [PMID: 29249078 DOI: 10.1007/s11547-017-0841-8]

24 **Yang J**, Frassica FJ, Fayad L, Clark DP, Weber KL. Analysis of nondiagnostic results after image-guided needle biopsies of musculoskeletal lesions. *Clin Orthop Relat Res* 2010; **468**: 3103-3111 [PMID: 20383617 DOI: 10.1007/s11999-010-1337-1]

25 **Sebro R**, Mari-Aparici C, Hernandez-Pampaloni M. Value of true whole-body FDG-PET/CT scanning protocol in oncology: optimization of its use based on primary diagnosis. *Acta Radiol* 2013; **54**: 534-539 [PMID: 23463863 DOI: 10.1177/0284185113476021]

26 **Adams MC**, Turkington TG, Wilson JM, Wong TZ. A systematic review of the factors affecting accuracy of SUV measurements. *AJR Am J Roentgenol* 2010; **195**: 310-320 [PMID: 20651185 DOI: 10.2214/AJR.10.4923]

27 **Parman LM**, Murphey MD. Alphabet soup: cystic lesions of bone. *Semin Musculoskelet Radiol* 2000; **4**:

89-101 [PMID: 11061694 DOI: 10.1055/s-2000-6857]
28 **Motamedi K**, Seeger LL. Benign bone tumors. *Radiol Clin North Am* 2011; **49**: 1115-1134, v [PMID: 22024291 DOI: 10.1016/j.rcl.2011.07.002]
29 **Pitt MJ**, Graham AR, Shipman JH, Birkby W. Herniation pit of the femoral neck. *AJR Am J Roentgenol* 1982; **138**: 1115-1121 [PMID: 6979213 DOI: 10.2214/ajr.138.6.1115]
30 **Resnick D**, Niwayama G, Coutts RD. Subchondral cysts (geodes) in arthritic disorders: pathologic and radiographic appearance of the hip joint. *AJR Am J Roentgenol* 1977; **128**: 799-806 [PMID: 404905 DOI: 10.2214/ajr.128.5.799]
31 **Resnick D**. *Bone and Joint Imaging, 2nd ed*. Philadelphia, PA: WB Saunders Company; 1996; 325-327
32 **Kwee TC**, de Klerk JMH, Nix M, Heggelman BGF, Dubois SV, Adams HJA. Benign Bone Conditions That May Be FDG-avid and Mimic Malignancy. *Semin Nucl Med* 2017; **47**: 322-351 [PMID: 28583274 DOI: 10.1053/j.semnuclmed.2017.02.004]
33 **Perry MT**, Sebro R. Accuracy of Opposed-phase Magnetic Resonance Imaging for the Evaluation of Treated and Untreated Spinal Metastases. *Acad Radiol* 2018; **25**: 877-882 [PMID: 29398437 DOI: 10.1016/j.acra.2017.11.022]
34 **Hara H**, Akisue T, Fujimoto T, Kishimoto K, Imabori M, Kishimoto S, Kawamoto T, Yamamoto T, Kuroda R, Fujioka H, Doita M, Kurosaka M. Magnetic resonance imaging of medullary bone infarction in the early stage. *Clin Imaging* 2008; **32**: 147-151 [PMID: 18313581 DOI: 10.1016/j.clinimag.2007.07.005]
35 **McDonald MD**, Sadigh S, Weber KL, Sebro R. A Rare Case of an Osteolytic Bone-infarct-associated Osteosarcoma: Case Report with Radiographic and Histopathologic Correlation, and Literature Review. *Cureus* 2018; **10**: e2777 [PMID: 30112253 DOI: 10.7759/cureus.2777]
36 **Elangovan SM**, Sebro R. Accuracy of CT Attenuation Measurement for Differentiating Treated Osteoblastic Metastases From Enostoses. *AJR Am J Roentgenol* 2018; **210**: 615-620 [PMID: 29323547 DOI: 10.2214/AJR.17.18638]
37 **Murphey MD**, Flemming DJ, Boyea SR, Bojescul JA, Sweet DE, Temple HT. Enchondroma versus chondrosarcoma in the appendicular skeleton: differentiating features. *Radiographics* 1998; **18**: 1213-37; quiz 1244-5 [PMID: 9747616 DOI: 10.1148/radiographics.18.5.9747616]
38 **Pannier S**, Legeai-Mallet L. Hereditary multiple exostoses and enchondromatosis. *Best Pract Res Clin Rheumatol* 2008; **22**: 45-54 [PMID: 18328980 DOI: 10.1016/j.berh.2007.12.004]
39 **Subhawong TK**, Winn A, Shemesh SS, Pretell-Mazzini J. F-18 FDG PET differentiation of benign from malignant chondroid neoplasms: a systematic review of the literature. *Skeletal Radiol* 2017; **46**: 1233-1239 [PMID: 28608242 DOI: 10.1007/s00256-017-2685-7]
40 **Kushchayeva YS**, Kushchayev SV, Glushko TY, Tella SH, Teytelboym OM, Collins MT, Boyce AM. Fibrous dysplasia for radiologists: beyond ground glass bone matrix. *Insights Imaging* 2018; **9**: 1035-1056 [PMID: 30484079 DOI: 10.1007/s13244-018-0666-6]
41 **Qu N**, Yao W, Cui X, Zhang H. Malignant transformation in monostotic fibrous dysplasia: clinical features, imaging features, outcomes in 10 patients, and review. *Medicine (Baltimore)* 2015; **94**: e369 [PMID: 25621678 DOI: 10.1097/MD.0000000000000369]
42 **Bernard SA**, Murphey MD, Flemming DJ, Kransdorf MJ. Improved differentiation of benign osteochondromas from secondary chondrosarcomas with standardized measurement of cartilage cap at CT and MR imaging. *Radiology* 2010; **255**: 857-865 [PMID: 20392983 DOI: 10.1148/radiol.10082120]
43 **Hadjipavlou A**, Lander P, Srolovitz H, Enker IP. Malignant transformation in Paget disease of bone. *Cancer* 1992; **70**: 2802-2808 [PMID: 1451058 DOI: 10.1002/1097-0142(19921215)70:12<2802::AID-CNCR2820701213>3.0.CO;2-N]
44 **Cabarrus MC**, Ambekar A, Lu Y, Link TM. MRI and CT of insufficiency fractures of the pelvis and the proximal femur. *AJR Am J Roentgenol* 2008; **191**: 995-1001 [PMID: 18806133 DOI: 10.2214/AJR.07.3714]
45 **Panteli M**, Puttaswamaiah R, Lowenberg DW, Giannoudis PV. Malignant transformation in chronic osteomyelitis: recognition and principles of management. *J Am Acad Orthop Surg* 2014; **22**: 586-594 [PMID: 25157040 DOI: 10.5435/JAAOS-22-09-586]
46 **Smith J**, Mello LF, Nogueira Neto NC, Meohas W, Pinto LW, Campos VA, Barcellos MG, Fiod NJ, Rezende JF, Cabral CE. Malignancy in chronic ulcers and scars of the leg (Marjolin's ulcer): a study of 21 patients. *Skeletal Radiol* 2001; **30**: 331-337 [PMID: 11465774 DOI: 10.1007/s002560100355]

Published By Baishideng Publishing Group Inc
7041 Koll Center Parkway, Suite 160, Pleasanton, CA 94566, USA
Telephone: +1-925-2238242
Fax: +1-925-2238243
E-mail: bpgoffice@wjgnet.com
Help Desk: https://www.f6publishing.com/helpdesk
https://www.wjgnet.com

ISSN 1949-8470 (online)

World Journal of *Radiology*

World J Radiol 2019 July 28; 11(7): 94-109

Published by Baishideng Publishing Group Inc

WJR

World Journal of Radiology

Contents

Monthly Volume 11 Number 7 July 28, 2019

ORIGINAL ARTICLE

Retrospective Study

Observational Study

Contents

World Journal of Radiology

Volume 11 Number 7 July 28, 2019

AIMS AND SCOPE

World Journal of Radiology (*World J Radiol*, *WJR*, online ISSN 1949-8470, DOI: 10.4329) is a peer-reviewed open access academic journal that aims to guide clinical practice and improve diagnostic and therapeutic skills of clinicians.

The *WJR* covers topics concerning diagnostic radiology, radiation oncology, radiologic physics, neuroradiology, nuclear radiology, pediatric radiology, vascular/interventional radiology, medical imaging achieved by various modalities and related methods analysis. The current columns of *WJR* include editorial, frontier, mini-reviews, review, medical ethics, original articles, case report, *etc*.

We encourage authors to submit their manuscripts to *WJR*. We will give priority to manuscripts that are supported by major national and international foundations and those that are of great basic and clinical significance.

INDEXING/ABSTRACTING

The *WJR* is now abstracted and indexed in Emerging Sources Citation Index (Web of Science), PubMed, PubMed Central, China National Knowledge Infrastructure (CNKI), China Science and Technology Journal Database (CSTJ), and Superstar Journals Database.

RESPONSIBLE EDITORS FOR THIS ISSUE

Responsible Electronic Editor: *Yu-Jie Ma*

Proofing Production Department Director: *Yun-Xiaojian Wu*

NAME OF JOURNAL
World Journal of Radiology

ISSN
ISSN 1949-8470 (online)

LAUNCH DATE
January 31, 2009

FREQUENCY
Monthly

EDITORS-IN-CHIEF
Venkatesh Mani

EDITORIAL BOARD MEMBERS
https://www.wjgnet.com/1949-8470/editorialboard.htm

EDITORIAL OFFICE
Jin-Lei Wang, Director

PUBLICATION DATE
July 28, 2019

INSTRUCTIONS TO AUTHORS
https://www.wjgnet.com/bpg/gerinfo/204

GUIDELINES FOR ETHICS DOCUMENTS
https://www.wjgnet.com/bpg/GerInfo/287

GUIDELINES FOR NON-NATIVE SPEAKERS OF ENGLISH
https://www.wjgnet.com/bpg/gerinfo/240

PUBLICATION MISCONDUCT
https://www.wjgnet.com/bpg/gerinfo/208

ARTICLE PROCESSING CHARGE
https://www.wjgnet.com/bpg/gerinfo/242

STEPS FOR SUBMITTING MANUSCRIPTS
https://www.wjgnet.com/bpg/GerInfo/239

ONLINE SUBMISSION
https://www.f6publishing.com

World Journal of Radiology

Submit a Manuscript: https://www.f6publishing.com

World J Radiol 2019 July 28; 11(7): 94-101

DOI: 10.4329/wjr.v11.i7.94

ISSN 1949-8470 (online)

ORIGINAL ARTICLE

Retrospective Study

Genial tubercles: Morphological study of the controversial anatomical landmark using cone beam computed tomography

Yasser A Araby, Ahmed A Alhirabi, Abdelaleem H Santawy

ORCID number: Yasser A Araby (0000-0002-5340-5875); Ahmed A Alhirabi (0000-0002-3663-3999); Abdelaleem H Santawy (0000-0001-7506-9561).

Author contributions: Araby YA, Alhirabi AA and Santawy AH contributed equally to this work; Araby YA conceived and designed research; Alhirabi AA and Santawy AH collected data; Araby YA, Alhirabi AA and Santawy AH analyzed data; Araby YA and Alhirabi AA wrote the paper with the support of Santawy AH.

Institutional review board statement: The study protocol was reviewed and conducted with approval by the Ethical Committee, Dental Research Center, College of Dentistry, Qassim University, Saudi Arabia.

Informed consent statement: Patients were not required to give informed consent to the study because the analysis used anonymous data that were obtained from the Radiology Department Archive, Dental Clinics Center, Qassim University, KSA after each patient agreed to treatment by written consent.

Conflict-of-interest statement: All authors declare that they have no conflicts of interest.

Yasser A Araby, Department of Prosthetic Dental Sciences, College of Dentistry, Qassim University, Qassim 51452, Saudi Arabia

Ahmed A Alhirabi, Dental Intern, College of Dentistry, Qassim University, Qassim 51452, Saudi Arabia

Abdelaleem H Santawy, Department of Maxillofacial Surgery and Diagnostic Sciences, College of Dentistry, Qassim University, Qassim 51452, Saudi Arabia

Corresponding author: Yasser A Araby, BSc, MSc, PhD, Lecturer, Department of Prosthetic Dental Sciences, College of Dentistry, Qassim University, Burayadh, Qassim 51452, Saudi Arabia. dr.yasser.araby@qudent.org
Telephone: +966-5-30488300
Fax: +966-1-63801761

Abstract

BACKGROUND

Identification of the morphology of the genial tubercles (GTs) is valuable for different dental applications. The morphological pattern of the GTs is still controversial, and therefore, the study of its morphology using cone beam computed tomography (CBCT) plays a valuable role in resolving the controversy.

AIM

To assess the morphological pattern, dimensions and position of the GTs using CBCT among a selected Saudi population.

METHODS

CBCT records of 155 Saudi subjects (49 female and 106 male) were used to assess the pattern and size of the GTs and to determine the distance from the apices of the lower central incisors to the superior border of the incisors (I-SGT) and the distance from the inferior border of the GTs to the menton (IGT-M).

RESULTS

The results of this study showed that the most common morphological pattern was of two superior GTs and a rough impression below them (36.8%), followed by two superior GTs and a median ridge representing fused inferior GTs below them (22.6%) and a single median eminence or projection (20%). The classically described pattern, of two superior and two inferior GTs placed one above the other, was found in only 14.2% of cases, while 6.4% of the studied cases had no GTs. The mean width and height were 6.23 ± 1.93 mm and 6.67 ± 3.04 mm, respectively, while the mean I-SGT and IGT-M measurements were 8.26 ± 2.7 mm

Manuscript source: Unsolicited manuscript

Received: April 23, 2019
Peer-review started: May 8, 2019
First decision: June 17, 2019
Revised: July 9, 2019
Accepted: July 25, 2019
Article in press: July 25, 2019
Published online: July 28, 2019

P-Reviewer: Gao BL
S-Editor: Cui LJ
L-Editor: A
E-Editor: Ma YJ

and 8.13 ± 3.07 mm, respectively.

CONCLUSION
The GTs are a controversial anatomical landmark with wide variation in their morphological pattern. The most common pattern among the studied Saudi sample was of two superior GTs and a rough impression below them, and there were no significant differences between males and females.

Key words: Genial tubercles; Cone beam computed tomography; Morphological analysis; Mandible; Anatomical landmark

Core tip: The morphological pattern of the genial tubercles (GTs) is controversial. Classically, they are described as four elevations equidistant between the upper and lower edges of the mandible that are arranged in pairs and surround the lingual foramina bilaterally; however, several osteological and radiological studies proved that there is wide variation in their morphology. This retrospective study was conducted to determine the morphological pattern, size and position of the GTs using cone beam computed tomography among a selected Saudi population.

Citation: Araby YA, Alhirabi AA, Santawy AH. Genial tubercles: Morphological study of the controversial anatomical landmark using cone beam computed tomography. *World J Radiol* 2019; 11(7): 94-101
URL: https://www.wjgnet.com/1949-8470/full/v11/i7/94.htm
DOI: https://dx.doi.org/10.4329/wjr.v11.i7.94

INTRODUCTION

Genial tubercles (GTs), also known as spinae mentalis, genial apophysis and mental spines GTs are small eminences of bone found on the lingual side of the mandible at the midline and are important landmarks for maxillofacial surgeons, radiologists, prosthodontists and general dentists[1,2].

The GTs serve as the insertion of the geniohyoid muscles in the lower and the genioglossus muscles in the upper portions of the tubercles. The action of these muscles is related to tongue mobility and swallowing, which are important for speech and feeding[3].

Although the genial tubercles are classically described in different anatomy textbooks as four mental spines on the lingual surface of the symphysis menti arranged in two pairs placed one above the other, they show different patterns in their positions and shapes[4,5].

Cone beam computed tomography (CBCT) is an accurate method to evaluate the morphology, size and position of the GTs[6,7].

Accurate identification of the GTs morphology, size and/or position using three-dimensional (3D) imaging is valuable for different applications, such as preparation for genioglossus advancement in the treatment of obstructive sleep apnea[8,9], estimation of the safe zone before implant surgery in the interforaminal region of the mandible[6] and evaluation of mandibular asymmetry on CBCT images[10].

In cases of extreme atrophy of the aged edentulous mandibles, when the GTs remain as bony projections in the floor of the mouth, they can pose a great prosthodontic challenge[11-13].

In this context, it is very important to identify the morphology of the GTs and their relation to the mandibular anterior teeth and to the margins of the mandible.

In the literature, there is no study describing the morphology of the GTs among the Saudi population; thus, the aim of this study is to determine the morphological pattern, size and position of the GTs using CBCT among a selected Saudi population.

MATERIAL AND METHODS

Study design

CBCT images used in this study were obtained from the Radiology Department Archive of the Dental Clinics Center, Qassim University, and the study protocol was approved by the Ethical Committee of the Dental Research Center, College of Dentistry, Qassim University, Saudi Arabia.

The inclusion criteria included patients from both sexes, above the age of 17 years and with full anterior dentition. The exclusion criteria included completely edentulous patients; patients with missing anterior teeth or those with mandibular asymmetry, congenital or developmental deformities; patients with traumatic injury or pathologic changes in the mandible; and patients with blurred or distorted CBCT images.

CBCT images were acquired using the Galileos® Comfort ^{plus} System (Sirona 3D, Germany) with settings as follows: X-ray generator, 98 kV and 3-6 mA. Focal spot size according to IEC 60336 was 0.5 mm, and the total filtration according to IEC 60522 was > 2.5 mm. The detector was an Image Intensifier by Siemens with the following settings: Pixels: 1000; FPS: 15-30; dynamics: 12 Bits; image volume: 15.4 cm, spherical volume – collimated 15 cm × 8.5 cm; voxel size 0.25/0.125 mm; scan time/exposure time 14 s/2-5 s. Galileos software was used, which allowed linear measurements of images and detection of the GT pattern.

CBCT scans were oriented to standardize the measurements so that the bilateral zygomatic structures were at the same level in the axial view. The infra orbital foramina of the right and left sides were parallel to the horizontal line in the coronal view. In the sagittal view, the Frankfort plane represented the true horizontal axis.

To reduce measurement error, all measurements were repeated on 2 separate occasions in 1-wk intervals, and the average values were recorded. Differences between the 2 readings were used to assess intra examiner variation with a paired *t*-test.

GTs pattern assessment

The morphological patterns of the GTs were studied and grouped into five patterns as follows: The classic description of four spines, two superior and two inferior tubercles (Type I); two superior GTs and a median ridge representing fused inferior GTs below them (Type II); two superior GTs and a rough impression below them (Type III); a single median eminence or projection (Type IV); and absence of the GTs (Type V). The pattern of the GTs was evaluated in the axial view, together with the sagittal view. (Figure 1).

GTs position and size assessment

The following parameters were measured in millimeters: GTs height (GTH), GTs width (GTW), distance from the superior border of the GTs to the apex of the lower central incisors (I-SGT) and the distance from the inferior border of the GTs to the menton (IGT-M).

GTW was measured in the axial view at the level of the widest level of the GTs, while GTH was measured in the sagittal view as the vertical distance between the level of the most superior and the most inferior borders of the GTs.

I-SGT and IGT-M were measured by drawing tangential lines from the apex of the lower central incisors to the superior border of the GTs and from the inferior border of the GTs to the inferior border of the mandible (menton), respectively (Figure 2).

Statistical analysis

The collected data were tabulated and analyzed using SPSS 20.0 (Statistical Package for Scientific Studies) for Windows. A paired *t*-test was used for intra examiner calibration, and a chi square test was used for comparison between genial tubercle patterns in both sexes. All statistical tests were adjusted at a significance level of $P < 0.05$.

RESULTS

The data were collected from 155 Saudi patients aged 17 to 63 years of both sexes, who were treated at the Dental Clinics Center of Qassim University and fulfilled the inclusion and exclusion criteria. The sex distribution was 106 (69.4%) males and 49 females (31.6%). The intraexaminer reliability showed no statistically significant difference between the 2 image readings by using a paired *t*-test ($P > 0.05$) and had almost perfect agreement ($P = 0.92$ for the measurements and $P = 0.94$ for the pattern distribution).

Regarding the pattern distribution of the GTs among the selected sample (Table 1 and Figure 3), Type III (36.8%) was the most common pattern, followed by Type II (22.6%), Type IV (20%) and Type I (14.2%), while Type V was the least common

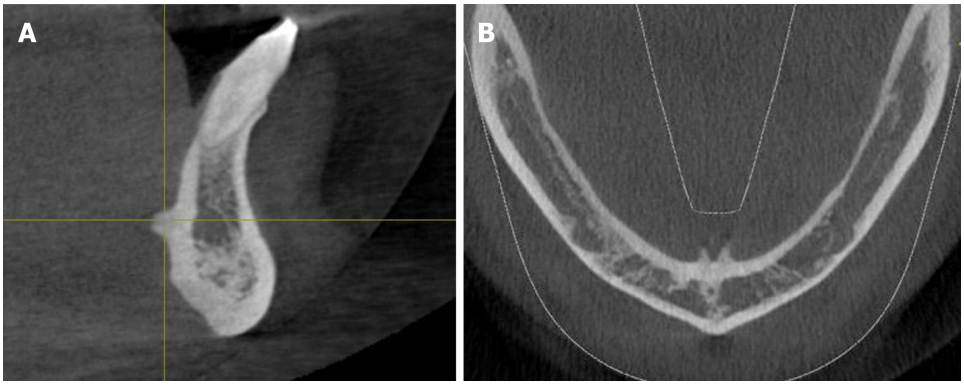

Figure 1 Detection of the genial tubercles pattern in the sagittal and axial views.

among the pattern types (6.4%). Regarding the correlation of the pattern of the GTs with sex, there was no statistically significant difference between sexes at $P \leq 0.05$ using the chi-square test.

The GTH and GTW as well as the distance from the GTs superior border to the apices of the I-SGT and the distance from the inferior border of the GTs to theIGT-M are tabulated in Table 2.

The mean GTH measured was 6.67 ± 3.04 mm, and the mean GTW was 6.23 ± 1.93 mm. The average I-SGT was 8.26 ± 2.7 mm, and the average IGT-M was 8.13 ± 3.07 mm.

DISCUSSION

The main advantages of CBCT are accessibility, ease of handling, and availability of in-office imaging, and it offers a real-size dataset with multiplanar cross-sectional and 3-dimensional reconstructions from a single scan with a low radiation dose and relatively low cost compared with conventional computed tomography[14].

Several studies demonstrated an acceptable accuracy of linear measurements of alveolar bone and mandibular anatomy in CBCT[15]. The results of a study conducted by Hueman *et al*[9] showed the accuracy of CBCT in identifying the anatomic location of the GTs. Therefore, we used CBCT to explore the morphological pattern, dimensions and position of this important landmark.

The morphological pattern of the GTs is controversial and debated; classically, it is described as four elevations equidistant between the upper and lower edges of the mandible that are arranged in pairs and surround the lingual foramina bilaterally. However, several osteological and radiological studies proved that there is wide variation in their morphology.

Regarding the GTs pattern distribution among our selected sample, Type III was the most common type, and type V was the least common type, indicating that type I (the classic pattern) is not the most common type. This observation was also previously described in 2 osteological studies, one conducted among the Indian population by Singh *et al*[4] and one conducted among the Brazilian population by Oda *et al*[5].

The results of the width and height measurements of our study were 6.23 ± 1.93 mm and 6.67 ± 3.04 mm, respectively, which is in line with the results of the radiological study conducted by Wang *et al*[7], who examined the CBCT records of ninety Taiwanese patients and stated that the ranges of GTH measurements were 6.5-7.9 mm and the ranges of the GTW measurements were 7.1-8.2 mm. This is also in line with the study conducted by Yin *et al*[16], who studied the morphometry of GTs in the Chinese population with both anatomical and imaging techniques and correlated them. He concluded that the height and width of the GTs, which were measured by spiral computed tomography, were 6.17 ± 0.71 mm and 7.01 ± 1.13, respectively.

The IGT-M measurements in our study (8.13 ± 3.07 mm) were in line with the measurements made by Hueman *et al*[9] (11.2 ± 3.6 mm), who measured the distance from the middle part of the tubercle to the menton.

The mean I-SGT measurement in our study was 8.26 ± 2.7 mm, and a similar result was discussed by Kolsuz *et al*[17], who studied the anatomy of the genial tubercle using CBCT among a Turkish sample population and found that the mean I-SGT was 8.1 ± 1.7 mm in males and 7.7 ± 1.8 in females with class I occlusion.

In conclusion, the morphological pattern of the GTs is controversial; the GTs are

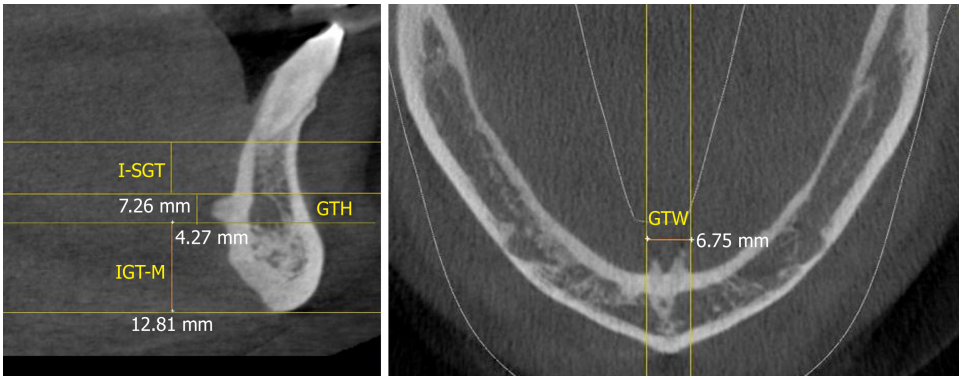

Figure 2 Measurements of the genial tubercle height, distance from the superior border of the genial tubercles to the apex of the lower central incisors and the distance from the inferior border of the genial tubercles to the mentonin the sagittal view and genial tubercles width in the axial view. GTH: Genial tubercles height; GTW: Genial tubercles width; I-SGT: Lower central incisors; IGT-M: Genial tubercles to the menton.

classically described as four elevations equidistant between the upper and lower edges of the mandible that are arranged in pairs, but this is not the most common pattern. The most common pattern among the studied Saudi sample population is of two superior GTs and a rough impression below them with no significant difference between males and females. Further studies should be conducted with larger sample sizes to obtain an accurate morphological analysis of the GTs among different ethnic groups.

Table 1 Genial tubercles pattern distribution as a function of sex

Type	Gender				Total	
	Male (n = 106) (% = 32%)		Female (n = 49) (% = 68%)			
	No	%	No	%	No	%
I	14	13.20%	8	16.30%	22	14.20%
II	24	22.60%	11	22.40%	35	22.60%
III	39	36.80%	18	36.70%	57	36.80%
IV	23	21.70%	8	16.30%	31	20%
V	6	5.70%	4	8.20%	10	6.40%

$\chi^2 = 1.0391$, $P = 0.9$

Table 2 Dimensions of the genial tubercles

Dimensions	Mean ± SD	Maximum	Minimum
GTH (mm)	6.67 ± 3.04	16.08	2.34
GTW (mm)	6.23 ± 1.93	11.77	1.8
I-SGT (mm)	8.26 ± 2.7	15.82	1.57
IGT-M (mm)	8.13 ± 3.07	14.9	1.31

GTH: Genial tubercles height; GTW: Genial tubercles width; I-SGT: Lower central incisors; IGT-M: Genial tubercles to the menton.

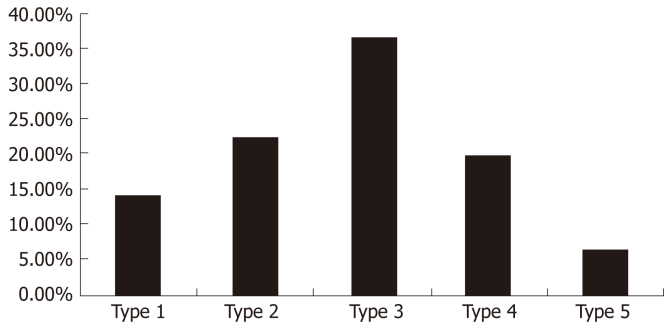

Figure 3 Genial tubercles pattern distribution.

ARTICLE HIGHLIGHTS

Research background

The genial tubercles (GTs) are an important anatomical landmark that is located in the midline of the lingual side of the mandible and is important for multiple clinical and surgical interventions. For years, it was described as four spines arranged in two pairs, one above the other, and few osteological and radiological studies demonstrated the wide variation in its morphology. cone beam computed tomography (CBCT) is an effective and simple method to use in the assessment of GTs morphology among different ethnic groups.

Research motivation

To the best of our knowledge, no previous studies have assessed the pattern of GTs using CBCT, and no previous studies have assessed the dimensions and position of the GTs among the Saudi population or any other Arab population using either osteological or radiological methods.

Research objectives

The aim of this study was to assess the pattern, size and position of the GTs using CBCT among a selected Saudi population.

Research methods

We used CBCT images of 155 male and female Saudi subjects who fulfilled the inclusion and exclusion criteria for this study. Galileos software was used to assess the GTs pattern and to

collect all the linear measurements required to determine its dimensions and position in relation to the menton and the apices of the mandibular central incisors.

Research results

Of the 155 studied subjects, 106 were males, and 49 were females; ages ranged from 17 to 63 years. According to the analysis of the pattern of the GTs , we found that the prevalence of Type III was 36.8%, followed by Type II (22.6%) and Type IV (20%), while the classically described pattern (Type I) was 14.2%. Type V was the least common among the pattern types (6.4%). There was no statistically significant difference between the sexes. Regarding its dimensions and position, we found that the mean GTs height was 6.67 ± 3.04 mm, the mean width was 6.23 ± 1.93 mm, and the average distance from the apices of the mandibular central incisors to its superior border was 8.26 ± 2.7 mm. the average distance between the GTs inferior border and the menton was 8.13 ± 3.07 mm.

Research conclusions

The morphological pattern of the GTs is controversial; the classically described GTs pattern of four elevations, equidistant between the upper and lower edges of the mandible, that are arranged in pairs, is not the most common pattern. The most common pattern among the studied Saudi sample was of two superior GTs and a rough impression below them with no significant difference between the sexes.

Research perspectives

Our results suggest that CBCT might be a simple, valuable and effective tool for conducting an accurate morphological analysis of the GTs among different ethnic groups and resolving the controversy about their morphology.

ACKNOWLEDGEMENTS

The authors would like to thank the College of Dentistry, Qassim University, Saudi Arabia, for providing the radiographic records and the approval of this study.

REFERENCES

1 **Thomson A**. On the Presence of Genial Tubercles on the Mandible of Man, and their Suggested Association with the Faculty of Speech. *J Anat Physiol* 1915; **50**: 43-74 [PMID: 17233052]
2 **Mintz SM**, Ettinger AC, Geist JR, Geist RY. Anatomic relationship of the genial tubercles to the dentition as determined by cross-sectional tomography. *J Oral Maxillofac Surg* 1995; **53**: 1324-1326 [DOI: 0278-2391(95)90594-4]
3 **Ryan JM**, Ross D, Obeid G. Genial tubercle fracture: a case report and review of the literature. *J Oral Maxillofac Surg* 2010; **68**: 2338-2341 [PMID: 20576336 DOI: 10.1016/j.joms.2010.02.032]
4 **Singh V**, Anand MK, Dinesh K. Variations in the pattern of mental spines and spinous mental foramina in dry adult human mandibles. *Surg Radiol Anat* 2000; **22**: 169-173 [PMID: 11143309 DOI: 10.1007/s00276-000-0169-1]
5 **Oda LS**, Iyomasa MM, Watanabe IS. Morphologic analysis of the "spina mentalis" in adult mandibles of Brazilian whites and negroes. *Rev Bras Pesqui Med Biol* 1977; **10**: 357-360 [PMID: 609772]
6 **Voon YS**, Patil PG. Safe zone in anterior mandible related to the genial tubercle for implant osteotomy in a Chinese-Malaysian population: A CBCT study. *J Prosthet Dent* 2018; **119**: 568-573 [PMID: 28838820 DOI: 10.1016/j.prosdent.2017.05.011]
7 **Wang YC**, Liao YF, Li HY, Chen YR. Genial tubercle position and dimensions by cone-beam computerized tomography in a Taiwanese sample. *Oral Surg Oral Med Oral Pathol Oral Radiol* 2012; **113**: e46-e50 [PMID: 22668717 DOI: 10.1016/j.oooo.2011.11.021]
8 **Barbick MB**, Dolwick MF. Genial tubercle advancement for obstructive sleep apnea syndrome: a modification of design. *J Oral Maxillofac Surg* 2009; **67**: 1767-1770 [PMID: 19615597 DOI: 10.1016/j.joms.2009.03.051]
9 **Hueman EM**, Noujeim ME, Langlais RP, Prihoda TJ, Miller FR. Accuracy of cone beam computed tomography in determining the location of the genial tubercle. *Otolaryngol Head Neck Surg* 2007; **137**: 115-118 [PMID: 17599577 DOI: 10.1016/j.otohns.2007.02.035]
10 **Lee SY**, Choi DS, Jang I, Song GS, Cha BK. The genial tubercle: A prospective novel landmark for the diagnosis of mandibular asymmetry. *Korean J Orthod* 2017; **47**: 50-58 [PMID: 28127539 DOI: 10.4041/kjod.2017.47.1.50]
11 **Păuna MR**, Babiuc I, Farcaşiu AT. Prosthodontic management of an extreme atrophy of the mandible correlated with a prominent genial tubercle - a clinical report. *Rom J Morphol Embryol* 2015; **56**: 867-870 [PMID: 26429188]
12 **Solomon EG**. A critical analysis of complete denture impression procedures: contribution of early prosthodontists in India-part I. *J Indian Prosthodont Soc* 2011; **11**: 172-182 [PMID: 22942577 DOI: 10.1007/s13191-011-0089-2]
13 **Shohat I**, Shoshani Y, Taicher S. Fracture of the genial tubercles associated with a mandibular denture: a clinical report. *J Prosthet Dent* 2003; **89**: 232-233 [PMID: 12644795 DOI: 10.1067/mpr.2003.46]
14 **Fatemitabar SA**, Nikgoo A. Multichannel computed tomography versus cone-beam computed tomography: linear accuracy of in vitro measurements of the maxilla for implant placement. *Int J Oral Maxillofac Implants* 2010; **25**: 499-505 [PMID: 20556248]
15 **Ludlow JB**, Laster WS, See M, Bailey LJ, Hershey HG. Accuracy of measurements of mandibular anatomy in cone beam computed tomography images. *Oral Surg Oral Med Oral Pathol Oral Radiol Endod* 2007; **103**: 534-542 [PMID: 17395068 DOI: 10.1016/j.tripleo.2006.04.008]

16 **Yin SK**, Yi HL, Lu WY, Guan J, Wu HM, Cao ZY, Yu DZ, Huang YY, Wu CG. Anatomic and spiral computed tomographic study of the genial tubercles for genioglossus advancement. *Otolaryngol Head Neck Surg* 2007; **136**: 632-637 [PMID: 17418264 DOI: 10.1016/j.otohns.2006.10.034]
17 **Kolsuz ME**, Orhan K, Bilecenoglu B, Sakul BU, Ozturk A. Evaluation of genial tubercle anatomy using cone beam computed tomography. *J Oral Sci* 2015; **57**: 151-156 [PMID: 26062865 DOI: 10.2334/josnusd.57.151]

World Journal of Radiology

Submit a Manuscript: https://www.f6publishing.com

World J Radiol 2019 July 28; 11(7): 102-109

DOI: 10.4329/wjr.v11.i7.102

ISSN 1949-8470 (online)

ORIGINAL ARTICLE

Observational Study

Y90-radioembolization *via* variant hepatic arteries: Is there a relevant risk for non-target embolization?

Markus Zimmermann, Maximilian Schulze-Hagen, Federico Pedersoli, Peter Isfort, Alexander Heinzel, Christiane Kuhl, Philipp Bruners

ORCID number: Markus Zimmermann (0000-0002-2632-800X); Maximilian Schulze-Hagen (0000-0002-9182-2688); Federico Pedersoli (0000-0001-5870-9299); Peter Isfort (0000-0002-0978-8995); Alexander Heinzel (0000-0002-2430-4557); Christiane Kuhl (0000-0001-8696-2363); Philipp Bruners (0000-0002-5790-3687).

Author contributions: Zimmermann M, Schulze-Hagen M, Isfort P, Kuhl C and Bruners P contributed to study conception and design; Zimmermann M, Pedersoli F and Heinzel A contributed to data acquisition, data analysis and interpretation, and writing of article; Zimmermann M, Schulze-Hagen M, Pedersoli F, Heinzel A, Isfort P, Kuhl C and Bruners P contributed to editing, reviewing and final approval of article.

Institutional review board statement: Approval for this retrospective study was granted by the institutional review board, internal reference number: EK 308/18.

Informed consent statement: The need for informed consent was waived by the institutional review board due to the retrospective study design and use of fully anonymized patient data.

Conflict-of-interest statement: On behalf of all authors, the corresponding author states that there is no conflict of interest.

Markus Zimmermann, Maximilian Schulze-Hagen, Federico Pedersoli, Peter Isfort, Christiane Kuhl, and Philipp Bruners, Department of Diagnostic and Interventional Radiology, RWTH Aachen University Hospital, Aachen 52074, Germany

Alexander Heinzel, Department of Nuclear Medicine, RWTH Aachen University Hospital, Pauwelsstrasse 30, Aachen 52074, Germany

Corresponding author: Markus Zimmermann, MD, Attending Doctor, Department of Diagnostic and Interventional Radiology, University Hospital RWTH Aachen, Pauwelsstr 30, Aachen 52074, Germany. mzimmermann@ukaachen.de
Telephone: +49-241-8037443
Fax: +49-241-8082411

Abstract

BACKGROUND

The hepatic arterial anatomy is highly variable, with the two most common variants being a replaced right hepatic artery (RHA) originating from the superior mesenteric artery (SMA) and a left hepatic artery (LHA) originating from the left gastric artery (LGA). These anatomical variants could potentially increase the risk for non-target embolization during Y90-Radioembolization due to the close proximity between hepatic and enteric vessel branches.

AIM

To evaluate the safety of Yttrium-90 radioembolization (^{90}Y-RE) with resin microspheres in patients with a variant hepatic arterial anatomy.

METHODS

In this retrospective single-center observational study, 11 patients who underwent RE with ^{90}Y-resin microspheres *via* a LHA originating from the LGA, and 13 patients *via* a RHA originating from the SMA were included. Patient and treatment data were reviewed regarding clinical and imaging evidence of non-target embolization of ^{90}Y-resin microspheres to the GI tract. Positioning of the tip of the microcatheter in relationship to the last hepatoenteric side branch was retrospectively analyzed using angiographic images, cone-beam CT and pre-interventional CT-angiograms.

RESULTS

None of the 24 patients developed clinical symptoms indicating a potential non-target embolization to the GI tract within the first month after ^{90}Y-RE. On the

Data sharing statement: No additional data are available.

STROBE statement: The authors have read the STROBE Statement-checklist of items, and the manuscript was prepared and revised according to the STROBE Statement-checklist of items.

Received: May 8, 2019
Peer-review started: May 10, 2019
First decision: June 6, 2019
Revised: July 3, 2019
Accepted: July 25, 2019
Article in press: July 25, 2019
Published online: July 28, 2019

P-Reviewer: Vosmik M
S-Editor: Dou Y
L-Editor: A
E-Editor: Ma YJ

postinterventional ^{90}Y-bremsstrahlung images and/or ^{90}Y-positron emission tomographies, no evidence of extrahepatic ^{90}Y-activity in the GI tract was noted in any of the patients. The mean distance between the tip of the microcatheter and the last enteric side branch during delivery of the ^{90}Y microspheres was 3.2 cm (range: 1.9-5 cm) in patients with an aberrant LHA originating from a LGA. This was substantially shorter than the mean distance of 5.2 cm (range: 2.9-7.7 cm) in patients with an aberrant right hepatic originating from the SMA.

CONCLUSION

^{90}Y-RE *via* aberrant hepatic arteries appears to be safe; at least with positioning of the microcatheter tip no less than 1.9 cm distal to the last hepatoenteric side branch vessel.

Key words: Radioembolization; Yttrium 90; Aberrant hepatic arteries; Hepatic arterial variants; Safety

Core tip: Anatomical variants of the hepatic arteries may complicate treatment with ^{90}Y-Radioembolization (^{90}Y-RE) due to a close proximity of hepatic and enteric vessel branches. Left hepatic arteries originating from the left gastric artery usually have a substantially shorter main stem than right hepatic arteries originating from the superior mesenteric artery. However, even a minimum distance of 1.9 cm between the tip of the microcatheter and the last hepatoenteric side branch appears to be sufficient to avoid reflux of ^{90}Y microspheres. Therefore, ^{90}Y-RE should be feasible and safe in most patients with aberrant hepatic arteries without a significantly increased risk for non-target embolization.

Citation: Zimmermann M, Schulze-Hagen M, Pedersoli F, Isfort P, Heinzel A, Kuhl C, Bruners P. Y90-radioembolization *via* variant hepatic arteries: Is there a relevant risk for non-target embolization? *World J Radiol* 2019; 11(7): 102-109
URL: https://www.wjgnet.com/1949-8470/full/v11/i7/102.htm
DOI: https://dx.doi.org/10.4329/wjr.v11.i7.102

INTRODUCTION

Radioembolization with Yttrium-90 (^{90}Y) is a liver-directed cancer treatment which has been shown to be effective and prolong overall survival in patients with irresectable primary or metastatic liver cancer[1-6]. ^{90}Y-Radioembolization (^{90}Y-RE) is being increasingly used over the last couple of years, since studies have shown that it significantly prolongs time-to-progression compared to transarterial chemoembolization in patients with hepatocellular cancer (HCC) for example, while simultaneously resulting in less toxicity[7,8]. In general, side effects after ^{90}Y-RE are uncommon and mostly include mild post-interventional symptoms such as fatigue, abdominal pain, nausea and vomiting[9,10]. A rare, but serious complication however is non-target embolization of ^{90}Y particles to the GI tract, which may lead to radiation-induced gastrointestinal ulceration and is thus associated with significant morbidity and mortality[11].

Non-target embolization of the GI tract during ^{90}Y-RE may result either from hepatoenteric vessels distal to the position of the catheter tip during delivery of the ^{90}Y microspheres, or from reflux of particles into enteric branches proximal to the location of the catheter tip. A pre-treatment mapping angiogram to assess the hepatic arterial anatomy and embolization of any hepatoenteric vessels deemed to pose a risk for non-target embolization using coils, plugs or glue is therefore routinely performed before radioembolization[12,13]. Additionally, the catheter is usually placed as distally as possible during delivery of the ^{90}Y microspheres to minimize the risk of reflux into enteric branches.

However, patients with a variant arterial supply of the liver, such as hepatic arteries originating from the left gastric artery (LGA) or the superior mesenteric artery (SMA) for example, may have an increased risk of non-target embolization due to the close proximity between hepatic and enteric vessel branches.

Therefore, the purpose of this study is to evaluate whether ^{90}Y-RE with resin microspheres can be safely performed *via* a replaced right or left hepatic artery (LHA) originating from the SMA or LGA.

MATERIALS AND METHODS

This single-center retrospective study was approved by the institutional review board (IRB, internal reference no. EK 308/18).

Patients

Computed tomography (CT) angiographies and fluoroscopic angiograms of all patients that had undergone radioembolization with ^{90}Y-resin microspheres (SIRSpheres, Sirtex Medical Ltd, Lane Cove, Australia) between 2010 and 2018 at our institution were retrospectively reviewed and screened for a variant hepatic arterial anatomy. All patients in whom a ^{90}Y-RE was performed *via* a replaced right or LHA and with a minimum follow-up of one month were included in this retrospective analysis.

In general, the indication for ^{90}Y-RE included HCC (BCLC Stage C) and liver-only or liver-dominant metastatic disease of different primary tumors (Table 1 for further details on patient characteristics). All treatment decisions were established by consensus in a multidisciplinary tumor board attended by hepatobiliary surgeons, oncologists, radiotherapists, pathologists and interventional radiologists.

Pre-treatment mapping angiogram

Written informed consent was obtained from all patients before the procedure. All procedures were performed by interventional radiologists with at least 5 years of experience in transarterial oncologic procedures.

As part of the routine work-up before ^{90}Y-RE, a standard mapping angiogram of the celiac axis, superior mesenteric and hepatic arterial vessels was obtained in all patients several days prior to the actual ^{90}Y-RE to assess the hepatic vascular anatomy and identify any hepatoenteric vessels deemed at risk for non-target embolization to the GI tract. Wherever possible, these hepatoenteric vessels, *e.g.*, a right phrenic artery arising from an aberrant left hepatic artery, were subsequently embolized using coils.

The microcatheter was then advanced as distally as possible into the respective hepatic artery to a location that was considered appropriate for subsequent delivery of the ^{90}Y particles. At this location, an arterial phase cone beam CT (Artis Zee or ZeeGo, Siemens Healthcare, Forchheim, Germany) with undiluted contrast agent (Ultravist®-300, Bayer, Leverkusen, Germany) an injection rate of 0.8-1 mL/s with a total volume of 6.4-8 mL and an injection timing delay of 8 s was performed to screen for possible extrahepatic contrast enhancement. If no extrahepatic enhancement was seen, technetium-99m–labeled macroaggregated albumin (^{99m}Tc MAA) was injected and the patient was subsequently transferred to the Department of Nuclear Medicine for a ^{99m}Tc MAA-singe-photon emission CT/CT (^{99m}Tc-SPECT/CT) scan to determine the lung shunt fraction and to screen for the presence of extrahepatic activity.

^{90}Y-Radioembolization

For the eventual treatment, the tip of the microcatheter was placed at an identical position as during the ^{99m}Tc MAA-test-injection and again a cone beam CT was performed with injection of contrast material through the microcatheter to screen for possible hepatoenteric arterial communications. In 23 out of the 24 patients, ^{90}Y-RE was performed in a lobar fashion. One patient received three segmental treatments (segments II, III and IV) *via* a replaced LHA at one-month intervals due to the fact that he had previously undergone right hepatic lobectomy and was therefore considered to have an increased risk of radiation-induced liver disease. Infusion of the ^{90}Y microspheres was performed slowly, manually under intermittent fluoroscopy to ensure antegrade blood flow at all times. Complete administration of all of the calculated activity was achieved in all cases.

After completion of the procedure, each patient received post-interventional ^{90}Y bremsstrahlung images and/or a ^{90}Y positron emission tomography (PET) to evaluate the ^{90}Y distribution in the liver as well as to screen for any extrahepatic activity as a result of a possible non-target embolization.

Follow-up

After radioembolization, all patients were routinely admitted to the nuclear medicine ward at our institution for 48 h, where they were closely monitored for any signs of acute toxicity by daily clinical examination and laboratory analysis of complete blood count, liver function tests and metabolic panel. After discharge, all patients resumed a

Table 1 Patient characteristics

	Total *n* = 24
Male/female	12/12
Mean age (yr)	60 ± 10
Type of tumor	
Hepatocellular carcinoma	10
Colorectal cancer	4
Breast cancer	3
Pancreatic cancer	2
Neuroendocrine tumor of the gastrointestinal tract	2
Endometrial carcinoma	1
Cholangiocellular carcinoma	1
Oropharyngeal cancer	1
Hepatic vascular anatomy	
Left hepatic artery originating from left gastric artery	11
Right hepatic artery originating from superior mesenteric artery	13
Distance between microcatheter tip and last enteric side branch (cm)	
Left hepatic artery originating from left gastric artery	3.2 ± 1.0
Right hepatic artery originating from superior mesenteric artery	5.0 ± 1.7
Mean administered activity (Mbq)	
Treatment of left hepatic lobe	612 ± 190
Treatment of right hepatic lobe	1262 ± 540

The values are expressed as means ± standard deviation. Mbq: Megabecquerel

routine schedule for follow-up with clinical examination, laboratory analysis (complete blood count, liver function tests, metabolic panel, tumor markers) and cross-sectional imaging (contrast-enhanced MRI or PET/CT) one month after treatment and then every 2-3 mo thereafter.

Data analysis and assessment of toxicity

The primary outcome variable of this study was presence or absence of clinical or imaging evidence of non-target embolization of ^{90}Y-microspheres to the GI tract.

Therefore, electronic medical records of all patients were reviewed for presence of nausea, vomiting, abdominal pain and fever as symptoms of potential gastrointestinal complications on days 1-3 and 4 wk after ^{90}Y-RE. These data were graded according to the common terminology criteria for adverse events (CTCAE version 5.0); toxicities of level ≥ 3 were defined as clinically relevant. Additionally, all post-interventional ^{90}Y bremsstrahlung images and ^{90}Y-PETs, as well as the ^{99m}Tc MAA- SPECT/CTs and arterial cone beam CTs, were retrospectively reviewed for evidence of extra-hepatic/gastrointestinal activity or extrahepatic contrast enhancement.

Since catheter positioning is critical for target or non-target embolization, the distance between the position of the microcatheter tip during the administration of the ^{90}Y particles and the last enteric side branch was determined using angiographic images, cone-beam CT images and pre-interventional CT angiograms (including maximum-intensity projections and curved multi-planar reconstructions whenever necessary). Continuous variables were summarized using proportions, mean and median.

RESULTS

Out of 158 patients who had been treated by means of ^{90}Y-RE between 2011 and 2018 at our institution, 24 patients (12 females, 12 males, mean age of 60 ± 10 years) had been treated *via* an aberrant hepatic artery and were therefore included in this retrospective study. There were 11 patients with an LHA originating from the LGA and 13 patients with a right hepatic artery (RHA) originating from the SMA.

Safety and toxicities

^{90}Y-RE was successfully performed in all 24 patients. All patients were discharged as

planned on the second post-interventional day and no clinically relevant toxicities (grade ≥ 3; nausea, vomiting, abdominal pain and fever) were detected during follow-up. No imaging evidence of non-target-embolization of ^{90}Y -microspheres to the GI tract and good tumoral ^{90}Y -uptake was noted on all of the postinterventional ^{90}Y bremsstrahlung images and/or ^{90}Y-PETs.

In one patient with a replaced LHA, extrahepatic activity was noted on the preliminary ^{99m}Tc MAA- SPECT/CTs along the ventral abdominal wall due to a falciforme artery arising from LHA. This falciforme artery could not be embolized due to its very small caliber, however a previous study has shown that there seems to be no absolute need for prophylactic embolization[14]. ^{90}Y-RE was subsequently performed and resulted in non-target embolization of minor amounts of ^{90}Y microspheres along the ventral abdominal wall; the patient remained clinically asymptomatic however.

Catheter positioning

The mean distance between the tip of the microcatheter and the last enteric side branch during administration of the ^{90}Y-microspheres was 3.2 cm (range: 1.9-5 cm) in patients with an aberrant LHA and 5.0 cm (range: 2.1-7.7 cm) in patients with an aberrant RHA (Table 1 for a summary of patient demographics and treatment characteristics). None of the arterial cone beam CTs that were performed through the microcatheter in place for treatment showed extrahepatic, gastrointestinal contrast enhancement (Figure 1A-D).

DISCUSSION

The hepatic arterial anatomy is highly variable; previous studies have shown that 39-49% of all patients have some form of variant arterial blood supply to the liver[15,16]. The two most common variants include a replaced RHA originating from the SMA with a reported prevalence of 12%-15%, and a LHA originating from the LGA with a prevalence between 4.5% and 8%[15,16]. These anatomic variants may complicate treatment by means of ^{90}Y-RE, because of the close proximity of hepatic and enteric branches, which may increase the risk of non-target embolization of the GI tract through reflux of ^{90}Y microspheres. This is particularly true for patients with an LHA originating from the LGA, since the distance between the origin of a replaced LHA at the LGA and the first intrahepatic side branch of the LHA is often particularly short.

In our study, the mean distance between catheter position during delivery of the ^{90}Y particles and the last enteric side branch was shortest in patients with an LHA arising from the LGA, with the minimum distance being 1.9 cm. However, none of the patients developed clinically relevant signs and symptoms of gastrointestinal non-target embolization during follow-up and there was no evidence of ^{90}Y activity in the GI tract on the postinterventional ^{90}Y bremsstrahlung images or PET images in any of the patients. The results of this case series therefore suggest, that ^{90}Y-RE with resin microspheres can be safely performed *via* hepatic arteries originating from either the SMA or the LGA.

Of course, the infusion rate of the ^{90}Y particles can also significantly impact the risk of reflux and thus non-target embolization. Although administration of the ^{90}Y particles was done manually without recording the infusion rate, we did not observe any reflux of contrast agent on the arterial cone beam CTs during the interventions. These were performed with mechanical infusion of contrast agent at a rate of 0.8-1 mL/s, and this rate could be therefore considered a safe starting point. However, hemodynamics will usually change during the procedure due to an increasing number of small vessels getting occluded by the microspheres and therefore intermittent fluoroscopy to adjust the infusion rate and verify antegrade blood flow at all times is strongly recommended. Alternatively, the use of glass microspheres (Theraspheres, BTG International, Ottawa, Ontario, Canada) instead of resin microspheres may decrease the risk for stasis and reflux of particles during treatment due to the decreased embolic load of glass microspheres compared with resin microspheres.

Several studies have explored the option of coil embolization of variant hepatic arteries before ^{90}Y-RE as a method to redistribute and simplify the hepatic blood flow[17-19]. For example, coil embolization of an LHA arising from the LGA may be used to induce redistribution of the intrahepatic arterial blood flow to the left hepatic lobe *via* collaterals from the RHA and therefore facilitate whole liver treatment from a single treatment position in the RHA. While this technique can be used to avoid a potential non-target embolization to the LGA, it also eliminates the option of a selective lobar treatment in patients with a predominantly left hepatic tumor load.

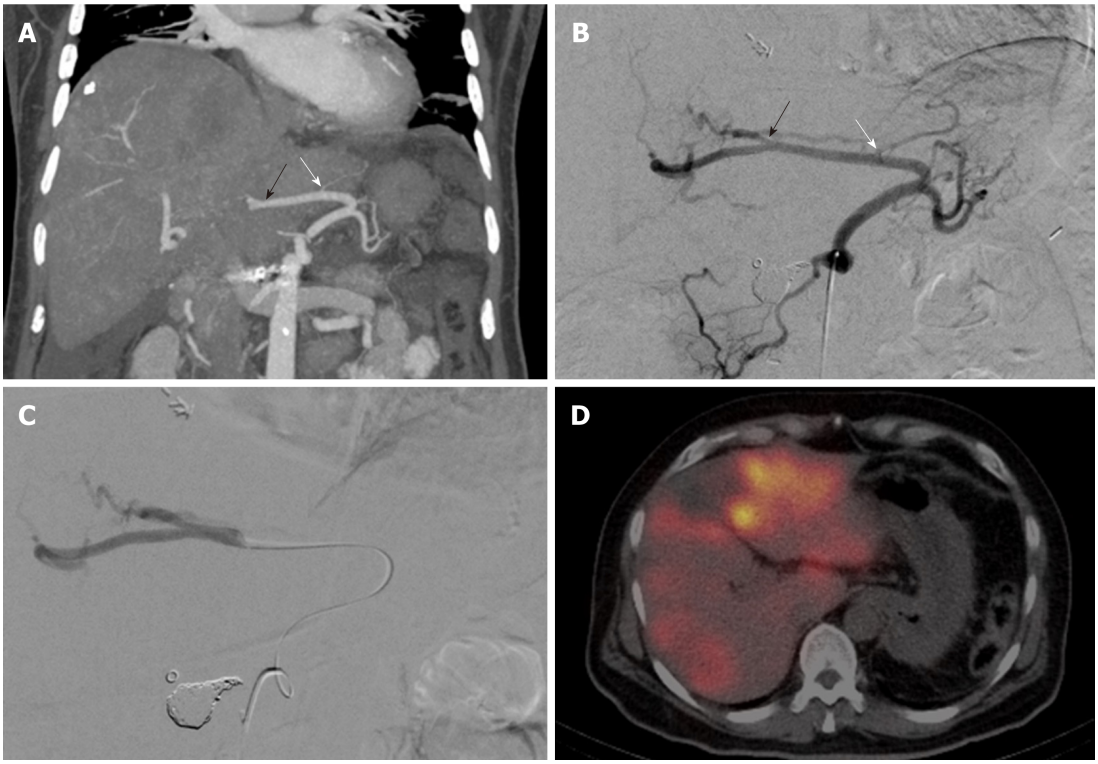

Figure 1 Sample case. 52-year-old patient with an aberrant left hepatic artery originating from the left gastric artery and multifocal colorectal liver metastases in both hepatic lobes. A: Preinterventional computed tomography (CT) angiogram (coronal maximum intensity projection) displaying the distance between the most distal hepatoenteric side branch (white arrow) and the first intrahepatic branch of the aberrant left hepatic artery (LHA) (black arrow); B: Vascular anatomy on the preliminary mapping angiogram. (white arrow: most distal hepatoenteric side branch; black arrow: first intrahepatic branch of the aberrant LHA); C: Catheter position during test injection of technetium ^{99mTc} macro aggregated albumin (99mTc-MAA) (and subsequently also during delivery of the ^{90}Y microspheres); D: Post- 99mTc-MAA SPECT/CT showing good tumoral 99mTc-MAA uptake and no extrahepatic activity.

Additionally, due to the irreversibility of the coil embolization, it may limit future selective transarterial treatment options as well as surgical options, should the patient respond extremely well to the treatment and become a surgical candidate.

The main limitations of this study include its retrospective study design and the small patient cohort. As mentioned before, the individual hepatic arterial anatomy is highly variable and so are the number of hepatoenteric vessels and the distance between hepatic and enteric branches, which significantly impacts the risk of non-target embolization to the GI tract. Therefore, the results of this study may not be applicable to all patients and careful evaluation of the individual arterial anatomy before and during ^{90}Y-RE is still necessary in all patients. Lastly, gastrointestinal complications after ^{90}Y-RE are occasionally not diagnosed until several months after treatment[20]. However, this appears to be mostly attributable to misrecognition of the rather unspecific abdominal symptoms, something that appears avoidable when follow-up is performed by specialists who are familiar with these potential postinterventional complications.

In conclusion, ^{90}Y-RE with resin microspheres *via* an RHA originating from the SMA and/or a LHA replaced to the LGA appears to be feasible and safe. We did not observe any evidence of non-target embolization in 24 patients with placement of the tip of the microcatheter at least 1.9 cm distal of the last enteric side branch and slow manual infusion of the ^{90}Y-particles.

ARTICLE HIGHLIGHTS

Research Background

Radioembolization with Yttrium-90 (^{90}Y) microspheres is commonly used for treatment of primary or secondary liver tumors. It is generally a well-tolerated treatment with few side effects, however non-target embolization of ^{90}Y microspheres to the gastrointestinal tract is a severe potential complication. The risk for non-target embolization is very low in patients with a normal hepatic arterial anatomy. However, around 45% of patients have some form of variant hepatic arterial anatomy and patients with aberrant hepatic arteries might have a higher risk for reflux and non-target embolization of ^{90}Y microspheres due to the close proximity between hepatic and enteric vessel branches.

Research motivation
So far, no study has specifically evaluated the safety of ^{90}Y-Radioembolization in patients with a variant hepatic arterial anatomy. Therefore, this study aimed to evaluate whether there is an increased risk for non-target embolization during ^{90}Y Radioembolization in this specific patient population.

Research objectives
To evaluate the safety of ^{90}Y Radioembolization with resin microspheres in patients with one of the two most common hepatic arterial variants: A right hepatic artery (RHA) originating from the superior mesenteric artery (SMA) or a left hepatic artery (LHA) originating from the left gastric artery (LGA).

Research methods
For this study, electronic medical records and imaging studies of 24 patients who had been treated with Radioembolization *via* an aberrant hepatic artery were retrospectively reviewed regarding clinical and imaging evidence of non-target embolization of ^{90}Y-resin microspheres to the GI tract. 11 patients who underwent ^{90}Y Radioembolization *via* an LHA originating from the LGA and 13 patients who underwent ^{90}Y Radioembolization *via* an RHA originating from the SMA were included. Positioning of the tip of the microcatheter in relationship to the last hepatoenteric side branch was retrospectively analyzed using angiographic images, cone-beam CT and pre-interventional CT-angiograms.

Research results
None of the 24 patients developed clinical symptoms indicating a potential non-target embolization to the GI tract within the first month after ^{90}Y-RE and there was no imaging evidence of non-target embolization on the postinterventional ^{90}Y-bremsstrahlung images and/or ^{90}Y-PETs in any of the patients. The distance between the tip of the microcatheter and the last enteric side branch was substantially shorter in patients with an aberrant LHA originating from a LGA (mean distance of 3.2 cm (range: 1.9-5 cm) than in those patients with an aberrant RHA originating from the SMA (mean distance of 5.2 cm (range: 2.9-7.7 cm). However even a minimum distance of 1.9 cm was sufficient to avoid reflux and non-target embolization of ^{90}Y microspheres.

Research conclusions
This study suggests that ^{90}Y Radioembolization may be safely performed in patients with aberrant hepatic arteries. A minimum distance of 1.9 cm between the tip of the microcatheter and the last enteric side branch in combination with slow, manual infusion of the ^{90}Y microspheres was sufficient to avoid reflux of microspheres and non-target embolization in this study.

Research perspectives
Although this study provides clinical evidence that patients with aberrant hepatic arteries can generally be safely treated with ^{90}Y Radioembolization, further studies with standardized infusion rates and catheter positions would be desirable to systematically determine exact cut-off values at which reflux and non-target embolization of ^{90}Y microspheres occurs.

REFERENCES

1 **Coldwell DM**, Kennedy AS, Nutting CW. Use of yttrium-90 microspheres in the treatment of unresectable hepatic metastases from breast cancer. *Int J Radiat Oncol Biol Phys* 2007; **69**: 800-804 [PMID: 17524567 DOI: 10.1016/j.ijrobp.2007.03.056]

2 **D'Avola D**, Lñarrairaegui M, Bilbao JI, Martinez-Cuesta A, Alegre F, Herrero JI, Quiroga J, Prieto J, Sangro B. A retrospective comparative analysis of the effect of Y90-radioembolization on the survival of patients with unresectable hepatocellular carcinoma. *Hepatogastroenterology* 2009; **56**: 1683-1688 [PMID: 20214218]

3 **Hoffmann RT**, Paprottka PM, Schön A, Bamberg F, Haug A, Dürr EM, Rauch B, Trumm CT, Jakobs TF, Helmberger TK, Reiser MF, Kolligs FT. Transarterial hepatic yttrium-90 radioembolization in patients with unresectable intrahepatic cholangiocarcinoma: factors associated with prolonged survival. *Cardiovasc Intervent Radiol* 2012; **35**: 105-116 [PMID: 21431970 DOI: 10.1007/s00270-011-0142-x]

4 **Kennedy AS**, Coldwell D, Nutting C, Murthy R, Wertman DE, Loehr SP, Overton C, Meranze S, Niedzwiecki J, Sailer S. Resin 90Y-microsphere brachytherapy for unresectable colorectal liver metastases: modern USA experience. *Int J Radiat Oncol Biol Phys* 2006; **65**: 412-425 [PMID: 16690429 DOI: 10.1016/j.ijrobp.2005.12.051]

5 **Kennedy AS**, Dezarn WA, McNeillie P, Coldwell D, Nutting C, Carter D, Murthy R, Rose S, Warner RR, Liu D, Palmedo H, Overton C, Jones B, Salem R. Radioembolization for unresectable neuroendocrine hepatic metastases using resin 90Y-microspheres: early results in 148 patients. *Am J Clin Oncol* 2008; **31**: 271-279 [PMID: 18525307 DOI: 10.1097/COC.0b013e31815e4557]

6 **Seidensticker R**, Denecke T, Kraus P, Seidensticker M, Mohnike K, Fahlke J, Kettner E, Hildebrandt B, Dudeck O, Pech M, Amthauer H, Ricke J. Matched-pair comparison of radioembolization plus best supportive care versus best supportive care alone for chemotherapy refractory liver-dominant colorectal metastases. *Cardiovasc Intervent Radiol* 2012; **35**: 1066-1073 [PMID: 21800231 DOI: 10.1007/s00270-011-0234-7]

7 **Salem R**, Gordon AC, Mouli S, Hickey R, Kallini J, Gabr A, Mulcahy MF, Baker T, Abecassis M, Miller FH, Yaghmai V, Sato K, Desai K, Thornburg B, Benson AB, Rademaker A, Ganger D, Kulik L, Lewandowski RJ. Y90 Radioembolization Significantly Prolongs Time to Progression Compared With Chemoembolization in Patients With Hepatocellular Carcinoma. *Gastroenterology* 2016; **151**: 1155-

1163.e2 [PMID: 27575820 DOI: 10.1053/j.gastro.2016.08.029]
8 **Salem R**, Lewandowski RJ, Kulik L, Wang E, Riaz A, Ryu RK, Sato KT, Gupta R, Nikolaidis P, Miller FH, Yaghmai V, Ibrahim SM, Senthilnathan S, Baker T, Gates VL, Atassi B, Newman S, Memon K, Chen R, Vogelzang RL, Nemcek AA, Resnick SA, Chrisman HB, Carr J, Omary RA, Abecassis M, Benson AB, Mulcahy MF. Radioembolization results in longer time-to-progression and reduced toxicity compared with chemoembolization in patients with hepatocellular carcinoma. *Gastroenterology* 2011; **140**: 497-507.e2 [PMID: 21044630 DOI: 10.1053/j.gastro.2010.10.049]
9 **Salem R**, Lewandowski RJ, Mulcahy MF, Riaz A, Ryu RK, Ibrahim S, Atassi B, Baker T, Gates V, Miller FH, Sato KT, Wang E, Gupta R, Benson AB, Newman SB, Omary RA, Abecassis M, Kulik L. Radioembolization for hepatocellular carcinoma using Yttrium-90 microspheres: a comprehensive report of long-term outcomes. *Gastroenterology* 2010; **138**: 52-64 [PMID: 19766639 DOI: 10.1053/j.gastro.2009.09.006]
10 **Sangro B**, Carpanese L, Cianni R, Golfieri R, Gasparini D, Ezziddin S, Paprottka PM, Fiore F, Van Buskirk M, Bilbao JI, Ettorre GM, Salvatori R, Giampalma E, Geatti O, Wilhelm K, Hoffmann RT, Izzo F, Iñarrairaegui M, Maini CL, Urigo C, Cappelli A, Vit A, Ahmadzadehfar H, Jakobs TF, Lastoria S; European Network on Radioembolization with Yttrium-90 Resin Microspheres (ENRY). Survival after yttrium-90 resin microsphere radioembolization of hepatocellular carcinoma across Barcelona clinic liver cancer stages: a European evaluation. *Hepatology* 2011; **54**: 868-878 [PMID: 21618574 DOI: 10.1002/hep.24451]
11 **Yip D**, Allen R, Ashton C, Jain S. Radiation-induced ulceration of the stomach secondary to hepatic embolization with radioactive yttrium microspheres in the treatment of metastatic colon cancer. *J Gastroenterol Hepatol* 2004; **19**: 347-349 [PMID: 14748889 DOI: 10.1111/j.1440-1746.2003.03322.x]
12 **Lewandowski RJ**, Sato KT, Atassi B, Ryu RK, Nemcek AA, Kulik L, Geschwind JF, Murthy R, Rilling W, Liu D, Bester L, Bilbao JI, Kennedy AS, Omary RA, Salem R. Radioembolization with 90Y microspheres: angiographic and technical considerations. *Cardiovasc Intervent Radiol* 2007; **30**: 571-592 [PMID: 17516113 DOI: 10.1007/s00270-007-9064-z]
13 **Paprottka PM**, Jakobs TF, Reiser MF, Hoffmann RT. Practical vascular anatomy in the preparation of radioembolization. *Cardiovasc Intervent Radiol* 2012; **35**: 454-462 [PMID: 21567273 DOI: 10.1007/s00270-011-0169-z]
14 **Ahmadzadehfar H**, Möhlenbruch M, Sabet A, Meyer C, Muckle M, Haslerud T, Wilhelm K, Schild HH, Biersack HJ, Ezziddin S. Is prophylactic embolization of the hepatic falciform artery needed before radioembolization in patients with 99mTc-MAA accumulation in the anterior abdominal wall? *Eur J Nucl Med Mol Imaging* 2011; **38**: 1477-1484 [PMID: 21494857 DOI: 10.1007/s00259-011-1807-z]
15 **Covey AM**, Brody LA, Maluccio MA, Getrajdman GI, Brown KT. Variant hepatic arterial anatomy revisited: digital subtraction angiography performed in 600 patients. *Radiology* 2002; **224**: 542-547 [PMID: 12147854 DOI: 10.1148/radiol.2242011283]
16 **Winston CB**, Lee NA, Jarnagin WR, Teitcher J, DeMatteo RP, Fong Y, Blumgart LH. CT angiography for delineation of celiac and superior mesenteric artery variants in patients undergoing hepatobiliary and pancreatic surgery. *AJR Am J Roentgenol* 2007; **189**: W13-W19 [PMID: 17579128 DOI: 10.2214/AJR.04.1374]
17 **Abdelmaksoud MH**, Louie JD, Kothary N, Hwang GL, Kuo WT, Hofmann LV, Hovsepian DM, Sze DY. Consolidation of hepatic arterial inflow by embolization of variant hepatic arteries in preparation for yttrium-90 radioembolization. *J Vasc Interv Radiol* 2011; **22**: 1364-1371.e1 [PMID: 21961981 DOI: 10.1016/j.jvir.2011.06.014]
18 **Bilbao JI**, Garrastachu P, Herráiz MJ, Rodríguez M, Iñarrairaegui M, Rodríguez J, Hernández C, de la Cuesta AM, Arbizu J, Sangro B. Safety and efficacy assessment of flow redistribution by occlusion of intrahepatic vessels prior to radioembolization in the treatment of liver tumors. *Cardiovasc Intervent Radiol* 2010; **33**: 523-531 [PMID: 19841973 DOI: 10.1007/s00270-009-9717-1]
19 **Karunanithy N**, Gordon F, Hodolic M, Al-Nahhas A, Wasan HS, Habib N, Tait NP. Embolization of hepatic arterial branches to simplify hepatic blood flow before yttrium 90 radioembolization: a useful technique in the presence of challenging anatomy. *Cardiovasc Intervent Radiol* 2011; **34**: 287-294 [PMID: 20700593 DOI: 10.1007/s00270-010-9951-6]
20 **Voruganti IS**, Godwin JL, Adrain A, Feller E. A Woman with Black Beads in Her Stomach: Severe Gastric Ulceration Caused by Yttrium-90 Radioembolization. *Case Rep Med* 2018; **2018**: 1413724 [PMID: 29849654 DOI: 10.1155/2018/1413724]

Published By Baishideng Publishing Group Inc
7041 Koll Center Parkway, Suite 160, Pleasanton, CA 94566, USA
Telephone: +1-925-2238242
Fax: +1-925-2238243
E-mail: bpgoffice@wjgnet.com
Help Desk: https://www.f6publishing.com/helpdesk
https://www.wjgnet.com

ISSN 1949-8470 (online)

World Journal of *Radiology*

World J Radiol 2019 August 28; 11(8): 110-115

Published by Baishideng Publishing Group Inc

World Journal of Radiology

Contents

Monthly Volume 11 Number 8 August 28, 2019

CASE REPORT

World Journal of Radiology
Volume 11 Number 8 August 28, 2019

Contents

NAME OF JOURNAL
World Journal of Radiology

ISSN
ISSN 1949-8470 (online)

LAUNCH DATE
January 31, 2009

FREQUENCY
Monthly

EDITORS-IN-CHIEF
Venkatesh Mani

EDITORIAL BOARD MEMBERS
https://www.wjgnet.com/1949-8470/editorialboard.htm

EDITORIAL OFFICE
Jin-Lei Wang, Director

PUBLICATION DATE
August 28, 2019

INSTRUCTIONS TO AUTHORS
https://www.wjgnet.com/bpg/gerinfo/204

GUIDELINES FOR ETHICS DOCUMENTS
https://www.wjgnet.com/bpg/GerInfo/287

GUIDELINES FOR NON-NATIVE SPEAKERS OF ENGLISH
https://www.wjgnet.com/bpg/gerinfo/240

PUBLICATION MISCONDUCT
https://www.wjgnet.com/bpg/gerinfo/208

ARTICLE PROCESSING CHARGE
https://www.wjgnet.com/bpg/gerinfo/242

STEPS FOR SUBMITTING MANUSCRIPTS
https://www.wjgnet.com/bpg/GerInfo/239

ONLINE SUBMISSION
https://www.f6publishing.com

World Journal of Radiology

Submit a Manuscript: https://www.f6publishing.com

World J Radiol 2019 August 28; 11(8): 110-115

DOI: 10.4329/wjr.v11.i8.110

ISSN 1949-8470 (online)

CASE REPORT

Duodenal variceal bleeding with large spontaneous portosystemic shunt treated with transjugular intrahepatic portosystemic shunt and embolization: A case report

Rohit Anand, Saad Emhmed Ali, Driss Raissi, Wesam M Frandah

ORCID number: Rohit Anand (0000-0002-6587-2825); Saad Emhmed Ali (0000-0002-3481-0365); Driss Raissi (0000-0002-6751-2997); Wesam M Frandah (0000-0001-8068-7030).

Author contributions: Emhmed Ali S, Anand R, Raissi D and Frandah WM designed the paper. Emhmed Ali S, Anand R, Raissi D and Frandah WM wrote the paper. All authors contributed equally to this paper. An author may list more than one contribution, and more than one author may have contributed to the same aspect.

Informed consent statement: Informed consent was obtained from the patient.

Conflict-of-interest statement: No conflict of interest declared.

CARE Checklist (2016) statement: The authors have read the CARE Checklist (2016), and the manuscript was revised according to the CARE Checklist (2016).

Rohit Anand, Saad Emhmed Ali, Departament of Internal Medicine, University of Kentucky, Lexington, KY 40536, United States

Driss Raissi, Wesam M Frandah, Department of Interventional Radiology, University of Kentucky, Lexington, KY 40536, United States

Corresponding author: Saad Emhmed Ali, FACP, MD, Assistant Professor, Departament of Internal Medicine, University of Kentucky, 800 Rose St, Lexington, KY 40536, United States.
saad.ali@uky.edu
Telephone: +1-859-2184991
Fax: +1-859-2283352

Abstract

BACKGROUND

Duodenal variceal bleeding is a rare cause of gastrointestinal bleeding. The most common site is the duodenal bulb. It is usually detected endoscopically but it can be very challenging to diagnose if it is located distal to the second part od duodenum. The pre- transjugular intrahepatic portosystemic shunt (TIPS) presence of spontaneous portosystemic shunt (SPSS) was found to be associated with an increased risk of early morbidity and mortality after TIPS placement.

CASE SUMMARY

A 43-year-old cirrhotic male presented with melena for three days. Upper endoscopy was performed and showed active blood oozing from the distal duodenum concerning for ectopic duodenal varix. A computed tomography (CT) angiogram was performed and showed an enlarged cluster of venous collaterals around the distal duodenum. He underwent TIPS placement. He had another episode of melena three days later. Push enteroscopy with injection sclerotherapy into the duodenal varices was performed with no success. A repeat CT angiogram showed occluded TIPS shunt. Therefore, a TIPS revision was performed and there was an extensive portal venous thrombosis with a large shunt between the inferior mesenteric vein and left renal vein *via* the left gonadal vein. Thrombectomy and TIPS shunt balloon angioplasty was performed, followed by embolization of the portosystemic. The melena was resolved, and patient was discharged with arranged hepatology follow up.

CONCLUSION

It importance to look and embolize the SPSS shunts in patients with early TIPS

Manuscript source: Unsolicited manuscript

Received: July 13, 2019
Peer-review started: July 26, 2019
First decision: August 2, 2019
Revised: August 14, 2019
Accepted: August 18, 2019
Article in press: August 19, 2019
Published online: August 28, 2019

P-Reviewer: Garbuzenko DV, Tarantino G
S-Editor: Ma RY
L-Editor: A
E-Editor: Zhou BX

dysfunction and recurrent duodenal variceal bleeding.

Key words: Portasystemic shunt; Gastrointestinal hemorrhage; Liver cirrhosis; Duodenum; Endoscopy; Angioplasty; Case report

Core tip: Portal hypertension leads to the formation of varices, which can be present at the gastroesophageal region or ectopic locations. Bleeding ectopic varices are challenging to manage, and in many cases, transjugular intrahepatic portosystemic shunt (TIPS) is a safe and effective therapy. The pre-TIPS presence of spontaneous portosystemic shunt (SPSS) was found to be associated with an increased risk of early morbidity and mortality after TIPS placement. We have successfully treated a patient with duodenal variceal bleeding with TIPS and embolization of SPSS after he failed TIPS monotherapy.

Citation: Anand R, Ali SE, Raissi D, Frandah WM. Duodenal variceal bleeding with large spontaneous portosystemic shunt treated with transjugular intrahepatic portosystemic shunt and embolization: A case report. *World J Radiol* 2019; 11(8): 110-115
URL: https://www.wjgnet.com/1949-8470/full/v11/i8/110.htm
DOI: https://dx.doi.org/10.4329/wjr.v11.i8.110

INTRODUCTION

Duodenal variceal bleeding is a rare cause of gastrointestinal bleeding. It can be life-threatening with a mortality rate of up to 40%[1]. Portal hypertension due to liver cirrhosis is the most common cause of portosystemic shunts and duodenal varices[2]. The most common site is at the duodenal bulb, and it is usually detected endoscopically[3]. However, it can be difficult to diagnose if it is located distal to the second part of duodenum. The pre-transjugular intrahepatic portosystemic shunt (TIPS) presence of spontaneous portosystemic shunt (SPSS) was found to be associated with an increased risk of early morbidity and mortality after TIPS placement [4]. We have successfully treated a patient with duodenal variceal bleeding with TIPS and embolization of SPSS after he failed TIPS monotherapy.

CASE PRESENTATION

Chief complaints

A 43-year-old male presented to the emergency department complaining of melena for three days.

History of present illness

He had two loose bowel movements with black tarry stool every day for the last three days with lightheadedness.

History of past illness

He denies any hematemesis, abdominal pain, or similar episodes in the past.

Personal and family history

Past medical history was remarkable for liver cirrhosis due to untreated hepatitis C and alcohol abuse. Family history was unremarkable.

Physical examination upon admission

On presentation, vitals revealed a blood pressure of 100/60 mmHg; pulse rate of 110 per minute, temperature of 98.5 Fahrenheit, and respiratory rate of 18 per minute. Physical exam revealed an ill-looking patient with mild confusion, pale conjunctiva, non-icterus sclera, mildly distended abdomen with no tenderness, and trace pitting edema in both legs.

Laboratory examinations

Laboratory findings displayed hemoglobin of 6.8 g/dL, leukocytes 10000/mm^3, and platelet 105000/mm^3. Serum biochemistry revealed creatinine 0.6 mg/dL, blood urea nitrogen 16 mg/dL, albumin 2.4 g/dL, total protein 4.8 g/dL, aspartate aminotransferase 34 IU/L, alanine aminotransferase 60 IU/L, alkaline phosphatase 95 IU/L, international normalized ratio 1.1 and total bilirubin 1.5 mg/dL.

FINAL DIAGNOSIS

Duodenal variceal bleeding with large spontaneous portosystemic shunt.

TREATMENT

Emergency esophagogastroduodenoscopy (EGD) was performed on the day of admission and showed grade B esophagitis and small esophageal varices with no active bleeding.

OUTCOME AND FOLLOW-UP

He continued to have melena, and drop in hemoglobin concertation over the next 48 h. So, repeat EGD was performed and showed oozing of fresh blood in the distal duodenum, concerning for a bleeding ectopic duodenal varix. A computed tomography (CT) angiogram was performed and showed an enlarged cluster of venous collaterals around the distal duodenum. He underwent TIPS *via* using VIATORR® 10 mm × 6 cm stent-graft, which decreased the portosystemic gradient from 21 mmHg to 5 mmHg with complete decompression of the intestinal varices (Figure 1).

Seventy-two hours later, the patient had a recurrence of melena with worsening anemia. A push enteroscopy was performed and showed fresh blood oozing from ectopic varix in the fourth portion of the duodenum (Figure 2). One ml of glue (n-Butyl Cyanoacrylate) was injected into varix. Despite all of that, he continued to have gastrointestinal bleeding that requires a blood transfusion. A repeat CT angiogram showed a nearly occluded TIPS shunt. Therefore, a TIPS revision was preceded, and TIPS was occluded with extensive portal venous thrombosis (Figure 3).

Interestingly, there was a large, competing, non-physiological shunt between the inferior mesenteric vein and left renal vein *via* the left gonadal vein (Figure 4). Maceration thrombectomy and TIPS shunt balloon angioplasty was performed, followed by embolization of the portosystemic (Figure 5). The patient remained stable for the rest of the hospital course with no signs of recurrent bleeding. He was discharged with arranged hepatology follow up.

DISCUSSION

Patients with portal hypertension develop SPSS with hepatofugal flow that serve as non-physiologic communications between branches of the systemic and portal venous systems which allow excess flow to bypass the liver. One of these SPSS is the splenorenal shunt (SRS), which is associated with boosted occurrence of hepatocellular carcinoma in an obese patient[5]. SPSS when dilating form varices, which they can be present at numerous regions of the body. Since duodenal varices were initially defined by Alberti[6] in 1931 and envisioned *via* the scope by Kunisaki *et al*[7] in 1973, there have been hundreds of cases published. In a study reviewing 169 cases of bleeding ectopic varices, 17% were in the duodenum[1]. Bleeding ectopic varices account for up to 5% of all variceal bleeding noted in cirrhotic patients. They can be very challenging to diagnose and manage, and as a result, in some cases, can have mortality rates as high as 40%[1,8,9]. Currently, there are no set guidelines for the treatment of ectopic variceal bleeding. Management varies based on the location and size of these ectopic varices. Endoscopic band ligation (EBL) and endoscopic injection sclerotherapy (EIS) has been tried in multiple studies for bleeding ectopic varices with some degree of success[10-15]. However, as in our case, EBL or EIS can fail to control the bleeding, and TIPS can be used as second-line therapy[16,17]. A combined therapeutic technique such as a balloon-occluded retrograde transvenous obliteration (BRTO) with embolization or sclerotherapy has been investigated by Copelan *et al*[18] and showed a bleeding control rate of 90% and it suggested to be a safe treatment option when TIPS is contraindicated.

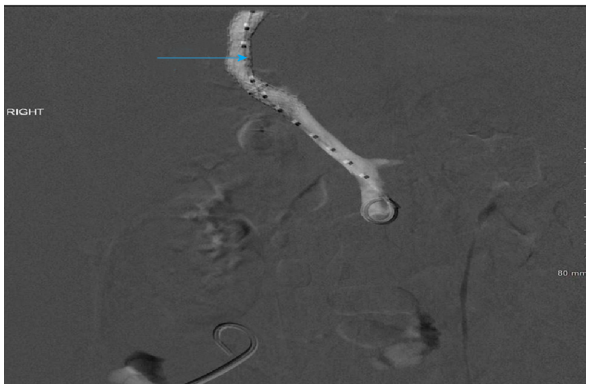

Figure 1 Portal vein angiography image showing hepatopetal flow through transjugular intrahepatic portosystemic shunt (blue arrow) with no filling of varices.

TIPS reduce the hepatic venous pressure gradient (HVPG), which results in portal venous decompression and variceal bleeding control. Studies have shown that bleeding risk from varices decreases significantly once the HVPG falls below 12 mmHg[19,20]. TIPS dysfunction is a complication with TIPS placement. It is defined as a loss of portal vein system decompression, due to thrombosis or stenosis (> 50%) of the TIPS. The pre-TIPS presence of SPSS was found to be associated with an increased risk of early morbidity and mortality after TIPS placement[4].

Our patient had an infrequent and unusual cause for TIPS thrombosis. He was noted to have a large non-physiological spontaneous portosystemic shunt between the inferior mesenteric vein and left renal vein *via* the left gonadal vein. The shunt promoted hepatofugal flow that was competing with the TIPS. As a result, it decreased the flow across the shunt and led to early thrombosis and TIPS dysfunction, which led to recurrent variceal bleeding. Once the shunt was embolized, TIPS revision was successful, and the patient's variceal bleeding resolved.

CONCLUSION

This case illustrates the importance to look for these competing shunts in patients with early TIPS dysfunction and recurrent bleeding when other causes have been ruled out. Also, as noted in our case, portosystemic pressure gradient measurements are unreliable in patients with large competing SPSS. Embolization of these shunts is crucial to control the duodenal variceal bleeding and prevent early thrombosis of TIPS.

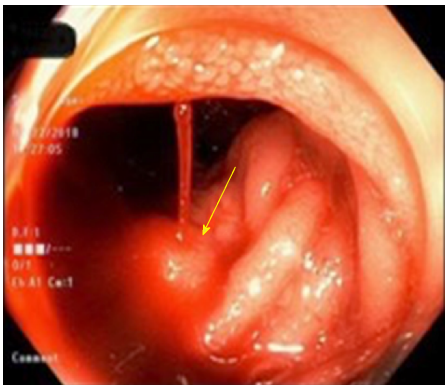

Figure 2 Endoscopic image showing active oozing of fresh blood (yellow arrow) from the ectopic varix in the fourth portion of the duodenum.

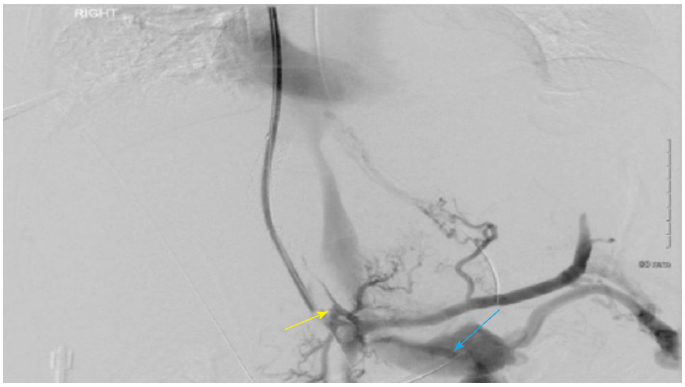

Figure 3 Angiographic image showing filling defect in the transjugular intrahepatic portosystemic shunt and the portal vein (yellow arrow) with portosystemic shunting to left renal vein (blue arrow).

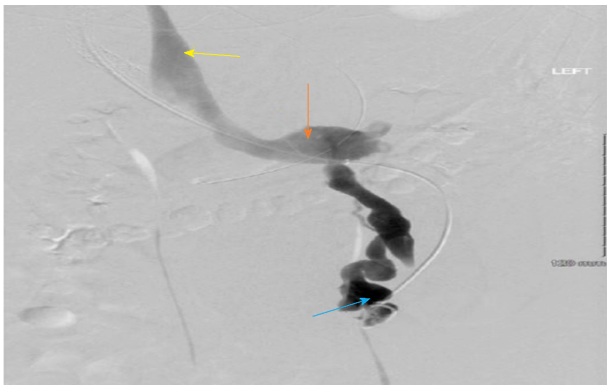

Figure 4 Angiographic image showing a large mesenterico-gonadal venous shunt (blue arrow) draining into the inferior vena cava (yellow arrow) *via* the left renal vein (orange arrow).

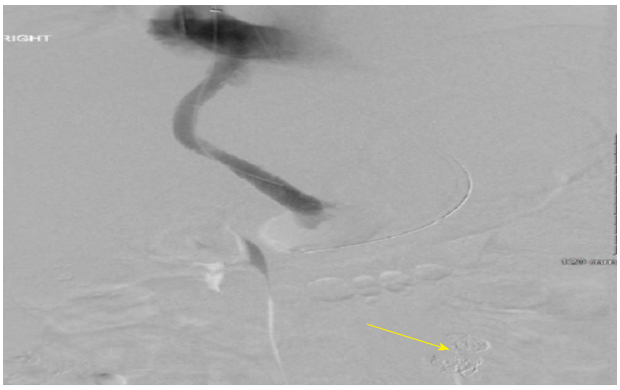

Figure 5 Angiographic image of the portal vein showing the restoration of hepatopetal flow through the transjugular intrahepatic portosystemic shunt after the portosystemic shunt was embolized (yellow arrow).

REFERENCES

1 **Norton ID**, Andrews JC, Kamath PS. Management of ectopic varices. *Hepatology* 1998; **28**: 1154-1158 [PMID: 9755256 DOI: 10.1002/hep.510280434]
2 **Kotfila R**, Trudeau W. Extraesophageal varices. *Dig Dis* 1998; **16**: 232-241 [PMID: 9732183 DOI: 10.1159/000016871]
3 **Christidou A**, Tzathas C, Khuffash O, Triantaphyllou G. Upper gastrointestinal bleeding due to ectopic varices in a patient with alcoholic cirrhosis. *Ann Gastroentol* 2003; **16**: 179-182
4 **Borentain P**, Soussan J, Resseguier N, Botta-Fridlund D, Dufour JC, Gérolami R, Vidal V. The presence of spontaneous portosystemic shunts increases the risk of complications after transjugular intrahepatic portosystemic shunt (TIPS) placement. *Diagn Interv Imaging* 2016; **97**: 643-650 [PMID: 26947721 DOI: 10.1016/j.diii.2016.02.004]
5 **Tarantino G**, Citro V, Conca P, Riccio A, Tarantino M, Capone D, Cirillo M, Lobello R, Iaccarino V. What are the implications of the spontaneous spleno-renal shunts in liver cirrhosis? *BMC Gastroenterol* 2009; **9**: 89 [PMID: 19930687 DOI: 10.1186/1471-230X-9-89]
6 **Alberti W**. Uberden roentgenologischen nachweis von varizen in buolbus duodeni. *Fortschro Geb Koentgenstr* 1931; **43**: 60-65
7 **Kunisaki T**, Someya N, Shimokava Y. Varices in the distal duodenum seen with a fiberduodenoscope. *Endoscopy* 1973; **5**: 101-104 [DOI: 10.1055/s-0028-1098222]
8 **Graham DY**, Smith JL. The course of patients after variceal hemorrhage. *Gastroenterology* 1981; **80**: 800-809 [PMID: 6970703 DOI: 10.1016/0016-5085(81)90144-X]
9 **Sarin SK**, Kumar CKN. Ectopic varices. *Clin Liver Dis (Hoboken)* 2012; **1**: 167-172 [PMID: 31186880 DOI: 10.1002/cld.95]
10 **Akhter NM**, Haskal ZJ. Diagnosis and management of ectopic varices. *Gastrointest Intervention* 2012; **1**: 3-10 [DOI: 10.1016/j.gii.2012.08.001]
11 **Akazawa Y**, Murata I, Yamao T, Yamakawa M, Kawano Y, Nomura N, Isomoto H, Mizuta Y, Murase K, Kohno S. Successful management of bleeding duodenal varices by endoscopic variceal ligation and balloon-occluded retrograde transvenous obliteration. *Gastrointest Endosc* 2003; **58**: 794-797 [PMID: 14595327 DOI: 10.1016/S0016-5107(03)02008-X]
12 **Yoshida Y**, Imai Y, Nishikawa M, Nakatukasa M, Kurokawa M, Shibata K, Shimomukai H, Shimano T, Tokunaga K, Yonezawa T. Successful endoscopic injection sclerotherapy with N-butyl-2-cyanoacrylate following the recurrence of bleeding soon after endoscopic ligation for ruptured duodenal varices. *Am J Gastroenterol* 1997; **92**: 1227-1229 [PMID: 9219810]
13 **Hekmat H**, Al-toma A, Mallant MP, Mulder CJ, Jacobs MA. Endoscopic N-butyl-2-cyanoacrylate (Histoacryl) obliteration of jejunal varices by using the double balloon enteroscope. *Gastrointest Endosc* 2007; **65**: 350-352 [PMID: 17259003 DOI: 10.1016/j.gie.2006.07.001]
14 **Chen WC**, Hou MC, Lin HC, Chang FY, Lee SD. An endoscopic injection with N-butyl-2-cyanoacrylate used for colonic variceal bleeding: a case report and review of the literature. *Am J Gastroenterol* 2000; **95**: 540-542 [PMID: 10685765 DOI: 10.1016/S0002-9270(99)00841-2]
15 **Ota K**, Shirai Z, Masuzaki T, Tanaka K, Higashihara H, Okazaki M, Arakawa M. Endoscopic injection sclerotherapy with n-butyl-2-cyanoacrylate for ruptured duodenal varices. *J Gastroenterol* 1998; **33**: 550-555 [PMID: 9719241 DOI: 10.1007/s005350050131]
16 **Selçuk H**, Boyvat F, Eren S, Korkmaz M, Gür G, Yilmaz U, Boyacioğlu S. Duodenal varices as an unusual cause of gastrointestinal bleeding due to portal hypertension: a case report. *Turk J Gastroenterol* 2004; **15**: 104-107 [PMID: 15334321]
17 **Jonnalagadda SS**, Quiason S, Smith OJ. Successful therapy of bleeding duodenal varices by TIPS after failure of sclerotherapy. *Am J Gastroenterol* 1998; **93**: 272-274 [PMID: 9468260 DOI: 10.1111/j.1572-0241.1998.270_3.x]
18 **Copelan A**, Chehab M, Dixit P, Cappell MS. Safety and efficacy of angiographic occlusion of duodenal varices as an alternative to TIPS: review of 32 cases. *Ann Hepatol* 2015; **14**: 369-379 [PMID: 25864218 DOI: 10.1016/S1665-2681(19)31277-3]
19 **Vangeli M**, Patch D, Terreni N, Tibballs J, Watkinson A, Davies N, Burroughs AK. Bleeding ectopic varices--treatment with transjugular intrahepatic porto-systemic shunt (TIPS) and embolisation. *J Hepatol* 2004; **41**: 560-566 [PMID: 15464235 DOI: 10.1016/j.jhep.2004.06.024]
20 **Boyer TD**, Haskal ZJ; American Association for the Study of Liver Diseases. The role of transjugular intrahepatic portosystemic shunt in the management of portal hypertension. *Hepatology* 2005; **41**: 386-400 [PMID: 15660434 DOI: 10.1002/hep.20559]

Published By Baishideng Publishing Group Inc
7041 Koll Center Parkway, Suite 160, Pleasanton, CA 94566, USA
Telephone: +1-925-2238242
Fax: +1-925-2238243
E-mail: bpgoffice@wjgnet.com
Help Desk: https://www.f6publishing.com/helpdesk
https://www.wjgnet.com

ISSN 1949-8470 (online)

World Journal of *Radiology*

World J Radiol 2019 September 28; 11(9): 116-125

Published by Baishideng Publishing Group Inc

WJR World Journal of Radiology

Contents

Monthly Volume 11 Number 9 September 28, 2019

CASE REPORT

World Journal of Radiology
Volume 11 Number 9 September 28, 2019

Contents

NAME OF JOURNAL
World Journal of Radiology

ISSN
ISSN 1949-8470 (online)

LAUNCH DATE
January 31, 2009

FREQUENCY
Monthly

EDITORS-IN-CHIEF
Venkatesh Mani

EDITORIAL BOARD MEMBERS
https://www.wjgnet.com/1949-8470/editorialboard.htm

EDITORIAL OFFICE
Ruo-Yu Ma, Director

PUBLICATION DATE
September 28, 2019

INSTRUCTIONS TO AUTHORS
https://www.wjgnet.com/bpg/gerinfo/204

GUIDELINES FOR ETHICS DOCUMENTS
https://www.wjgnet.com/bpg/GerInfo/287

GUIDELINES FOR NON-NATIVE SPEAKERS OF ENGLISH
https://www.wjgnet.com/bpg/gerinfo/240

PUBLICATION MISCONDUCT
https://www.wjgnet.com/bpg/gerinfo/208

ARTICLE PROCESSING CHARGE
https://www.wjgnet.com/bpg/gerinfo/242

STEPS FOR SUBMITTING MANUSCRIPTS
https://www.wjgnet.com/bpg/GerInfo/239

ONLINE SUBMISSION
https://www.f6publishing.com

World Journal of Radiology

Submit a Manuscript: https://www.f6publishing.com

World J Radiol 2019 September 28; 11(9): 116-125

DOI: 10.4329/wjr.v11.i9.116

ISSN 1949-8470 (online)

CASE REPORT

Metastatic appendiceal cancer treated with Yttrium 90 radioembolization and systemic chemotherapy: A case report

Ambarish P Bhat, Philip A Schuchardt, Roopa Bhat, Ryan M Davis, Sindhu Singh

ORCID number: Ambarish P Bhat (0000-0002-8628-7465); Philip A Schuchardt (0000-0002-3090-687X); Roopa Bhat (0000-0002-7772-2509); Ryan M Davis (0000-0002-0858-3330); Sindhu Singh (0000-0003-4125-1693).

Author contributions: Bhat AP planned and performed the Y90 radioembolization, wrote the paper, and responded to edits from both the University of Missouri care team and publication editors. Schuchardt PA wrote the paper and participated in the editing process. Bhat R wrote the paper and participated in the editing process. Davis RM planned and performed the Y90 radioembolization and participated in the editing process. Singh S prescribed the patient's chemotherapy and provided advice regarding recommended treatments.

Informed consent statement: Informed consent was obtained from the patient.

Conflict-of-interest statement: No conflict of interest declared.

CARE Checklist (2016) statement: The authors have read the CARE Checklist (2016), and the manuscript was revised according to the CARE Checklist (2016).

Ambarish P Bhat, Philip A Schuchardt, Roopa Bhat, Ryan M Davis, Department of Vascular and Interventional Radiology, University of Missouri Columbia, Columbia, MO 65212, United States

Sindhu Singh, Department of Medicine, Section of Hematology-Oncology, University of Missouri-Columbia, Columbia, MO 65212, United States

Corresponding author: Ambarish P Bhat, MD, Assistant Professor, Department of Vascular and Interventional Radiology, University of Missouri Columbia, One Hospital Drive, Columbia, MO 65212, United States. bhatap@health.missouri.edu
Telephone: +1-573-8821025
Fax: +1-573-8844457

Abstract

BACKGROUND

Primary appendiceal cancers are rare, and they generally present with liver and/or peritoneal metastases. Currently there are no guidelines to treat metastatic appendiceal cancer, and hence they are treated as metastatic colorectal cancer. Combining Yttrium 90 (Y-90) radioembolization (RE) with systemic chemotherapy early in the treatment of right sided colon cancers has been shown to improve survival. Based on this data, a combination of systemic chemotherapy and Y-90 RE was used to treat a case of metastatic appendiceal cancer.

CASE SUMMARY

A 76-year-old male presented to the emergency room with progressive right lower quadrant pain. A Computed Tomography of the abdomen and pelvis was performed which showed acute appendicitis and contained perforation. Urgent laparoscopic appendectomy was then followed by histological analysis, which was significant for appendiceal adenocarcinoma. After complete workup he underwent right hemicolectomy and lymph node dissection. He received adjuvant chemotherapy as the local lymph nodes were positive. Follow-up imaging was significant for liver metastasis. Due to rapid growth of the liver lesions and new peritoneal nodules, the patient was treated with a combination of Y-90 RE and folinic acid, fluorouracil, and irinotecan with bevacizumab and not microwave ablation as previously planned. Follow up imaging demonstrated complete response of the liver lesions. At 12-mo follow-up, the patient continued to enjoy good quality of life with no recurrent disease.

CONCLUSION

Utilization of Y-90 RE concomitantly with systemic chemotherapy early in the

Manuscript source: Unsolicited manuscript

Received: March 2, 2019
Peer-review started: March 4, 2019
First decision: August 2, 2019
Revised: August 10, 2019
Accepted: August 21, 2019
Article in press: Auguet 21, 2019
Published online: September 28, 2019

P-Reviewer: Bazeed MF, Gavriilidis P
S-Editor: Ma RY
L-Editor: A
E-Editor: Liu MY

treatment of appendiceal cancer may provide improved control of this otherwise aggressive cancer.

Key words: Colorectal cancer; Liver metastases; Radioembolization; Yttrium 90 microspheres; Appendix cancer with peritoneal metastasis; Hyperthermic intraperitoneal chemotherapy; Case report

Core tip: Primary appendiceal cancers are rare and there are no current guidelines for treatment of metastatic appendiceal cancer. We describe an unusual case of appendiceal cancer metastatic to the liver and peritoneum that was successfully treated with a combination of systemic chemotherapy and Yttrium 90 radioembolization. This complete and sustained response may support a role for combination therapy in the more aggressive right sided colon cancers.

Citation: Bhat AP, Schuchardt PA, Bhat R, Davis RM, Singh S. Metastatic appendiceal cancer treated with Yttrium 90 radioembolization and systemic chemotherapy: A case report. *World J Radiol* 2019; 11(9): 116-125
URL: https://www.wjgnet.com/1949-8470/full/v11/i9/116.htm
DOI: https://dx.doi.org/10.4329/wjr.v11.i9.116

INTRODUCTION

Primary cancers of the appendix are rare and often aggressive. There are no evidence based guidelines to deal with patients who present with aggressive metastatic appendiceal cancers. Surgical cytoreduction and hyperthermic intraoperative chemotherapy (HIPEC) have shown survival benefit in some patients[1]. However, it is a rather extensive and major operation and not suitable for all patients. In patients who are not suitable candidates, there are very limited options and hence, they have a dismal prognosis. In the past decade, the role of Yttrium 90 (Y-90) radioembolization (RE) in chemorefractory metastatic colorectal cancer (CRC) has been extensively studied and has produced promising results[2-4]. Due to its proven synergistic role with systemic chemotherapy, a combination of Y-90 RE and chemotherapy was used to successfully treat a patient with metastatic appendiceal cancer.

CASE PRESENTATION

Chief complaints

A 76-year-old male initially presented to the emergency room with progressive pain in the right lower quadrant.

History of present illness

The pain was localized to the right lower quadrant without any radiation. The pain was associated with anorexia, without nausea or vomiting. Low grade fever was present.

History of past illness

Significant for hypertension controlled with medications and benign prostatic hyperplasia.

Personal and family history

No history of alcohol, or drug abuse.

Physical exam upon admission

Vital signs: Heart rate 108/min, respiratory rate 23/min, BP 130/82 mmHg. Temperature: 37.1 °C.

Cardiovascular: Tachycardia with normal heart sounds.

Respiratory: Normal breath sounds.

Abdomen: Moderate tenderness in the right lower quadrant. No abdominal

distension. Normal bowel sounds. Neurological: Alert, oriented, without neurological deficits.

Laboratory examinations

The blood work showed leukocytosis, with white blood cell: 12 × 10^9 L. The rest of the labs were normal.

Imaging examinations

Contrast-enhanced computed tomography (CT) of the abdomen and pelvis demonstrated a markedly dilated appendix with surrounding inflammatory changes (Figure 1) and regional lymphadenopathy. This was originally interpreted as acute appendicitis with contained perforation.

TREATMENT

The patient then underwent urgent laparoscopic appendectomy and drainage of the intra-abdominal abscess. Pathology of the surgical specimen revealed a moderately differentiated appendiceal adenocarcinoma, measuring 1.7 cm, with tumor invading the mesoappendix. Extensive transmural inflammatory changes were noted, though the base of the appendix was not involved. The patient underwent colonoscopy to excluded synchronous lesions. As the colonoscopy was negative for additional lesions, the patient subsequently underwent laparoscopic right hemicolectomy with primary anastomosis and lymph node dissection. During the operation the rest of the abdomen was thoroughly inspected for metastatic disease. After performing laparoscopic right hemicolectomy with primary anastomosis and lymph node dissection, histopathology demonstrated 6/18 lymph nodes positive for metastatic adenocarcinoma with extra-nodal extension present in the largest lymph node. The distal ileum and cecum were free of malignancy. The staging was completed by obtaining a CT of the chest (as it had not been obtained in the initial presentation), and it showed no evidence of metastatic disease.

The patient then received 12 cycles of adjuvant folinic acid, fluorouracil, and oxaliplatin (FOLFOX) chemotherapy for a duration of 7 mo from the initial diagnosis. Follow-up CT 10 mo after the last cycle of chemotherapy demonstrated three hypodense hypovascular lesions in the right lobe of the liver (two in segment 7 and one in segment 2) (Figure 2) with concurrent rise in serum carcinoembryonic antigen level. Ultrasound guided biopsy of the liver lesions revealed metastatic adenocarcinoma, consistent with an appendiceal primary.

FINAL DIAGNOSIS

Final diagnosis was stage IIIC (T3, N2, Mx) moderately differentiated appendiceal adenocarcinoma.

MULTIDISCIPLINARY EXPERT CONSULTATION

Due to the complexity of the case. It was presented at the multidisciplinary tumor board and a decision was made to proceed with microwave ablation of the liver lesions. Fluorodeoxyglucose (FDG) positron emission tomography (PET) CT obtained prior to microwave ablation demonstrated an increase in the size of the liver lesions (FDG avid) and new sub-centimeter FDG avid lesions in the peritoneum, suggestive of metastatic implants (Figure 3). Two of the three lesions, now measured more than 3 cm, prompting us to hold off on the microwave ablation. The patient was again presented to the multidisciplinary tumor board and was not considered a surgical candidate for hepatic metastasectomy or HIPEC due to general deconditioning, including severe weight loss. In light of the progressive hepatic and limited extrahepatic disease burden, the patient was offered selective internal radiation treatment or RE with Y90 and initiation of folinic acid, fluorouracil, and irinotecan (FOLFIRI) with bevacizumab, as a palliative measure. FOLFIRI was initiated prior to the Y-90 RE procedure; however, the bevaxizumab was not started until after the RE procedure.

A mapping angiogram was performed one week prior to the Y-90 RE treatment to evaluate the vascular anatomy and estimate the lung shunt fraction (LSF). As a part of the mapping angiogram, the gastroduodenal artery was embolized using 4 and 5 mm 0.018″ Azur® CX coils (Terumo Interventional Systems). Based on the planar images

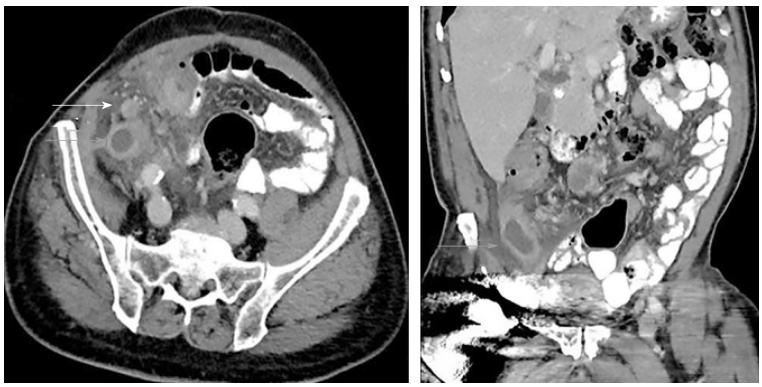

Figure 1 Axial and coronal abdominal contrast enhanced computed tomography images depict a fluid filled and dilated appendix (gray arrows) and adenopathy (white arrow). Surrounding inflammatory changes present.

obtained after injection of ^{99m}technetium-labeled macroaggregated albumin (^{99m}TcMAA) into the right hepatic artery, the shunt fraction toward the lung was calculated at approximately 2.5%.

Calculations of liver and tumor volumes were performed on a 3D segmentation application (TeraRecon Inc Foster City, CA, United States). The whole liver volume was 1325 mL. The right lobe measured 875 mL, the tumor volume was 150 mL, and the tumor to normal liver ratio (T:N) based off the ^{99m}TcMAA injection during the mapping angiogram was 3:1. The prescribed activity was calculated using the DAVYR application (Dose and activity visualizer for Y-90 RE) (Figure 4) and the SIR sphere microsphere activity calculator (SMAC) chart provided by the manufacturer and a 1.0 Gigabecquerel (Gbq) activity of Y90 was prescribed for treatment of the right lobe metastatic lesions. Based on the body surface area (BSA) method recommended by the manufacturer, the dose to the tumor was estimated as 126 Gray (Gy) and dose to the healthy liver was estimated at 40.9 Gray (Gy) (Figure 4). The prescribed activity was successfully administered by positioning a Progreat 2.8 F 130 cm catheter (Terumo Interventional Systems) in the right hepatic artery distal to the origin of the cystic artery (Figure 5). Post procedure Bremsstrahlung planar and single photon emission computed tomography (SPECT) demonstrated appropriate distribution of Y90 spheres in the hepatic lobe without evidence of non-target embolization (Figure 6).

OUTCOME AND FOLLOW-UP

Post RE FDG PET/CT performed two months after treatment (Figure 7) showed complete response, with no residual FDG-avid lesions in the liver or peritoneum. No new lesions were identified. At this point, based on the good response to treatment, the oncologist switched him to a combination of oral capecitabine and bevacizumab. The patient has been followed for 12 mo after the Y-90 treatment and continues to demonstrate good quality of life with no recurrent disease. There were no significant changes to his liver functions after treatment, except slight elevation of his alkaline phosphatase. The only toxicity was hyperpigmentation of the fingers and oral ulcers (hand foot mouth disease) which started 10 mo into the treatment and resolved with reduction of the capecitabine dose.

DISCUSSION

The incidence of appendiceal cancer is 1.2 per 100000 people per year in the United States. Potentially due in part to this rarity, there are no accepted American Joint Commission on Cancer staging system or National Comprehensive Cancer Network evidence-based guidelines recommended for appendiceal cancer[5]. Colon cancer workup, staging, and treatment is commonly applied to appendiceal carcinoma.

Appendiceal cancers can either present with or progress to peritoneal dissemination and the optimal therapy is complete surgical cytoreduction in combination with HIPEC[6]. For patients not eligible for complete cytoreduction and HIPEC, as in this case, systemic chemotherapy with regimens utilized for metastatic CRC are generally considered the mainstay therapy. We embarked on a literature review to find potential treatment options for our patient.

A systematic review of the literature was performed using Pubmed for articles from

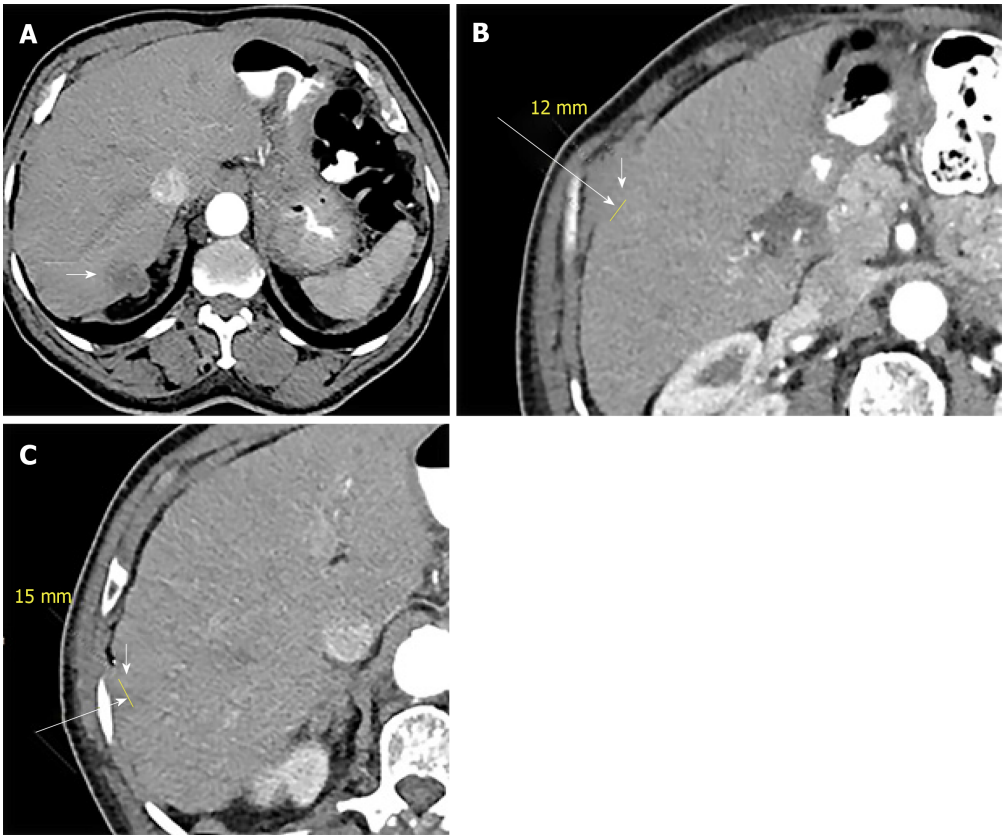

Figure 2 Axial sequential abdominal contrast enhanced computed tomography images (A-C) depict 3 new hepatic lesions in the right lobe (white arrows).

inception to January 2019 using the key words "Y90", "metastatic Appendix cancer" and "systemic chemotherapy". We did not find any studies in which Y-90 RE was used to treat liver metastasis form appendix cancer. However we found several studies using Y 90 in the salvage setting following failure of chemotherapy with improved overall survival numbers[2-4]. Data was extracted by two extractors.

Interventional oncology treatments for liver dominant CRC metastasis include, RE, drug eluting beads irinotecan (DEBIRI) transarterial chemoemboization (TACE) and thermal ablation.

RE with Y-90 microspheres is based on the same principle as that of TACE, in that the hepatic artery provides the primary vascular supply to the tumor, while the portal vein provides the majority of blood flow to normal hepatic parenchyma[7]. Furthermore, the microvascular density of hepatic tumors is much higher than the hepatic parenchyma[8], resulting in a proportionately higher exposure to microspheres. CRC cells are highly radiosensitive and even chemo-refractive lesions do not generally demonstrate any cross-resistance to radiation. Additionally, radiation works synergistically when used with radiation-sensitizing chemotherapeutic drugs.

The two commercial manufacturers of Y-90 microspheres are TheraSpheres (BTG International, ON, Canada) and SIR-spheres (Sirtex Medical Inc., Sydney, Australia). These microspheres, that have been specifically developed to deliver Y-90, measure 20-60 μm in size. Y-90 primarily emits beta radiation, with a half-life of 64.1 h and an average energy of 0.94 MeV. The beta particles have a range of 1.1 cm (average 2.5 mm *in vivo*) from the source, with 94% of the dose being deposited within the first 11 d of administration[9]. Hence, RE works from "inside out" and inflicts minimal damage to the normal liver. This is in contrast to external beam radiation which exposes the normal liver parenchyma to excessive amounts of radiation, in the process of killing multifocal tumors, thus increasing collateral damage. One of the most critical components of the RE procedure is the dosimetry. There is one activity calculation method for Y-90 glass microspheres[10], however three alternatives exist for resin microspheres[11-13].

Both liver and tumor volumes, calculated based on CT or magnetic resonance imaging are used to determine resin microsphere activity. The empiric model recommends administration of 2.0 GBq for < 25% involvement, 2.5 GBq for 25%-50% involvement, and 3.0 GBq for > 50% involvement[13]. This method has low safety

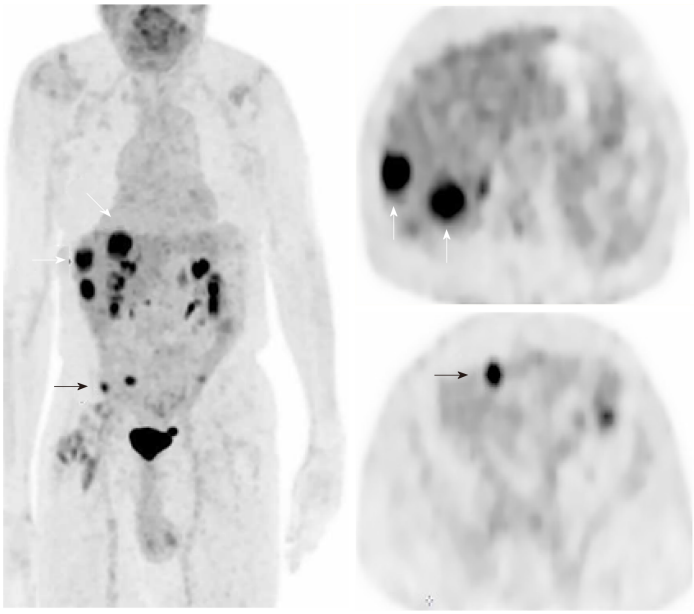

Figure 3 Coronal and axial fluorodeoxyglucose positron emission tomography images show fluorodexoyglucose avid liver (white arrows) and peritoneal (black arrows) metastases.

margins[13,14] and is generally not recommended. The empiric method adjusted for patient BSA has been more widely utilized to calculate the activity needed to treat liver tumors[12]. This model assumes that the patient's BSA is proportional to liver volume, thus leading to a method of dose adjustment. Activity in GBq = (BSA - 0.2) + [V_{Tumor} / (V_{Tumor} + V_{Liver})]. Where V_{Tumor} is the tumor volume and V_{Liver} is liver volume[12].

Lastly, the partition model is the only calculation method predicated on Medical Internal Radiation Dose principles (MIRD)[15-17]. The partition model identifies the lungs, tumor, and uninvolved liver parenchyma as three distinct vascular compartments that can be partitioned during RE[15] and the dose to the individual components can be estimated for optimization and safety of the procedure. A slightly simplified MIRD based equation calculates the dose to the liver as follows: D liver (Gy) = Injected activity (GBq) × 50 × fractional uptake liver × [m liver (kg)] – 1.

With fractional uptake (FU) of the liver defined as: FU_{liver} = (1-LSF) [m_{liver}/TLR × m_{tumor}+ m_{liver}], where m_{liver} is the liver mass, TLR is tumor to liver ratio and LSF is LSF.

This model usually works well with discrete tumor that can be separated from the surrounding parenchyma (generally hepatocellular cancer). The BSA activity planning is suited for small lesions with diffuse or infiltrative margins, which cannot be separated from the uninvolved liver parenchyma (generally metastasis).

A tumoricidal dose for SIR spheres is considered to be 120 Gy, so little benefit is gained when exceeding this dose, while parenchymal damage continues to increase with larger radiation doses[18,19]. The dose for uninvolved, normal parenchyma should preferably be at 50 Gy and should never exceed 70 Gy.

For TheraSphere® noncompartmental MIRD macrodosimetry proposed for by Salem *et al*[11] is used. It uses the following equation for computation of the activity and assumes Y 90 distributes uniformly within the liver and decays completely *in situ*. Activity required (GBq) = [desired dose (Gy)] × [target liver mass (kg)]/50.

Of note, Therasphere dosimetry is independent of the tumor volume and depends solely on the infused tissue mass. For Therasphere, the recommended mean absorbed is between 80 and 150 Gy per lobe[11]. The recommended tumoricidal doses is 120 Gy for HCC (due to the underlying cirrhosis) and 150 Gy for metastases[11]. Maximum exposure to the lungs should be less than 30 Gy per session and 50 Gy cumulatively[17]. Both manufacturers recommend prescribed activity reductions for patients with lung shunts higher than 10%[10,13].

Several investigators have studied the application of Y-90 RE in the salvage setting for liver dominant metastatic CRC[2,3]. Van Hazel *et al*[4] reported results of combined Y-90 RE with systemic irinotecan therapy in patients who failed initial 5-FU chemotherapy. In a group of 25 patients, 11 (48%) had partial response (PR) and 9 (39%) had stable disease. Median survival was 12.2 mo.

DEBIRI TACE has been proposed by some as a possible alternative to RE, however evidence within the literature is currently limited. In our institute we consider it in cases where Y-90 RE is contraindicated or in the setting of failed RE therapy. TACE

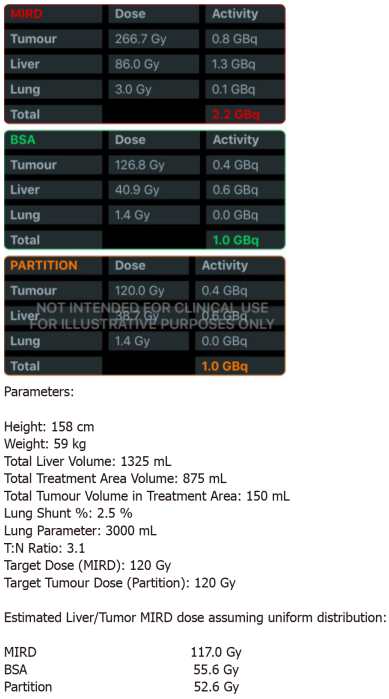

Figure 4 Dose and activity visualizer for Yttrium-90 radioembolization (DAVYR) application chart obtained after inputting the necessary fields, displaying the medical internal radiation dose, body surface area and partition models with prescribed activity Gigabecquerel, estimated dose to the tumor, liver and lungs Gray.

with DEBIRI involves two separate treatment sessions for each lobe, with each session occurring 4 wk apart[20]. Based on this, patients with bilobar disease, may need four procedures. During each treatment session, as much as one vial of 100- to 300-μm LC Beads (Biocompatibles, Oxford, CT) loaded with 100-mg irinotecan is selectively delivered to treat the hepatic lesions. Furthermore, post-embolization syndrome is more severe after DEBERI as compared to Y-90, with moderate to severe abdominal pain observed in up to 30% of treatment sessions[20,21].

Thermal ablation has been successfully used in treatment of non rescectable CRC liver metastasis, with best outcomes for isolated liver lesions less than 3 cm without systemic spread[22]. Although our patient initially appeared to be a good candidate for thermal ablation, his staging PET showed increased in size of the hepatic lesions and new lesions in the peritoneum, making him a less suitable candidate for liver ablation alone and prompted us to use systemic therapy and more aggressive liver directed therapy in the form of Y-90 RE to the right lobe.

Several studies in the past 2 years have reported that patients have worse survival outcomes with right sided colon cancer, and they may benefit less from standard therapies[23,24]. The subset of patients with right sided tumors in the SIRFLOX, FOXFIRE and SIRFLOX global trials had a better overall survival from addition of RE in combination with first line chemotherapy[25]. Gene expression analyses have identified 4 consensus molecular subtypes (CMSs) which are different with right and left-sided CRCs, with greater proportions of the "microsatellite unstable/immune" CMS1 and the "metabolic" CMS3 subtypes found in right-sided colon cancers[26], which may explain their different behavior and natural history.

CONCLUSION

To the best of our knowledge, this is the first report of Y-90 RE used with systemic chemotherapy to treat hepatic metastatic disease from appendiceal cancer. The aggressive disease progression demonstrated in this case appears to mirror the aggressiveness one might see from typical right sided colonic malignancies. Most studies using Y90 RE in the salvage setting report PR of liver lesions. The patient in this case report had a complete response of both liver and peritoneal metastases presumably form a combination of Y-90 RE and systemic chemotherapy. The relative contribution of the two individual treatments or any possible synergy between the treatments is unknown, however initiating Y-90 RE early in the treatment may have contributed to the excellent control of what was otherwise a rapidly progressive

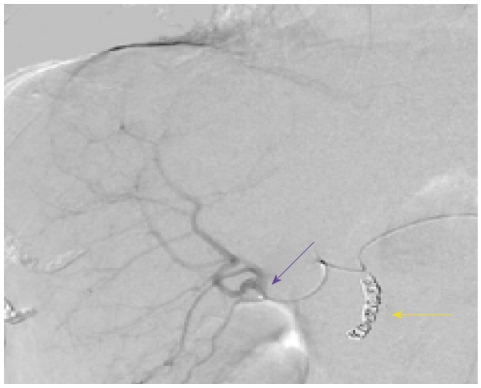

Figure 5 Hepatic angiogram. Yttrium 90 administration to the right lobe. The tip of the catheter (purple arrow) is at the bifurcation of the sectoral branches of the right hepatic artery. Coils in the gastro-duodenal artery (yellow arrow).

cancer. More studies are needed to assess the benefit of adding Y-90 RE to chemotherapy treatments early in the course of appendiceal/right sided colon cancers.

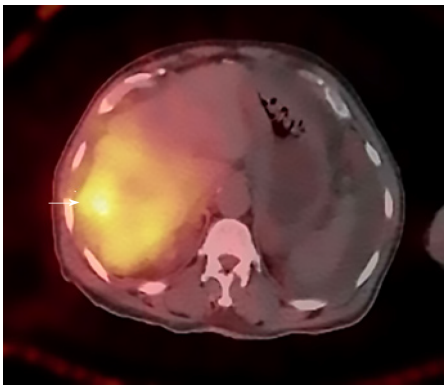

Figure 6 Axial post procedure single photon emission tomography image shows appropriate distribution of Yttrium 90 particles in the right hepatic lobe with increased focal uptake in one of the right lobe lesions (white arrow).

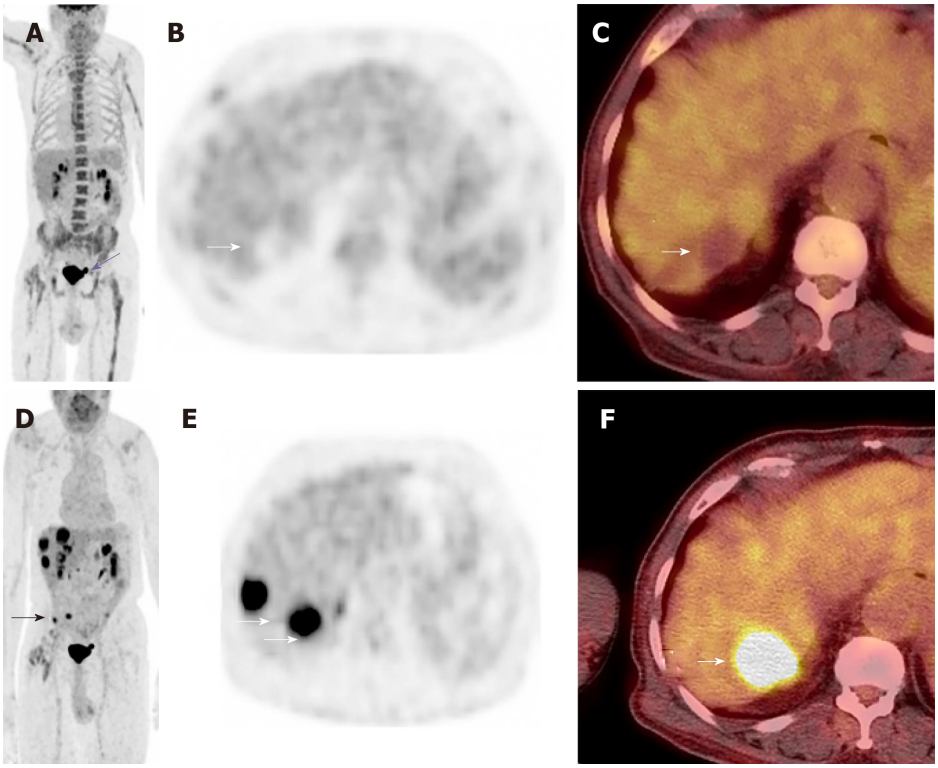

Figure 7 A restaging skull base to mid-thigh fluorodeoxyglucose positron emission tomography/computed tomography scan was performed after injection of 4.9 mCi of flurodexoyglucose 2 mo following Yttrium 90 radioembolization. The post Yttrium 90 treatment positron emission tomography (PET) maximum intensity projection (MIP) coronal (A), attenuation corrected axial (B) and fused axial (C) PET images show complete resolution of all lesions with focal photopenia in the right hepatic lobe (white arrowheads). Incidentally, there is chemotherapy induced diffuse skeletal uptake and a small urinary bladder diverticulum (purple straight arrow A). The pre-therapy Positron emission tomography images are provided for comparison. Coronal MIP image (D) axial attenuation correction (E), and fused axial (F). Pretreatment PET images show multiple flurodexoyglucose avid right lobe hepatic (white arrows) and peritoneal (black arrows) lesions. PET: Positron emission tomography; MIP: Maximum intensity projection.

REFERENCES

1 **Verwaal VJ**, van Ruth S, de Bree E, van Sloothen GW, van Tinteren H, Boot H, Zoetmulder FA. Randomized trial of cytoreduction and hyperthermic intraperitoneal chemotherapy versus systemic chemotherapy and palliative surgery in patients with peritoneal carcinomatosis of colorectal cancer. *J Clin Oncol* 2003; **21**: 3737-3743 [PMID: 14551293 DOI: 10.1200/JCO.2003.04.187]

2 **Cosimelli M**, Golfieri R, Cagol PP, Carpanese L, Sciuto R, Maini CL, Mancini R, Sperduti I, Pizzi G, Diodoro MG, Perrone M, Giampalma E, Angelelli B, Fiore F, Lastoria S, Bacchetti S, Gasperini D, Geatti O, Izzo F; Italian Society of Locoregional Therapies in Oncology (SITILO). Multi-centre phase II clinical trial of yttrium-90 resin microspheres alone in unresectable, chemotherapy refractory colorectal liver metastases. *Br J Cancer* 2010; **103**: 324-331 [PMID: 20628388 DOI: 10.1038/sj.bjc.6605770]

3 **Bester L**, Meteling B, Pocock N, Pavlakis N, Chua TC, Saxena A, Morris DL. Radioembolization versus standard care of hepatic metastases: comparative retrospective cohort study of survival outcomes and

adverse events in salvage patients. *J Vasc Interv Radiol* 2012; **23**: 96-105 [PMID: 22079516 DOI: 10.1016/j.jvir.2011.09.028]
4 **van Hazel GA**, Pavlakis N, Goldstein D, Olver IN, Tapner MJ, Price D, Bower GD, Briggs GM, Rossleigh MA, Taylor DJ, George J. Treatment of fluorouracil-refractory patients with liver metastases from colorectal cancer by using yttrium-90 resin microspheres plus concomitant systemic irinotecan chemotherapy. *J Clin Oncol* 2009; **27**: 4089-4095 [PMID: 19652069 DOI: 10.1200/JCO.2008.20.8116]
5 **McCusker ME**, Coté TR, Clegg LX, Sobin LH. Primary malignant neoplasms of the appendix: a population-based study from the surveillance, epidemiology and end-results program, 1973-1998. *Cancer* 2002; **94**: 3307-3312 [PMID: 12115365 DOI: 10.1002/cncr.10589]
6 **Sugarbaker PH**, Zhu BW, Sese GB, Shmookler B. Peritoneal carcinomatosis from appendiceal cancer: results in 69 patients treated by cytoreductive surgery and intraperitoneal chemotherapy. *Dis Colon Rectum* 1993; **36**: 323-329 [PMID: 8458256 DOI: 10.1007/BF02053933]
7 **Breedis C**, Young G. The blood supply of neoplasms in the liver. *Am J Pathol* 1954; **30**: 969-977 [PMID: 13197542]
8 **Lien WM**, Ackerman NB. The blood supply of experimental liver metastases. II. A microcirculatory study of the normal and tumor vessels of the liver with the use of perfused silicone rubber. *Surgery* 1970; **68**: 334-340 [PMID: 5450714]
9 **Kalva SP**, Thabet A, Wicky S. Recent advances in transarterial therapy of primary and secondary liver malignancies. *Radiographics* 2008; **28**: 101-117 [PMID: 18203933 DOI: 10.1148/rg.281075115]
10 Package Insert-TheraSphere® Yttrium-90 Glass Microspheres. Available from: http://www.therasphere.com
11 **Salem R**, Thurston KG. Radioembolization with 90Yttrium microspheres: a state-of-the-art brachytherapy treatment for primary and secondary liver malignancies. Part 1: Technical and methodologic considerations. *J Vasc Interv Radiol* 2006; **17**: 1251-1278 [PMID: 16923973 DOI: 10.1097/01.RVI.0000233785.75257.9A]
12 **Lau WY**, Kennedy AS, Kim YH, Lai HK, Lee RC, Leung TW, Liu CS, Salem R, Sangro B, Shuter B, Wang SC. Patient selection and activity planning guide for selective internal radiotherapy with yttrium-90 resin microspheres. *Int J Radiat Oncol Biol Phys* 2012; **82**: 401-407 [PMID: 20950954 DOI: 10.1016/j.ijrobp.2010.08.015]
13 **Kennedy A**, Nag S, Salem R, Murthy R, McEwan AJ, Nutting C, Benson A, Espat J, Bilbao JI, Sharma RA, Thomas JP, Coldwell D. Recommendations for radioembolization of hepatic malignancies using yttrium-90 microsphere brachytherapy: a consensus panel report from the radioembolization brachytherapy oncology consortium. *Int J Radiat Oncol Biol Phys* 2007; **68**: 13-23 [PMID: 17448867 DOI: 10.1016/j.ijrobp.2006.11.060]
14 **Kennedy AS**, McNeillie P, Dezarn WA, Nutting C, Sangro B, Wertman D, Garafalo M, Liu D, Coldwell D, Savin M, Jakobs T, Rose S, Warner R, Carter D, Sapareto S, Nag S, Gulec S, Calkins A, Gates VL, Salem R. Treatment parameters and outcome in 680 treatments of internal radiation with resin 90Y-microspheres for unresectable hepatic tumors. *Int J Radiat Oncol Biol Phys* 2009; **74**: 1494-1500 [PMID: 19157721 DOI: 10.1016/j.ijrobp.2008.10.005]
15 **Ho S**, Lau WY, Leung TW, Chan M, Ngar YK, Johnson PJ, Li AK. Partition model for estimating radiation doses from yttrium-90 microspheres in treating hepatic tumours. *Eur J Nucl Med* 1996; **23**: 947-952 [PMID: 8753684 DOI: 10.1007/BF01084369]
16 **Gulec SA**, Mesoloras G, Stabin M. Dosimetric techniques in 90Y-microsphere therapy of liver cancer: The MIRD equations for dose calculations. *J Nucl Med* 2006; **47**: 1209-1211 [PMID: 16818957]
17 **Ho S**, Lau WY, Leung TW, Chan M, Johnson PJ, Li AK. Clinical evaluation of the partition model for estimating radiation doses from yttrium-90 microspheres in the treatment of hepatic cancer. *Eur J Nucl Med* 1997; **24**: 293-298 [PMID: 9143467 DOI: 10.1007/BF01728766]
18 **Lau WY**, Leung WT, Ho S, Leung NW, Chan M, Lin J, Metreweli C, Johnson P, Li AK. Treatment of inoperable hepatocellular carcinoma with intrahepatic arterial yttrium-90 microspheres: a phase I and II study. *Br J Cancer* 1994; **70**: 994-999 [PMID: 7947110 DOI: 10.1038/bjc.1994.436]
19 **Campbell AM**, Bailey IH, Burton MA. Tumour dosimetry in human liver following hepatic yttrium-90 microsphere therapy. *Phys Med Biol* 2001; **46**: 487-498 [PMID: 11229728 DOI: 10.1088/0031-9155/46/2/315]
20 **Martin RC**, Howard J, Tomalty D, Robbins K, Padr R, Bosnjakovic PM, Tatum C. Toxicity of irinotecan-eluting beads in the treatment of hepatic malignancies: results of a multi-institutional registry. *Cardiovasc Intervent Radiol* 2010; **33**: 960-966 [PMID: 20661569 DOI: 10.1007/s00270-010-9937-4]
21 **Fiorentini G**, Aliberti C, Tilli M, Mulazzani L, Graziano F, Giordani P, Mambrini A, Montagnani F, Alessandroni P, Catalano V, Coschiera P. Intra-arterial infusion of irinotecan-loaded drug-eluting beads (DEBIRI) versus intravenous therapy (FOLFIRI) for hepatic metastases from colorectal cancer: final results of a phase III study. *Anticancer Res* 2012; **32**: 1387-1395 [PMID: 22493375]
22 **Tanis E**, Nordlinger B, Mauer M, Sorbye H, van Coevorden F, Gruenberger T, Schlag PM, Punt CJ, Ledermann J, Ruers TJ. Local recurrence rates after radiofrequency ablation or resection of colorectal liver metastases. Analysis of the European Organisation for Research and Treatment of Cancer #40004 and #40983. *Eur J Cancer* 2014; **50**: 912-919 [PMID: 24411080 DOI: 10.1016/j.ejca.2013.12.008]
23 **Petrelli F**, Tomasello G, Borgonovo K, Ghidini M, Turati L, Dallera P, Passalacqua R, Sgroi G, Barni S. Prognostic Survival Associated With Left-Sided vs Right-Sided Colon Cancer: A Systematic Review and Meta-analysis. *JAMA Oncol* 2017; **3**: 211-219 [PMID: 27787550 DOI: 10.1001/jamaoncol.2016.4227]
24 **Venook AP**, Niedzwiecki D, Innocenti F. Impact of Primary (1°) Tumor Location on Overall Survival (OS) and Progression-Free Survival (PFS) in Patients (Pts) with Metastatic Colorectal Cancer (mCRC): Analysis of CALGB/SWOG 80405 (Alliance). *J Clin Oncol* 2016; 34 [DOI: 10.1200/JCO.2016.34.15_suppl.3504]
25 **Wasan HS**, Gibbs P, Sharma NK, Taieb J, Heinemann V, Ricke J, Peeters M, Findlay M, Weaver A, Mills J, Wilson C, Adams R, Francis A, Moschandreas J, Virdee PS, Dutton P, Love S, Gebski V, Gray A; FOXFIRE trial investigators; SIRFLOX trial investigators; FOXFIRE-Global trial investigators, van Hazel G, Sharma RA. First-line selective internal radiotherapy plus chemotherapy versus chemotherapy alone in patients with liver metastases from colorectal cancer (FOXFIRE, SIRFLOX, and FOXFIRE-Global): a combined analysis of three multicentre, randomised, phase 3 trials. *Lancet Oncol* 2017; **18**: 1159-1171 [PMID: 28781171 DOI: 10.1016/S1470-2045(17)30457-6]
26 **Lee MS**, Menter DG, Kopetz S. Right Versus Left Colon Cancer Biology: Integrating the Consensus Molecular Subtypes. *J Natl Compr Canc Netw* 2017; **15**: 411-419 [PMID: 28275039 DOI: 10.6004/jnccn.2017.0038]

Published By Baishideng Publishing Group Inc
7041 Koll Center Parkway, Suite 160, Pleasanton, CA 94566, USA
Telephone: +1-925-2238242
E-mail: bpgoffice@wjgnet.com
Help Desk: https://www.f6publishing.com/helpdesk
https://www.wjgnet.com